Supercontinuum Absorption Spectroscopy for Combustion Diagnostics

Dissertation

Niels Göran Blume

Reactive Flows and Diagnostics

Technische Universität Darmstadt

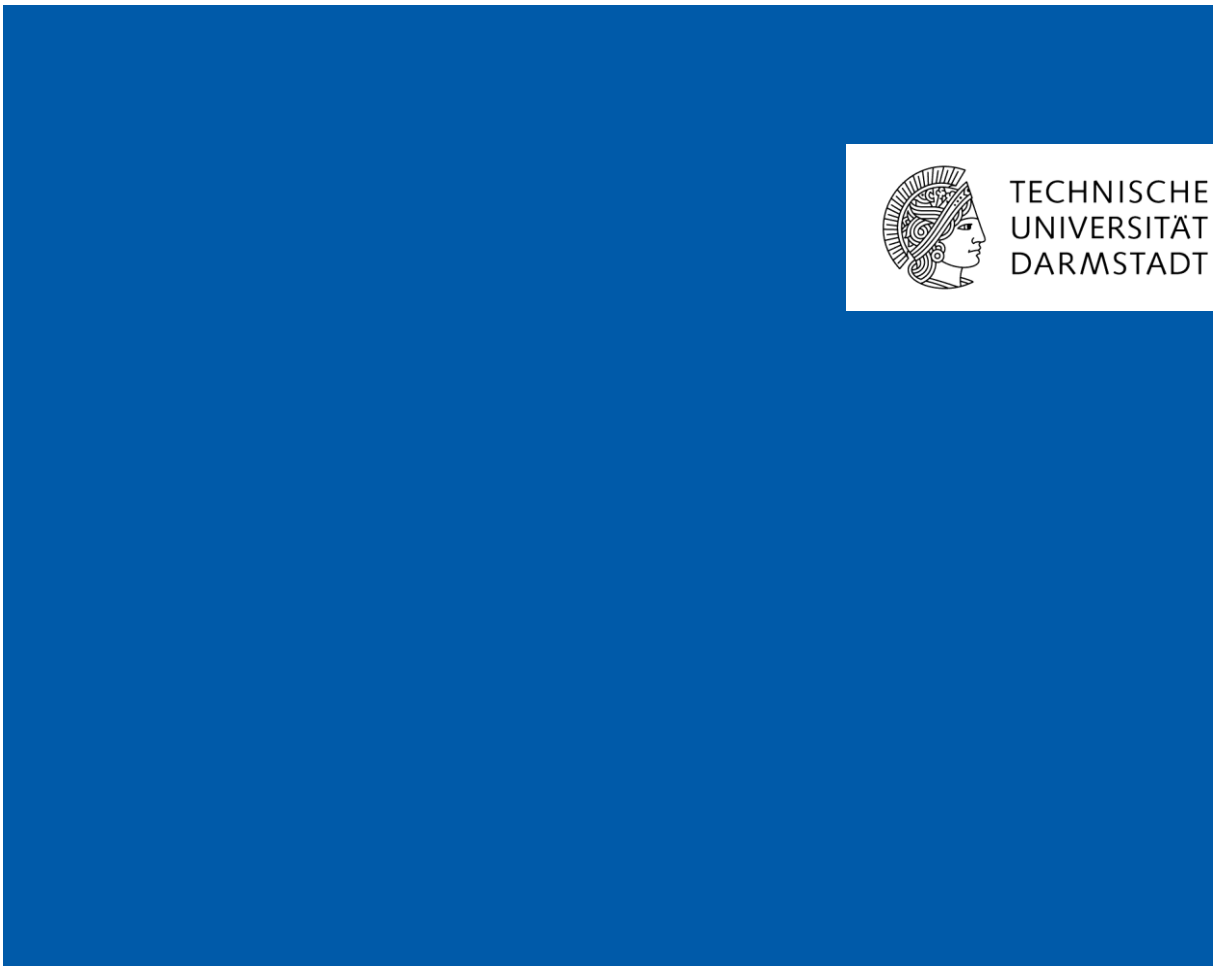

Supercontinuum Absorption Spectroscopy for Combustion Diagnostics

Am Fachgebiet Maschinenbau

der Technischen Universität Darmstadt

zur Erlangung des akademischen Grades eines

Doktor-Ingenieurs (Dr.-Ing.)

genehmigte

DISSERTATION

vorgelegt von

Niels Göran Blume, M.Sc.

aus Göttingen

Berichterstatter:	Prof. Dr. Andreas Dreizler
Mitberichterstatter:	Prof. Christopher S. Goldenstein
Tag der Einreichung:	19.06.2018
Tag der mündlichen Prüfung:	25.09.2018

Darmstadt 2018

D17

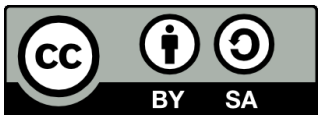

Erklärung / Statement

Hiermit erkläre ich, dass ich die vorliegende Arbeit, abgesehen von den in ihr ausdrücklich genannten Hilfen, selbständig verfasst habe. Ich erkläre außerdem, dass ich bisher noch keinen Promotionsversuch unternommen habe.

English translation for information purposes only:

I herewith declare that I have written the submitted dissertation independently, expect for explicitly quoted sources. I furthermore declare that I have not applied for a PhD before.

Datum / Date: Unterschrift / Signature:

_____ _____

Acknowledgements

First, and foremost, I would like to thank Prof. Andreas Dreizler and Dr. Steven Wagner for the opportunity to pursue a PhD in the field of optical diagnostic systems at the RSM in Darmstadt. Whenever someone asked me before my Master thesis at the RSM (and during the first two month), whether I considered a dissertation a viable option after my graduation, the answer was a clear and decisive “No, no way!”. Simply due to the fact, that up until then, the classes at TU Darmstadt were great, but not “Hands-On” enough, compared to being an engineer in the real-word (Thankfully, GML was born later to change that!). That changed during the Master thesis, quite substantially. I am thankful for creating and fostering that interest in a PhD, and the opportunity to fulfil this interest at the RSM and within the HTPD.

I would also like to thank Prof. Christopher Goldenstein for agreeing to be reviewer for this dissertation, including the necessary visit to Germany and the RSM for the oral defense.

Furthermore, I would like to thank my colleagues at HTPD and RSM, which during the last 5 years have been a pleasure to work with. There surely were times, when I seemed too obsessed with details (or actually was), but I hope it turned out for the best. I would like to especially thank all the members, former and current, of the High Temperature Process Diagnostics Research Group: Felix Stritzke, Sebastian Bürkle, Oliver Diemel, Sani van der Kley, Luigi Biondo, Johannes Emmert and Anna Schmidt - a highly creative and (most of the times) focused group of scientist and colleagues! Not to forget the post-docs: Benjamin Kühnreich, who taught me the basics of absorption spectroscopy and was always interested in trying a new, sometimes rather unusual idea.

As many colleagues before me, and hopefully after me, always stated: The interaction of RSM and EKT (and more recently STFS) is a unique combination, which offers many advantages: from simply overhearing aspects of numerical simulations to full corporation between simulations and experiments: A work environment ideally suited for research. Additionally, I would like to thank the administrative staff and the workshop for their support and flexibility in so many situations.

Alongside these bosses and colleagues, there is a group of people, which supported me unconditionally during this endeavor: first of all Melanie Loddemann, who by now has accepted my unique quirks for quite a few years, and actually seems to like them (sometimes). Furthermore, I would like to thank my family, especially my parents Margrit and Roland, who always got my back and supported me.

Thank you![1]

[1] Especially to those, who I forgot!

"The good thing about science is that it's true whether or not you believe in it."

Neil deGrasse Tyson (1958 - today)

"Contact light"

First words ever spoken on the moon
by Edwin Eugene "Buzz" Aldrin (1930 – today)

"42"

Answer to the Great Question of Life, the Universe and Everything
calculated by Deep Thought after 7.5 million years
The Hitchhiker's Guide to the Galaxy
Douglas Adams (1952 – 2001)

Kurzzusammenfassung

Sensoren und Messsysteme haben in den vergangenen Jahren eine erhöhte Nachfrage erfahren, bedingt sowohl durch striktere gesetzliche Vorschriften als auch durch gegenwärtige technische Trends wie das Internet der Dinge oder Industrie 4.0. Des Weiteren waren zahlreiche große wissenschaftliche Entdeckungen (z.B. der Nachweis von Gravitationswellen) das Ergebnis internationaler Zusammenarbeit auf dem Gebiet der Sensorik und Messsysteme. Die Möglichkeit, prozessrelevante Parameter, vorzugsweise in situ und störungsfrei, zu messen, ist essentiell für die Verbesserung vieler technischer Anlagen. Nur mit genauer Kenntnis der Prozesse kann eine Steigerung der Effizienz und eine Reduktion des Schadstoffausstoßes erreicht werden. Bedingt durch die Entwicklung der letzten Jahre sind die Anforderungen an Messsysteme weiter gestiegen. Viele dieser Anforderungen können nur mittels multi-skalarer Messtechniken mit zeitgleicher Erfassung mehrerer Prozess-Parameter erfüllt werden.

Um derartige Messungen durchführen zu können, ist ein optisches Messsystem oft unerlässlich, im Besonderen für in situ Messungen. Auf Grund ihrer Robustheit und Vielfältigkeit bietet Absorptionsspektroskopie vielfältige Möglichkeiten für derartige Messungen. Darüber hinaus wird, seit der Verfügbarkeit von Supercontinuum Laser Light Sources (SCLs) mit gepulsten breitbandigen Emissionen, die Supercontinuum Laser Broadband Absorption Spectroscopy (SCLAS) entwickelt, welche die Dispersion in der Zeit nutzt, um Spektren zu erfassen. Auf Grund des breiten spektralen Inhalts können mit diesem System viele Größen inklusive Spezies-Konzentrationen, Druck und Temperatur simultan rein optisch gemessen werden. Eine derartig breite spektrale Abdeckung ist außerdem für Messungen in Hochdruck-Umgebungen erforderlich. Ausgehend von einer umfassenden Diskussion der zu Grunde liegenden Effekte und Prozesse wurden notwendige spektroskopische Modelle und Algorithmen entwickelt, um die erfassten Messungen auszuwerten. Ausgehend von diesen Modellen wurden verschiedene Testfälle untersucht, einschließlich statischer Tests zur Quantifizierung von Unsicherheiten, sowie die Vermessung eines quasi-stationären laminaren Brenners. Ausgehend von diesen Experimenten wurde SCLAS anschließend auf transiente Systeme übertragen und für In-Zylinder-Messungen an einem Glas-Motor für die Forschung angewendet.

Zusätzlich, basierend auf den Ergebnissen der Validierung und Anwendungstests, wurden neue spektroskopische Modellierungsansätze entwickelt, um das volle Potenzial der SCL im Allgemeinen und von SCLAS im Speziellen zu erschließen. Diese neuen Modelle wurden mit etablierten Systemen verglichen und als Verbesserung hinsichtlich Komplexität und Rechenaufwand eingestuft. Des Weiteren können die Modelle, anders als Standardmodelle für Gas Absorptionsspektroskopie, auch zur Modellierung von Flüssigkeiten und komplexen, nicht-diskreten Absorbern, wie z.B. Propan und AdBlue, verwendet werden.

Insgesamt konnte die Messtechnik SCLAS sich gegenüber etablierten Messtechniken beweisen und innovative Messansätze für in situ Hochdruck- und Hochtemperatur-Messungen konnten entwickelt, erprobt und validiert werden.

Abstract

During recent years, sensors and diagnostic systems have seen an increase in demand, due to stricter legislative regulations for certification, as well as industry trends, such as Internet of Things and Industry 4.0. In addition, recent scientific discoveries (for example gravitational wave detection) are the result of international collaborations in the field of sensors and diagnostics. The ability to measure process-relevant parameters, preferably in situ and disturbance-free, is essential for improving performance of various systems, from chemical plants to internal combustion engines and energy power plants. Only with precise knowledge of the parameters of these processes, an improvement in efficiency and a reduction of pollutant emissions is achievable. Given the process optimizations in the last decade, the conditions under which a diagnostic system has to obtain valid measurements have significantly harshened. Most of the requirements can only be fulfilled with multi-scalar and multi-species measurements.

To obtain such measurements, an optical diagnostic system is often unavoidable, especially for in situ measurements. Given its robustness and versatility, absorption spectroscopy offers great possibilities for such measurements. With the recent arrival of Supercontinuum Laser Light Source (SCLs), which offer broad spectral coverage in pulsed form, the concept of Supercontinuum Laser Broadband Absorption Spectroscopy (SCLAS) was developed, relying on a dispersion in time to record optical spectra. Given the broad spectral coverage, it is possible to derive multiple scalars including species concentrations, pressure and temperature purely optical. Furthermore, such broad coverage is essential for measurements in high-pressure environments (i.e. within the cylinder of an internal combustion engine).

Based on an extensive discussion of the underlying effects and processes, necessary spectroscopic models and algorithms were developed to process the obtained measurements. Based on these models, several test cases for SCLAS were investigated, including static tests to quantify accuracy and uncertainty, as well as steady-state laminar flames. Based on the knowledge of these experiments, SCLAS was transferred to transient systems including high-pressure cells and was applied for in-cylinder measurements at a transparent engine test bed.

In addition, based on the results of the validation and application tests, new spectroscopic models were developed to fully utilize the potential of SCLs in general and SCLAS in particular. These new models were evaluated against standard practices and found to be an improvement with regards to complexity and speed of data-processing. Furthermore, these models, as opposed to standard gas absorption spectroscopy models, allow for modelling of liquids as well as complex non-discrete absorbing species, such as propane and AdBlue (DEF).

Overall, the diagnostic technique SCLAS was proven in comparison to established techniques, while advanced approaches to measure in situ in high-pressure high-temperature processes were developed and tested.

Contents

List of Tables

List of Figures

List of Abbreviations

Abbreviations	Explanation
Absorption feature	Combination of closely spaced absorption lines, that almost completely overlap (except at very low pressures)
Absorption line	Individual quantum transition, that corresponds to a specific energy difference and therefore a specific wavenumber
AdBlue	Commercial name of aqueous urea solution for exhaust gas after treatment
ADC	Analog-Digital Converter, IC used to convert analog signals to digital values
AOTF	Acusto-optical tunable filter
CAD	Crank-Angle Degree
DCF	Dispersion Compensating Fiber
DCM	Dispersion Compensating Module
DEF	Diesel Exhaust Fluid (additive to aid with exhaust after treatment)
DFB	Distributed Feedback laser diode
DLaTGS detector	Deuterated Lanthanum α Alanine doped TriGlycine Sulphate (DLaTGS) optical detectors (pyro-electric detector in the MIR)
FPGA	Field-Programmable Gate Array
FTIR	Fourier Transform Infrared Spectrometer
FWHM	Full Width at Half Maximum
HeNe	Helium-Neon laser at 632.8 nm
HITEMP	High-Temperature Molecular Spectroscopic Database
HITRAN	High-Resolution Transmission Molecular Absorption Database
IC	Integrated circuit
ICE	Internal Combustion Engine
IHM	Indirect Hard Modelling
Indicom	Engine Management System of the Research ICE used in the experiments

InGaAs detector	Photo diode using indium(In) gallium(Ga) arsenide(As) as the light sensitive material
LDV	Laser Doppler Velocimetry
LOS	Line of Sight
LUT	Look-Up Table
MFC	Mass Flow Controller
MI	modulation instability-induced breakup
MIR	Mid-Infrared Light (wavelengths from 3 µm to 50 μm)
MMF	Multi-Mode Fiber
NIR	Near Infrared Light (wavelengths from 780 nm to approx. 3 μm)
PCF	Photonic Crystal Fiber
RF	Radio Frequency
RPM	Rounds per Minute
SCL	Supercontinuum Laser Light Source
SCLAS	Supercontinuum Broadband Laser Absorption Spectroscopy
SMF	Single-Mode Fiber
SNR	Signal to Noise Ratio
TDLAS	Tunable Diode Laser Absorption Spectroscopy
(TE-)-ext-InGaAs	(thermo-electrically cooled) extended InGaAs photo detector
VCSEL	Vertical-Cavity Surface Emitting Laser diode
ZDW	Zero Dispersion Wavelength of a fiber, mostly used with PCFs

Nomenclature

Sign	Explanation
A_{21}, B_{21}, B_{12}	Einstein coefficients for probabilities of transitions
$Abs(\nu)$	Absorption of light at wavenumber ν when passing through a medium
c	Speed of light in vacuum (~299792458 m/s)
c_2	HITRAN-specific constant $(h \cdot c)/k$
E	Energy of a specific state of a molecule
f	Frequency (usually of a photon, unless otherwise noted)
h	Planck constant , relating energy of a photon to its frequency ($6.62607015 \times 10^{-34}$ J·s)
k_B	Boltzmann constant ($1{,}380649 \cdot 10^{-23}$ J/K)
L	Length of absorption path
m	Molecular mass
N	Number of molecules in a specific energy state
N	Temperature coefficient for collisional broadening as used by HITRAN
n_i	Number density of a species i
OD_e	Spectral absorbance to base e relating intensities of light entering and exiting a homogenous medium
p	Pressure (in different cases referring to species-specific partial pressure or system pressure)
P_i	Partial pressure of a specific species
q_i	Fractional quantity of a molecule i in a mixture
$Q(T)$	Partition function dependent on temperature as used by HITRAN
S(T)	Transition-specific absorption strength (unit: $1/(cm^2 \cdot atm)$), which also a function of temperature
T	Temperature
$Tr(\nu)$	Transmission of light at wavenumber ν when passing through a medium

T_{ref}	Reference temperature for normalized line strength tabulation as used by HITRAN; for HITRAN the reference temperature is $T_{ref} = 296\ K$.
X_i	Mole fraction of species i in a mixture
	Greek Lettering
α	Absorption coefficient per unit length
γ_C	Parameter for collision line broadening
γ_D	Parameter for Doppler line broadening
γ_N	Parameter for natural line broadening
δ_i	Pressure shift coefficient for species i
λ	Wavelength, usually expressed in nanometers (nm)
ν	Wavenumber, usually expressed in (1/cm)
ν_0	central vacuum wavenumber of a specific transition
τ	Lifetime of a specific state
$\phi(\nu)$	Absorption line-shape function

1 Introduction

During recent years, diagnostic systems, whether highly advanced optical systems, or rather simple electro-chemical sensors, have seen a significant increase in applications and industry use. Throughout these years, the market for sensors in general has seen an annual growth rate of over 30 % and is expected to rise to a volume of almost $50 billion by the year 2021 [1]. Fiber optic sensors are expected to reach a market volume of $3.2 billion by the year 2021 [2]. Aside for the commercial use, sensors are at the center of every scientific research project and every scientific discovery. Endeavors such as decoding the human genome or detecting the smallest of particles and their interactions with the Atlas detector at the *Large-Hadron Collider* (LHC) have only been possible due to advancements in sensors and sensor technologies [3]. When comparing early genome sequencers from 2001 with current systems (2015), the increase in performance and efficiency of the sequencing has exceeded Moore's Law[1] [4] allowing for significant advancements in the fields of genetics, biology and bio-technology. Based purely on optical measurement techniques, LIGO observatories detected gravitational waves in 2016 due to unprecedented performance of the interferometric sensor system [5]. While these scientific flagship projects show the potential of sensor technology, the aforementioned increase in sensor utilization within the industry is mainly due to two factors:

- Significantly extended use of sensors in machines and processes in the context of *Industry 4.0* [also known as (I)IoT – "(Industrial) Internet of Things"]
- Overall increase in legislative restrictions and laws limiting the emission of specific gases and pollutants, as well as certification of devices to adhere to these standards

While both causes share the need for extensive instrumentation of the processes involved, the gathered data from the various sensors are aimed at different objectives. In the case of *Industry 4.0,* the data gathered are mainly utilized to improve the performance of systems and processes or generate insights for predictive maintenance. In the case of pollutant emissions, diagnostic systems are applied to ensure compliance with applicable laws, for either certification or constant monitoring. Alongside this general increase in usage of diagnostic systems, there has been a trend of transferring laboratory system into industry-suited systems. These systems usually provide improved performance in terms of precision and accuracy or allow measurements that were previously not possible. Furthermore, advanced optical systems are allowing *in situ* insights into processes, where before only extractive or secondary (indirect) measurements were possible. To give an example of such a development, one can look at car engine exhaust gas analysis. Only a couple of years ago the de facto standard to analyze exhaust gases was *bag analysis* (collecting exhaust gas in large bags at the tail pipe and determining

[1] Moore's Law: Original based on integrated circuits, Moore's Law states that the number of integrated transistors in integrated circuits doubles approximately every two years. In the case of genome sequencing, it is assumed that the cost of sequencing the complete human genome is reduced to half every two years by improvements in the sequencing methods and systems.

composition averaged over different operating conditions of the car). Current (and future) legislation calls for direct measurements of the exhaust gas flow to ensure compliance with laws at all times and operating conditions. This development has caused a need for high-precision high-accuracy instrumentation for *in situ* gas diagnostics, especially aimed at combustion or, more general, chemical processes.

Alongside this increase in legislative regulations, companies strive more than ever to utilize resources to its fullest capabilities, increasing process efficiencies further and further. These increments are only possible with extensive and detailed process instrumentation and process control, which is, as mentioned earlier, part of the current trend towards an (I)IoT. Extensive knowledge of operational performance and system health is becoming increasingly important for efficient and effective operation of machinery and (chemical) processes. Similar trends can be seen for devices, down to the consumer level (i.e. fitness trackers). Much of these sensors data becomes part of what is commonly known as *Big (Analog) Data* as well as *Machine Learning / Artificial Intelligence* and is considered to be at the center of technological developments in the coming years.

Overall, it can be stated that any improvement in performance and applicability of diagnostic systems, is a welcome, if not required development to be able to address current and future challenges. Any diagnostic system or tool aiding in scientific discovery and the advancement of knowledge is considered one of *Grand Challenges for Engineering* [6].

Current developments in combustion such as *homogeneous-charge compression-ignition engines* (HCCI engines) or down-sized engines with an increased ratio of surface to volume and novel approaches in the area of exhaust gas after treatment, for example use of *AdBlue* as a *Diesel Exhaust Fluid* (DEF) yield a specific need for diagnostic systems for these processes. The process conditions itself require the sensor hardware to withstand harsh conditions and disturb the process as little as possible. The processes themselves require diagnostics options for high-pressure gas systems of varying composition as well as temperature and pressure measurements with sufficient time resolution. These conditions are also present in numerous chemical reactors and processes requiring similar sensor systems. A suitable diagnostic system therefore needs to be preferably *in situ* and require only optical access to the process. Since these processes become increasingly complex, combined diagnostics (for example all major components of the gas matrix at once) can offer new insights into the underlying fundamental phenomena.

Absorption spectroscopy, and *Tunable Diode Laser Absorption Spectroscopy* (TDLAS) in particular, has proven to be a valuable technique to fulfil these requirements for *in situ* gas measurements in harsh processes and systems. TDLAS systems have, for example, been applied to environmental process [7, 8], to study exhaust gas after treatment systems [9] and measure gas composition in food packaging (Modified Atmosphere Packaging, MAP) [10–13], as well as perform breath analysis for clinical diagnostic purposes [14]. Since TDLAS is based on basic physical principles and obtains it measurements directly, the technique can be considered suitable for a national transfer standard [15]. Due to its nature, TDLAS usually covers only a smaller portion of the light spectrum, in each case aimed at a specific species, and is therefore

limited in its applicability to high-pressure environments. Other cases with limited applicability include systems, where the gas matrix contains gases with overlapping absorption features, hindering a clear distinction of different gases.

With the inception of a novel pulsed, completely fiber-based broadband laser light source, referred to as *Supercontinuum Laser Light Source* (SCL), which covers a broad section of the visible (VIS) and near-infrared (NIR) spectrum [16], an innovative and unique diagnostic approach based on absorption spectroscopy and optical dispersion in fibers was introduced: *Supercontinuum Laser Broadband Absorption Spectroscopy* (SCLAS). While the approach itself was proposed over 40 years ago (see [17] and Chapter 2.6 for details), only recent advancements in the field of high-speed data acquisition and high-speed photo diodes, in combination with the aforementioned Supercontinuum Light Sources (SCL), barely allowed for actual implementation of this technique. The SCL itself has already become a versatile tool for optical diagnostics, for example Optical Coherence Tomography (OCT) in ophthalmology [18, 19], solar cell characterization [20] or food research [21]. Most of these use cases however don't resolve individual pulses, but use the source as a continuous light source, whereas SCLAS resolves each individual pulse (at pulse rates up to MHz).

While the inception and development of SCL sources allowed for the basic principle of SCLAS to be implemented for the first time, significant components of a fully usable spectrometer were still missing, including for example strategies for post-processing the recorded spectra. To be able to fully utilize the potential of SCL sources for spectroscopy, it was necessary to develop new ways of evaluating recorded data and handling broad absorbers (such as gaseous fuels like propane or the DEF *AdBlue*). Many of these issues will be addressed throughout this dissertation and additional ideas for explorative uses of the SCL will be given towards the end. Without addressing these issues and developing ideas for SCL's potential, the full advantage of SCLAS can hardly be utilized. SCLAS itself should become a new, versatile and proven tool for applied and fundamental research in combustion and reactive flows due to its unique abilities and its solemn reliance on fiber-components. By utilizing fiber components only, SCLAS is ideally suited for applications in harsh environments, such as chemical process plants and large combustion facilities, and can easily benefit from advancements in the fiber-optical telecommunication industry. For example, a single SCLAS system could be used in a sequential manner at multiple measurement locations using fiber-optic switches. The system would distribute the light to different locations after each other, while relying only on a system consisting of SCL light source, detection assembly and data acquisition system.

In terms of the underlying spectroscopy, SCLAS marks initially an advancement from approaches relying on single or few absorption features such as TDLAS [22–32]. A review presenting the current state of research in this area is recommended as an overview for combustion related infrared-absorption based sensing [33]. Alternative means of broadening the spectral coverage including VCSEL-laser diodes [34] and dual-frequency combs [35, 36]. Pushing towards broader spectral coverage (on the order of hundreds, if not thousands of absorption features the specific characteristics of SCLAS need to be addressed separately and

additional information contained within the recorded spectra need to be taken advantage of. When applying line-based spectral models to broadband spectra, the data processing needs to be improved and modified to handle such amounts of data [37]. In the context of broadband absorber species, a novel approach using *Indirect Hard Modelling* (IHM) will be discussed and applied to different scenarios. Developing such new approaches to simulate spectra of molecules, departing from constraint models such as HITRAN [38], requires fundamental investigations into the feasibility and reliability of said models.

While the NIR region of the optical spectrum is proven ground for spectroscopic diagnostics, the *mid-infrared* region (MIR) offers several advantages in terms of sensitivity and the availability of fundamental absorption bands for various molecules. While this in itself is promising, the required fiber technology has not yet sufficiently improved to allow comparable performance to NIR components (significantly higher attenuation and limited availability of options for in-fiber dispersion). With recent developments in the supercontinuum laser light generation, MIR supercontinuum laser light sources have become available, both as research systems [39, 40] and commercially [41]. To take advantage of these MIR SCLs in the context of SCLAS, unfortunately, significant development will be required to devise comparable means of dispersion generation in the MIR, while still maintaining other key parameters such as pulsed light and all-fiber systems. Despite this rather long-term development goal, current research has already shown, that the NIR region provides still opportunities for significant advancements of NIR-SCL sources by for example the utilization of all-normal dispersion supercontinuum-generating *Photonic Crystal Fibers* (PCFs) [42].

Given that SCLAS is able to record broadband spectra, it is possible to derive multiple parameters (pressure, temperature, species concentration) for multiple species simultaneously. Furthermore, SCLAS is ideally suited for high pressure and high temperature environments providing sufficient time resolution for the analysis of chemical processes. This diagnostic technique can therefore prove itself as a very valuable tool for the current and upcoming research in combustion and adjoining fields.

1.1 Aim and Overview of Dissertation

Given the broad, but largely unexplored field of SCLAS, this dissertation aims at providing a conclusive body of work ranging from source characterization to implementation and application in combustion research. By covering such a wide range of topics, it is possible to provide the basics of this novel technique alongside its validation and verification including uncertainty analysis, as well as potential unique and new spectroscopic approaches to benefit from the broad spectral coverage. The overall aim is to further establish SCLAS as a valuable and versatile diagnostic system within the context of absorption spectroscopy and optical measurement systems, while providing new insights into the technique itself and its potential for future use cases and developments.

The following work within this dissertation is structured as follows:

Chapter 2 will provide the fundamentals of spectroscopy, SCLAS and other topics required for the work presented in this dissertation. This chapter also includes a detailed description of the underlying processes of the SCL light source and additional components of a SCLAS system as well as specific fiber components and data acquisition systems. Parts of this section are published in Blume et al. [43].

Chapter 3 focuses on the unique Supercontinuum Laser Light Source utilized in SCLAS and will provide measures and characteristics of its performance and behavior required to develop a SCLAS spectrometer and implement necessary post processing.

Chapter 4 discusses the aforementioned post processing in more detail and provides an overview of several techniques used to handle SCLAS data. Furthermore, it presents challenges accompanying these post-processing routines unique to SCLAS or the SCL itself. Parts of this section are published in Blume et al. [37] and Emmert, Blume et al. [44].

Chapter 5 presents fundamental experiments based on gas cells and generic burners to evaluate the performance of SCLAS in the context of gas diagnostics and multi-parameter multi-species measurements. This experimental section is followed by a discussion of the uncertainties of SCLAS measurements and their influence on the following experiments and findings. Parts of this section are published in Blume et al. [45].

Chapter 6 will present SCLAS experiments and investigations into high-pressure processes using a gas cell for transient processes and a research-grade *Internal Combustion Engine* (ICE).

Chapter 7 will present and evaluate explorative diagnostic approaches for future use cases of SCLAS and their initial testing. These approaches utilize the broad spectral coverage in the context of broad absorber species (such as *AdBlue* and propane) as well as innovative approaches to increasing the evaluation speed of SCLAS measurements.

Chapters 8 and 9 will provide a summary of the presented work and its integration within the field of combustion research and diagnostic system development, followed by an outlook regarding future developments in the context of the Supercontinuum Light Source (SCL) as well as SCLAS.

2 Fundamentals

Before discussing individual aspects of SCLAS and accompanying experiments in detail, it is necessary to provide the fundamentals of this unique diagnostic system, mainly the underlying spectroscopic principles as well as fundamentals associated with the utilized Supercontinuum Light Source (SCL). Throughout this chapter [46–49] will be used as the main sources for the fundamentals. Specific details, that are especially relevant to a specific section of this work, are marked as such and linked to the relevant chapters. In addition to the main sources, literature sources are cited for each individual topic.

After discussing the fundamentals of absorption spectroscopy in general, different approaches to modelling absorption spectra are discussed. Within this topic, it is necessary to distinguish between discrete and non-discrete absorption spectra. When individual absorption features (which in itself could be a combination and overlay of multiple individual absorption lines) are sparsely distributed across the relevant portion of the optical spectrum, it is feasible and advantageous to model these lines separate from each other (see details in Chapter 2.2). In the case of non-discrete absorption spectra (as common with more complex molecules, for example propane), techniques need to be employed that depart from the idea of modelling individual features and rather focus on the overall shape of a spectrum (see details in Chapter 2.3). Since SCLAS utilizes Supercontinuum Light Sources (SCLs), fundamentals of such lights sources are important for this work and are discussed in Chapter 2.4. With basics of dispersion generation and characterization covered in Chapter 2.5, all essential components of a SCLAS diagnostic system have been covered and details of the combined application are presented in Chapter 2.6. The chapter will close with a short discussion of FTIR spectroscopy (see Chapter 2.7), since this spectroscopic instrument is essential for developing the advanced spectral modelling approaches discussed further in Chapter 7.

2.1 Absorption Spectroscopy

Given quantum mechanics, it is known, that molecules are only allowed to be in certain energetic states described by their quantum numbers. When transitioning from one such state to another, the specific energy for this transition is either to be absorbed or to be emitted. Such an energy transfer can occur in multiple ways (for example by collision with other molecules). In the case of optical sensors, this transition usually occurs via absorption or emission of a photon of the transition-specific energy difference ΔE, which corresponds to a specific wavenumber ν according to Equation (2.1).

$$\Delta E = E'' - E' = h \cdot c \cdot \nu \tag{2.1}$$

where E'' refers to the energy of molecule in the final state of the transition and E' to the energy of the molecule in the initial state of the transition.

This energy transfer can occur via one of three different ways (see also Figure 2.1):

- Spontaneous Emission
- Stimulated Emission
- Absorption

In the case of spontaneous emission, a molecule from a state of higher energy E'' transitions into a state of lower energy E'. This reduces the internal energy and results in a positive energy balance, emitting a photon according to

$$\Delta E = h \cdot f = h \cdot {}^{c}/_{\lambda} = h \cdot c \cdot \nu \tag{2.2}$$

where ΔE refers to the energy difference of a molecule between two states, h to the Planck constant, f to the frequency, λ to the wavelength and ν to the wavenumber of the photon.

In the case of stimulated emission, the transition occurring is identical to the case of spontaneous emission, while the transition is not spontaneous but rather stimulated by a second resonant photon (a photon of the identical transition-specific energy ΔE). This results in the emission of an additional photon, which is coherent to the incident photon. This principle is utilized in LASERS (Light Amplification by Stimulated Emission of Radiation). The third case is describing the absorption of a photon (of the *correct* energy and therefore wavenumber for the specific transition). This case is the core principle of absorption spectroscopy. By knowing at which wavenumbers specific molecules absorb light under given conditions, it is possible to determine the presence as well as additional parameters of that specific species from the light absorbed during transmission.

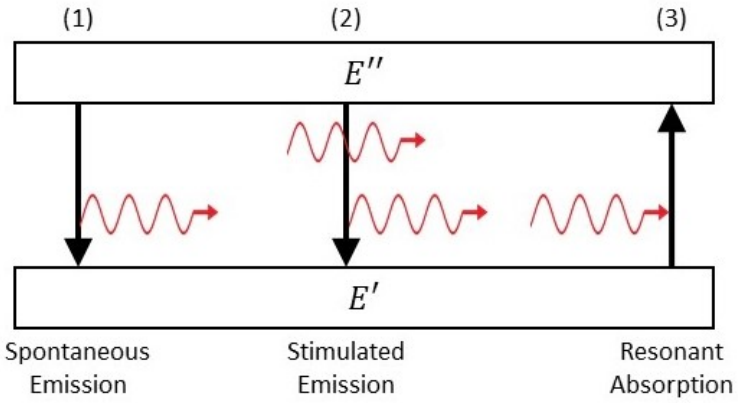

Figure 2.1 Schematic representation of energy transitions between different energy states of a molecule: spontaneous emission, stimulated emission and resonant absorption

Given that these three effects occur simultaneously, it is possible to determine a transition rate between the two states. Assuming N_2 molecules in the state of energy E_2 and N_1 molecules in the state of energy E_2, the likeliness of transitions between the states 1 and 2 can be described with the help of the Einstein Coefficients A and B and the spectral density of incident light. The

Einstein Coefficient A_{21} describes the probability of a spontaneous emission, independent of incident spectral density, whereas the coefficients B_{21} and B_{12} in combination with the spectral intensity give the probabilities of stimulated emission or absorption. The three rates of transition are described in Equations (2.3) to (2.5).

$$\text{Spontaneous Emission: } \left(\dot{N}_2\right)_{spon} = N_2 \cdot A_{21} \tag{2.3}$$

$$\text{Stimulated Emission } \left(\dot{N}_2\right)_{stim} = N_2 \cdot B_{21} \cdot \varrho(\nu) \tag{2.4}$$

$$\text{Absorption } \left(\dot{N}_1\right)_{abs} = N_1 \cdot B_{12} \cdot \varrho(\nu) \tag{2.5}$$

The individual energy states of a molecule can be calculated by solving Schrödinger's equation, which also, given its quantization, provides a nomenclature of different states and transitions based on the change in quantum numbers (). Since rotational transitions are generally smaller in terms of energy difference than vibrational transitions, rotational transitions give a so-called *fine structure* to vibrational transitions. Transitions with identical rotational quantum numbers in ground and excited state ($\Delta J = 0$) are referred to as the *Q-branch*, whereas a change of the rotational quantum number of $\Delta J = +1$ is referred to as the *R-branch* and consists of transitions towards larger wavenumbers. The *P-branch* on the other hand correlates to changes in the rotational quantum number of $\Delta J = -1$ and therefore lies in the direction of the lower wavenumber side of the *Q-branch*. For IR spectra, transitions usually consists of changes both in the rotational and vibrational quantum numbers, and are therefore often referred to as *rovibrational transitions*.

Beer-Lambert Law for Absorption

The amount and composition of a sample in a light path and the population of different energy states (Boltzmann distribution) influence the intensity and shape of absorption at a specific wavenumber. These parameters are external and independent of the specific molecule. The position of an absorption line and its relation to other absorption lines of the same molecule are on the other hand highly specific to the individual molecule. The relationship between the light intensity entering (I_0) and exiting (I) a homogeneous medium along an absorption path of length L is given as follows:

$$\text{Transmission } Tr(\nu) = {I(\nu)}/{I_0(\nu)} \tag{2.6}$$

$$\text{Absorption } Abs(\nu) = 1 - Tr(\nu) = 1 - {I(\nu)}/{I_0(\nu)} \tag{2.7}$$

The Beer-Lambert law, assuming a constant absorption along the absorption path ($dI/dL = -\alpha \cdot I$), further describes this relationship.

$$I(\nu)/I_0(\nu) = \exp(-OD_e(\nu)) \tag{2.8}$$

where the term OD_e is referred to as *absorbance (to base e)*. The (spectral) absorbance itself is a function of various parameters

$$OD_e = \alpha \cdot L = f(\nu, q, L, p, T) \tag{2.9}$$

where ν refers to the wavenumber, q describes the composition of the medium (concentrations of various components), p is the pressure and T is the temperature of the medium. It is necessary to account for the complete medium composition due to individual effects of all present species on the spectrum of a single species (see later on in this chapter).

To describe the absorbance of a specific molecule further, it is necessary to distinguish between spectra consisting of discrete absorption features and spectra consisting of continuous absorption features. Molecules such as methane (CH_4), water (H_2O) or acetylene (C_2H_2) exhibit discrete absorption spectra (see Figure 2.2) and are modelled accordingly. Other combustion relevant species, for example propane (C_3H_8) or iso-octane (also referred to as 2,2,4-Trimethylpentane, C_8H_{18}) (see Figure 2.3), show continuous absorbance spectra. [46–49]

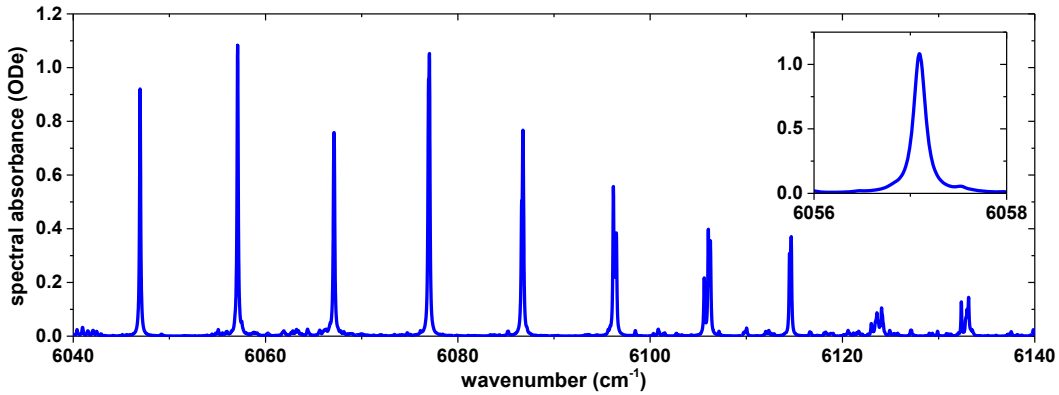

Figure 2.2 Example of a discrete spectrum of methane around 6090 cm^{-1}. Calculated using HITRAN 2012 [38] for an absorption length of 0.25 m and a concentration of 10 % methane.

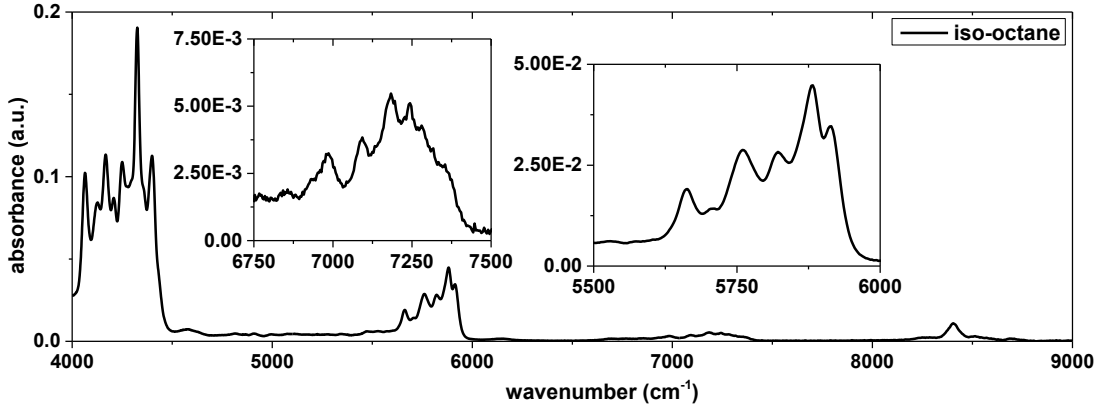

Figure 2.3 Example of a continuous spectrum of gaseous iso-octane ranging from 4000 cm^{-1} to 9000 cm^{-1}, measured with an FTIR Bruker Vertex V80V.

2.2 Modelling of Discrete Absorbance Spectra

Given a discrete absorption spectrum, the spectral absorbance of a single transition, or absorption line, can be described by

$$OD_e = \alpha \cdot L = (S \times \phi(\nu) \times P_i) \cdot L \tag{2.10}$$

where S refers to a transition-specific absorption strength (unit: $1/(cm^2 \cdot atm)$), $\phi(\nu)$ to a line-shape function describing the specific shape of this transition and P_i to the partial pressure of the species. HITRAN [38], which provides extensive data for absorption spectroscopy for various molecules, utilizes a number-density normalized absorption strength. Equation (2.10) can therefore be reshaped by substituting the number density of the absorber instead of the partial pressure of the absorber (accompanied by changed in the unit of S) to

$$OD_e = \alpha \cdot L = (S \times \phi(\nu) \times n_i) \cdot L \tag{2.11}$$

where S refers to a transition-specific absorption strength (unit: $cm^{-1}/(molecule \cdot cm^{-2})$), $\phi(\nu)$ to a line-shape function describing the specific shape of this transition and n_i to the number density of the species.

Assuming different models (with varying complexity) for individual species, it is possible to calculate species transitions based on the individual changes in quantum numbers. Ranging from simple models for diatomic molecules to complex models for polyatomic molecules (depending on the type and shape of the molecule), such calculations allow for the generation of databases and derivation of various parameters to model absorption spectra. For rovibrational spectra (IR spectra) a simple model is a vibrating rigid rotor, based on the Born-Oppenheimer approximation considering rotation and vibration separately. However, such models always contain approximations or assumptions to a certain degree, influencing the precision and accuracy of derived parameters. Such calculations will also become cumbersome and extensive, especially in the case of *hot bands*, which involve excited quantum states as initial states of a transition. Given these limitations and to verify numerically derived spectra, it is often necessary to measure these parameters as well (see Chapter 2.7). Given that these calculations only include the transition energy difference, no specific line shape is assumed and the resulting spectrum is often referred to as a *stick spectrum*, since the absorption lines do not possess any width, given that no broadening effects are modelled.

Before further addressing line shape functions and their underlying causes, it is helpful to correlate the absorption coefficient α with fundamental physical and molecular parameters. It is possible to correlate the absorption coefficient, assuming a rectangular line shape function with line width of $\delta\nu$ to fundamental parameters, including Einstein coefficients as follows (see [46] for details):

$$\alpha = \frac{h \cdot \nu}{c} \cdot \frac{1}{\delta\nu} \cdot n_1 \cdot B_{12} \cdot \left(1 - \exp\left(-\frac{h \cdot \nu}{k \cdot T}\right)\right) \tag{2.12}$$

where h refers to the Planck constant, ν to the central wavenumber of the transition, c to the speed of light, $\delta\nu$ to the line width, n_1 to the number density of molecule in state 1, B_{21} to the Einstein B Coefficient for the transition, k to the Boltzmann constant and T to the temperature.

To further simplify the description of absorption spectra, it is possible to establish normalized line shape functions, representing the individual line shape. Such a normalized line shape function $\phi(\nu)$ adheres to the following conditions:

$$\int_0^\infty \phi \, \delta\nu = 1 \tag{2.13}$$

When substituting this generic line shape function into Equation (2.12) the equation can be rewritten as

$$\alpha = \frac{h \cdot \nu}{c} \cdot \phi(\nu^*) \cdot n_1 \cdot B_{12} \cdot \left(1 - \exp\left(-\frac{h \cdot \nu}{k \cdot T}\right)\right) \tag{2.14}$$

where ν^* describes the specific wavenumber as opposed to ν describing the transition central wavenumber.

Integrating Equation (2.14) over the complete absorption line, it is possible to determine an integrated absorption or line strength for this particular absorption line, which in combination with the line shape function, describes the specific transition (aside from number density and temperature dependence of the line strength).

$$\int_0^\infty \alpha(\nu^*) \, \delta\nu^* = S_{12} \tag{2.15}$$

$$S_{12} = \frac{h \cdot \nu}{c} \cdot n_1 \cdot B_{12} \cdot \left(1 - \exp\left(-\frac{h \cdot \nu}{k \cdot T}\right)\right) \tag{2.16}$$

$$\alpha(\nu^*) = S_{12} \cdot \phi(\nu^*) \tag{2.17}$$

As stated before, this line strength is characteristic for individual transitions as well as dependent on temperature and the absorber density. It is therefore common, and also the case for HITRAN [38], to tabulate a normalized and scalable version of this parameter. Given that the line strength is normalized by absorber density and given for a specific temperature, it can be scaled to other temperatures with the help of partition function $Q(T)$. In the case of HITRAN, a reference temperature of $T_{ref} = 296\,K$ is used [38].

$$S_{ij}(T) = S_{ij}\left(T_{ref}\right) \cdot \frac{Q\left(T_{ref}\right)}{Q(T)} \cdot \frac{exp(-c_2 \cdot E''/T)}{exp\left(-c_2 \cdot E''/T_{ref}\right)} \cdot \frac{1 - \exp\left(-c_2 \cdot \nu_{ij}/T\right)}{1 - \exp\left(-c_2 \cdot \nu_{ij}/T_{ref}\right)} \tag{2.18}$$

where c_2 refers to the constant $(h \cdot c)/k$, E'' to the lower state energy and ν_{ij} to the characteristic wavenumber of the transition $i \rightarrow j$.

For the remainder of this work, the central wavenumber of a transition will be labeled ν_0, whereas the wavenumber, for which a certain parameter is calculated will be referred to as ν.

Given the need to simulate absorption spectra sufficiently for numerical fitting to recorded spectra, it is necessary to allow storage and retrieval of relevant coefficients in databases in an efficient manner. For this, as already shown for the line strength, a normalization is applied to the individual coefficients. Furthermore, as will be referred to later, the HITRAN database, as one of many, requires certain considerations, due to its users and therefore its focus. HITRAN is aimed at atmospheric research and consequently focusses on relevant effects for that community. One example of this is the focus on lower temperature absorption lines while omitting several *hot bands* from tabulation. To address this, the HITEMP database [50] is available accounting for significantly more absorption lines, which are only relevant in case of higher temperatures. Nevertheless, it is feasible to use HITRAN, in combination with other databases, such as *GEISA* (Gestion et Etude des Informations Spectroscopiques Atmosphériques; Management and Study of Atmospheric Spectroscopic Information) [51, 52]. For simplicity, it is assumed that HITRAN is used in the spectroscopic evaluation, while clearly marking situations where this necessitates a simplification or limitation of the applicability. Additionally, improved line data is available for various species and conditions [53, 54]. Since improved line data are often limited to specific transitions, that are relevant for specific applications, its influence on broadband system such as SCLAS is limited and incorporating said data into the post-processing is often cumbersome.

Lineshape modelling and functions

After establishing a measure for the strength of an absorption line (also representative of the probability of absorption at that frequency), it is necessary to discuss effects that lead to a broadened line shape function $\phi(\nu)$. For this it is necessary to separate two effects on an absorption line due to the thermodynamic state and composition of a gas mixture. Several effects cause a broadening of the line shape (FWHM in Figure 2.4), while others cause a shift of the complete line itself (a different central line position than theoretically calculated vacuum wavenumber, ν_0 in Figure 2.4).

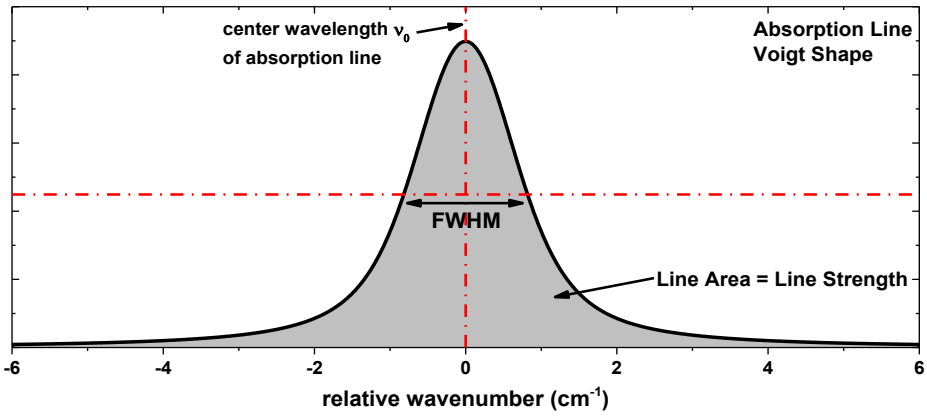

Figure 2.4 Schematic of a Voigt line shape function characterized by full width-half max (FWHM), line position and line area

Since line shape functions are defined to account for the specific shape of an absorption line, these functions can be used for the derivation of parameters that influence the shape of said line. When only the area under an absorption line is measured (often called *area fitting*), it is possible to determine the number density of a species, given knowledge of pressure and temperature acc. Equation (2.17) or, given pressure and number density, the temperature can be derived. As soon as the spectroscopic model is able to account for specific effects via line shape functions, the available measurements are numerous, including pressure, temperature and species concentration. [46–49]

2.2.1 Line Shifting Effects

Line shifting occurs mainly due to pressure. To a smaller amount, shifting also occurs due to the Doppler Effect. Since this effect is correlated with a gas velocity, it can be used to measure the velocity of gases. This effect will not be discussed here, but additional information can for example be found in [55].

Pressure Shift of Absorption Lines

The line shift is dependent on the composition of the gas under investigation and molecule specific pressure-shift coefficients. In general, this correlation can be written as the sum of the individual shifts caused by the different species present weighted with the total pressure in the system [46]. Furthermore, this coefficient needs to be corrected for temperature, as well.

$$\nu_0^* = \nu_0 + p \cdot \sum_A X_A \cdot \delta_A \tag{2.19}$$

$$\delta_A(T) = \delta_A\left(T_{Ref}\right) \cdot \left(\frac{T_{Ref}}{T}\right)^M \tag{2.20}$$

Due to its focus on atmospheric research, HITRAN currently only provides an air pressure shift coefficient, which is not temperature-corrected. This is mainly due to lack of reliable data. For the purpose of this work, the following relationship is applied for the pressure shift

$$\nu_0^* = \nu_0 + p \cdot \delta_{Air} \tag{2.21}$$

effectively shifting the line center by a factor proportional to the total pressure. This assumes that the mole fraction of the species under investigation is negligible compared to other species in the mixture and pressure-shift is calculated using air as the only other species in the mixture. [38–41]

2.2.2 Line Broadening Effects

Several physical effects within the investigated gaseous media cause a broadening of absorption lines. Depending on the effect and its characteristics, the influence on the shape can be modelled with different peak functions (for example Lorentzian and Gaussian function). Certain effects are more pronounced at specific pressures than others and vice versa (see Figure 2.5). At

pressures below 0.05 bar, the Doppler broadening is the mature contributor to line broadening, while above 0.110 bar collision broadening is the main contributor (at $T_{ref} = 296\,K$). Between these pressures, there is a region, where both effects contribute rather equally to line broadening. This could be used to omit certain effects for calculations depending on the pressure, but is rarely applied. It is however important to notice, that numerical approximations of the line shape differ in quality of approximation depending on the pressure (for example insufficient quality at very low pressures, see Chapter 2.2.3 for details).

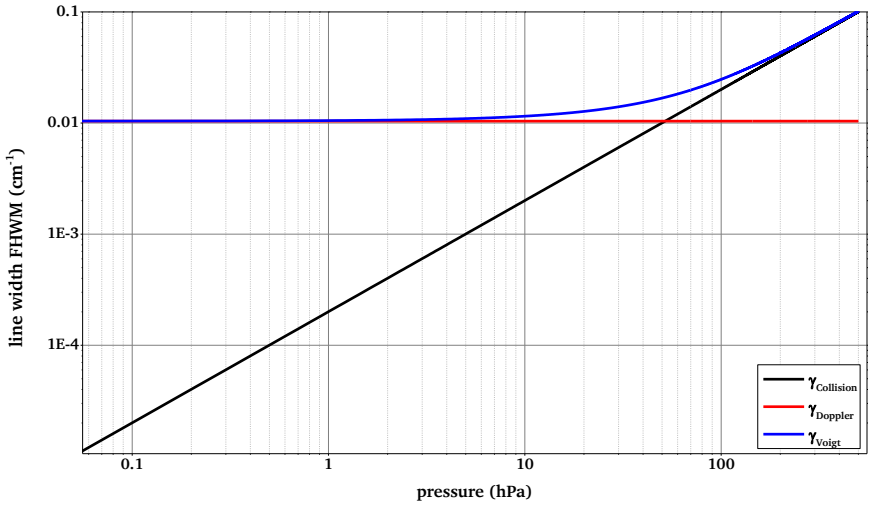

Figure 2.5 Pressure-dependence of line broadening mechanisms in discrete spectra at 296 K [7]

Natural Line Broadening

Natural line broadening is due to the Heisenberg Uncertainty Principle correlating energy and time. It is only dependent on the lifetime of a state τ. Given

$$\Delta E \cdot \tau \geq \frac{h}{2 \cdot \pi} \tag{2.22}$$

there is a limitation as to the precision of the energy of a transition based on its lifetime. The distribution of this energy around the center wavenumber of the transition can be described by a Lorentzian function as shown in Equation (2.23), where the parameter γ_N is derived from Equation (2.22) (as *full-width at half-maximum*, FWHM).

$$\Phi_N(\nu) = \frac{1}{\pi} \cdot \frac{\frac{1}{2}\gamma_N}{(\nu - \nu_0)^2 + \left(\frac{1}{2}\gamma_N\right)^2} \tag{2.23}$$

$$\gamma_N = \frac{1}{2\pi c\tau} \tag{2.24}$$

Doppler Line Broadening

The Doppler broadening, also referred to as *temperature broadening*, is caused by the motion of the molecules itself (collision are handled separately in the next section). Since molecules can move in all directions relative to the light propagation direction, every molecule encounters the photon at a different wavenumber due to the Doppler shift. This results in an energy for the photon that does not correspond with an allowed transition of the molecule and is therefore not being absorbed. Similarly, a photon, that does not fulfil the allowed transition, might appear suitable to the molecule due to the Doppler shift. Given that the velocity distribution of the molecules is known (acc. to Maxwell-Boltzmann distribution), it is possible to predict the distribution of the wavenumbers as encountered by the molecule as well. Since the velocity distribution adheres to a normal distribution, this effect is described by a Gaussian function.

$$\Phi_D(\nu) = \frac{1}{\gamma_D} \cdot \sqrt{\frac{4 \cdot \ln(2)}{\pi}} \cdot exp\left(-4 \cdot \ln(2) \cdot \left(\frac{\nu - \nu_0}{\gamma_D}\right)^2\right) \tag{2.25}$$

$$\gamma_D = \sqrt{8 \cdot \ln(2)} \cdot \sqrt{\frac{k_B \cdot T}{m}} \cdot \frac{\nu_0}{c} \tag{2.26}$$

where m refers to the molecular mass and k_B to the Boltzmann constant. Opposed to the natural line broadening, the Doppler line broadening depends on the individual wavenumber of the transition, as stated in Equation (2.25). Furthermore, this broadening mechanism is independent of the gas composition and only influenced by temperature changes of the gas.

Collisional Line Broadening

Any given number of molecules is in constant motion and therefore molecules collide with molecules of the same species, as well as other species present. Such a collision reduces the lifetime of a state, which in turn, according to Heisenberg's Uncertainty Principle, results in a broadening of a transition. Since the probability of such collisions correlates with increasing pressure (reduced mean free path), the Collisional Broadening is also referred to as pressure broadening. Since collisions occur with molecules of the same species as well as with molecules of other species, the collision broadening is often split between *own* and *foreign* broadening. This is for example the case in the HITRAN database. In this database, only two types of collisions are considered: collision with molecules of the same species (*own broadening*) and collision with air molecules (*air broadening,* see Chapter 2.2.1 as well). Other molecules, though present in the gas mixture, are neglected, since their concentration is considered negligible. It is represented by a Lorentzian function (as is the natural line broadening).

$$\gamma_C = \sum_j (\gamma_{ij} \cdot p_j) \cdot \left(\frac{T_0}{T}\right)^N \tag{2.27}$$

where the index i refers to the species in question, whereas the index j refers to all species in the mixture (including the species in question) and N describes the temperature coefficient to model the influence of temperature on collisional broadening.

In the case of HITRAN, Equation (2.27) can be simplified to the following equation (as mentioned earlier):

$$\gamma_C = \left(\gamma_{self} \cdot p_{self} + \gamma_{air} \cdot (p - p_{self})\right) \cdot \left(\frac{T_0}{T}\right)^N \tag{2.28}$$

Since the natural line broadening is a Lorentzian function as well, both broadening half-widths can be combined to form the resulting half-width used for calculation in the line shape functions according to $\gamma_L = \gamma_N + \gamma_C$. When compared to the natural line broadening, the collisional broadening is usually much greater and the natural line broadening can be neglected.

If necessary for reliable results, other non-molecule related broadening aspects need to be incorporated as well, for example instrument functions. If an instrument function (and the resulting broadening of line shapes) is not accounted for, it is not possible to derive any other information or parameter than the absorption line area, yielding only a number density (if several other parameters are measured separately), since the broadening effect of the instrument would be recreated by fitting incorrect parameters (pressure, temperature, etc.). [38–41]

2.2.3 Line Shape Functions

After examining the different broadening principles, it is necessary to combine the different mechanism into a single line shape approximation that can be applied for spectrum calculations. In this situation, it is necessary to address several issues:

- Precision and accuracy of the calculated approximation
- Speed of the calculation (especially important when calculating hundreds of absorption line)
- Necessary level of complexity (as a trade-off for accuracy) given a specific system under investigation

For the majority of spectroscopic systems, especially in the context of industrial processes and applications, the above-described broadening principles are sufficient for reliable and valid results. When neglecting the natural line broadening, the combination of collision broadening (using Lorentzian function) and Doppler broadening (using Gaussian function) is sufficient for most applications. The level of complexity regarding the line shape functions can be increased if necessary (see later in this chapter for different options and details). When combining the Gaussian line shape and the Lorentzian line shape, the resulting convolution is called a Voigt line shape function and described in detail in the next section.

Voight Line Shape Function and Numerical Approximations

The convolution of Gaussian and Lorentzian line shape functions for collision and Doppler broadening can be described as follows:

$$\Phi_{Voigt}(\nu) = \int_{-\infty}^{\infty} \phi_D(\nu') \cdot \phi_C(\nu - \nu') d\nu' \tag{2.29}$$

Since no analytical solution exists for this expression, several numerical approximations have been developed and tested. Each implementation offers its advantages. One of the most common implementation is by Humlicek [56, 57] from 1972, while more recent implementations exist, for example by Schreier et al. [58] or Liu et al. [59]. Additional implementations are [60, 61]. Especially the implementation by McLean et al. [62] is very promising given its reliance on four polynomials only (more specifically one polynomial with four sets of coefficients). Since these four polynomial sets are summed, the Voigt line shape approximation can be expressed as stated in Equation (2.30)

$$\mathrm{V(X,Y)} = \sum_{i=1}^{4} \frac{C_i \cdot (Y - A_i) + D_i \cdot (X - B_i)}{(Y - A_i)^2 + (X - B_i)^2} \tag{2.30}$$

with the four parameter sets specified in [62].

When evaluating the performance of these approximations and judging their usability for SCLAS spectroscopy, the comparison shown in Figure **2.6** suggests, that the McLean approximation has the highest absolute deviation from the numerical convolution, whereas Humlicek and Schreier show discontinuities due to their section-wise approximation. When considering the required time to calculate the approximations, the McLean algorithm is superior to all others by up to a factor of seven.

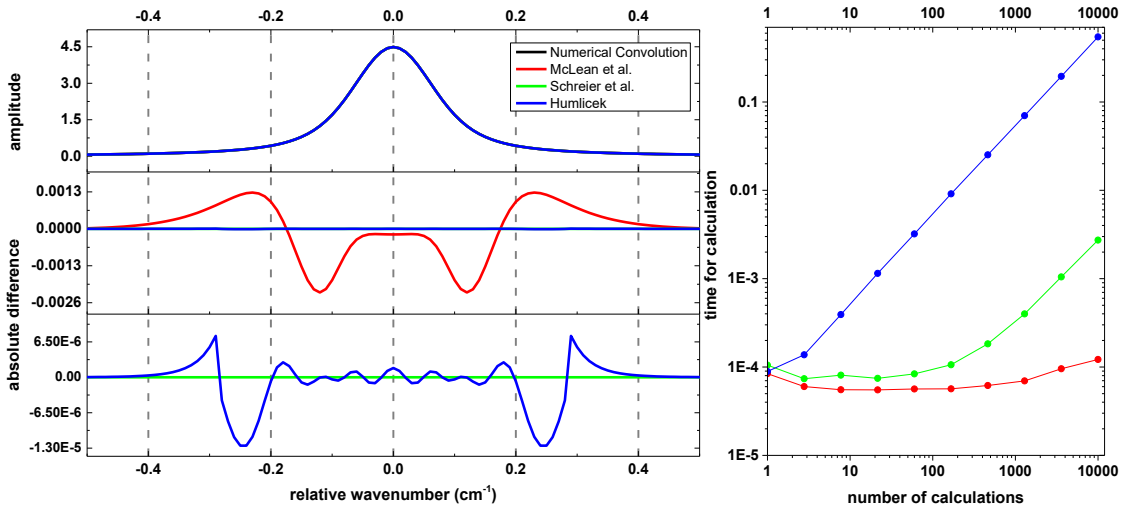

Figure 2.6 Different approximations of the Voigt line shape function in comparison with the numerical convolution and the required time to compute the approximations

Given the required and achievable resolution of SCLAS and the number of transitions to be computed for each step in the fitting process during post-processing, a quick and sufficiently accurate approximation as provided by McLean et al. [62] is best suited. Therefore, this approximation will be used throughout this work.

Advanced Line Shape Profiles

Under certain conditions, it may be necessary to utilize more complex line shape functions, for example to account for narrowing mechanisms [63]. The most common advanced line shapes are listed here including references for a detailed discussion.

Galatry line shape – [63, 64]

Rautian line shape – [63, 65]

Speed-dependent Voigt line shape – [66, 67]

While these advanced line shape profiles increase the quality of the spectroscopic model, they also increase the computational cost to perform the fitting of simulated spectra to recorded data. Especially in cases with a high absorption line count, or a significant variation in parameters, this additional cost can outweigh the gained advantages from higher accuracy in line shape modelling, especially when considering real-time process control applications. Aside from the numerical capabilities of more complex line shapes to account for a certain effect, the quality of available measurements for the corresponding effect needs to be sufficient as well.

2.3 Modelling of Non-Discrete / Continuous Absorbance Spectra

While the previous section discussed discrete spectral models, there are several promising approaches to use completely different approaches to spectrum calculation and modelling. To characterize the available options for spectrum calculation, different methods can be categorized depending on their level of *physicality*. This term refers to the degree to which a model is based on physical constants and principles.

On the one hand, there are models based solely on physical laws and physical constants. The shapes of absorption lines are based on physical models itself and the absorption lines and their parameters are simulated from quantum mechanics and correlated with measurements. This dictates that only effects well modelled mathematically and incorporated into the model are actually present in the calculated spectra. For example, in case of the HITRAN spectral model, only the broadening by air (as a mixture of 79 % nitrogen and 21 % oxygen) as well as the self-broadening is included in the model (see Chapter 2.2). This is due to the fact, that the model was developed for atmospheric research. When utilizing this model in other environments and not correcting for these limitations, the model-induced uncertainty increases. In the case of exhaust gas analysis, the gas-matrix under investigation yields the need to include other foreign-broadening effects as well as a constant change in this broadening based on the measured composition (creating a closed-loop under-determined problem).

On the other hand, there are “black box models” with no physicality which are trained with different spectra and the corresponding parameters and values (usually referred to as values and labels). Such approaches do not model specific effects in the spectra in any way, but rather try to correlate recorded spectra purely statistically with the separately determined labels. A typical representation of such a system is the *Principal Component Analysis* (PCA). These models are commonly used to reduce the dimension of a problem and then train the statistical model of reduced dimension with a certain data set. This step is followed by a validation step with a different data set not used for training. Such models are not able to provide a model based on the training that for example enhances the physical understanding of the underlying processes and effects. It is purely aimed at evaluating highly similar datasets and looking for common patterns. Due to the training of such models, the datasets used for training and later in evaluation need to be closely matched in terms of sample preparation and other environmental factors. In the case of optical spectroscopy, this might require normalization of spectra, homogenization of the sample or similar processing steps, before the sample can be used for training or evaluation. Black box approaches are regularly used in industrial NIR spectroscopy, since the investigated species and samples cannot be sufficiently modelled (i.e. meat, diary, fiber content of corn, etc.). Despite this almost brute-force like approach, NIR spectroscopy based on PCA is widely used in industry and research [68–74]. Advanced versions of this approach try to apply these algorithms to model building itself by aiding in selecting variables (portions of the spectrum) that should be used in modelling of the spectra in a more physical approach [75].

In-between these extremes there are “gray” models that utilize certain physical properties, but allow for a certain flexibility to account for effects not modelled yet. An example of such a “gray” model is the *Indirect Hard Modelling* (IHM, [76]). The IHM model assumes that, while not relying on individual absorption lines, the resulting absorption feature (or even complete absorption bands) can be modelled as Voigt peak shapes (or an overlapping number of such peaks). While these peaks are also used in absorption line-based modelling (HITRAN spectroscopic model), the peak shape parameters are not correlated to any physical value or quantity (while still having physical units). Other gray models utilize mathematical functions that are easier to handle or evaluate than for example Voigt line shapes (which in itself are also numerical approximation). The data itself is based on other models, i.e. the HITRAN model or direct measurements, while the mathematical representation of the spectra is handled differently. *PolySpec*, on example of such an approach, is described later on in this chapter. It utilizes the idea of approximating the resulting shape of a spectrum with higher-order polynomials for individual wavenumbers. These polynomials can easily and numerically cost-efficiently be evaluated and therefore offer a great alternative to calculating spectra line-by-line based on the HITRAN spectroscopic model.

The purpose of the following sections is not to fully describe and discuss the respective methods, but to give an introduction to these models and an idea of how these methods can be used as new approaches to model the spectra of various species in various states. Details regarding the

implementation and results when utilizing these techniques for absorption spectra modelling are described in detail in Chapter 7.

2.3.1 Indirect Hard Modelling

Indirect Hard Modelling is, different from for example *PCA*, directly aimed at the handling of spectra. As previously described, IHM aims to rebuild spectra by combining multiple peaks (in this case Voigt-shape) to recreate the spectral shape. To be able to predict parameters from recorded spectra, it is not sufficient to resemble spectra. A spectroscopic model needs to be able to predict spectra based on specified parameters. It is therefore necessary to extract models that govern the changes in the spectral shape (shifts, intensity changes, etc.). These models can then be used to calculate spectra for freely variable parameters. *IHM* relies therefore on Voigt peak shapes and the combination thereof to resemble the spectra in question. To give an example of a simple *IHM* spectrum, liquid *AdBlue* (aqueous urea solution, used as a *Diesel Exhaust Fluid* (DEF) in combustion engines) is shown in Figure 2.7 with a simple 3 peak model fitted to it. It can be seen, that while this is a simple model, it resemble the spectrum very well. Furthermore, the spectrum itself wouldn't have allowed for deriving individual absorption lines in the first place (even at very low pressures) due to its continuity, which is characteristic for most liquids. Identical behavior can also be observed for gases whose energy levels and transitions are too closely spaced to be separable. Similar effects and spectrum shapes can also be seen for various molecules at high pressure conditions.

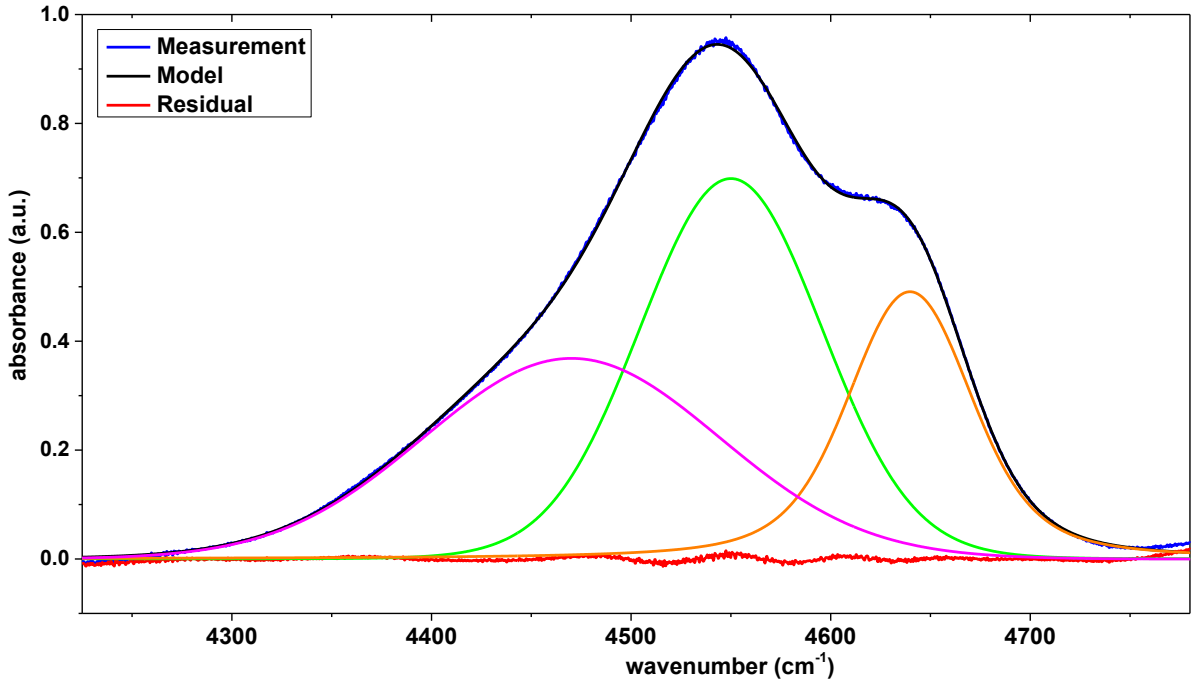

Figure 2.7 Exemplary spectrum of AdBlue (100 % in water) with an IHM model consisting of three peaks fitted to it (individually plotted for clarity). Deviation between recorded spectrum and IHM model is shown in orange.

Overall *IHM* offers a promising approach to model absorption spectra, specifically when no individual discrete absorption lines can be identified and spectrally separated to obtain reliable data for individual line-based models. Such spectra are also common for more complex molecules, for example iso-octane, which is used as a surrogate fuel for combustion research (internal combustion engines, etc.). Details for the application of *IHM* to liquid *AdBlue* and gaseous methane (CH_4) can be found in Chapter 7.

2.3.2 PolySpec – Polynomial Approximation of Absorption Spectra

PolySpec relies on polynomials to calculate spectra for various absorbers and conditions. The basic idea behind *PolySpec* is to approximate the absorbance at a specific wavenumber based on a polynomial, which uses physical parameters as input values (species concentration, pressure, temperature and absorption path length). This approach is not to be confused with resembling a spectral shape with a polynomial calculating the absorbance at various wavenumbers with a single polynomial.

Approximating an absorption spectrum for various absorber concentrations, pressures and temperatures as well as absorption path lengths across a wavenumber range can easily become insufficient and inaccurate. *Polyspec* positions polynomials *orthogonal* to the wavenumber axis to determine the absorbance at an individual wavenumber. Therefore, one polynomial is necessary for each wavenumber in the spectrum to be resolved, resulting in a significant number of polynomials for a broadband spectrum. To reduce this number, an interpolation can be used between the fixed spectral spacing of polynomials as well as omitting spectral regions, where no absorption lines are present. Due to the characteristics of polynomials allowing coefficients to be separated from base functions, it is easy to store all coefficients in a matrix, separated from the fixed set of base functions. Since *PolySpec* is an approach to resemble absorption spectra, it can be used on numerical simulation data, as well as recorded spectra from spectral line data measurements.

PolySpec in itself is not able to calculate a spectrum unless previously fitting the polynomial coefficients. Depending on whether a spectral model or measurements were used for the fitting of the matrix, the input parameters to the polynomials vary. *PolySpec* provides great improvements in terms of spectrum calculation times, since the evaluation of a matrix can be performed numerically cheaply and also implemented within *field-programmable gate arrays* (FPGAs) for high-speed calculation, as opposed to evaluating exponential functions within the HITRAN spectral model. To clarify the approach behind *PolySpec* an exemplary plot of normalized absorbance of an absorption line with respect to Lorentz width (and therefore the pressure) is shown in Figure 2.8. The red line shows the polynomial that represents the absorbance with respect to pressure at a specific position relative to the absorption line center.

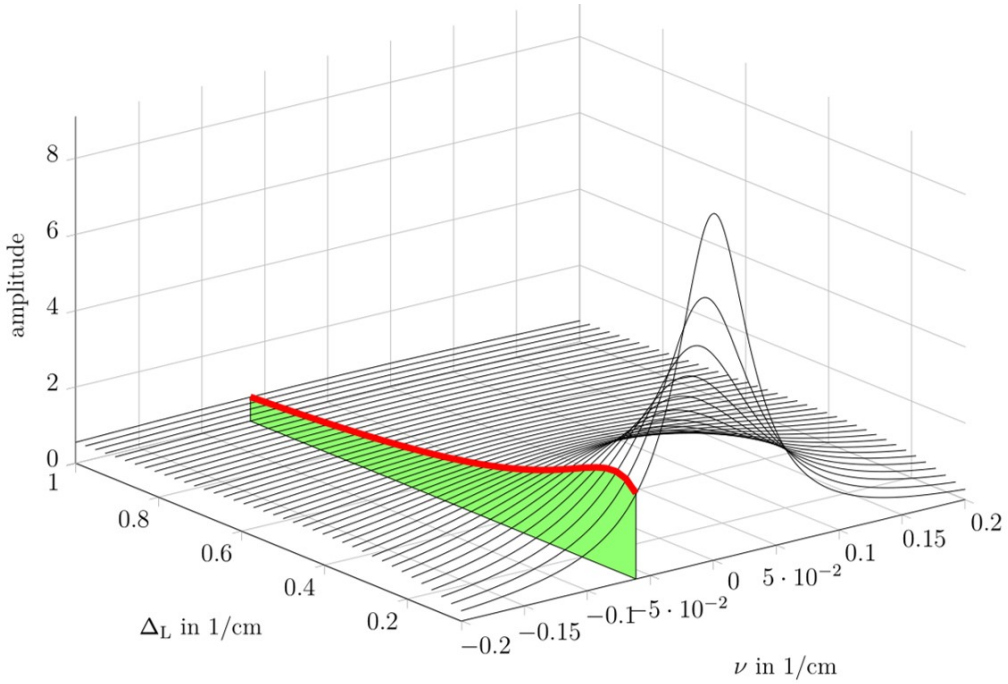

Figure 2.8 Exemplary plot of polynomial used for *PolySpec* representing the change in absorbance at a specific relative wavenumber for various Lorentz widths (and therefore pressure) of an absorption line. Source: [77]

When determining these polynomials based on a specific spectral model, characteristics and assumptions of this model can be utilized to accelerate spectra calculations. Absorption lines calculated using the HITRAN model are symmetrical around the line centerand can be normalized to a Voigt line shape, which is used as the basic line shape function for all absorption lines in HITRAN. Nevertheless, when using other spectral models or recorded measurements, these assumptions are not valid and the approximation and fitting need to take the specific spectral shape into account. To visualize this further, the change in absorbance with regards to pressure and temperature at a specific relative spectral position to the absorption line center is shown in Figure 2.9. The polynomials need to account for this shape to a high degree to be usable as a spectrum calculation method with high accuracy. The approximated shape of individual lines will then be super-imposed to form a single polynomial at each wavenumber. This results in the aforementioned matrix applicable for spectra in all conditions that were used as inputs for the approximation. A *PolySpec* model can only reliably account for changes in the spectrum for the parameter range that was used to create the matrix. Using the matrix beyond these boundaries can create large errors and unphysical results. Knowledge of the range for all relevant parameters is therefore essential for utilizing this method. In addition to the calculation speed of *PolySpec*-based spectra, using polynomials provides another great advantage, when fitting to recorded measurements is required. Since only polynomials are used, the derivatives of the polynomial functions can be calculated analytically. Since gradients of the cost function are heavily relied on by optimization algorithms such as least-square fitting (LSQ fitting), this increases the speed of the fitting process substantially. Instead of calculating numerical approximations of the gradient, an analytical expression can be used to directly determine the

gradient. This reduces the overall fitting time significantly, since the numerical approximation of the gradient requires multiple evaluation of the function itself (with small variations of the parameters) as opposed to a single evaluation of the derivative. Details regarding *PolySpec* can be found in [77].

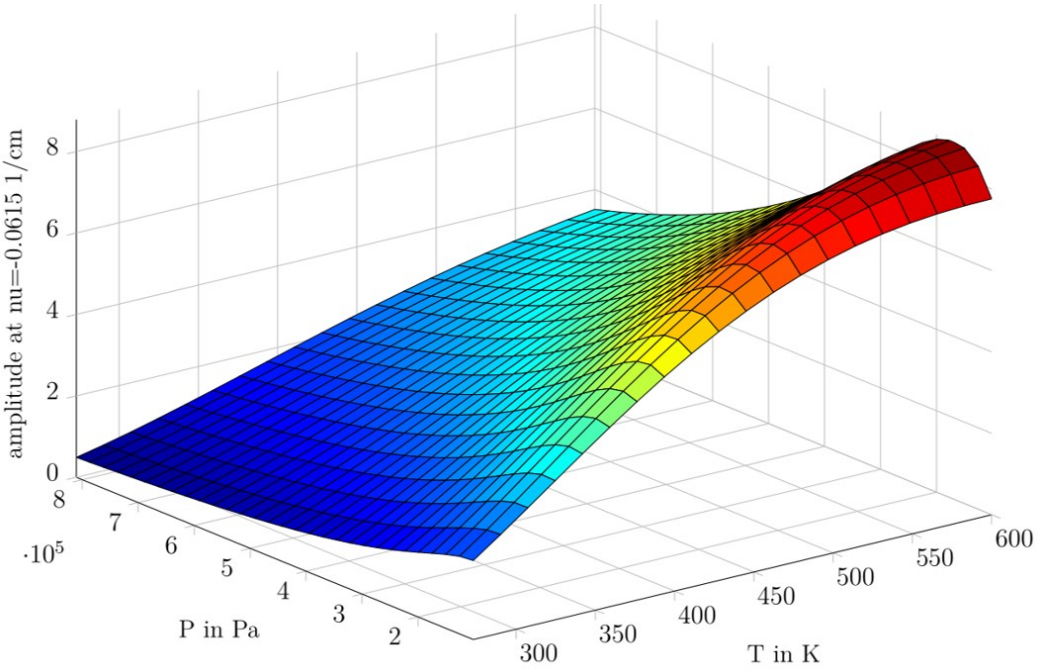

Figure 2.9 Graphic representation of the change in absorbance over pressure and temperature at a specific position relative to the center of an absorption line. Source: [77]

2.3.3 Machine Learning Approaches

Machine Learning approaches to evaluation of spectra are the current standard for most industrial spectrometers and spectroscopic system due to their flexibility and ease of utilization. Since these systems do not require a deep and detailed understanding of the inner working principles of a model or even require a model at all, they can be generated by simply recording a large set of spectra with variations in the required parameters (assuming that there is any correlation in the recorded signal with regards to the values in question). A typical approach would be to record spectra of a substance with varying concentration and for example temperature (assuming constant and equal pressure). Based on these measurements, an algorithm tries to find a correlation between the recorded spectra and the corresponding labels. Labels represent the values for all parameters in question for that specific sample and can be both qualitative and quantitative. These values need to be determined separately, either by a different measurement system or by setting the parameters accordingly while recording the measurements. An example from industrial spectroscopic systems would be the quantitative determination of the protein content in a grain for sorting and processing. Another example would be the homologation or the classification of a certain product and its variations (i.e. different varieties of apples). For such a task, a batch of samples with varying protein

content would be pre-processed to ensure comparable and reproducible recording conditions, spectra were recorded and the protein content of the samples would be separately determined by a different form of analysis, for example, chemical analysis. Based on the recorded spectra and the separately determined labels, a PCA could be performed, which is then verified by evaluating a separate set of samples with known protein content not used for model training by comparing the determined values by the model with the labels for these verification samples. When sufficient agreement is achieved, the model can be used to determine protein content of unknown samples as well, assuming that the samples are correctly prepared and handled. An example of multiple spectra recorded for salt (sodium chloride, NaCl) diluted in water as an aqueous solution is shown in Figure 2.10 and Figure 2.11 (spectra provided by Prof. Dr. Thomas Dreier, Universität Duisburg-Essen). In Figure 2.10 different spectra with a varying concentration for an identical temperature are shown. It is clearly visible that there is a correlation between the concentration and change in spectral shape and transmission. However, it is not possible to identify individual absorption lines or similarly distinct features. It is rather a change of a section of the spectrum in a certain direction. Both main features of absorption increase with an increase in concentration. In Figure 2.11 the temperature was varied between spectra for a constant concentration of salt in water. In this case, the left absorption feature increases with temperature, while the right absorption feature decreases with temperature, resulting in a crossing point at a certain wavenumber (roughly 6900 cm^{-1} in this case). If both parameters are to be determined in an unknown sample, the model needs to be trained and verified with all samples (concentration and temperature variation).

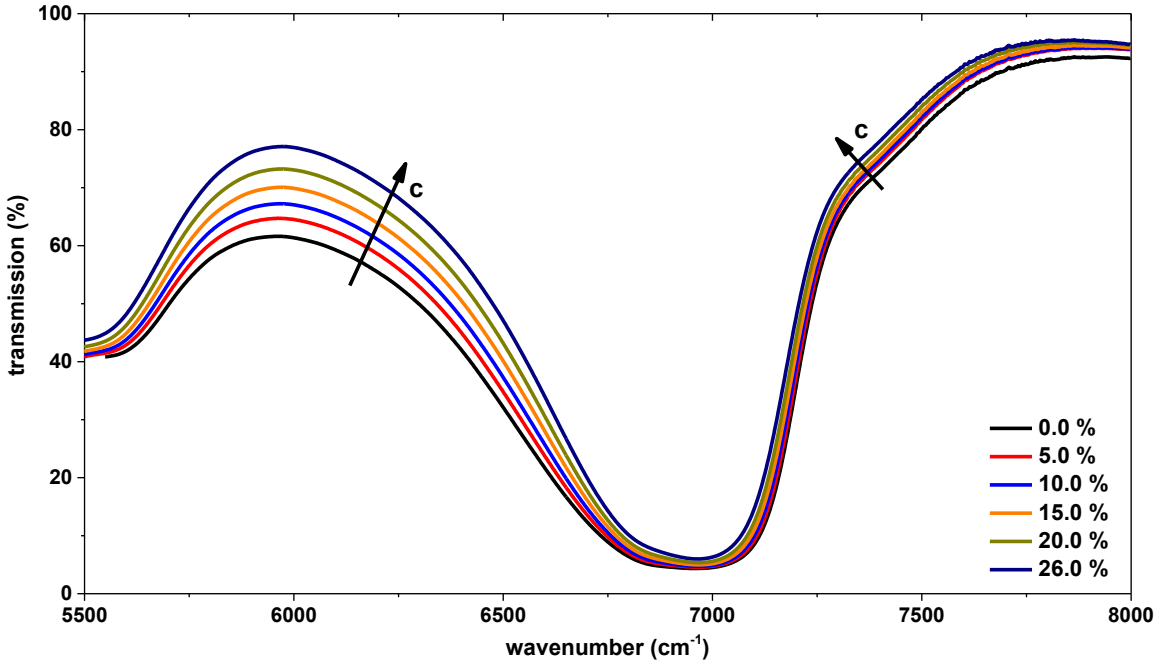

Figure 2.10 Spectra of sodium chloride (NaCl) in water as an aqueous solution for varying concentrations at a constant temperature of 318 K.
A trend for an increase in concentration is marked by arrows.
Data provided by Prof. Dr. Thomas Dreier, Universität Duisburg-Essen

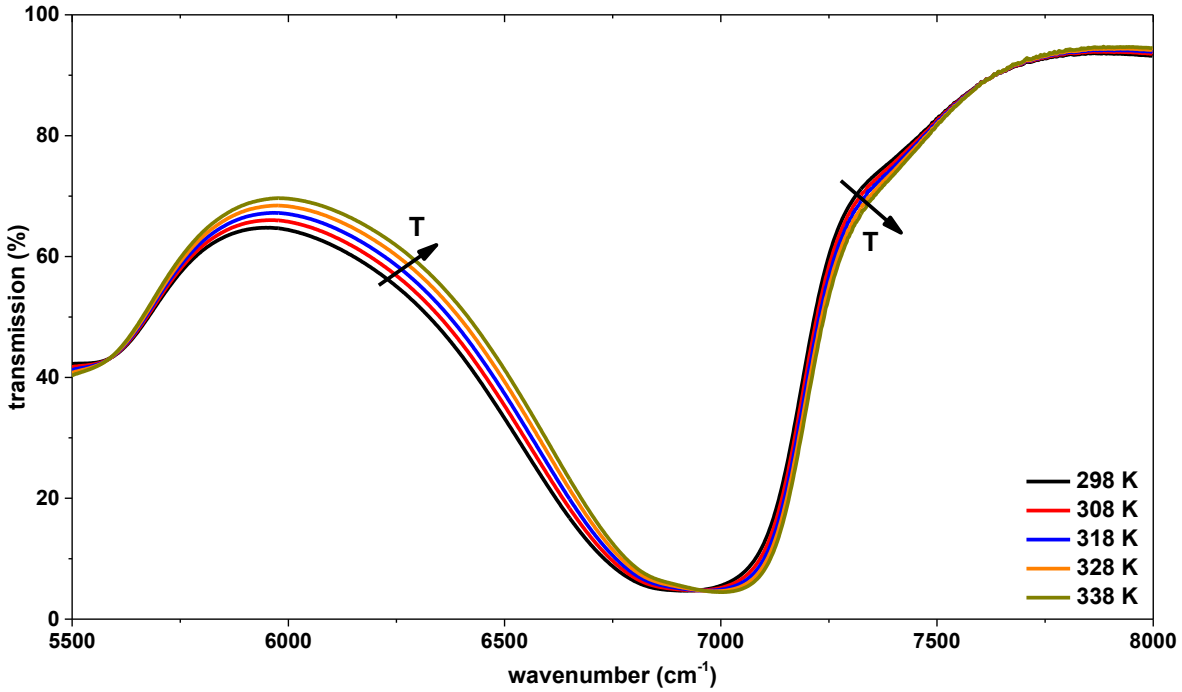

Figure 2.11 Spectra of sodium chloride (NaCl) for varying temperatures at a constant concentration by weight of 10 %. A trend for an increase in temperature is marked by arrows. Data provided by Prof. Dr. Thomas Dreier, Universität Duisburg-Essen

To further improve the accuracy and reliability of the derived models, advanced algorithms including neural networks and wavelets can be utilized in a similar fashion [75, 78–80]. However, all these system suffer from certain drawbacks. Sample preparation influences the recorded spectra significantly, yielding a need for all samples to be prepared exactly identical to the samples used for derivation and validation. Furthermore, these algorithms try to identify characteristics in the spectra that correlate to a certain parameter. By no means is there a validated correlation. For example the presence of a new substance, that wasn't in the samples used for derivation and validation, might completely invalidate the model or create large errors in the determined values without any indication of these errors or problems. Machine Learning algorithms are therefore powerful and quite promising, when it comes to trying to allow for spectral evaluation where no other model is available, but they also need to be carefully handled and steps to ensure applicability need to be taken.

2.4 Supercontinuum Laser Light Sources

Since SCLAS relies extensively on *Supercontinuum Laser Light Sources* (SCL), it is necessary to understand their fundamental concepts and operating principles. Nevertheless, the SCL itself is not at the focus of this work and therefore the level of detail in this section is limited to the basics of light generation and source operation, as well as the implications for spectroscopic applications of this light source. Additional resources are provided, since the design and

development of SCLs has grown in to a separate field of research over the last years. A thorough overview and numerous detailed sources are listed and discussed in [81]. Another extensive review can be found in [82], which also addresses the historical development of the field.

The basic component of a SCL is a specifically designed *Photonic Crystal Fiber* (PCF). Birks et al. [83–85] were first able to fabricate an *endlessly single mode* fiber from silica by embedding a core within a photonic crystal with hexagonally arranged longitudinal air tubes acting as cladding. A photonic crystal describes a highly non-linear material, which has a periodically varying index of refraction on the order of optical wavelengths [84]. The size of core and cladding of a PCF are comparable to standard *single mode fibers* (SMF) with a core diameter of around 9 μm (but can be reduced down to about 2-3 μm) and a cladding diameter of 125 μm. The individual structure of these tubes depends on the intended use case. By designing this pattern, it is possible to achieve a very specific dispersion characteristic for the fiber. An example pattern of the PCF used in the NKT SuperK EXW-12 SCL, used in this work, is shown in Figure 2.12, along a schematic of a PCF.

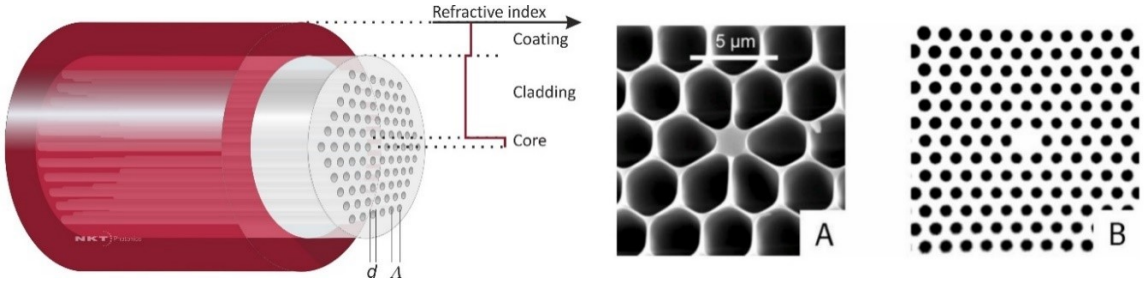

Figure 2.12 Schematic of a PCF – Important parameter: d = Diameter of tubes; Λ = Pitch between tubes; Inset A: SEM Pictures of a PCF; Inset B: Optical microscopy picture of PCF. Source: [86]

As originally reported by Alfano and Shapiro [87, 88] in 1969/1970, high power pulses broaden significantly in terms of spectral content, when propagating through nonlinear media. This is due to a number of non-linear effects and can occur in almost all media. Reports by Alfano and Shapiro [87] used BK-7 borosilicate glass and reported earlier observations in liquids. A short overview in [89] reports supercontinuum generation in various media, including liquids, solids, fibers, glycerol, glass, semiconductor dielectrics and zinc selenide (ZnSe). Since the underlying effects are strongly influenced by the dispersion characteristics of the non-linear medium, specifically tailored media significantly lowered the required power for this to occur. Furthermore, the energy requirements are lower, when the initial pump pulse appears near the *zero dispersion wavelength* (ZDW) of the nonlinear medium [90]. Especially the commercial availability of high-power microchip lasers at 532 nm and 1064 nm and specifically tailored PCFs with ZDWs at or near these wavelengths has made SCLs a viable light source [91]. Since the initial conception, various design have been proposed and model have been developed to predict behavior and properties [91–94].

Supercontinuum sources (based on PCFs) usually consist of five essential parts:

- Pump or seed laser, tailored to the chosen ZDW of the PCF

- Multi-stage amplification system
- Coupling system into the PCF
- Specifically tailored PCF
- Collimation optics after the PCF

A pulsed light source with a very short pulse duration (on the order of femto- or picoseconds) is amplified via various stages of amplification. The resulting high power light pulse (up to hundreds of kW) is coupled into the specific PCF with the designed ZDW via an optical coupling system designed for the high energy levels. After propagation through a specific length of PCF (the broadening is partly depending on the PCF length), the spectrally broadened pulse is emitted from the fiber and usually collimated for further utilization.

Depending on the pump pulse duration, two broadening schemes are commonly seen in PCFs for supercontinuum generation. If femtosecond pump pulses are used, soliton dynamics and self-phase modulation play the most significant role in spectral broadening. Self-phase modulation refers to the effect of a nonlinear phase delay which is caused by the Kerr effect, resulting in a nonlinear change of the refractive index of a medium due to high intensities [95]. When picosecond or longer pump pulses are used, modulation instabilities and four-wave mixing cause the majority of the broadening [96]. In the picosecond pumping regime, shot-to-shot noise becomes apparent and needs to be addressed (see Chapter 4.1). The SCL source used in this work is based on a picosecond mode-locked Ti:Sapphire pump laser (wavelength of 1064 nm, [97, 98]) operating at a pulse repetition rate of 80 MHz which is converted down via a pulse-picker. Besides the pump pulse duration, the pump pulse power and the pump pulse wavelength, aside from dispersion characteristics of the PCF and its length, greatly influence the broadening and its underlying processes. As opposed to femtosecond pump pulse SCLs, the propagation of picosecond pulses through the PCF can be described as quasi-CW (continuous wave) [16]. The most pronounced process for broadening of the optical pulse is phase-matched four-wave mixing, generating so-called sidebands, which are symmetrically spaced on either side of the initial wavelength. The broadening in this regime is also partly due to a pulse breakup, which creates multiple shorter pulses that in itself behave like femtosecond pulses. This pulse breakup is correlated with pump noise (referred to as *modulation instability-induced breakup* or *MI* [82]) and results in a higher shot-to-shot variation of the emitted pulses. This is more pronounced in the case of a pump wavelengths greater than the zero-dispersion wavelength (ZDW) of the PCF, effectively pumping in the anomalous dispersion regime (negative group velocity dispersion). To overcome this, as mentioned earlier, an all-normal dispersion PCF can reduce this modulation instability significantly [42]. While a higher shot-to-shot variation does require handling via averaging (therefore reducing the time resolution, see Chapter 3 for details), it is highly advantageous in terms of spectrum smoothness. When a SCL relies only on four-wave mixing (pumping in the normal dispersion regime), the traces of the discrete wavelength bands are visible in the spectrum. In Figure 2.13, spectral energy distribution measurements for a SCL are shown after propagating through a 6 m PCF (pumping

at 1064 nm, ZDW at 1069 nm, [16]). Two sidebands resulting from four-wave mixing are clearly visible at 1.3 μm and 0.9 μm. Their presence and shape is influenced by the initial pulse peak power when entering the PCF as well. While such a source might provide better shot-to-shot performance, several region of the spectrum, especially towards the longer wavelength, are not present in the output of the SCL. Similar characteristics are visible in the spectra of femtosecond pulsed SCLs as well [41].

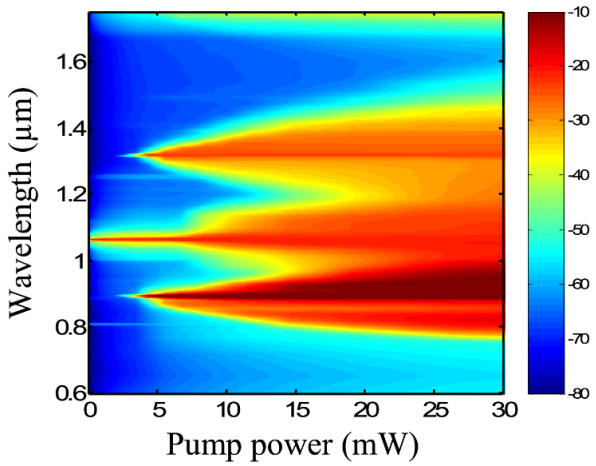

Figure 2.13 Spectral energy distribution after propagating through 6 m PCF with pumping at 1064 nm, and a ZDW at 1069 nm. Pumping occurs in the normal dispersion regime. Source: [16]

Performing similar measurements with identical pump wavelength, but slightly lower ZDW at 1040 nm, and with different length of PCF, it is visible, that the spectrum is significantly smoother and covers a broader range (see Figure 2.14). In this figure, the spectral energy distributions after 1 m, 3 m and 20 m are shown (left to right). While after a PCF fiber length of 1 m some of the symmetrical peaks of modulation instability are still visible, they are almost complete smoothed out after 3 m of PCF (especially for higher initial pulse powers). After 20 m of PCF, no traces of the modulation instability peaks remain visible. The only remaining peak is at pump wavelength. Given the application in spectroscopy, a smoother spectrum and broader spectral coverage is preferable. Measurements of the characteristics of the SCL used in this work are discussed in Chapter 3 in detail, including the emitted spectrum (see Figure 3.1 in Chapter 3), beam shape and quality, as well as the temporal pulse shape.

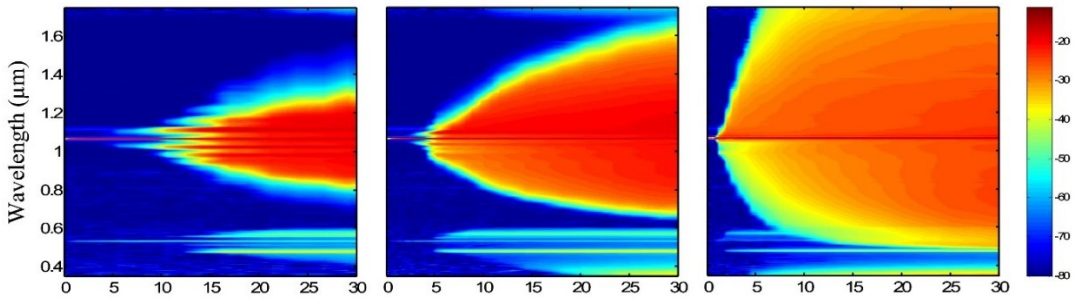

Figure 2.14 Spectral energy distribution measurements after propagating through 1 m, 3 m and 20 m of PCF, when pumping in anomalous dispersion regime. Source: [16]

2.5 Chromatic Dispersion Generation and Characterization

Aside from the SCL, another key component of a SCLAS system is the chromatic dispersion, which allows for the separate detection of individual wavenumbers. The pulse, emitted from the SCL, contains all wavelength, but in a very short time (duration of the pulses is around 100 ps). A detection of individual wavenumbers is mostly achieved one of two different types of chromatic dispersion: time or spatial dispersion. An example of spatial dispersion is a grating, which is standard in grating spectrometers. In this case, different wavelengths are reflected by the grating under different angles. Depending on the position of a detector in relation to the grating, only a specific wavenumber (or narrow wavenumber range) is detected. The amount of dispersion determines the optical resolution of such a system. In case of dispersion in the time-domain, a short pulse, containing all wavenumbers, is stretched in time so that different wavenumbers reach a detector after each other. This is caused by different propagation velocities for different wavenumbers, since the propagation velocities depend on the refractive index, which in itself is a function of the wavenumber.

This effect is present in all fibers, including standard telecommunication fibers. Since pulses are at the center of digital transmissions, transmission over long distance of fibers would not be possible, if the dispersion would not be countered. If the dispersion would not be compensated, individual pulses would overlap and it would not be possible to identify individual pulses. Such a dispersion compensation effectively compresses the pulses back to their original shape. Such a device is commonly referred to as a *Dispersion Compensation Module* (DCM). For SCLAS systems, this effect is used in an inverted manner and a short pulse in the time domain is intentionally dispersed in time according to its spectral content (preventing overlapping by selecting proper pulse rates).

For DCMs, specifically designed *dispersion compensating fibers* (DCFs) are used. These fibers usually show highly negative dispersion coefficients, since standard single mode fibers encounter positive dispersion coefficients (SMF-28e: $\sim 15\ ps/(nm \cdot km)$ [1] around 1550 nm). By providing a higher negative dispersion per unit length of the fiber, the required length of fiber can be reduced. The DCF used in the DCMs for this work has a dispersion of $-155\ ps/(nm \cdot km)$ around 1550 nm. Since the dispersion influences the separation of different wavenumbers in time, this parameter is directly influencing the optical resolution of the SCLAS system. While longer length of DCF provide higher dispersion and therefore higher optical resolution, they also have higher attenuation reducing the detectable optical intensity. The optimal length of fiber is a trade-off between required resolution and required signal level. Since the required optical resolution decreases with increasing pressure (see Chapter 2.6 for details), shorter lengths of fiber can be used in high-pressure systems without artificial broadening of the absorption lines (in form of an instrument function, see Chapter 4.4 for details).

[1] Specific characteristics of fibers are often normalized by fiber length and are therefore given in the unit for the characteristic divided by a unit of length

While there are other means of generating large dispersion for optical pulses [99–103], none of those was found to be suited for SCLAS. This is mainly due to the fact, that these techniques are open-path or require propagation of the light pulse through various media. These options are either not compatible with the intention for SCLAS (all-fiber system), impose a significant signal loss on the system or do not offer the required bandwidth for broadband spectra. Given that the dispersion fiber is a key component of a SCLAS system, it is necessary to characterize its performance and parameters precisely to incorporate these values into the spectral post-processing. Three methods are available to measure the dispersion of a specific DCM (in combination with all other components of the system). Two of these methods rely on adding an additional component to the system, while the third method utilizes only readily available components in the system. These methods will be described here in more detail in the following section, since they directly influence the performance of a SCLAS system.

2.5.1 AOTF-based Dispersion Characterization

This measurement method relies on the relationship between the delay an optical pulse encounters when propagating through a fiber and the dispersion of the fiber. The dispersion is the first derivative of the delay. When measuring the delay of pulses at different wavelength, the dispersion of the tested fiber can be found via derivation of the delay curve. For this approach to be feasible, especially with broadband light sources, it is necessary to easily apply varying limits in transmission to specific wavenumbers. This can be achieved by using an *Acusto-Optical Tunable Filter* (AOTF). This novel method is published in [43]. AOTFs employ specific crystals (anisotropic Tellurium Dioxide) and change their transmission behavior by applying sound waves to the crystal with piezo-transducers. Depending on the application, AOTFs can either diffract a certain wavelength in different directions or, in the case of filtering, diffract different wavelengths into the same direction (as the output of the filter).

With the SCL used in this work, the delay of pulses for a DCM with a dispersion of $D = -1500$ ps/nm (fiber length: 9382 m) was measured. The results are shown in Figure 2.15 alongside the first derivative and the reference measurements of the manufacturer for comparison. Good agreement between the measurement by the AOTF approach and the manufacturer data can be observed with remaining deviations less than 2 %. Furthermore, the novel approach provided data for a significantly broader range of the spectrum including the relevant range for NIR spectroscopy, as opposed to the manufacturer data, which is limited to the relevant telecommunication band.

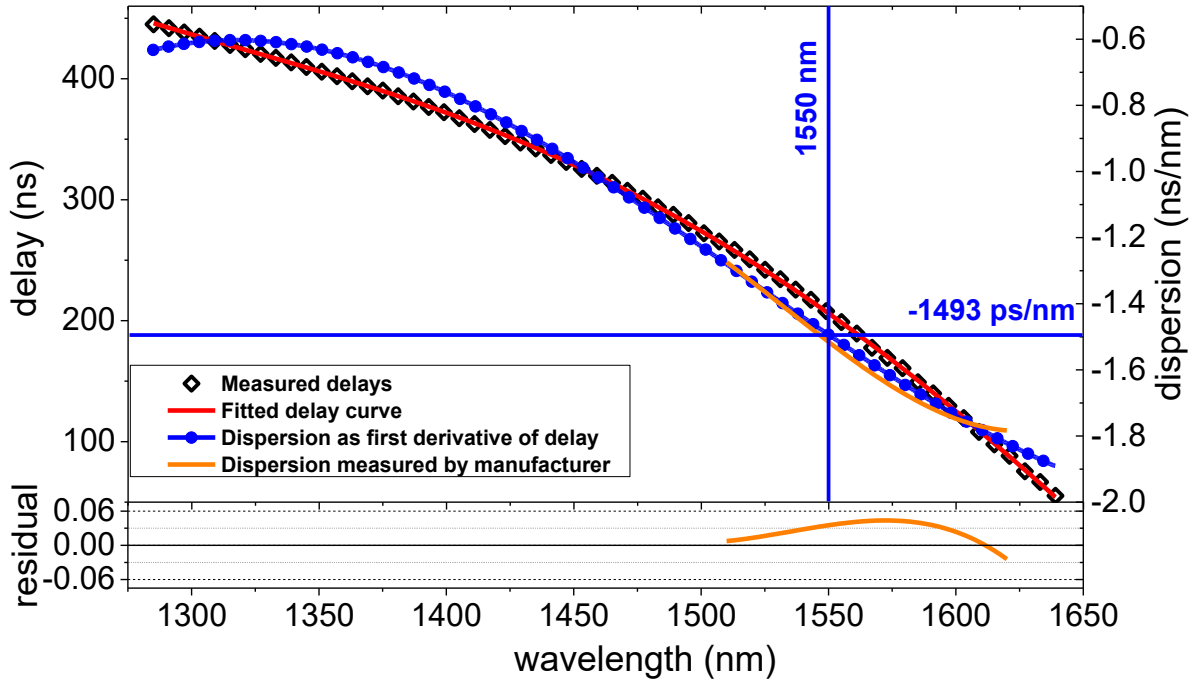

Figure 2.15 Dispersion measurements using a novel AOTF-based measurement approach [43]

2.5.2 Etalon-based Dispersion Characterization

The second option to determine the dispersion of the DCM in use, it based on interference fringes [104]. This approach is similar to the determination of tuning of diode lasers for TDLAS spectrometer. For this approach, two plane-parallel surfaces, referred to as *Etalon* (due to its geometry constraints), with partial reflection are inserted in to the light path of the system. Between these parallel surfaces, interference is occurring, which create so called fringes on the optical trace (shown in Figure 2.16). The spacing of these traces, called *Free Spectral Range* (FSR), is dependent on the index of refraction of the medium between the reflective surfaces and can approximately be described with Equation (2.31). Commonly etalons are either composed of air between two glass plates or solid materials, often using sapphire.

$$\mathrm{FSR} = \frac{1}{2 \cdot n_g \cdot L} \tag{2.31}$$

where n_g refers to the group index of the medium and L to the length of the etalon.

Given a limited spectral coverage, the group index of refraction is assumed constant. In the case of air as the optical medium, the index of refraction can be used instead of the group index. Based on the FSR and the corresponding time difference, a relative increase in wavenumber across the time can be determined, which is the result of the dispersion in the fiber. With the help of a known wavenumber at one of the peaks, the absolute wavenumbers at all peaks can be determined. When correlating the time, at which the peaks occur, with the corresponding

wavenumbers, a delay curve similar to Figure 2.15 can be derived. The first derivative once again provides the dispersion curve for the fiber.

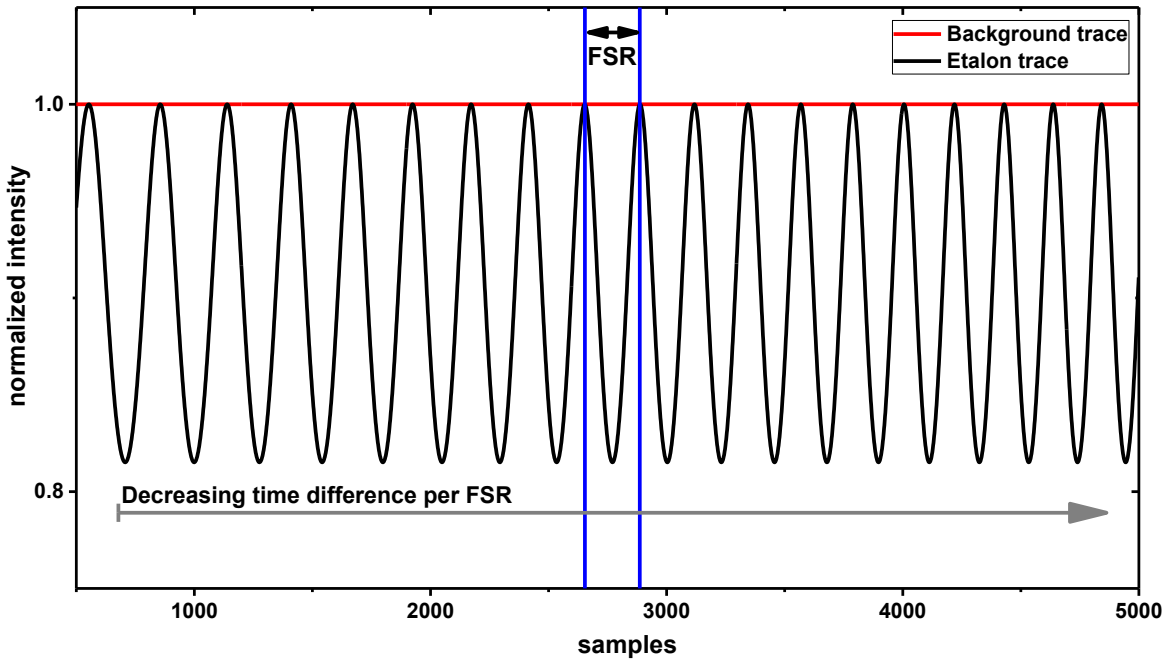

Figure 2.16 Etalon trace for dispersion determination by using the free-spectral range (FSR) of the etalon to measure relative increases in wavenumber.

To obtain the absolute wavenumber at one of the peaks, multiple methods can be employed. One options requires additional spectral intensity measurements, which allow a correlation between the shape of the envelope of the etalon measurements and the spectral intensity trace. A different approach might be to incorporate an absorption spectrum onto the etalon trace, allowing for determine the wavenumber at that position from the absorption line and its known position. The last option already points in the direction of the third, and most applicable approach to determining the dispersion of the fiber: using absorption features of known wavenumbers under known conditions, as is described in more detail in the following chapter.

2.5.3 Gas Absorption Feature-based Dispersion Characterization

As already pointed out in the previous section, instead of relying on a single known wavenumber and known wavenumber spacing (with the help of an etalon), complete absorption spectra can be used to generate dispersion curves for specific DCFs as well. This is especially well suited for applications, where a specific gas is being investigated in a sample compartment, such as absorption cells. In this case, it is easily possible to establish a known gas matrix within this cell. Since gases at reduced pressure (for example 100 mbar or 500 mbar) provide very narrow absorption lines, these are ideal conditions for dispersion measurements. The correlation between sampling times of certain absorption peaks and their wavenumber

position can be derived from the measured spectra via peak-finding algorithms and simultaneous spectrum simulation. In Figure 2.17, an example using a methane (CH_4) spectrum is shown with a second-order polynomial fitted to the recorded peaks. It is shown, that the residual between fitted polynomial and recorded positions is less than 0.05 nm or 0.003 %. When comparing this to the plot in Figure 2.15 it can be seen, that, while a second order polynomial is sufficient within this limited spectral range, it would be insufficient, when trying to cover the complete spectral coverage of the SCL. The obtained delay curve can again be used to determine the dispersion as the first derivative.

It has to be noted, that these delay measurements, which are essential to SCLAS, are very sensitive to even the smallest changes in the experimental setup. Replacing a signal cable with a longer one or adding a segment of fiber to the setup already changes the absolute delay times. While this influences the absolute values, the dispersion as the first derivative is not affected by these changes.

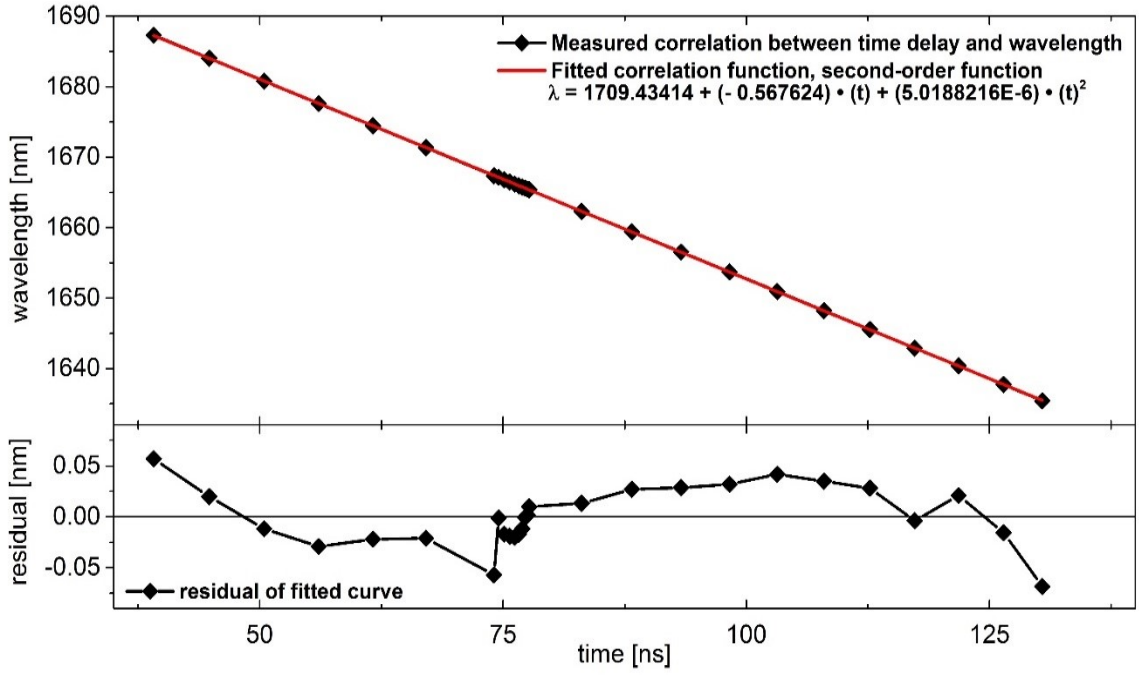

Figure 2.17 Correlation between absorption peak wavenumbers and the time of sampling to determine the dispersion of a DCM and provide a conversion function from the time to the wavenumber domain.

2.6 Supercontinuum Laser Broadband Absorption Spectroscopy

Supercontinuum Laser Broadband Absorption Spectroscopy (SCLAS) is a spectroscopic diagnostic technique, which combines *Supercontinuum Laser Light Sources* (SCL) with in-fiber dispersion and high-speed data acquisition to provide broadband spectra for optical diagnostics. The underlying idea to use short pulses with broad spectral content and disperse them in time was

originally published by Orofino and Unterleitner in 1976 [17]. While their original concept already included all required components of a current SCLAS system, the commonly available equipment, especially photo diodes and available fibers were limiting the applicability. Due to the available fibers, a fiber length of 68 km was suggested to achieve the required dispersion, due to the low dispersion of standard fibers. With the availability of high-speed photo detectors (rise and fall times on the order of 20 to 30 ps) and pulsed SCLs over the last decade, this concept could be implemented to achieve required resolutions and power levels.

Since its inception, the SCLAS technique has been used in various scenarios, but most often in the case of gas diagnostics. Early works include various proof-of-principle studies [105–111]. More recent works include applications in chemical sensing and microscopy [112], as well as applications with identical dispersion generation, but different pulsed sources [113]. Furthermore studies using cavity-enhanced approaches [114] and path-averaged measurements [115–117] have been published.

A standard SCLAS system consists mainly of the following components:

- Supercontinuum Light Source
- Optical Filter
- Dispersion Compensation Module
- Absorbing Medium (for example a flame)
- Data acquisition system including photo diode

Such a system is illustrated in Figure 2.18 alongside representations of the pulse duration and spectral content at each stage of the propagation.

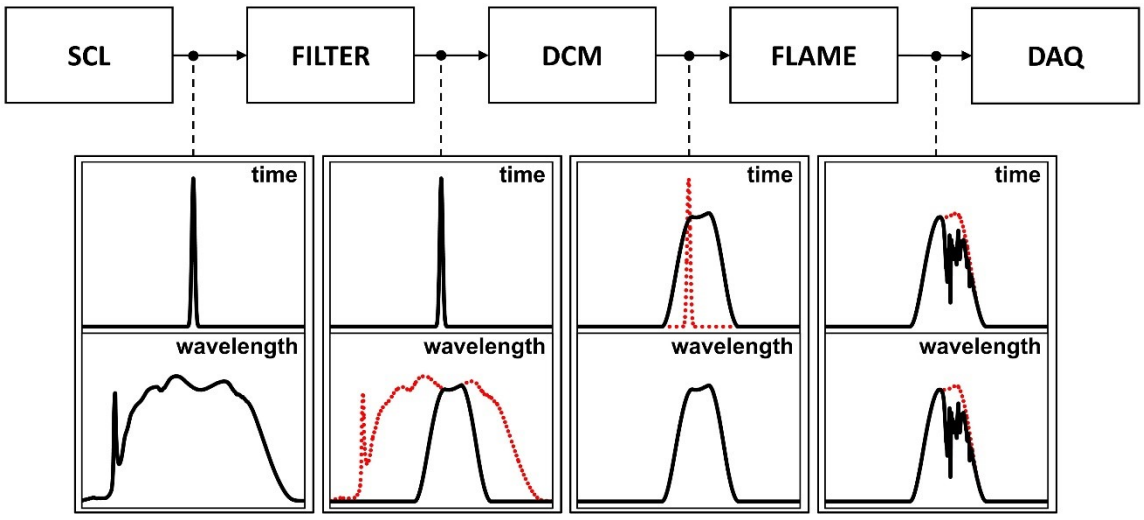

Figure 2.18 Visualization of *Supercontinuum Laser Broadband Absorption Spectroscopy* (SCLAS). After exiting the source, the pulse is filtered and dispersed in time by the *Dispersion Compensation Module* (DCM), before being modulated with the absorption signal. By sampling the pulse in the time domain with a high-speed photo-diode, a spectrum is recorded given the time-wavelength relationship imposed by the DCM.

Pulses that leave the SCL, are short in the time domain (on the order of ~100 ps), but cover a broad spectral range. In the case of the SCL used in this work, the coverage range from 400 nm to 2400 nm. Still visible in the spectral intensity is the high energy of the pump pulse. When the pulses pass through an optical filter, the spectral range is limited to the required range from the specific experiment. In this case a bandpass filter was used limiting the transmission to a central region of the spectrum. It has to be kept in mind, that, in addition to the filter, the transmission characteristics of all components along the propagation act as additional filters as well. After passing the filter, the pulse propagate through the DCF employed within the DCM. Most DCFs act as additional filters, since their transmissivity towards the longer wavelength is severely limited. A transmission above 1700 nm is barely possible and accompanied by large losses. Due to the dispersion in the DCM, the spectral information is transferred from the frequency domain to the time domain. The time trace resembles the spectral pattern closely. It has to be noted, that for this representation, an anomalous dispersion has been assumed. Anomalous dispersion (positive dispersion values) causes the shorter wavelength to travel faster through the medium, while normal dispersion (negative dispersion values) causes longer wavelength to travel faster. The later results in a *flipped* spectrum in the time domain as opposed to the wavenumber domain, since longer wavelength will arrive earlier at the detector than shorter wavelength. Throughout this work, DCMs with normal dispersion are used (for example $D = -1500\ ps/nm$), causing the recorded data to show longer wavelength (or smaller wavenumbers) towards smaller time values. When employing a dispersion of $D = -1500\ ps/nm$, the pulses are stretched to about 350 ns for a spectral content of 250 nm (1450 nm to 1700 nm).

After passing through the DCM, the stretched (or dispersed) pulses are than modulated by the absorbing medium, for example a flame or gases in an absorption cell. Since this absorption modulates the spectrum of the pulse, it can be determined in the spectral and similarly in the time domain. After this modulation, the optical signal is recorded with a high-speed data acquisition system. This data acquisition needs to take place with a triggered system due to the pulsed nature of the SCL. After recording a specific number of pulses (usually on the order of several thousand pulses), these pulses will be averaged to form a single spectrum. As mentioned previously (see Chapter 2.4 and Chapter 3), this averaging is required to account for variations in the emitted spectrum of the SCL. Since SCLs employ pulse frequencies on the order of MHz, recording this high number of pulses is not limiting the time resolution significantly. The source used in this work offers repetition rates between 2 MHz and 80 MHz by employing a pulse picker from the base frequency of 80 MHz. These averaged spectra can be evaluated according to the algorithms and procedures discussed in detail in Chapter 4. Given the nature of the components in a SCLAS system, all components are fiber-coupled or consists of fiber altogether. Photodiodes at the required bandwidth and rise-time are usually fiber-coupled as well creating an *all-fiber* system. This is advantageous, especially in harsh environment, since no moving parts are present in the system and particles outside the measurement volume cannot interfere with the measurements.

SCLAS systems have to be optimized for the specific application, since their operational parameters can be varied significantly. Choosing appropriate filters, as well as choosing appropriate pulse frequencies is necessary to obtain valid and useful data. In general, three important parameters are closely coupled with regards to performance of the system. Firstly, the pulse frequency influences the required time for averaging, as well as the time between pulses. Secondly, the achievable resolution is determined by the dispersion in the DCM and characteristics of the photodiode. Thirdly, the spectral content influences what species can be detected and how long the pulse will be after dispersion. Choosing dispersion, spectral content and pulse rate it needs to be ensure that two dispersed pulses do not overlay in time while contain the required spectral content with the required spectral resolution. To aid with this optimization, two quantities can be calculated: expected time duration of pulses after dispersion Δt and optical resolution of the system $\Delta\nu$. Constant dispersion is assumed for the limited wavenumber range.

$$\Delta t = \int_{\nu_1}^{\nu_2} D(\nu)\, d\nu \approx D \cdot (\nu_2 - \nu_1) \tag{2.32}$$

$$\Delta\nu = \dot{\nu} \cdot \tau = D^{-1} \cdot \tau \tag{2.33}$$

where Δt refers to the pulse duration after dispersion, $D(\nu)$ to the dispersion at wavenumber ν, $\Delta\nu$ to the optical resolution and $\dot{\nu}$ to the tuning rate, which is the inverse of the dispersion, and τ to the combined rise and fall time of the photo diode as a measure for the minimum pulse response time of the detection system.

Given that the dispersion of a DCM is not constant across the NIR spectrum, the optical resolution of an SCLAS system it not constant as well, but depends on the specific wavenumbers. In the case of normal dispersion, (negative dispersion values), the resolution decreases from the longer wavelength towards the shorter wavelength. As an example, the parameters for a measurement of methane (CH_4) are given here:

$$\text{Spectral range: } \nu_1 = 6060.6\ cm^{-1} = 1650\ nm,\ \nu_2 = 5882.4\ cm^{-1} = 1700\ nm \tag{2.34}$$

$$\Delta t \approx D \cdot (\nu_2 - \nu_1) = -1.9\ \frac{ns}{nm} \cdot \left(1700\ nm - 1650\ nm\right) = 95\ ns \tag{2.35}$$

$$\Delta\nu = D^{-1} \cdot \tau = \frac{1}{1.9\frac{ns}{nm}} \cdot 61.2\ ps = 0.002\ \frac{cm^{-1}}{ps} \cdot 61.2\ ps = 0.1224\ cm^{-1} \tag{2.36}$$

When limiting the spectral content of the SCL pulses to just 50 nm from 1650 nm to 1700 nm, the stretched pulses only last about 95 ns. Aiming for a separation of 100 ns to ensure proper spacing and no pulse overlap, a theoretical pulse repetition rate of up to 10 MHz could be used. Given the combined response time of the detection system of 61.2 ps (based on the components used in the experiments in later chapters), this would achieve an optical resolution of 0.1224 cm^{-1}. Such a resolution is sufficient for measurements at ambient or higher pressures.

2.7 Fourier-Transform Infrared Spectroscopy (FTIR)

Fourier-Transform Infrared Spectrometry (FTIR) is one of the most versatile tools in absorption and IR spectroscopy in general. In this work, it has been used for obtaining broadband sample spectra for exploratory spectroscopic model development (see Chapter 7) and is therefore included in this fundamentals section. While only an introduction and an example measurement is discussed here, extensive details, including detailed performance and error discussions, can be found in [48]. Due to its ability to obtain broadband spectra, it is able to provide spectra for gases, liquids as well as solids. It is therefore a versatile tool for sample identification as well as quantification. Furthermore, the obtained spectra can be used to develop and calibrate spectroscopic models. High resolution versions of FTIR are often used to generate the afore mentioned line databases (such as HITRAN [38] or GEISA [52]), while FTIR spectrometers with reduced resolution, but faster sampling times are used in industrial applications for in-line process control. One of the largest drawbacks of FTIR is their slow sampling frequency (usually on the order of Hz). Such a sampling time limits the applicability to steady-state process or constant samples. An application to for example an *Internal Combustion Engine* (ICE) for crank-angle resolved measurements is not possible.

A FTIR spectrometer utilizes the principle of interferometry to obtain interferograms, which in itself contain broad spectra. To extract the spectra from the interferogram, the inverse Fourier transform (and more precise the *Fast Fourier Transform*, FFT, [118]) is applied. Most commonly used are spectrometers based on the two-beam Michelson-Interferometer [119]. In this configuration, a light beam is split into two beams by a beam splitter (special mirror with approximately 50 % transmission and 50 % reflection). One of these beams propagates along a fixed distance, while the second beam is traversing a variable distance. These propagation paths are referred to as *arms* of the interferometer. Afterwards, both beams are recombined and therefore interfere with each other. The resulting signal is the so called interferogram. Based on this interferogram, it is possible to obtain information of the complete frequency content of the initial light entering the interferometer. This principle is shown in Figure 2.19.

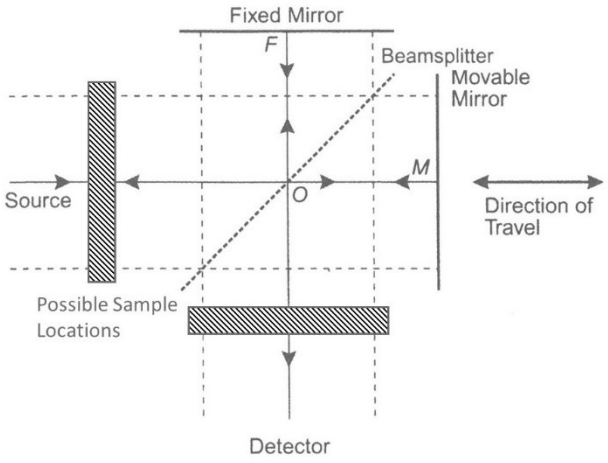

Figure 2.19 Schematics of a Michelson interferometer with one moving mirror, commonly used in FTIR spectrometer. Source: [48]

Depending on the spectral content of the pulse entering the interferometer, different interferograms can be obtained. An ideal monochromatic light source, for example generates a cosine wave signal, since the moving mirror creates varying path differences in optical path, that periodically create conditions ranging from destructive interference to constructive interference. A broadband light source on the other hand creates only a sharp peak in the interferogram, so called *center burst*. An example of two interferograms with center bursts are shown in Figure 2.20. In one case (S-IF), the light has passed through an absorption cell with various gases present. This absorption cell could either be placed before or after the interferometer. In the other case (R-IF), the absorption cell was evacuated. Due to its design, the achievable resolution of a FTIR spectrometer is coupled to the transversable distance of the movable mirror. If this distance could be increased to infinity, an infinitely high resolution would be achievable. Therefore, high resolution FTIR spectrometer have a very long arm for the movable mirror (up to several meters). The measurement of the movement of the mirror itself is performed via a second interferometer, which uses a HeNe laser of known wavenumber 15803 cm^{-1} (632.8 nm). Based on the sinusoidal interferogram of this nearly monochromatic light source, each recorded interference peak is caused by a movement of the mirror of $632.8\,nm/2$.

While there is a minute difference between the two signals, only after performing the *Inverse (Fast) Fourier Transform* [I(F)FT] and obtaining the corresponding spectra (see Figure 2.21), it is possible to see the differences in the spectral content of both light beams.

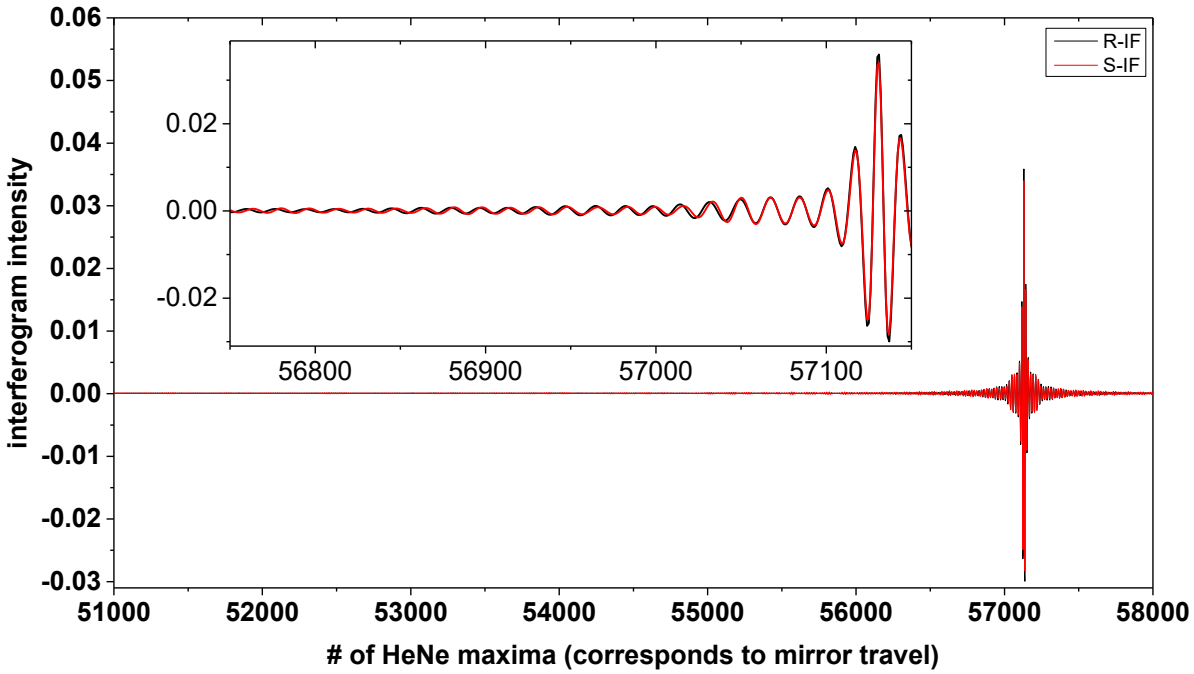

Figure 2.20 Interferograms of a FTIR spectrometer. R-IF: Interferogram after light passed through evacuated absorption cell. S-IF: Interferogram after light passed through absorption cell containing various gases.

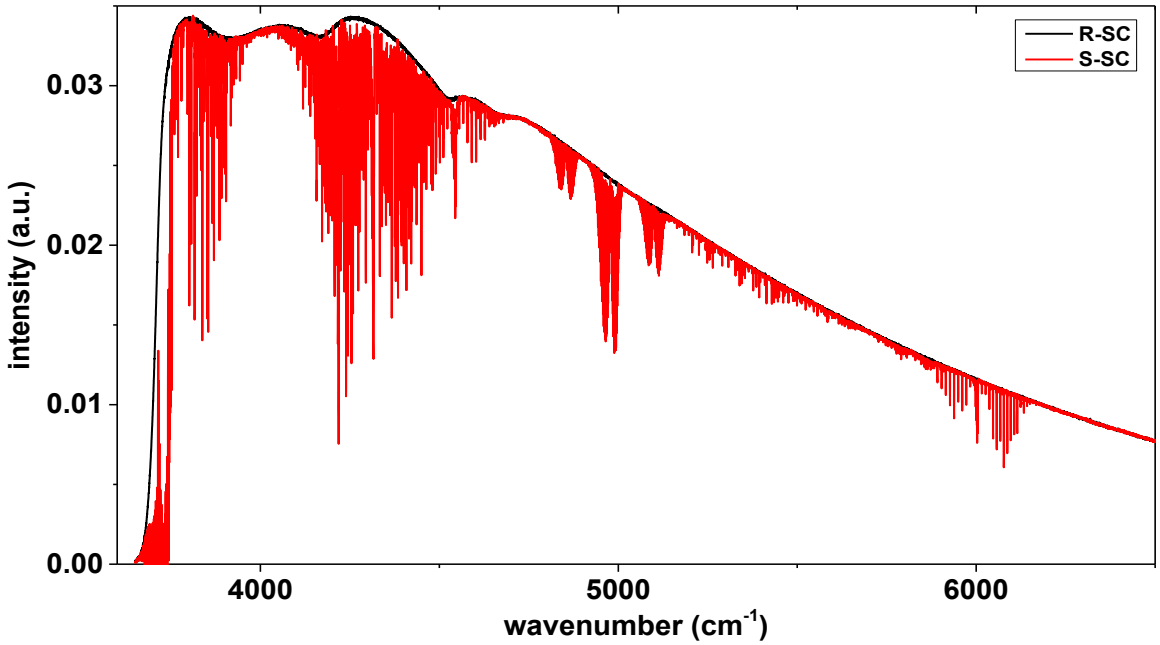

Figure 2.21 Transmission spectra of a FTIR spectrometer in the intensity domain. R-SC: Spectrum after light passed through evacuated absorption cell. S-SC: Spectrum after light passed through absorption cell containing various gases.

When applying the Beer-Lambert law, the spectral absorbance to base e, according to Equation (2.8), can be calculated and comparing the spectra to a database allows for the identification of the gases in the absorption cell (see Figure 2.22).

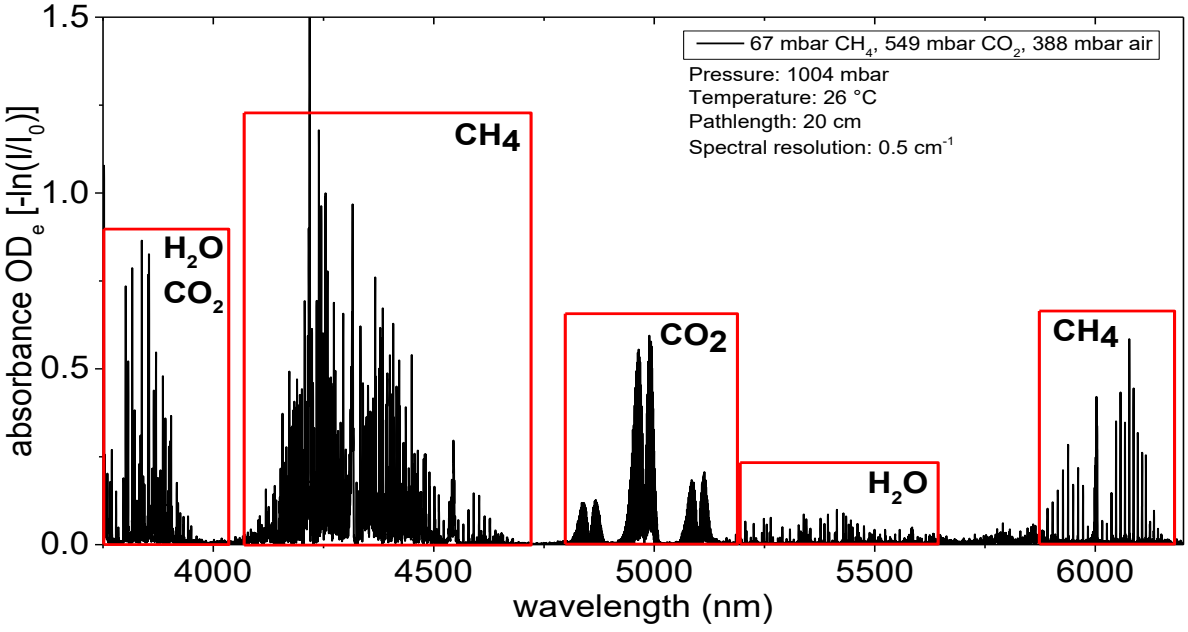

Figure 2.22 Spectral absorbance spectra of a FTIR spectrometer.
R-SC: Spectrum after light passed through evacuated absorption cell.
S-SC: Spectrum after light passed through absorption cell containing various gases.
Gases present in the absorption cell can be clearly identified.

This example clearly shows the potential that FTIR spectroscopy has to offer, especially when investigating new spectroscopic models and generating absorption line data for databases or model calibration and verification. See Chapter 7 for the application of FTIR spectrometry in this work.

3 Supercontinuum Laser Light Source

Utilizing a diagnostic system to its fullest capabilities requires understanding its inner workings and behavioral characteristics. In case of SCLAS, this requires first and foremost a thorough investigation and understanding of the novel light source used. SCLAS utilizes Supercontinuum Laser Light Sources (see Chapter 2.4 for theoretical details), which provide pulsed broadband laser light with a spectrum ranging from 400 nm to 2400 nm (for the NIR versions of the source). This spectrum can be extended and shifted based on the pump system and PCF (photonic crystal fiber) used in the source. Currently in development are MIR versions of the light source as well as UV versions.

To understand and characterize the light source and its performance characteristics, several aspects were individually investigated. Besides the emitted spectrum and the spatial beam characteristics, the temporal pulse shape as a direct influence on achievable spectral resolution was measured and characterized in combination with the high-speed photodiode. The emitted spectrum directly influences the possible absorption measurements, while the spatial beam profile influences the spatial resolution that can be achieved for different wavelengths as well as the performance of SCLAS over longer absorption path lengths. Since the SCLAS spectra will be recorded in the time-domain, the pulse-to-pulse behavior of the SCL was evaluated as well in combination with the pulse energy to evaluate the feasibility of averaging. Since filters are used in SCLAS, the combination of SCL and different filter options was also investigated to ensure required spectral behavior for broadband absorption measurements. Given that light generation and power distribution processes within the PCF adhere to stochastic patterns, it was further necessary to investigate the spectra of individual pulses and their effect on averaging.

3.1 Emitted Spectrum

The first step in characterizing a novel broadband laser light source such as the SCL is a measurement of the emitted spectrum to quantify spectral content and coverage, as well as specifics of the source that are presents in the spectrum (such as peaks or sections of reduced intensity). When measuring such a spectrum, it is necessary to keep in mind, that these measurements will be effected by several effects beside the source itself. Due to the nature of the source a broadband spectrometer needs to be used, which in itself has an additional spectral response function. Therefore, it was refrained from using this emission spectrum characterization as a quantification of spectral density and spectral power distribution. This was also due to the fact, that an FTIR (Bruker Vertex V80V) was used for this measurement. Such a FTIR is not well suited for use with pulsed light sources, due to its scanning nature in recording spectra (see Chapter 2.7). In addition, to allow for sufficient detector sensitivity an extended TE-InGaAs detector (thermo-electrically cooled extended InGaAs) was used, which is sensitive

to infrared radiation from roughly 900 nm up to 2200 nm (decreasing sensitivity towards both ends of the spectrum). This resulted in a limited detection of wavelengths above 2200 nm and below 900 nm, which are emitted by the source. Given the relative measurement approach of the FTIR no specific intensity correction is applied to the measurement. InGaAs detectors in general exhibit an increasing photosensitivity towards longer wavelength, followed by a sharp decline at the cut-off wavelength. Given additional optical components in the FTIR, an intensity correction could not be performed. Important for the characterization as a light source for SCLAS is its spectral range and coverage, rather than the absolute intensity levels. SCLAS measurements itself also require no absolute intensity values, given the relative approach to absorption spectrum fitting (see Chapter 2.1). Furthermore, due to the optical layout of the FTIR an open path coupling into the instrument is necessary resulting in absorption features of water vapor being present on the signal. The resulting measurement is shown in Figure 3.1.

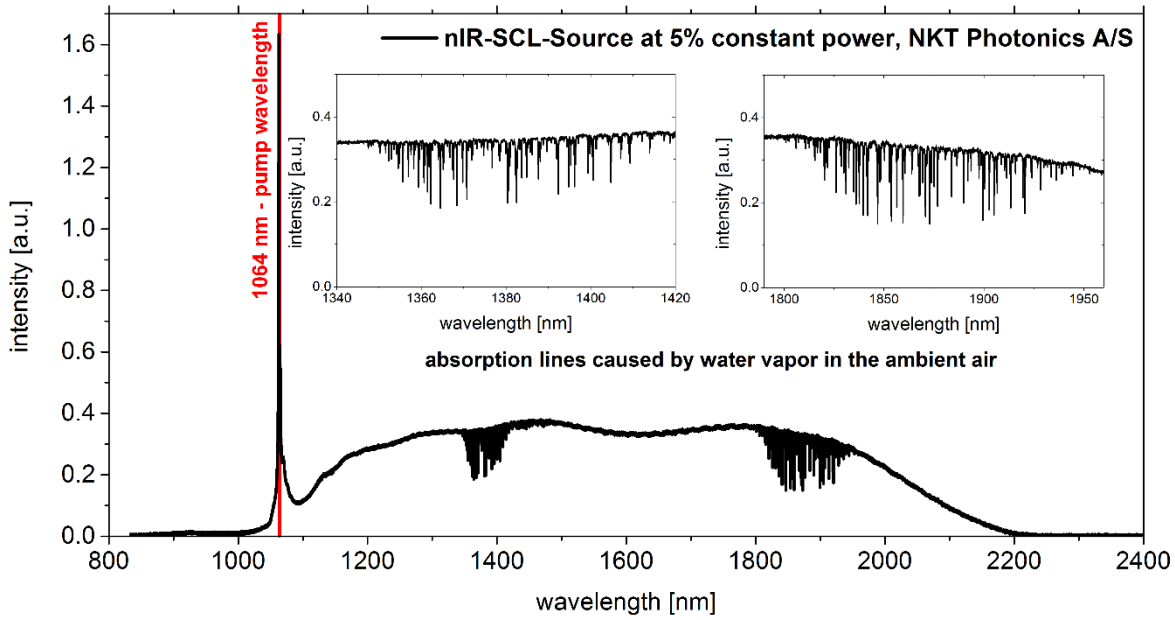

Figure 3.1 Emission spectrum of the SCL in the NIR range (900 nm – 2200 nm) measured with a FTIR. The spectrum is not compensated for detector sensitivity and is therefore not representative for quantitative energy distribution and spectral power density.
The FTIR detector is spectrally limited towards 400 nm and 2200 nm, limiting the recorded spectral content towards both ends of the spectrum.

The most pronounced feature is the residual intensity peak of the pump laser source at 1064 nm. The emitted spectrum covers the complete range in the NIR with no significant gaps in coverage or changes in intensity and is therefore well suited for use in absorption spectroscopy in the NIR region.

3.2 Spatial Beam Profile

When characterizing the beam shape and energy distribution in broadband light sources, there are several specifics to address. Since it is not useful, to measure the spatial power distribution for all wavelength combined, it is necessary to separate different wavelength ranges by filtering the light output. Due to this, the measured distribution is a combination of the filter system and source performance. Furthermore, a SCL is a fiber-coupled system, which is permanently combined with a specifically tailored collimator at the end of the PCF. This combination of source, fiber and collimator has been developed by the manufacturer and cannot be changed at a later time. Due to the inherent difficulties and problems with handling PCFs this combination was left unchanged (comparable to the fiber-coupling of DFB laser diodes within the laser's butterfly casing) in the context of this SCL characterization. The measured beam profile therefore represents the combination of light source, PCF, fiber coupling optics and *acusto-optical tunable filter* (AOTF) system. While the *AOTF* system only represents a single option for the necessary filtering (see Chapter 2.6 for details), the crystals in the AOTF system influence the beam profile more significantly than a standard interference band pass filter and are therefore the worst case scenario regarding beam profile and shape. To reduce the influence of the AOTF system nevertheless, a filter module by the same manufacturer as the SCL was chosen, which also offers direct integration with the fiber coupling of the light source. The beam profile measurements were performed with central wavelength of the filter ranging from 1200 nm to 1750 nm every 50 nm. For the beam profiling a rotating-slit beam profiler (Thorlabs BP104-IR2) was used, offering a measurement rate of up to 20 Hz. In comparison to the SCL repetition rate of 80 MHz, the source can be considered continuous.

Below in Figure 3.2 exemplary beam profile images from central wavelength at 1200 nm, 1450 nm and 1650 nm are shown. Residual line structures in the image are caused by the beam profiler due to its operating principle. It can be seen from the images that the beam waist diameter increases from the lower end of the spectrum towards the middle and decreases again towards the upper end of the spectrum. Furthermore, the amplification level was adjusted for each measurement resulting in increased noise levels towards the longer wavelength, since the power of the source decreases towards the longer wavelengths. The color scale was adjusted as well to the minimum and maximum intensity values to provide easy evaluation of homogeneity of the power distribution. Along with this decrease in power, the beam gets a slightly wider shape. To assert the shape of the beam profile further, Gaussian peak functions were fitted to the measured intensity curves in the center for both directions (shown in Figure 3.2 as a red line). It can be seen that these fitted curves are coinciding very well with the measured curves (yellow). The beam profile can therefore be described as Gaussian across the central region and even further out into the wings of the peak.

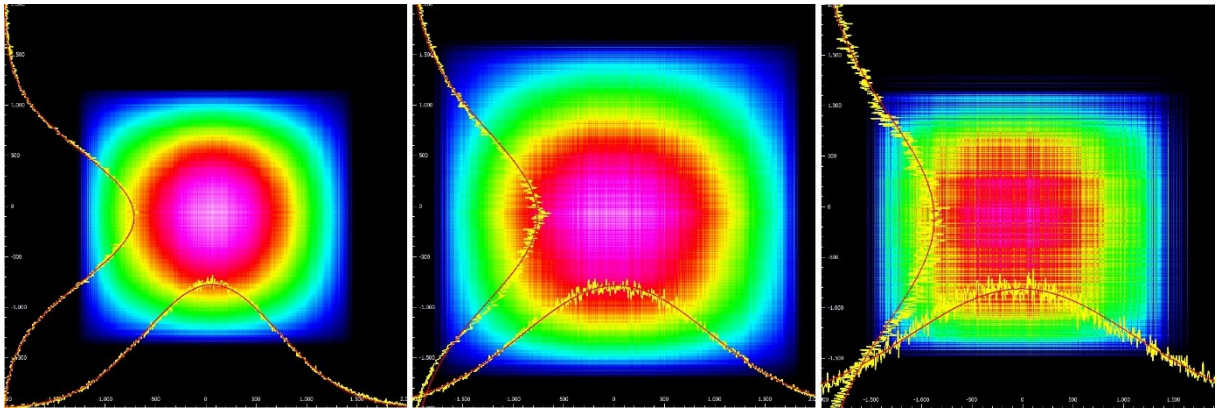

Figure 3.2 Comparison of the beam profile of the SCL at 1250 nm, 1450 nm and 1650 nm (All images are to the same scale).

When evaluating the spatial FWHM measurements for all recorded central wavelengths, the trend depicted in Figure 2.1 can be seen, showing a almost linear increase in spatial FWHM with longer wavelengths.

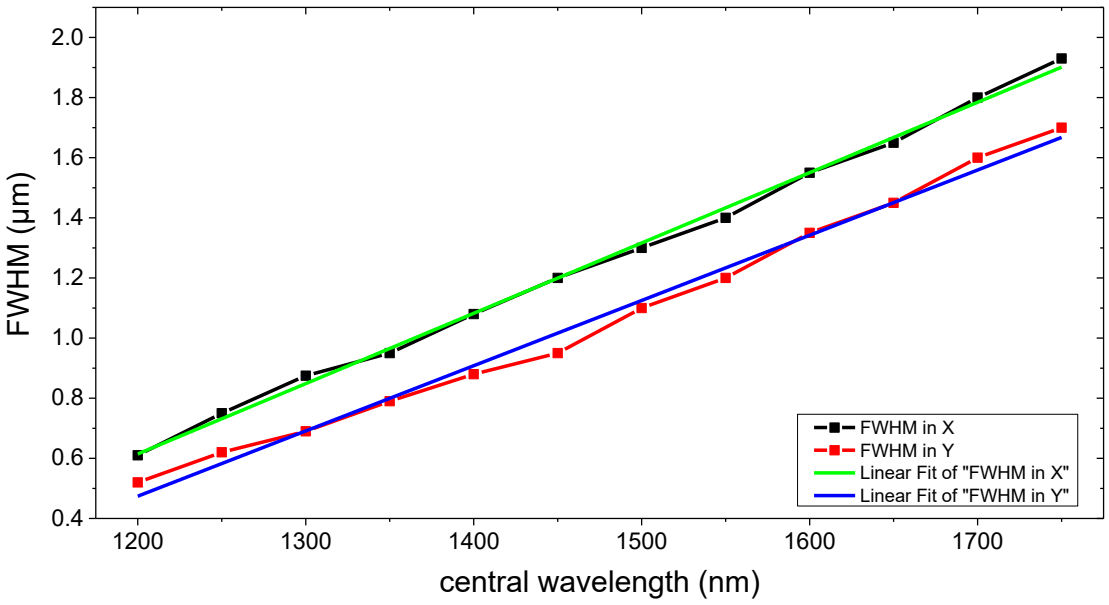

Figure 3.3 Evaluation of beam spatial FWHM in orthogonal directions X and Y with linear trends fitted to the data.

Given that the used SCL is a fiber-based system, the combination of PCF and collimator can be considered very well matched. All measured beam shapes and beam widths are sufficient for use in absorption spectroscopy, even when position-resolved measurements are to be performed, and the possibility of fiber-based light delivery of a broadband NIR spectrum offers great potential for optical in situ diagnostic systems.

3.3 Temporal Pulse Shape

Due to the high power and high repetition rate, a characterization of individual pulses is necessary, but challenging at the same time. Characterizing the temporal pulse shape and its distribution across thousands of pulses allows for a characterization of the SCL itself, as well as ensures that the influences of the variations in temporal pulse width on the spectral resolution and the pulse averaging are negligible. Since high-speed photo diodes (as utilized in these experiments with bandwidth of up to 12 GHz) are limited in the incident power, it is again necessary to filter the emitted light spectrally and only measure the light from a specific range in the spectrum. To filter the light and change the emitted bandpass range, the AOTF system described in Chapter 2.5.1 was used and tuned to different wavelengths throughout the measurements. Inherent to such high-speed system is a phenomenon called diode or electrical ringing. When a pulsed signal is applied to either a photo diode or an analog acquisition device (for example the *ADC* of an oscilloscope), the recorded time series also includes oscillations before and after the pulse itself, which result from the high sensitivity of the system to any input signals. An oscillation circuit as part of the amplifier electronics causes this effect. Trans-impedance amplifiers, which are used in this work to amplify the current signal from the photo diode, incorporate an internal feedback signal (between current input and amplified voltage output) consisting of resistors and capacitors. This circuitry creates the possibility of oscillation in the output signal for pulsed input signals, while this oscillation worsens with increasing amplification. This phenomenon also influences the data evaluation as described later in Chapter 4. In addition to these oscillations, which are expected to be present in the recorded signals, the required time resolution to even measure pulses of the SCL is on the order of tens of pico seconds, since the pulse itself is expected to last around 100 ps (according to manufacturer specifications). Under-resolving these pulses in time may result in incorrect estimation of pulse shape parameters such as FWHM and $1/e^2$ width. The main possibility to address these issues is to apply some form of interpolation or pulse fitting to the recorded data to obtain a better representation of the pulses. Several options are available for these cases: Gauss peak fitting, Sech pulse fitting and Sinc interpolation (sin(x)/x) are among the most commonly used options. Based on communications with the manufacturer (see [120]) it is expected that the pulse shape itself is a combination of a Gauss and Sech pulse, while there are no measurements (i.e. Streak camera measurements) available at this time for this SCL in the near infrared region. Furthermore, a pulse shape characterization has to account for the fact that the photo diode itself also influences the recorded shapes. The photo diode used in these experiments is a high-speed photodiode (Newport New Focus 1544-B-50), which offers a bandwidth of 12 GHz and being directly fiber coupled with a 50 μm multimode fiber within the casing itself to shield the amplifier circuit from external noises. The amplifying circuit itself provides an conversion gain of -700 V/W and a transimpedance gain of -1000 V/A with an optical saturation power of 0.7 mW. The rise-time of the combination of photo diode and amplification circuit is specified at 32 ps. When using this photo diode in combination with the SCL for temporal pulse characterization, assuming twice the rise time as a lower limit of the

resolution, the system can roughly be used to characterize pulses with a temporal width larger than 64 ps.

Exemplary temporal pulse shape measurements for a bandpass filter central wavelength of 1200 nm are shown in Figure 3.4. The SCL was operated at 80 % constant power with a repetition rate of 20 MHz. A Sinc interpolation was used on the raw measurements of the oscilloscope (time resolution 25 ps/pt) to achieve a time resolution of 500 fs/pt.

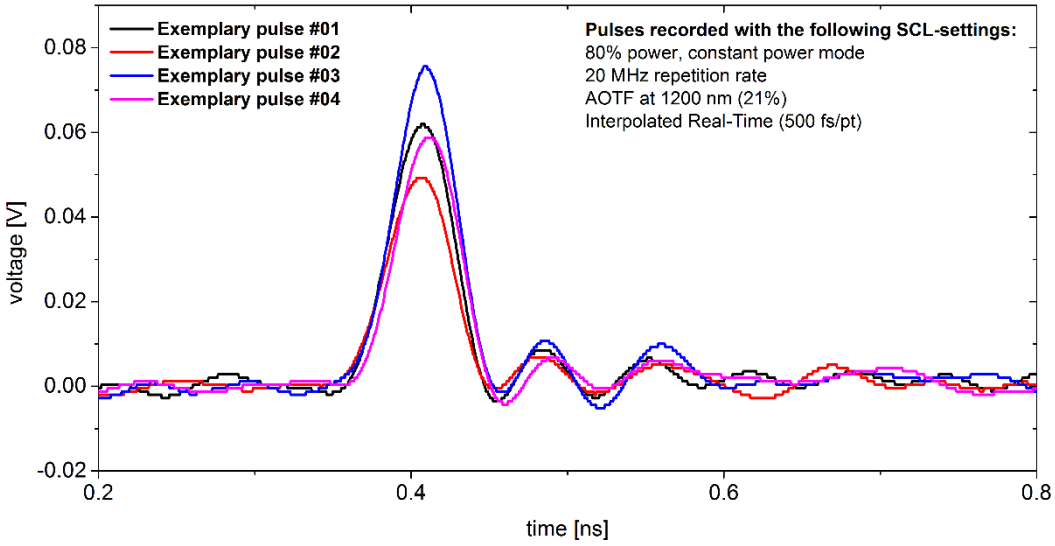

Figure 3.4 Exemplary pulses recorded at 25 ps/pt with Sinc interpolation (500 fs/pt).

To further characterize the temporal pulse shape and to allow for the derivation of characteristics for the temporal pulse shape, several interpolation and peak fitting schemes were compared as shown in Figure 3.5. It can be seen, that all schemes show a rather good agreement between pulse shape as recorded and as interpolated in the central region of the peak. Nevertheless, only the Sinc interpolation is able to recreate the oscillation in the signal prior to and after the actual main peak itself. This is mostly due to the fact, that a Gaussian or Sech peak pulse interpolation itself doesn't allow any oscillation outside the peak itself. Since these effects are also taking place when recording absorption spectra (each absorption feature is in essence such a peak, only inverted), any interpolation scheme utilized should to be able to resemble the effects of system ringing and other oscillations. If this is not the case, the interpolation needs to ensure proper separation of ringing oscillations from the actual measurement signal itself for all operating conditions of the system. Otherwise, oscillations from diode ringing might be interpreted as absorption features or vice versa. Overall, it is preferable, if necessary, to use an interpolation scheme that properly resembles the input signal (in this case the diode signal with oscillation) and treat these oscillations separately from the interpolation. In the case of SCLAS, the effect of diode ringing is incorporates into the spectrum simulation to ensure proper fitting to recorded measurement signals.

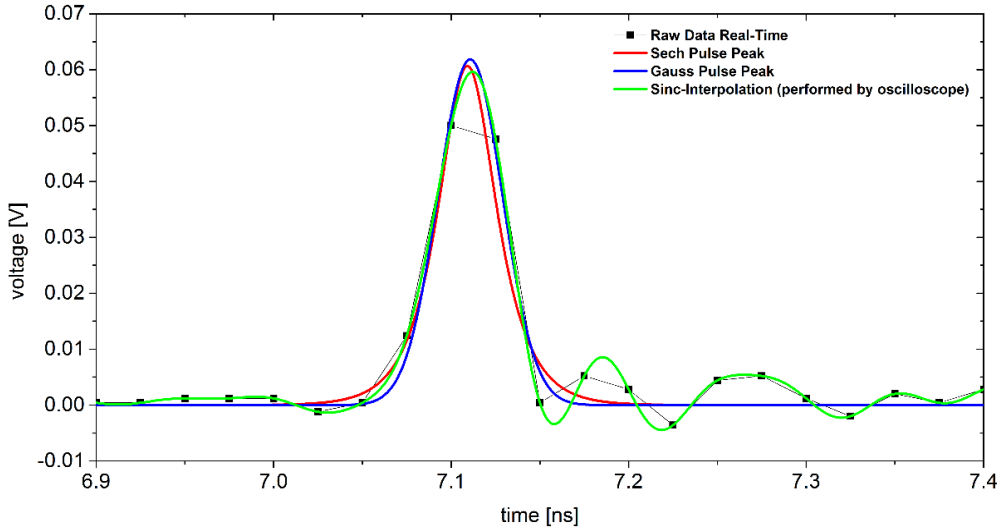

Figure 3.5 Comparison of possible interpolation and peak fitting schemes to improve temporal pulse shape measurement to allow for the derivation of pulse characteristics and metrics.

When deriving metrics from the temporal pulse shape, there are several parameters, which are usually assessed to characterize a pulse shape in time. For the purpose of this characterization, the *FWHM* (full width at half maximum) and the $1/e^2$ width (width at ~13.5 % of peak height) of the pulses were chosen and evaluated for various central wavelength of the filter system. The combination of *FWHM* and $1/e^2$ width allows for a measure of steepness of the peak. For the diagnostic system itself it would be beneficial if these parameters would be distributed close to a Gaussian (or normal) distribution for ease of post-processing. The results of the FWHM measurements are shown in Figure 3.6 in form of a boxplot.

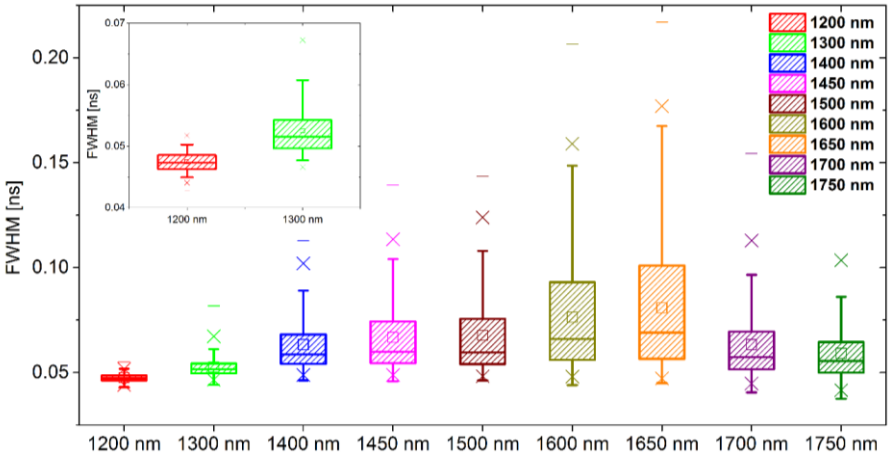

Figure 3.6 Boxplot of the *FWHM* distribution of the temporal pulse shape of pulses from the SCL with AOTF at various ventral wavelengths. The shaded box represents the inner 50 % of all recorded values, while the thick line in the middle of the box represents the center of a normal distribution fitted to the measurements.

From these measurements, it can be seen that, while the lower and upper ends of the central wavelengths are distributed rather normally, the distribution differs quite significantly from a normal distribution in the middle of the range of central wavelengths being distorted towards longer FWHM times. When comparing this to the measurements of the beam width in space (see Chapter 3.2), this trend is not resembled. The spatial FWHM increases rather linearly with longer wavelength.

When measuring the *1/e²* width of a pulse (intensity at ~13.5 % of maximum intensity) a rather similar behavior can be observed as shown in Figure 3.7, though slightly less pronounced and more evenly distributed changes in the distribution of the *1/e²* width. It has to be kept in mind, that these measurements are the results of the combined system consisting of SCL, photo diode and data acquisition system.

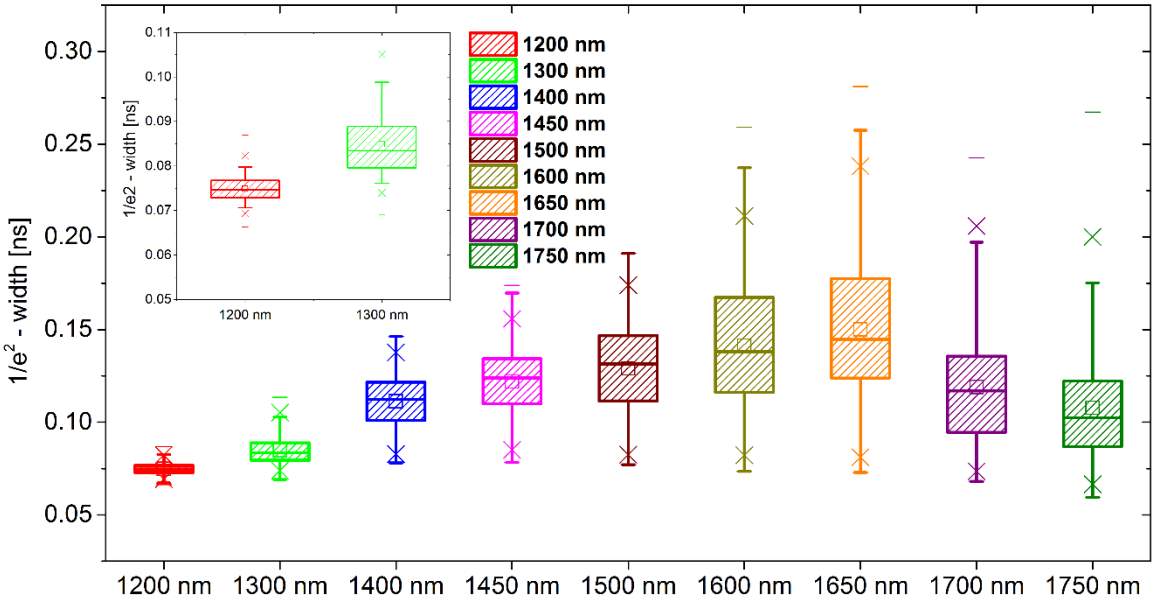

Figure 3.7 Boxplot of the 1/e² width distribution of the temporal pulse shape of pulses from the SCL with AOTF at various ventral wavelengths. The shaded box represents the inner 50 % of all recorded values, while the thick line in the middle of said box represent represents the average value of the distribution. The smaller light square represents the center of a normal distribution fitted to the measurements.

3.4 Pulse to Pulse Behavior and Pulse Energy

When utilizing a pulsed light source and averaging a significant number of pulses for the determination of absorption spectra, it is necessary to ensure that this procedure can be performed consistently and there are no issues related to pulse to pulse variations and repetition rate jitter. To assert this behavior measurement of the pulse to pulse time for various repetition rates of the SCL were performed and are shown in Figure 3.8. For these measurements to be representative of the full range of emitted wavelength, a combination of AOTF central

wavelength was used (1300 nm, 1400 nm, 1500 nm and 1600 nm). Since all SCLAS spectra are recorded in time, the pulse-to-pulse variations play a significant role in asserting the precision and accuracy of the recorded spectra and the achieved optical resolution (in combination with the DCM). Since pulse trains, as used when recording spectra for averaging, need to be split into sections with identical spectral content anyway before averaging can be performed, the individual pulses could, if necessary, be aligned prior to averaging. For this the NIM pulse train, which is created simultaneously with the optical output, provides a single pulse each time the seed laser fires.

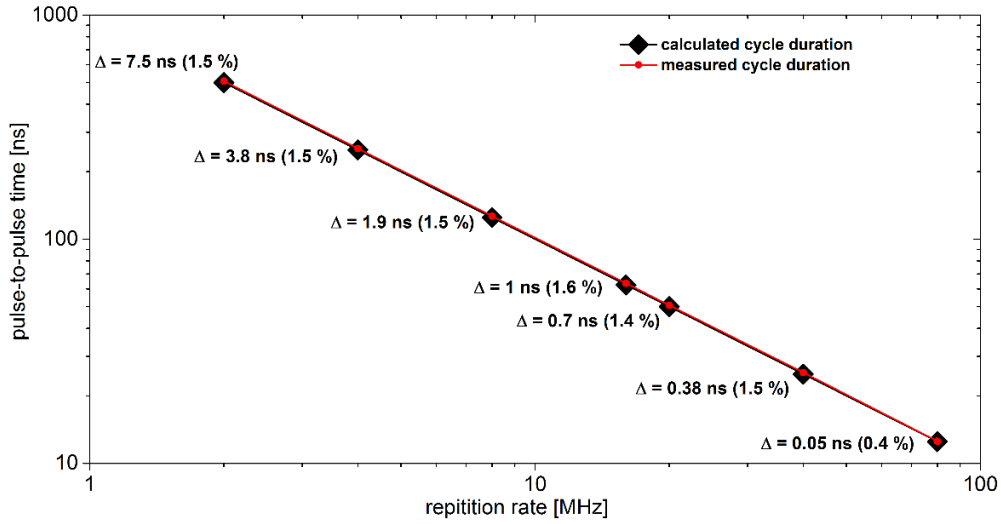

Figure 3.8 Pulse to pulse time measurements for various repetition rates when using central wavelengths of the AOTF at 1300 nm, 1400 nm, 1500 nm and 1600 nm simultaneously.

It can be seen from the measurements, that the deviation in pulse to pulse times are low compared to the time between pulses. With the exception of a 80 MHz repetition rate, the deviation is on the order of 1 to 2 %. In the case of 80 MHz it has be taken into account that this is the natural operating frequency of the pulse generator and therefore, no pulse picking is active. As pulsed systems usually have the tendency to vary in energy per pulse depending on the pulse frequency, it is also necessary to characterize the pulse energy of individual pulses. Since a direct measurement of this pulse energy is not feasible due to the high repetition rates, the power of the laser beam was measured as continuous and an even distribution of energy among the pulses was assumed. Figure 3.9 shows the results of the pulse energy measurements for various repetition rates of the SCL.

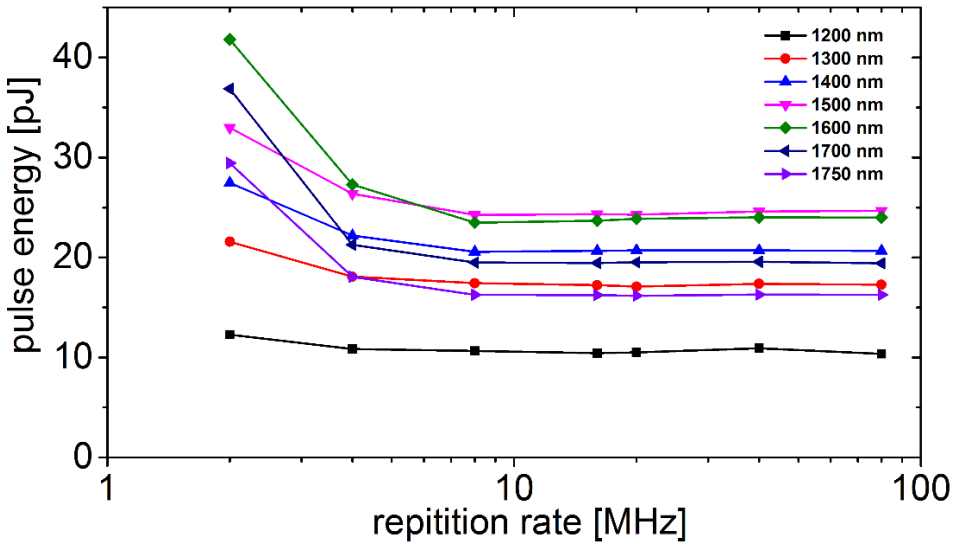

Figure 3.9 Pulse energy for various repetition rate of the SCL by measuring the emitted power as a continuous source and assuming even distribution of the energy among the pulses.

Since all repetition rates of the SCL are even dividers of the base frequency of the seed laser (80 MHz), the slowest repetition rate achievable is 2 MHz (maximum divider of 40). Except for this repetition rate the energy per pulse is almost constant (variation less than 2 %) across the full range of repetition rates, showing no correlation between repetition rate and pulse energy. This is mostly due to the fact, that the basic optical system in the source is designed for continuous operation at 80 MHz. Reduction of the repetition rate reduces the load on the amplifiers and pump systems, since the pulse picker works on the non-amplified seed pulses. The measured increase in power at 2 MHz repetition rate might be caused by the power meter used in these measurements. The power meter allows for power measurements at a rate of up to 100 kHz under resolving the pulse only by a factor of 20 (instead for example of a factor of 800 in the case of 80 MHz).

3.5 Variations in Pulse Shape and Pulse Shape Area

Since the processes behind the spectral broadening within the SCL are stochastically distributed, it is necessary to average a certain number of pulses to obtain spectra with complete spectral coverage. To estimate this need for averaging measurements were performed with different averaging and different central wavelengths of the AOTF system, while evaluating the pulse shape area as an indicator of sufficient averaging. Figure 3.10 shows the behavior of this parameters over various amounts of averaging for different central wavelengths. In the case of TDLAS, this parameter is usually determined by the Allan-Werle- variation [121], which provides an indication to the amount of averaging beneficial to the signal quality. This parameter nevertheless requires measurements without any averaging to start with, which are not possible with SCLAS due to the nature of the SCL. The pulse shape area indicator was therefore devised as an alternative to the Allan-Werle variation. From these measurements it is

determined, that an averaging of 200 pulses or more seems to be sufficient for obtaining stable pulse shape areas.

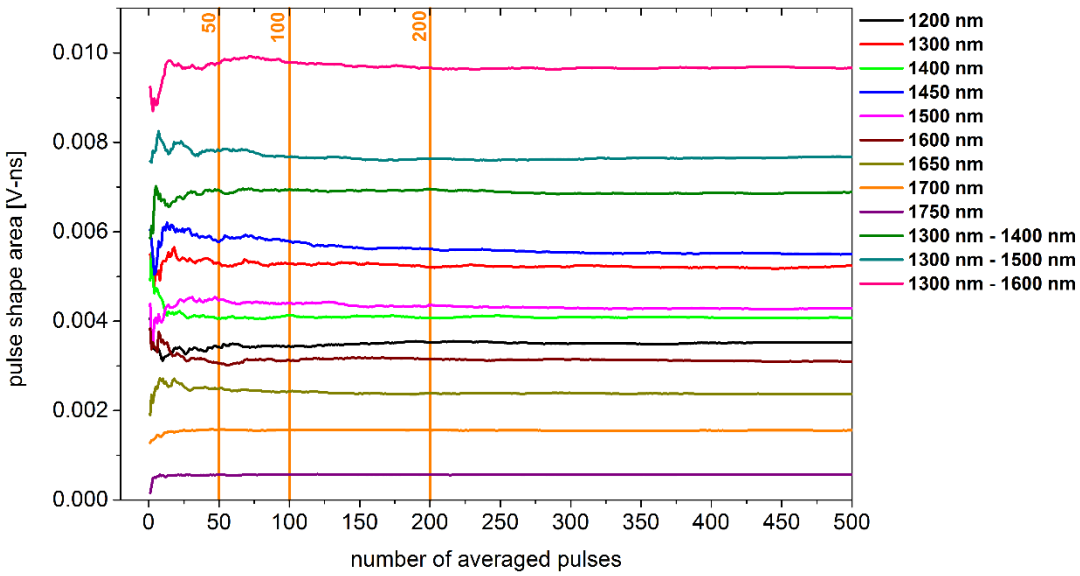

Figure 3.10 Effect of various amounts of averaging on the pulse shape area for different central wavelengths of the AOTF system.

To further investigate if this behavior is also influenced by the presence of a DCM in the optical train, similar measurements were performed with a DCM present in the optical path. The results, shown in Figure 3.11 normalized to the final pulse shape area, suggest that averaging an equal number of 200 pulses or more is sufficient in this case as well.

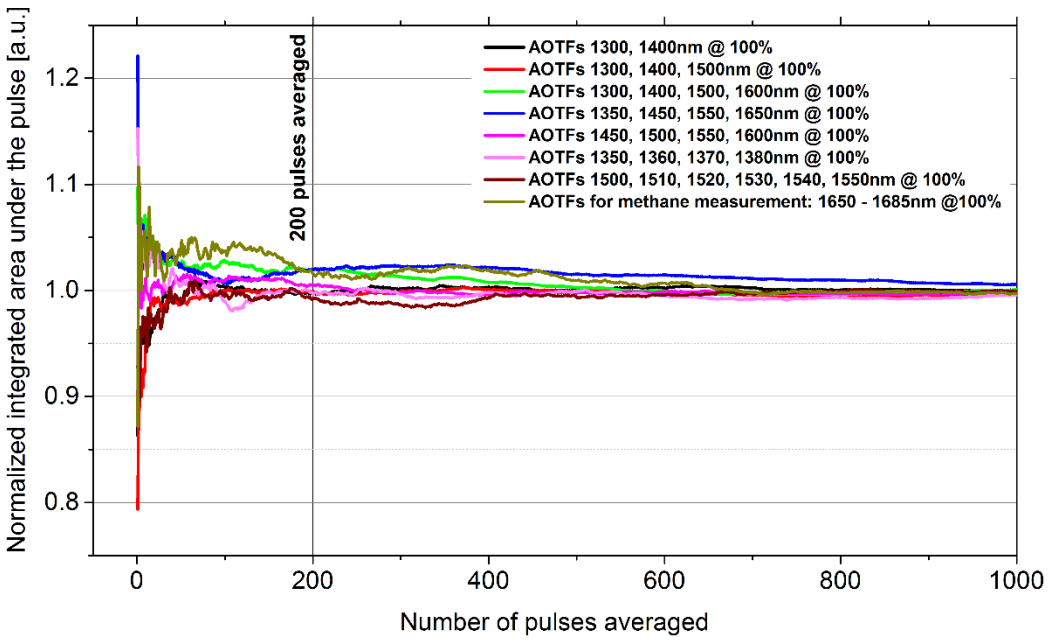

Figure 3.11 Effect of various amounts of averaging on the pulse shape area for different central wavelengths of the AOTF system when including a DCM in the optical path.

4 Principles of the Evaluation of SCLAS Measurements

Aside from the Supercontinuum Laser Light Source, the second major component of a SCLAS system is the data processing and evaluation algorithm, which allows the derivation of multiple parameters from the measured signal [25, 37]. Due to the characteristics of a SCLAS system, such an algorithm needs to address multiple challenges that are not part of a typical processing and evaluation setup for other spectroscopic instruments (i.e. grating spectrometers). This chapter will present these challenges and cover the basics of such an algorithm before discussing the specifics and unique characteristics in more detail.

Before discussing the details of the evaluation algorithm, it is necessary to look at the specifics of a SCLAS spectrum that this algorithm needs to process. In Figure 4.1, an exemplary measurement of SCLAS is shown. From the time axis, it can be seen that this spectrum, ranging from roughly 1300 nm to 1700 nm, lasts about 500 ns and includes absorption features of water vapor and methane (marked in the figure). The resolution is different for each wavenumber (see Chapter 2.6 for details). The complete spectrum consists of 20,000 data points with a time resolution of 25 ps/pt and represents the averaging of about 10,000 pulses at a repetition rate of 2 MHz. To evaluate such a spectrum, it is necessary to divide this spectrum into several sections to be processed separately (for example depending on different species in different spectral regions) and fit spectroscopic models, suited for SCLAS, to the measured data.

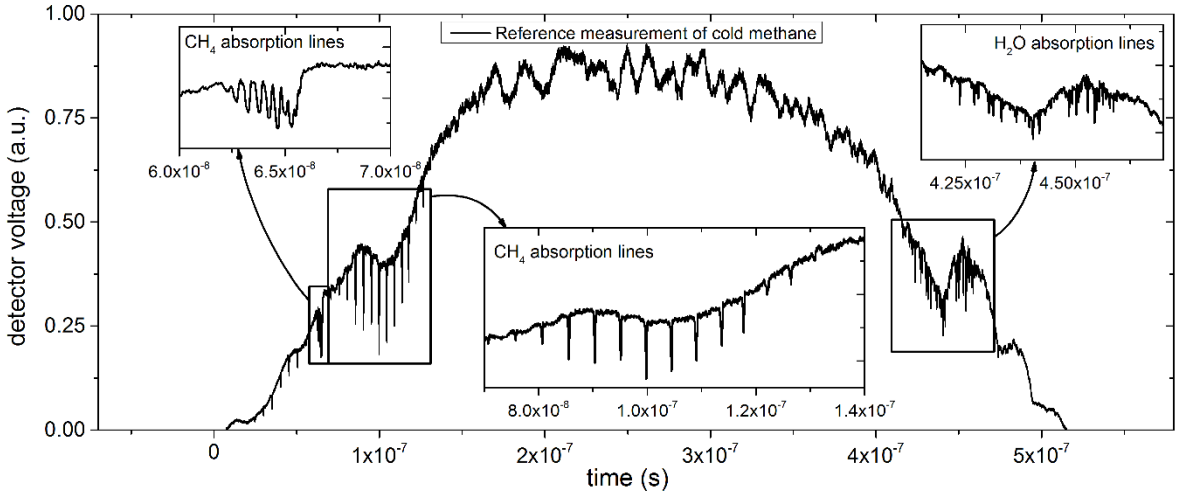

Figure 4.1 Exemplary spectrum of water vapor and methane recorded with SCLAS. Both species are visible on the spectrum, alongside several oscillations, which are part of the spectrum as emitted by the SCL.

Depending on the situation, the spectroscopic models will be of different complexity levels. While it might be necessary to fit different temperatures for different species in the measurement volume (for example in the case of stratification), it is feasible to assume equal

pressure for all species. Given the amount of information contained within a broadband spectrum, the determination of the suitable spectroscopic model is part of the data evaluation. Furthermore, proper selection of the evaluated region of the spectrum (specific features or sections), can increase the quality and performance (i.e. sections with insufficient or highly erroneous line data should be omitted). It is therefore highly unlikely that a single algorithm suits all needs and can simply be run without adaption to the specific problem. This process will be covered in this chapter, alongside necessary steps to prevent “cross-talks” between parts of the algorithms. Some of the techniques discussed here have not reached full potential yet, but are considered promising and worth the development.

4.1 Challenges in the Evaluation of Broadband Absorption Spectra

During the development of post processing approaches and specific algorithms for SCLAS, several challenges were identified, that need to be addressed:

- Amount of data recorded / data per spectrum recorded
- Spectroscopic model capable of accounting for diode ringing and other SCLAS related effects
- Determination of reference intensity of the signal (usually called the background of the signal, incident intensity)
- Performing partially constraint optimization of the spectroscopic model for the fitted parameters
- Advanced spectrum modelling approaches to accelerate spectrum calculation and fitting

Determining the relationship between time and wavenumber of the recorded spectra was also identified as a challenge, which was addressed during this development. Details regarding this can be found in Chapter 2.5. Since the solution merely relied on applying previously known techniques, this challenges was omitted from the list.

All of these challenges share certain characteristics in their nature, but differ in the extent to which they can be handled by simply improving existing approaches as compared to needing to develop complete new systems. The mentioned issues can be asserted regarding their possible solutions as follows: Most issues are caused by the fact, that these high resolution spectra are spectrally broader than the spectra usually utilized in high- resolution spectroscopy. This can be partially addressed by increased available computing power and similar approaches such as parallelization in computation. The amount of data recorded in combination with the size of a single spectrum can be addressed with parallelization, while accounting for diode ringing needs extensive changes to the spectroscopic model to include these effects in simulated spectra. Determining the reference intensity is closely coupled with the efficient calculation of spectra, since only the simultaneous calculation of spectrum and reference intensity can be used to simulate realistic SCLAS spectra as required for post-processing. Alongside the actual calculation of the spectra, there is the need for fast and high quality fitting of the spectrum

parameters (namely concentration, pressure and temperature). Since this step relies on optimization algorithms, it can be greatly aided by advanced design of the spectrum calculation routine (i.e. easier calculation of derivatives, and therefore avoiding numerical derivatives). Furthermore, to address multiple challenges combined, it can be beneficial to develop completely new spectroscopic models, which are mostly suited for SCLAS data evaluation, but will also offer advantages in other spectroscopic techniques. Examples in this area include simplified models, black-box models (see Chapter 7 and [44]) and advanced machine learning approaches.

In the following sections, each of these challenges will be discussed separately alongside different solutions.

4.2 Processing Large Amounts of Spectral Data

Since an SCLAS system is sampling the time series signal at very high sampling rates (up to 40 GS/s, resulting in a time resolution of 25 ps/point) it is necessary to handle these number of samples in post-processing. Since the DAQ equipment for SCLAS (mainly oscilloscopes) is not yet capable of recording continuously due to insufficient data storage speeds, SCLAS signals are limited in the amount of time that can be recorded within a single measurement. For possible solutions to this limitation, see Chapter 8. Nevertheless, a single recording of an SCLAS signal consists of multiple tens of thousands of data points (depending on optical resolution and dispersion in the DCM). A single recorded time trace before averaging of an absorption spectrum can reach up to 500 MB. Any post processing needs to account for this number of data points and still perform sufficiently to allow post processing in a timely manner. Furthermore, such large amount of data also challenges the computer systems used for post processing due to limitations in memory and drive space.

To address these issues, several options are available. The memory storage issue can be resolved by averaging on a separate system and post-processing separately. To address the number of data points in a single absorption spectrum, it is necessary to apply several techniques simultaneously. The first approach is to implement a spectrum calculation method that is fast enough to be iterated several hundreds of times per spectrum during the fitting process (for additional information regarding the commonly used method for spectrum calculation see Chapter 2.2). When using line-by-line based spectrum calculation approaches (such as HITRAN), this was achieved by parallelizing the spectrum calculation for all points and all absorption lines in the spectrum at the same time (combined later by aggregation of absorbance) and implementing highly efficient numerical approximations for the underlying Voigt line-shape (see [62]), which provides significant improvements over previously used approximations (see [56–58]). Additionally, the required number of iterations for convergence was reduced by providing proper initial guesses to the fitting algorithm. Furthermore, spectrum calculation was limited for the first iterations to areas of the spectrum, which contained the most information for the fitting algorithm. The complete spectral section was only included at a later stage in the fitting process. Such areas include the absorption features itself and more

importantly the areas with larger derivatives, as they are providing the most valuable information to the optimization algorithm. To further improve spectrum calculation performance, advanced spectroscopic models are required as described in Chapter 4.4 later on in this section.

4.3 Determination of Reference Intensity from the Recorded Signal

Since both TDLAS and SCLAS are based on relative intensity measurements (I/I_0, see Chapter 2.1) an estimation or measurement of the reference intensity I_0 is required. Given that the typical application scenarios rarely allow for the separate measurement of the reference intensity (especially if for example optical process windows are involved, that become covered with time), it is necessary to determine this value from the recorded signal itself. This can be achieved by assuming a specific numerical model for the reference intensity (i.e. a polynomial), to which the calculated absorption spectrum is applied and then the resulting combination is fitted to the signal. Alternating iterative fitting of both components (i.e. background, followed by absorption spectrum, followed by background, followed by absorption spectrum, etc.) is not feasible, since the absorption feature itself will influence the reference intensity determination and vice versa. In the context of TDLAS, p-order polynomials are used as the numerical model for the reference intensity. The order of the polynomial is in most cases below five, rarely higher. Should a higher-order polynomial be required, this is an indication, that optical effects are present, which should be otherwise addressed (i.e. wavenumber-related transmission properties of fibers resulting in multi-mode behavior or etalon-caused fringe patterns). Unfortunately, for SCLAS, a p-order polynomial, even of higher order, it not feasible as can be seen from Figure 4.1. For SCLAS an approach using B-splines curve consisting of third order polynomials is used (see [37]). Such a curve allows for greater flexibility in reproducing the necessary fine structure in the reference intensity of a signal. Additional details for the SCL light source and its influence on the shape and structure of the reference intensity can be found in Chapter 3.

Using a B-spline curve alone would nevertheless be insufficient to provide a proper representation of the reference intensity due to the presence of absorption features on the signal. To overcome this, certain sections of the signal were removed from the fitting process by limiting their influence on the cost function. For this, their weight in the cost function of the fitting algorithm was set to zero. Such sections were identified with a peak finding algorithm beforehand. In Figure 4.2 a section of an absorption spectrum for a methane-air-mixture is shown. The reference intensity for this section was determined by fitting a B-spline curve to the measurement trace, after parts of the trace, as identified by the peak finding algorithm, were weighted to zero for the fitting of the reference intensity. The width of such a zero-weighted sections needs to dependent on the process conditions. For example in environments with elevated pressure, these sections need to be wider than in sub-atmospheric conditions. To ensure proper peak finding, the threshold should be defined relative to the immediate peak neighborhood. Other approaches to peak-free reference intensity determination utilize the

rolling-ball principle, where an imaginary ball is rolled “on top” of the spectrum, following its contour. Since its size prevents the ball from following the contour into individual peaks, its trace is used as a reference intensity having suppressed the influence of individual peaks.

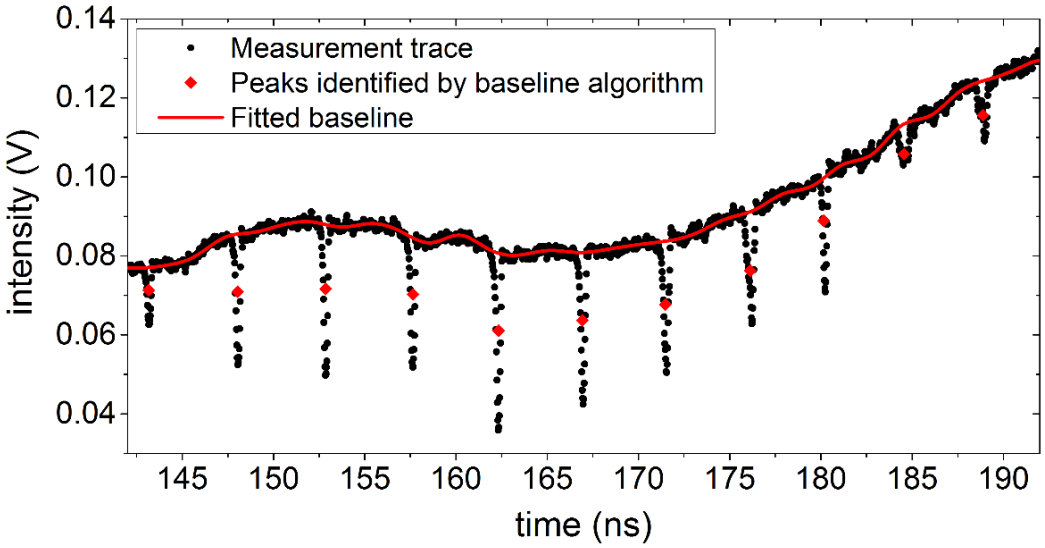

Figure 4.2 Baseline fitted to SCLAS signal of methane showing the identified peaks, which are removed from the signal by weighting before determining the reference intensity.

This approach is not feasible in high pressure environments, since the pressure broadening of the absorption lines will result in a merging of peaks and there is no section between peaks that is only part of the reference intensity trace. Nevertheless, the removal of the peaks from the (initial) fitting of the reference intensity is also not necessary at higher pressures. When fitting the B-spline based reference intensity model together with the spectroscopic model, as recommended earlier in this section, with properly chosen initial values for species parameters (pressure, temperature, species concentration), standardized fitting algorithms are capable of correctly deriving the parameters of the B-spline reference intensity, since no steep peaks distort the derivatives (as essentials for gradient-based fitting, see Chapter 4.5).

4.4 SCLAS-capable Spectroscopic Model

As previously described in the fundamentals (see Chapter 2.6), SCLAS records the absorption spectra in the time domain using an all-fiber approach. Therefore, time-related effects can greatly influence the recorded signal and consequently the measurement quality. A major effect when recording amplified high-speed high-bandwidth optical signals (effectively electrical signals when recorded with a photodiode) is diode ringing. This term describes a phenomenon, which occurs in electrical amplification circuits, especially those aimed at high bandwidth applications (see Chapter 3.3 as well). The internal electronics of a photo-diode and amplifier module, required to achieve the necessary bandwidth (internal feedback including resistors and capacitors), introduce a distortion in the form of oscillations to the signal to be recorded. This is common among high-speed optical sensors and is therefore a performance characteristic of such diodes which needs to be characterized and addressed in post-processing. Manufacturers

of high-speed photo diodes characterize their detectors by applying an optical pulse to the diode and recording the diode response with a well characterized electrical system. This impulse response can be used to derive the step response as well. It is necessary for SCLAS systems to account for this effect in the time domain, before transferring the time to the wavenumber domain. This is due to the fact, that the behavior of diode and the system is consistent for all points in time, but not for all wavenumbers. Pulses with identical time traces but different spectral content result in similar distortions of the recorded time trace (aside from slight variations in the photo current due to the different responsivities). Pulses with identical spectral content, but different time traces, result in very different distortions of the recorded trace. The impulse response of the utilized photo diode (Newport New Focus 1544-B-50) is shown in Figure 4.3 (normalized to amplitude of one, negative amplification). It is visible from the graph that the diode ringing also effects the signal before the actual signal is recorded, while the introduced oscillation can be considered subsided after 500 ps. This response is dependent on the individual photo diode and needs therefore be adapted, when a different diode is used. This effect and its modelling, together with other effects on the signal in the time domain, are described in detail later in this chapter.

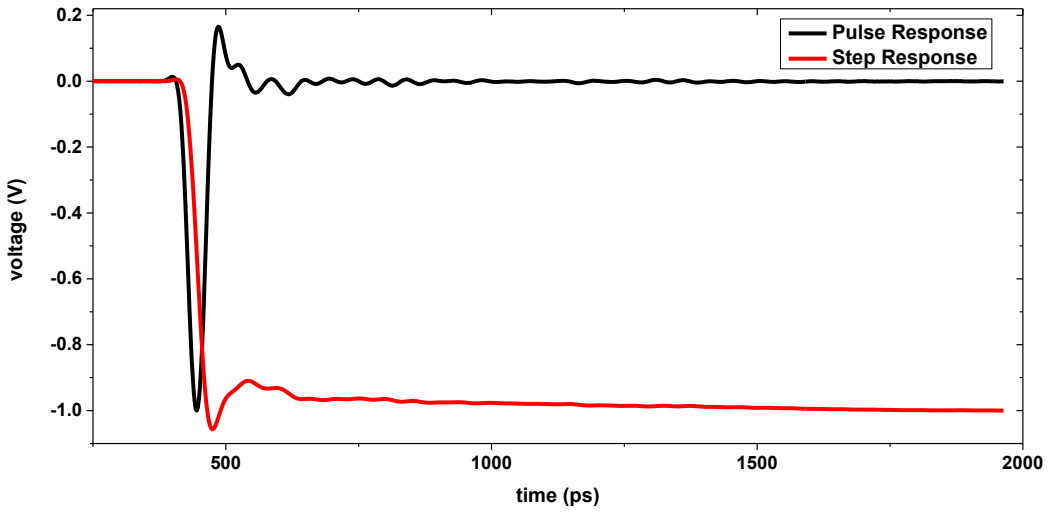

Figure 4.3 Normalized impulse response function of the photo diode used in the experiments

Additional effects in a SCLAS system that need to be accounted for in post processing include temporal shape of the pulses emitted by the SCL, the effect of the DAQ system as well potentially additional effects that are as of yet unknown, but present in the recorded spectra. More importantly, whenever key parameters of the SCLAS system are changed (i.e. the repetition rate of the SCL or the utilized photo-diode), the instrument function needs to be recalculated to account for these changes. For a grating spectrometer on the other hand, a replacement of the camera with a camera of identical pixel width does not change the instrument function in terms of spectral resolution. To account for these effects (diode ringing, etc.) and to create a representative instrument function, a measurement-based approach was chosen over a theoretical calculation. Nevertheless, the model is based on theoretical derivations, but incorporates unknown effects in the modelling as well. Additional details regarding this hybrid

approach can be found in Emmert, Blume et al. [44]. The approach includes several known effects based on individual parameters and mathematical models for these effects as well as an additional component, which accounts for as of yet undetermined, but quantifiable effects in the SCLAS system. For a given set of sample parameters (mole fraction, temperature, pressure, absorption length), the corresponding expected spectrum will be compared to the recorded signal and used to determine the additional instrument function accounting for unmodelled effects which needs to be applied to achieve accordance between simulation and measurement. For this, since SCLAS systems operate in the time domain primarily, the instrument function of the system is applied to the simulated absorption spectrum to generate the expected signal in the time domain. This approach provides significant advantages over trying to reverse the effects on the recorded signal due to additional noise sources present in the signal. Three individual parts of the instrument function were identified along the path of propagation of the light through the system:

- SCL (initial pulse shape, etc.)
- Photo Diode and all accompanying effects (i.e. diode ringing, etc.)
- Data Acquisition System (finite sampling, bandwidth, etc.)
- Unknown effects, that are present in the instrument function, will also be accounted for, since its determination is based on measurements.

The effect of the SCL could not be described explicitly, since no measurements regarding this specific SCL regarding pulse shape are available for the SCL (for example streak camera measurements). In general, it is assumed that the DCM itself does not influence the signal in the time domain and is therefore not required for modelling of effects in the time domain, since its effects are limited to the wavenumber domain (different attenuations for different wavelength, but independent of time, see Chapter 2.5 for details). Any dispersion like effect within the SCL, which is present, but very small compared to the dispersion of the DCM, will be modelled as a part of the DCM. The individual influences will be discussed in the following section.

SCL

Since SCL and the underlying processes of spectral broadening within the PCF (see Chapter 2.4) are very complex processes and effects, certain simplifications need to be made to model the influence on the instrument function. As shown in Figure 2.14 and by measurements in Chapter 3, the spectrum exiting the PCF can be considered fairly stable after averaging. A valid approximation is therefore to consider the spectral intensity distribution of the pulse constant across the duration of the pulse only allowing for the intensity to be time-dependent. This separates the spectral distribution of the energy within the pulse from the intensity trace in the time domain, which can be expressed as follows

$$\mathrm{I}_{SCL}(\mathrm{t},\nu) = I_{SCL}(t) \cdot \hat{I}_{SCL}(\nu) \tag{4.1}$$

where $I_{SCL}(t, \nu)$ refers to the intensity depending on time and wavenumber, while $I_{SCL}(t)$ refers to the intensity trace over time, representative for all wavenumbers ν, whereas $\hat{I}_{SCL}(\nu)$ describes the spectral intensity distribution constant for all points in time as solely a function of wavenumber. When this pulse traverses the DCM, the time axis now needs to be compensated for the delay introduced by the DCM. The dispersion of the DCM is modelled as a function $D(t) \rightarrow \nu$ mapping points in time to wavenumbers (see Chapter 2.5). The intensity trace in the time domain and the spectral intensity distribution are therefore no longer considered independent. This can be modelled as a mapping between the large time scale of the dispersed pulse (on the order of 500 ns) and the significantly shorter time scale of the SCL pulse (on the order of 100 ps), as shown in Equation (4.2). This intensity is then modulated with the absorption by a medium according to the Beer-Lambert law (as described in Chapter 2.1).

$$I_{DCM}(t, \nu) = I_{SCL}(t - D^{-1}(\nu)) \cdot \hat{I}_{SCL}(\nu) \tag{4.2}$$

$$I_{ABS}(t, \nu) = I_{SCL}(t - D^{-1}(\nu)) \cdot \hat{I}_{SCL}(\nu) \cdot \exp(-\alpha(\nu) \cdot L) \tag{4.3}$$

where $\alpha(\nu)$ refers to the spectral absorption coefficient and L to the length of the absorption.

After passing through the medium, the remaining light needs to be detected by a high-speed photo diode, which influences the instrument function as well.

Photo Diode and Data Acquisition System

Since SCLAS measurements take place in the time domain and photo diodes detect the integrated intensity independent of the incident wavenumbers, it is necessary to reduce Equation (4.3) to an expression in the time domain only. This can be achieved by integrating Equation (4.3) over the wavenumber and replacing any dependency on wavenumber by a dependency on wavenumber with the help of the dispersion function D. Since the pulses exiting the SCL are significantly shorter in time compared to the pulses after dispersion and assuming a constant derivative of the dispersion function $dD(t)/dt$ over the relevant spectral (or time) range evaluated, it is possible to model the intensity reaching the photo diode as a convolution of the intensity trace of the SCL $I_{SCL}(t)$ and the absorption modulated onto a reference intensity (see Equation (4.4)).

$$I_{ABS}(t) = I_{SCL}(t) \times (I_0(\nu) \cdot \exp(-\alpha(\nu) \cdot L)) = I_{SCL}(t) \times (I_0(D(t)) \cdot \exp(-\alpha(D(t)) \cdot L)) \tag{4.4}$$

Since a photo-diode can be considered as linear time-invariant in its behavior, this system can be modelled based on the impulse response alone. This assumption requires the diode to behave linearly with intensity, which is to be ensured during operation since photo-diodes will become non-linear in the vicinity of saturation. The output of such a system is therefore the convolution of the impulse response of the photo-diode $[h_{PD}(t)]$ and the input intensity $[I_{SCL}(t)]$. The data acquisition system can be modelled similarly as a linear time-invariant system $[h_{DAQ}(t)]$,

resulting in an additional convolution. This convolution can be restated as a single convolution $[h_{SYS}(t)]$, shown in Equation (4.6).

$$I_{DAQ}(\mathrm{t}) = h_{DAQ}(t) \times h_{PD}(t) \times I_{SCL}(t) \times (I_0(D(t)) \cdot \exp(-\alpha(D(t)) \cdot L)) \tag{4.5}$$

$$I_{DAQ}(\mathrm{t}) = h_{SYS}(t) \times (I_0(D(t)) \cdot \exp(-\alpha(D(t)) \cdot L)) \tag{4.6}$$

To further simplify fitting, the determination of the reference intensity can be transferred to the time domain, since the dispersion function is constant for the system, yielding Equation (4.7).

$$\mathrm{I}_{DAQ}(\mathrm{t}) = h_{SYS}(t) \times (I_0(t) \cdot \exp(-\alpha(D(t)) \cdot L)) \tag{4.7}$$

This continuous convolution becomes a discrete convolution, since measurements of $\mathrm{I}_{DAQ}(\mathrm{t})$ are obtained at fixed sampling intervals. Since the system response function $h_{SYS}(t)$ is modelled short compared to the actual measurement duration, the discrete convolution becomes a system of linear equations, consisting of as many equations as there are sampling points in time. This overdetermined system provides an estimate of the system response function (see Figure 4.4 for an exemplary system response function). By using Equation (4.7) and measuring the time trace of the absorption signal of a known sample (gas composition, pressure, temperature, absorption length) and dispersion of the DCM, the system response function $h_{SYS}(t)$ can be fitted iteratively.

Utilizing this measurement-based approach to model the effects of all components in the light path as well as the spectral absorbance by the medium under investigation itself, allows for precise simulation of the spectra as needed for post-processing (fitting) the recorded spectra. In this approach the determined system response function applied to a simulated theoretical spectrum (using Equation (4.7)), yield the spectrum as recorded in the time domain.

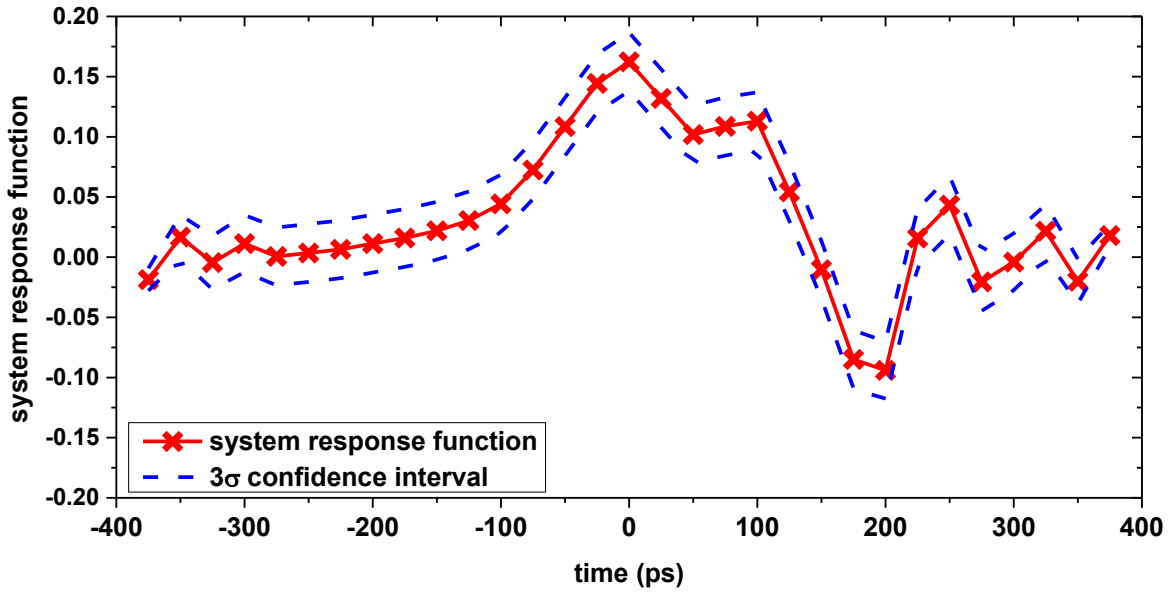

Figure 4.4 Instrument function recreating the effects of all components of the SCLAS system. This function can be used via convolution to obtain simulated spectra incorporating the effects of all components of the SCLAS system, including SCL, photo diode and data acquisition system.

4.5 Partially constrained optimization of the spectroscopic model

SCLAS, as opposed to standard post processing algorithms for TDLAS, requires advanced fitting algorithms and additional constraints to derive valuable data from the recorded measurements. This is due to multiple reasons, that all influence the fitting procedure and several other aspects of post-processing. Due to its inherent time-domain approach and the effect of diode ringing and its counter-measures (see Chapter 4.4 above for details), recorded signals and derived spectra need to be compared in the time domain, whereas TDLAS measurements are usually compared in the wavenumber domain (after being transferred from the time domain). In the case of TDLAS, this is due to ease of handling and experience of the users with regards to the spectral domain. The tuning characteristic of a diode laser can spectrally distort absorption feature shapes and therefore handling the measurements in the wavenumber domain is easier. In the case of SCLAS, however, at least the numerical evaluation of a fitting process needs to be evaluated in the time domain. As shown previously, it is also very beneficial to handle diode ringing and other sampling related effects in the time-domain. The simulated spectra are therefore transformed to the time-domain by applying the inverted time-wavelength correlation (see Chapter 2.5 for details). After applying the convolution with the system instrument function, this signal resembles, in combination with the reference intensity function, the expected time signal of the absorption signal. This signal then can be optimized to resemble the actually recorded signals by means of optimizing (and therefore minimizing) the cost function. Such an optimization can be performed relying on proven and tested methods such as

Levenberg Marquardt algorithm (see [122]) or Trust-Region algorithm (see [123]). Both algorithms rely on minimizing a least-square cost function in the form of

$$F(\boldsymbol{a}) = \sum_{i}^{n} (y_i - f_i(x_i, \boldsymbol{a}))^2 \tag{4.8}$$

where y_i describes the recorded value at a specific sample x_i and f_i the calculated corresponding model value for the parameter set $\boldsymbol{a}$. Inherent in SCLAS, this parameter set is consisting of a number of parameters. The essential parameters are temperature, pressure and mole fraction of the species in question, as well as all parameters of the reference intensity model. Additional parameters include the parameters of the time-wavelength conversion and the diode ringing model, which are considered constant for a post-processing algorithm, since they are determine before and are constant for a specific set of operating conditions of a SCLAS system. Due to slight fluctuations in the triggering of the DAQ system with regards to the SCL, there is a need to also include a shift in the wavenumber axis under certain conditions. This parameter would not change the time wavelength correlation, but rather move the determined non-linear wavenumber axis by a small offset to account for jitter on the triggering circuit of the SCLAS-DAQ system. After this shift is determined, it is set as constant and not fitted together with the spectrum. It can therefore be considered as an alignment step of separate measurements.

All utilized algorithms used to solve the minimization problem share a common trait: all algorithms rely on the Jacobi matrix to determine changes to the current set of parameters. These numerical approaches are therefore considered gradient based methods, since they use the gradient to determine the search direction (i.e. the direction of change for the parameter set). It is therefore of great importance for the fitting and processing speed to provide efficient methods to determine the Jacobi matrix. Since the signal in question (the simulated absorption signal in the time domain) is well known, it is helpful to implement individual methods of Jacobi matrix determination as opposed to using numerical estimator (as usually used in Levenberg-Marquardt or similar implementations to generalize their applicability). In the case of SCLAS, it is possible to separate different parts of the spectrum simulation and treat their Jacobi matrix calculation separately. The effect of the instrument function as well as the reference intensity function can be calculated separately and combined later (see Chapter 4.3 for details on the combination of reference intensity and absorption signal). Identical approaches can be applied when determining the gradient with regards to the medium parameters temperature, pressure and absorber density. Since the HITRAN spectroscopic model (see Chapter 2.2 for details and formulas) is used in most cases in this work, the unique formulas provide more efficient techniques to determine the corresponding parts of the Jacobi matrix. In addition, under certain circumstances, it is possible to use the calculated for several iteration steps, even with a changed parameter set, since all discussed fitting algorithms incorporate a damping parameter, which softens the calculated change in the parameters between iterations (comparable to relaxation in numerical simulations).

To further enhance the performance of the fitting algorithms and improve their effectiveness in finding the minimum of the cost function, it is helpful to limit the ranges for specific parameters eliminating unphysical values and furthermore limiting the valid parameter range to reasonable values (useful pressure, temperature and mole fraction range). In addition to applying these limitations, it is common to scale the parameter range to similar values. When for example comparing pressure (in Pascal [Pa] for HITRAN model) and temperature (in Kelvin for HITRAN model) values, they can differ on the order of several magnitudes.

4.6 Estimation of the Fit Uncertainties

It is common for diagnostic systems to be evaluated regarding their uncertainties. Since SCLAS systems are rather complex, partly due to the underlying spectroscopy, and partly due to the employed hardware, it is more feasible to provide a general discussion of the uncertainty estimation process here and later on only provide specifics in the context of individual measurements and experiments.

When discussing uncertainties of a diagnostic system, which relies on a model being fitted to the recorded data, the uncertainties can be divided among three groups:

- Inherent uncertainties of the model (i.e. neglected effects)
- Uncertainties of the fitting process (i.e. under-optimization)
- Uncertainties in secondary sensors (i.e. uncertainties of a pressure sensor)

While the uncertainties of models in general and spectroscopic models in particular are part of the uncertainty of the fitted results, they are fixed for the specific use case, especially when they dependent on a database and the quality of the stored data. Since HITRAN models are used extensively in gas spectroscopy, there are many publications available that address uncertainties of line data and possibilities for improvement, as well as provide improved line data for relevant and regularly used transitions [53, 54, 124–129]. Rothman et al. [38] provide so called uncertainty indexes with every absorption line. These indexes allow for a classification of the uncertainties, ranging from less than 1 % up to greater or equal than 20 % for several parameters in the database. While this information is especially important for narrow band absorption spectroscopy, which under certain conditions rely on merely a single absorption line, it becomes increasingly difficult to consolidate these indexes for various absorption lines, when using up to thousands of lines in a single spectrum. For the purpose of this discussion, the uncertainties in the line data are considered as non-present. The model itself will be considered as *perfect*, since, aside from uncertainties in the tabulated data, the HITRAN model itself introduces additional uncertainties due to neglecting certain effects (i.e. foreign-broadening with other species than air, see Chapter 2.2.2 for details). By separating the model uncertainties and the fitting uncertainties, one can evaluate the performance of SCLAS separate from the performance of the chosen spectral model.

Furthermore, the uncertainties from secondary sensors can be neglected for most application cases, since SCLAS provides multi-parameter measurements including pressure, temperature and species concentrations. This significantly reduces the necessity for secondary sensors and therefore their influence on the uncertainties of the system. Whereas narrow-band systems, such as TDLAS, often need to rely on secondary pressure measurements, and often temperature measurements as well, SCLAS provides these values inherently. Under certain conditions, it might be helpful or necessary to substitute a measurement instead of fitting a certain parameter. In this case, the influence on the uncertainty will be discussed separately.

As discussed in detail in previous chapters, the SCLAS signal fitting process relies heavily on two experimentally determined function: dispersion characteristic D $(t \rightarrow \nu)$ and the system response function $h_{SYS}(t)$. Both functions and their uncertainties due to experimental determination, as well as the inherent measurement noise influence the uncertainty of the measurement [44]. Since the underlying algorithms used to simulate the signal as recorded by the data acquisition system, modulation by the absorbing medium and detection by the photo diode is a non-linear model, several calculations are required to quantify the influence of uncertainties on the fitted parameters as shown in the following section.

Least-square optimization relies on the gradient of a cost function $F(\boldsymbol{a}) = \sum_i^n (y_i - f_i(x_i, \boldsymbol{a}))^2$ (y_i being the measured value / data set, x_i being the independent variable and $\boldsymbol{a}$ the parameter vector of length m) to find its optimum:

$$\frac{\partial F}{\partial a_j} = 0 \tag{4.9}$$

When differentiating the implicit Equation (4.9) with respect to the data set y_i this equation is valid [130] $(1 \leq l \leq m)$:

$$\frac{\partial^2 F}{\partial a_l \partial y_i} + \sum_{j=1}^{m} \frac{\partial^2 F}{\partial a_j \partial a_l} \cdot \left(\frac{\partial a_j}{\partial y_i} \right) = 0 \tag{4.10}$$

This equation can be used to obtain the following relationship for the relevant noise induced standard deviation of fitted parameters σ_{a_j} [130]:

$$\sigma_{a_j}^2 = \sum_{i=1}^{n} \left(\sum_{l=1}^{m} \frac{1}{\sigma_i} \epsilon_{jl} \frac{\partial}{\partial a_l} f(x_i, \boldsymbol{a}) \right)^2 \tag{4.11}$$

where ϵ_{jl} is the inverse of the curvature matrix of the function F and σ_i is the standard deviation of the values y_i.

Similar procedures extended to account for correlated deviations allow for the derivation of an equation set determining the derivative of $\partial a_j / \partial D$, which in turn can be used to determine the uncertainty on parameters caused by a shift in the dispersion function [44].

$$\sigma_{a_{j,D}}^2 = \left(\frac{\partial a_j}{\partial D}\right)^2 \cdot \sigma_D^2 \tag{4.12}$$

Given that the system response function in itself is a least square fit to solve an overdetermined system of equations, its uncertainty can be determined as outlined by [130] and be propagated similar to Equations (4.9), (4.10) and (4.12).

The combination of the three uncertainties (measurement noise, dispersion function uncertainties, system response function uncertainty) can be considered as the fit uncertainty and will be quantitatively evaluated for specific measurements in a later chapter. The uncertainties of SCLAS, separated from the uncertainties of the models, are dependent on the individual measurements itself. Therefore, the individual measurement noise dictates the uncertainty, and therefore the detection limit. It has to be kept in mind, that in addition to the obvious parameters quantity, pressure and temperature, also all other fitted parameters, in this case all variables for the reference intensity, are subject to uncertainties.

5 Application and Validation of SCLAS for Gas Diagnostics

As with all new diagnostic techniques, a thorough and detailed application of the technique combined with different validations are required. To perform this important step with SCLAS, several systems were chosen, that offer unique challenges as well as possibilities for SCLAS to offer additional insights compared to other diagnostic systems. For the following chapter two systems were investigated in detail, since these systems show the advantages of SCLAS most clearly and are representative for all systems tested. The first case is gas cell measurements that allow the evaluation of SCLAS under controlled conditions with a reasonable parameter range. The focus in this experiment was on the characteristics of SCLAS in multi-parameter high-pressure environments combined with multi-species situations, as well as higher concentrations of species. The second experiment focuses on high-temperatures as well as combustion related issues. For this test case the *Wolfhard Parker* burner (WHP, details about the burner will be given later in this chapter, [23, 131–133]) was chosen due to its extensive database of reference measurements available in combination with temperatures up to 2000 K (up to 1400 K in the investigated regions of the flame). Since SCLAS is an absorption-based line of sight (LOS) technique, it is necessary for a system under investigation to provide homogeneous conditions along the relevant absorption path, which the WHP burner is especially designed to ensure.

The gas cell measurements will be presented first, since they provide additional insights to the implemented evaluation and data processing algorithms, while the second part focusses on the WHP burner trials. Both trials are followed by a discussion of the achieved performance and uncertainty. It has to be kept in mind, that during the development of SCLAS, the system was continuously improved. These validation trials are therefore among the first performed measurements with SCLAS.

5.1 Multi-Parameter Multi-Species Gas Cell Measurements

Two main aspects were at the focus of the validation trials of SCLAS using gas cell measurements. Primarily, it was the goal to apply this new technique to a controlled gas environment to assess its capabilities and performance. Secondly, it was intended to achieve an understanding of its precision and accuracy when measuring under stationary conditions. Since SCLAS offers the ability to perform multi-parameter measurements in combination with multi-species measurements, this combination offers additional ways to evaluate the performance of such a system. By comparing system-wide values such as pressure and temperature derived from different species (sections of the spectrum) at equilibrium and proper mixture (which would yield the need for these values to be identical) allows or an evaluation of consistency. Furthermore, SCLAS relies on the evaluation of very broad spectra that include hundreds, if not thousands of absorption lines and features. This requires a different approach when performing

an error analysis, since these different absorption lines are specified with individual uncertainties (in the HITRAN database). When only relying on a single absorption feature (such as for example TDLAS), individual uncertainties are far more significant in the uncertainty budget and cannot be cleared separated from the fit uncertainty. SCLAS on the other hand reduces these influences by utilizing the complete spectrum. The approach to evaluate the overall performance of SCLAS and the underlying fit with regards to precision and accuracy has previously been described in detail in Chapter 4. Secondary measurements will be used to evaluate overall precision and accuracy. Secondary measurements allow for comparison of the fitted parameters with known values (temperature, pressure, quantity).

5.1.1 Experimental Setup

For the gas cell measurements, a pipe-based gas cell, shown in Figure 5.1 as a cut-away drawing, was used. This absorption cell allows for high-pressures (up to 15 bar in this configuration) and offers a variable absorption path due to its pipe and fitting-based design. By adding or removing pieces of pipe, the path length can be adjusted. For these experiments, the cell was setup for an absorption path length of 0.367 m (±0.002 m). To reduce the cell volume (and therefore simplify achieving homogeneous conditions within the cell) while offering sufficient absorption path length, a double-pass optical beam layout was chosen. For the optical access, a special window fixture was developed. This fixture uses a double-wedged sapphire window with an average thickness of 3 mm (clear aperture: 12 mm) and is fused into a stepped tube to provide proper sealing up to several hundred bar, while avoiding optical interference between parallel optical surfaces on the signal. The opposite side consisted of a ½ inch gold mirror, mounted in a tube, which was completely placed inside the cell to simplify the sealing. If optical alignment is an issue, a retro-reflector can be used instead of the plane mirror due to the lens tubes utilized for mounting the mirror.

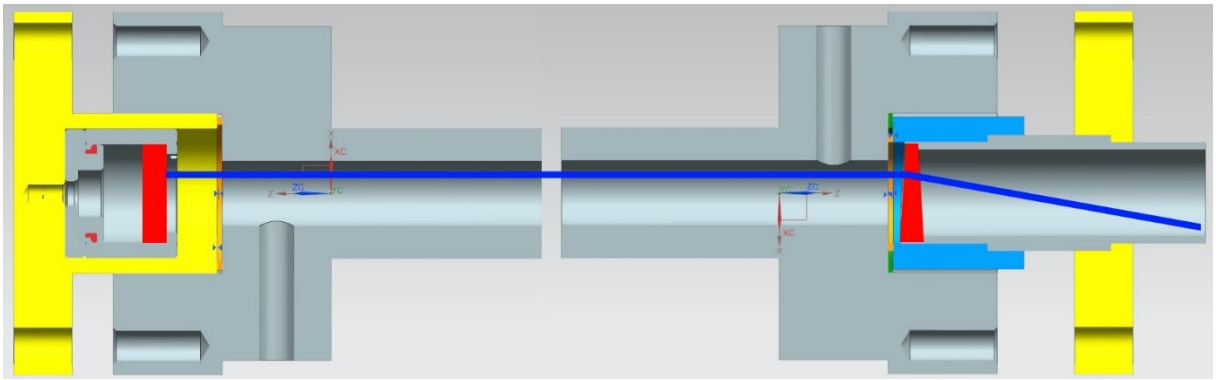

Figure 5.1 Sectional drawing of the high-pressure absorption cell used for validation trails of SCLAS. On the left the mirror is shown in red, while on the right side, the window is shown in red. Both end caps, which are also responsible for sealing, are shown in yellow. The light path is shown in dark blue. Due to the double-wedged window, the incident beam needs to be placed at a steep angle to reach the opposite mirror at level.

Given its small form factor, this cell design allows for fast gas exchange as well as reduces the risks of accumulation of combustible gas mixtures under high pressure due to its small volume.

During the experiments, the cell was combined with a premixing vessel, which ensured proper mixing of the gases as well as multiple pressure sensors to determine gas composition based on partial pressures (Keller PAA-33X 0-10 bar, digital read-out, accuracy: 0.05 % of full-scale, accuracy: 0.01 % of full-scale). In addition to the pressure sensors, type E thermocouples (-270 to 870 °C) were placed within the gas in the cell itself to ensure homogeneous temperature distribution along the absorption path. For details regarding the SCLAS system in general, please refer to Chapter 2.6. The utilized DCM provided a dispersion of - 1500 ps/nm at 1550 nm. For methane this results in an optical resolution of 0.1224 cm^{-1}, while for acetylene the achieved resolution is 0.49 cm^{-1} averaged across the relevant spectral range using Equations (2.32) and (2.33). In the case of measurements at ambient pressure, the absorption lines are rather narrow and a high optical resolution is required to be able to resolve these absorption lines. For post-processing, the approach in Chapter 4.3 was applied using B-splines as a model for reference intensity and a SCLAS spectroscopic model based on HITRAN data was fitted to the measurements using least-square fitting methods (see Chapters 4.4 and 4.5 for details).

Utilizing the above described absorption cell, a series of experiments were performed aimed at specific aspects of SCLAS. The first experiment was performed at ambient pressure (1000 mbar ±10 mbar) and ambient temperature (305 K ±2.9 K, thermocouple type E), but measuring multiple gases and multiple parameters (gas concentration, temperature and pressure) simultaneously at once. The gases under investigation were methane (CH_4) with a concentration of 35.0 % (±1 %) and acetylene (C_2H_2) with a concentration of 25.0 % (±1 %) based on partial pressure measurements during gas mixing. This experiment is specifically looking at the performance of SCLAS under ambient conditions, which requires the highest optical resolution to resolve individual absorption features. Under-resolving absorption features greatly influences the ability to derive the pressure within the cell optically (see discussion of results for specific measurements).

In a second measurement, the performance of SCLAS at elevated pressure was evaluated. For this purpose a single species (methane, CH_4), diluted in air, was measured at ambient and high pressure. The measurements were performed at a temperature of 295.6 K ±2.9 K and at pressures of 0.980 bar ±10 mbar and 8.732 bar ±10 mbar. The concentration of methane (CH_4) was determined to be 18.06 % ±0.5 % based on partial pressure measurements during the mixing of methane and compressed air. Based on the spectral fitting of the recorded traces, the parameters species concentration, pressure and temperature of the gas were determined. These measurements provide the basis of the following uncertainty analysis (following the approach outlined in Chapter 4.6 for the fit uncertainty). During these measurements, multiple traces of identical gas composition were recorded to be able to address averaging and distribution of measured values (and therefore precision and accuracy). Additionally, averaging of the secondary measurements (pressure and temperature) allowed for the derivation of reference values for temperature, pressure and gas composition with higher precision.

5.1.2 Evaluation and Results

For a first evaluation of performance of the SCLAS system, a combination of methane (CH_4) and acetylene (C_2H_2) was measured at ambient pressure and temperature. Given the simulated spectrum of the gas mixture in Figure 5.2, the relevant spectral range is between 1500 nm (6660 cm^{-1}) and 1700 nm (5880 cm^{-1}). Based on the SCLAS setup described in Chapter 2.6, a corresponding long-pass hard-coated spectral filter was applied to select the proper range of the spectrum.

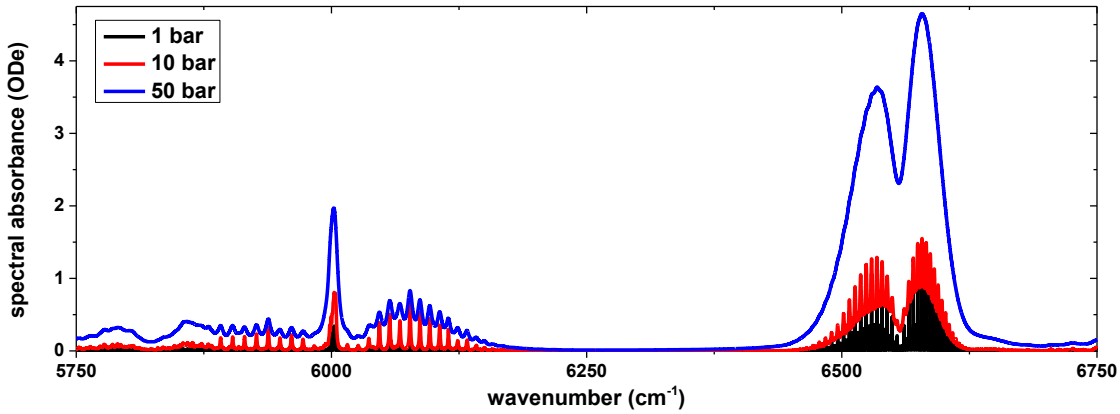

Figure 5.2 Simulation of absorption spectra of a gas composition of methane and acetylene for various pressures and HITRAN reference temperature of 296 K.
Line broadening and spectral *lift-off* are visible.

To fully utilize the potential of SCLAS, the recorded measurements were evaluated with regards to pressure, temperature and mole fraction of the respective species methane and acetylene. This evaluation was performed separately for sections of the spectrum representing methane (left section in Figure 5.3, fit result overlaid in red) and acetylene (right section in Figure 5.3, fit result overlaid in blue), while simultaneously fitting temperature and pressure. For methane, absorption lines ranging from approx. 6000 cm^{-1} to 6145 cm^{-1} were included in the fitting (due to reduced signal intensity towards longer wavelength), while the acetylene spectrum included absorption lines across the whole band from 6480 cm^{-1} to 6620 cm^{-1}.

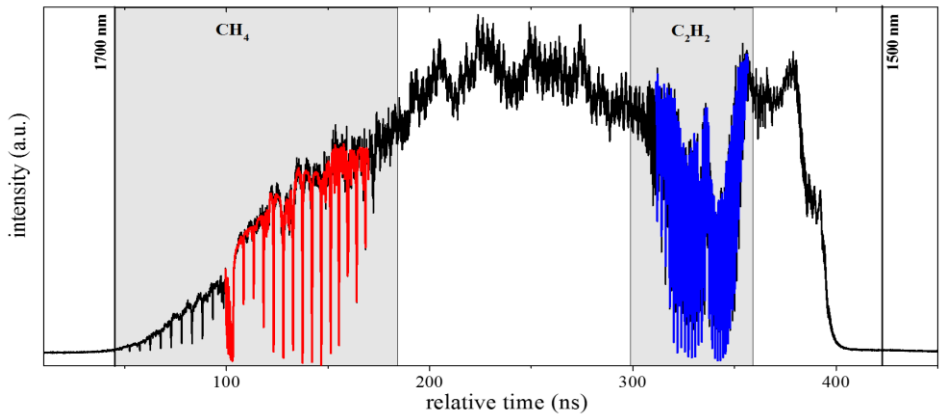

Figure 5.3 Overview of processed measurements of SCLAS for gas cell measurement trials

Based on the methane spectrum (shown in Figure 5.4 in detail), a pressure of 1074.3 mbar and a temperature of 307.3 K was determined. The methane quantity was determined to be 34.21 %. In addition, spectral fringes of the hard-coated spectral filter in the light path are visible (see Chapter 2.5.2 for details on Etalon fringes).

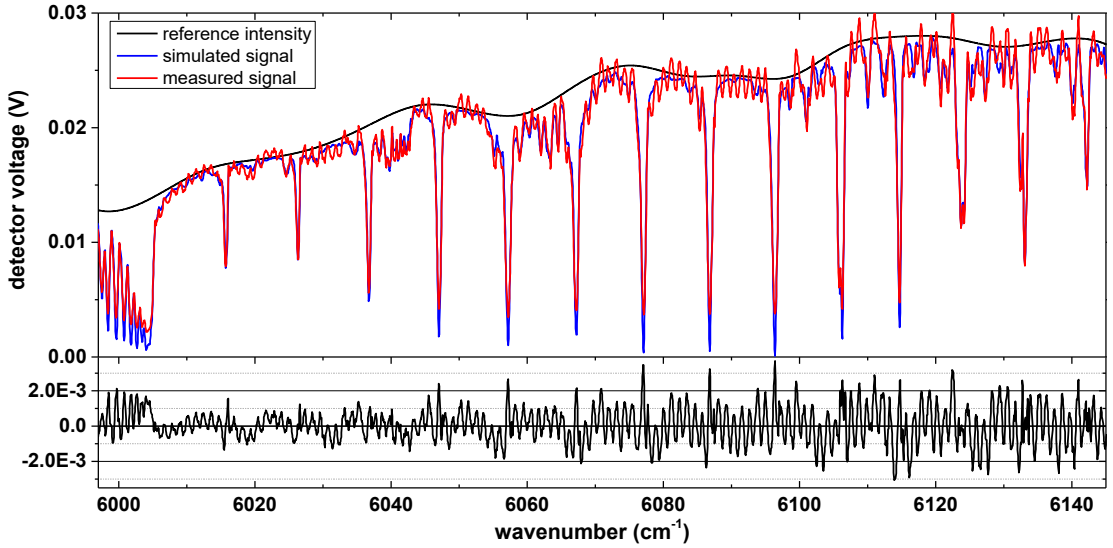

Figure 5.4 Methane spectrum as derived by fitting a SCLAS spectroscopic model based on HITRAN data to the measurements as described in Chapter 4.5

Based on the acetylene spectrum (shown in Figure 5.5 in detail), a pressure of 911.46 mbar and a temperature of 307.9 K was determined. The acetylene quantity was determined to be 23.57 %.

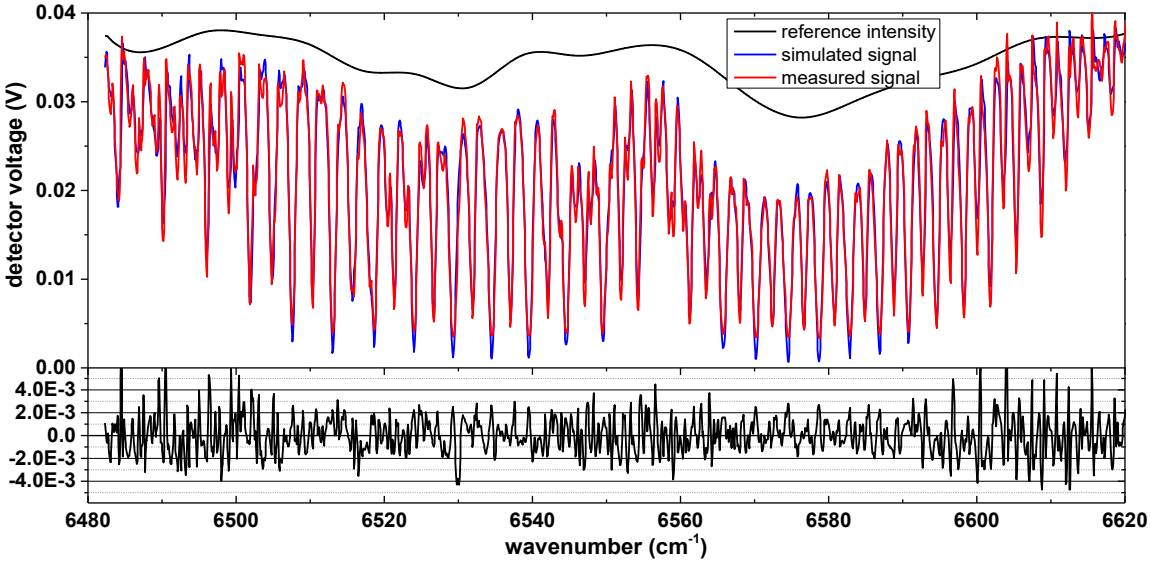

Figure 5.5 Acetylene spectrum as derived by fitting a SCLAS spectroscopic model based on HITRAN data to the measurements as described in Chapter 4.5

Based on the residuum in Figure 5.4 and Figure 5.5, it can be stated, that the fit performed well and was able to approximate the recorded signal very well. In the case of methane, the characteristic structure for an over-estimation of the absorbance can be seen in the residual. This is due to the limited optical resolution of the chosen DCM. At ambient pressure, the investigated gases (especially methane) show sharp absorption peaks that are on the edge of the resolution limit of the SCLAS system. Nevertheless, due to the shape of the absorption features and the broad coverage of the source, the recorded measurement can be used for parameter derivation. This effect will be less present in signals recorded at higher pressures (SCLAS intended field of application), since absorption features encounter substantial broadening at increased pressures (see Chapter 2.2.2 for details).

When comparing the derived parameters for both species with the expected quantities based on separately recorded pressures and temperatures, the results are shown in Table 5.1. The deviation between reference value and measured value for temperature and pressure is expressed in percent relative to the reference value. For the gas species the absolute difference is given. The methane and acetylene quantities are converted to concentrations assuming a path length of 1 m. It can be seen that the largest error by far is in determining the pressure. Deriving pressure from a recorded signal is most sensitive to any kind of disturbance (i.e. slight offset in the time wavenumber conversion). Acetylene is especially sensitive in this regard, since the spectrum varies only slightly with pressures around ambient pressure (as can be seen in Figure 5.2) compared to methane.

Table 5.1 Comparison of measurements for methane concentration, acetylene concentration, pressure and temperature compared to the secondary measurements

Parameter	Reference value (accuracy)	Methane spectrum (absolute deviation)	Acetylene spectrum (absolute deviation)
Temperature	305 K (±2.9 K)	307.3 K (0.75 %)	307.9 K (0.95 %)
Pressure	1.000 bar (±0.010 bar)	1.0743 bar (7.43 %)	0.91146 bar (8.85 %)
Methane	35.0 % (±1 %) (0.350 bar ±10 mbar)	34.21 % (0.79 %)	--
Acetylene	25.0 % (±1 %) (0.250 bar ±10 mbar)	--	23.57 % (1.43 %)

With this initial test, SCLAS has shown great potential for providing complete sets of parameters in various environments (i.e. high pressure). Combustion-relevant species (methane and acetylene) were measured with high accuracy. Temperature measurements were sufficient as well for this test. The only exception is the pressure measurement, where deviation as high as 8.9 % were measured. As stated before, sensitivity for pressure measurement at these pressures is low.

5.2 Multi-Parameter High-pressure Gas Cell Measurements

With an identical setup, high pressure measurements were performed as well to compare the performance to the measurements at ambient conditions. For these measurements, methane was chosen and recordings at different pressure levels were obtained (ambient and elevated pressure). The instrument function and dispersion function were determined as described in Chapters 2.5 and Chapter 4.4 from measurements of pure methane at pressures lower than ambient (0.1 bar and 0.2 bar). As described before, a premixing vessel was used to ensure proper mixing of methane and air before evacuating the absorption cell and filling the cell to the required pressure level. For these measurements, the derived relations from Chapter 4.3 to Chapter 4.6 were used to fit a SCLAS-spectroscopic model (using HITRAN data) to the data using the B-splines for the reference intensity by means of partially constrained optimization, while determining the uncertainty of the fit itself (comparable to a *single-shot* uncertainty).

5.2.1 Evaluation and Results

For the evaluation of the methane concentration in the sample, a wavenumber range from 5995 cm^{-1} to 6145 cm^{-1} with 1381 absorption lines was used. The fit range of the parameters was limited to sensible values in terms of temperature (273 K to 500 K) and pressure (0.1 bar to 20 bar). Since a similar filtering system was used in these measurement as in the measurement reported in Chapter 5.1, the overall shape of the intensity trace is comparable to Figure 5.3. Since only methane was present in the gas under investigation in this case, the additional absorption bands between 300 ns and 400 ns, attributed to acetylene, are not present in these signals.

When evaluating the measurements of pure methane at roughly 0.5 bar, the results are shown in Table 5.2. The fit uncertainties are smaller or on the order of the uncertainties of the secondary sensors (averaged from 10 measurements). For the fit uncertainty of the species concentration an estimation of ±2.1 %, whereas for temperature an estimation of ±1.7 K and for the pressure of ±0.009 bar is given.

Table 5.2 Comparison of measurements for pure methane concentration, pressure and temperature

Parameter	Reference value (sensor accuracy)	Methane spectrum (fit uncertainty)	Deviation (relative)
Temperature	295.5 K (±2.9 K)	301.04 K (±1.7 K)	5.9 K (2 %)
Pressure	0.4968 bar (±0.005 bar)	0.49977 bar (±0.009 bar)	0.0009 bar (0.2 %)
Methane	100.0 % (0.4968 bar)	100.0 % (±2.1 %)	0.0 % (0.0 %)

The recorded spectrum and the fitted spectrum are shown in Figure 5.6 alongside the fitted reference intensity. The major contributor to the residuum are the remaining effects of photo diode ringing, despite including the system instrument function according to Equation (4.7) in the spectroscopic model. This is mainly due to the fact, that absorption lines at this pressure are well below the optical resolution of the SCLAS system, though the system response function is mostly able to correct the broadening of the lines. The fitted values are in good agreement with the secondary measurements with temperature encountering the largest deviation. This is caused by a relatively high temperature insensitivity of the spectrum, as the difference in transmission between the peak absorption lines for 295 K and 302 K is less than 0.02 %.

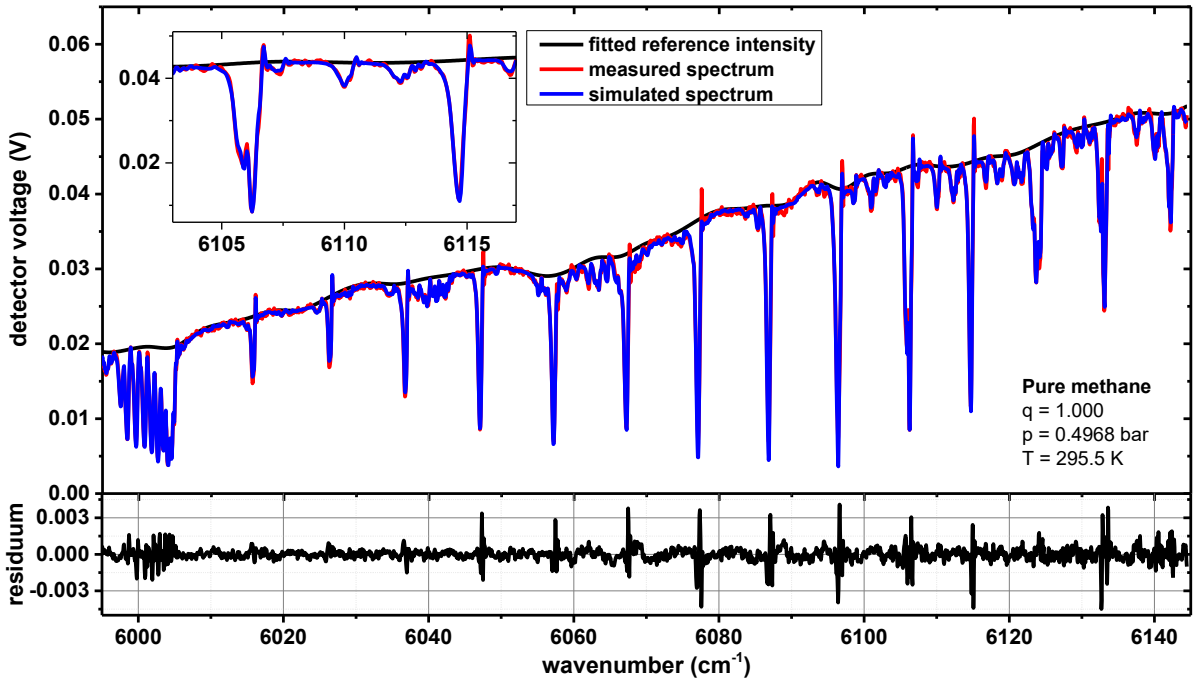

Figure 5.6 Methane spectrum for a measurement at 295.5 K and 0.49 bar with a methane concentration of 100 %.

To further evaluate the performance of SCLAS, measurements with the conditions listed in Table 5.3 were performed (highlighted are the specific challenges in the specific measurement). In case #1 the relatively low concentration of only 3.71 % is challenging regarding the measurement noise. In case #2, the high concentration of 18.06 % challenges the ability of the spectroscopic model to handle high concentration values (in part to the design of HITRAN to handle primarily low concentrations [5 % and below]). In the third case #3 the influence of elevated pressure on the spectrum is investigated. It is expected that significant line broadening will take place and effects such as photo diode ringing will likely have subsided due a reduction in the gradients on each side of absorption line. Furthermore, closely spaced absorption lines (around 6000 cm^{-1} in Figure 5.6) are expected to by indistinguishable and merged together.

Table 5.3 Comparison of measurements #1 to #3

Parameter	Measurement #1	Measurement #2	Measurement #3
Temperature	295.5 K (±2.9 K)	295.6 K (±2.9 K)	295.6 K (±2.9 K)
Pressure	1.0488 bar (±0.005 mbar)	0.9795 bar (±0.005 mbar)	**8.732 bar** (±0.005 mbar)
Methane	**3.71 %** (±0.5 %)	**18.06 %** (±0.5 %)	22.35 % (±0.5 %)

Before discussing the fitted results and their uncertainties in comparison to the secondary measurements, the individual spectra should be discussed. Shown in Figure 5.7 is measurement #1 including measured spectrum, simulated spectrum and simulated reference intensity. Measurement #2 is shown in Figure 5.8 and measurement #3 is shown in Figure 5.9.

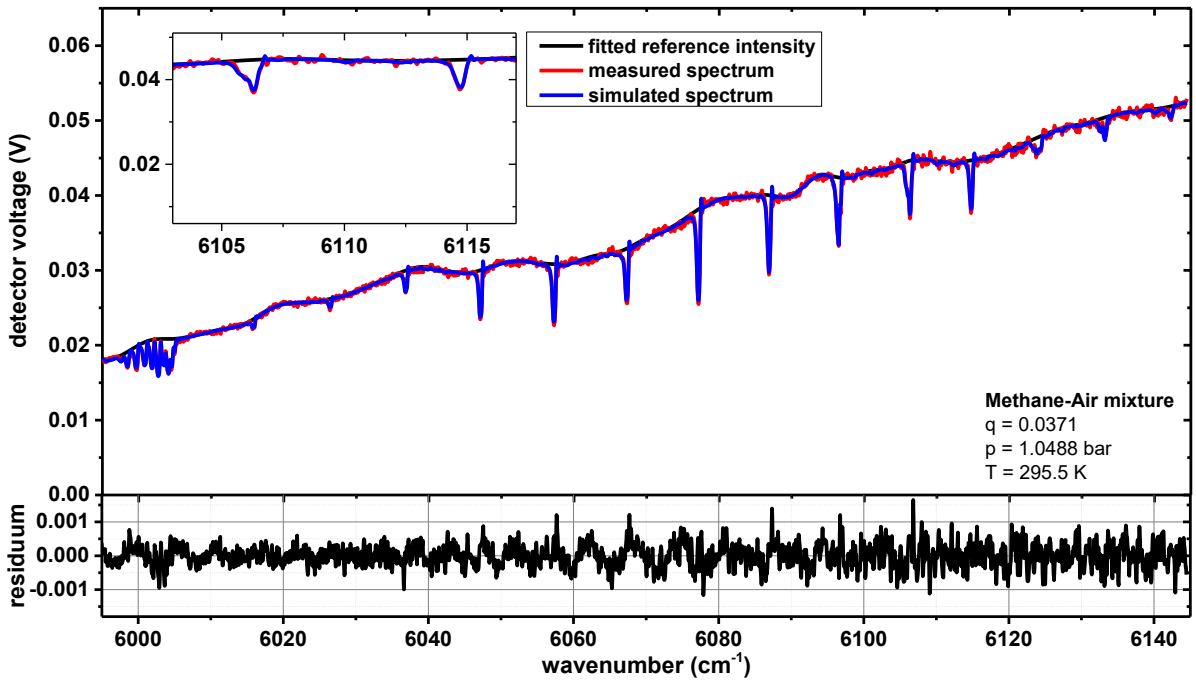

Figure 5.7 Methane spectrum for measurement #1 at 1.05 bar and 295 K with a methane concentration of 3.7 %. Despite this low concentration the spectra resembles the measured signal very closely (see residuum). Furthermore, the system response function allows for spectrum calculations including effects such as photo diode ringing.

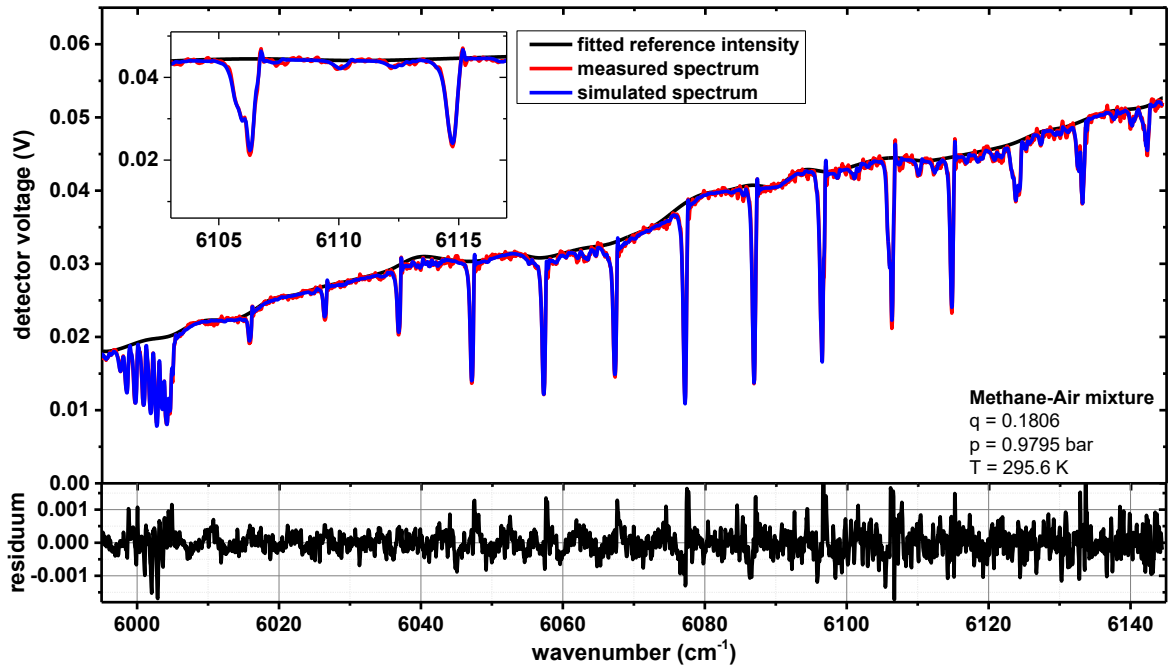

Figure 5.8 Methane spectrum for measurement #2 at 0.98 bar and 295 K with a methane concentration of 18.6 %.

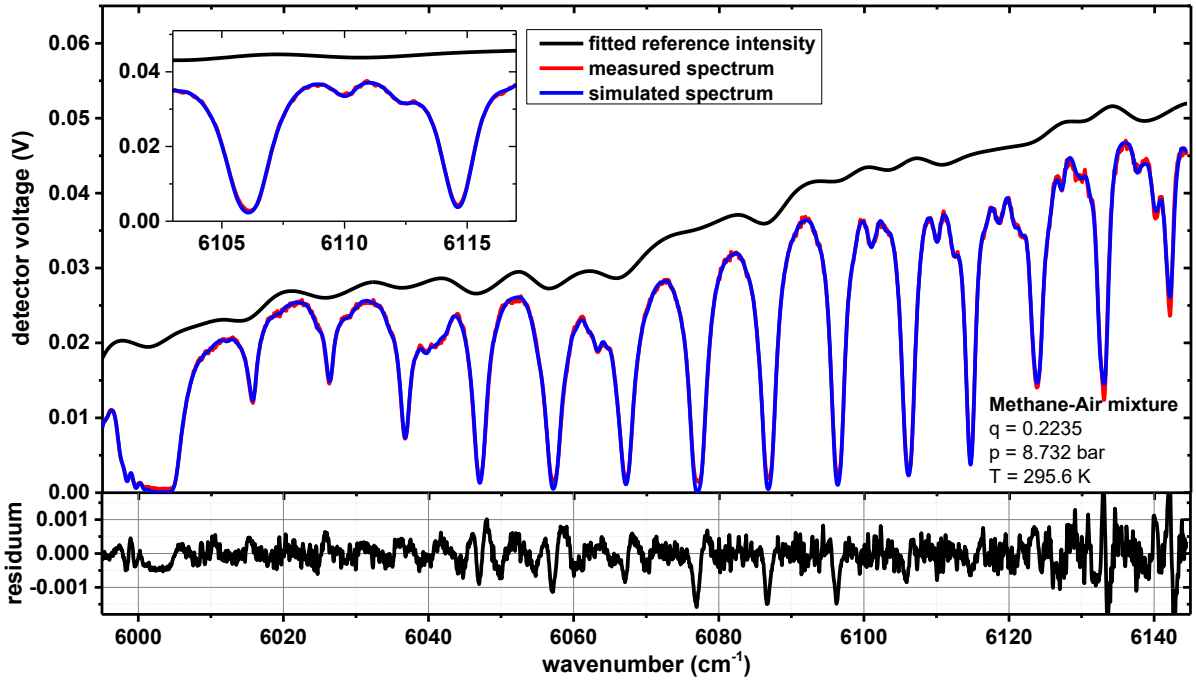

Figure 5.9 Methane spectrum for measurement #3 at 8.732 bar and 295 K with a methane concentration of 22.25 %.

To compare the fitted results with the secondary measurements, Table 5.3 is extended as shown in Table 5.4.

Table 5.4 Absolute comparison of measurements #1 to #3 in comparison with secondary measurements

Parameter	Measurement #1	Measurement #2	Measurement #3
Temp	295.5 K (±2.9 K)	295.6 K (±2.9 K)	295.6 K (±2.9 K)
T - SCLAS	299.1 K (±2.4 K)	305.1 K (±1.4 K)	312.6 K (±1.2 K)
Pressure	1.0488 bar (±0.005 bar)	0.9795 bar (±0.005 bar)	**8.732 bar** (±0.005 bar)
P - SCLAS	1.1188 bar (±0.0315 bar)	1.0347 bar (±0.017 bar)	**8.7320 bar** (±0.0713 bar)
Methane	**3.71 %** (±0.5 %)	**18.06 %**(±0.5 %)	22.35 %(±0.5 %)
Q - SCLAS	**4.28 %** (±0.1 %)	**18.82 %** (±0.3 %)	24.41 % (±0.2 %)

The agreement between the measured values and the secondary measurements is generally very good. For temperature, the deviation reaches at maximum 17 K, while the pressure reaches at maximum a deviation of 0.08 bar. For the methane concentration, a deviation of 2 % is reached for the high-pressure case. The determined SCLAS fit uncertainties are quite low (often below the uncertainties of the secondary sensor).

It has to be kept in mind, that the SCLAS measurements are *single-shot* measurements with an uncertainty estimation based on the individual fit of the spectroscopic model for as single measurement. Therefore, these uncertainties are different for different measurements. The uncertainties of the secondary measurements are based on the accuracy of the sensors used and their propagation to derived values (for example species concentration). These uncertainties are therefore constant for different measurements (effectively single-shot uncertainties as well). Averaging secondary measurements would lower the uncertainty. This is not reflected in Table 5.2, Table 5.3 and Table 5.4 to allow for a comparison of single-shot performance. Considering an averaging of 10 measurements, the uncertainties of the secondary sensors would be ±0.9 K for temperature, ±0.002 bar for pressure and ±0.2 % for concentration.

Performing multiple SCLAS measurements for identical gas mixtures and stable conditions would allow for averaging measurements and reduced uncertainties. This approach cannot be applied in transient conditions (i.e. combustion processes). Given SCLAS intended field of application, it was therefore relevant to determine its performance for single-shot measurements rather than averaged measurements.

Given the uncertainties for the secondary measurements after averaging in comparison to the fit uncertainties, it is visible that model-related uncertainties have to be considered as well given the discussion in Chapter 4.6. In this case they are likely caused by the used HITRAN line data and its uncertainties.

5.3 Application of SCLAS in the Wolfhard-Parker burner

To validate the performance of SCLAS in combustion environments, it is necessary to choose a trial system that offers reproducible performance and operating conditions, a broad coverage of reference measurements utilizing other diagnostic systems as well as suited conditions for the new system to be validated. All of these characteristics are present with the *Wolfhard Parker* burner (WHP). By providing a very stable flame with an absorption path of 41 mm, the WHP burner is well suited for a trial of SCLAS, since it provide sufficient absorption path length and homogeneous conditions along this path (see Chapter 5.3.1 for details on the burner design). Furthermore, the WHP burner has been investigated extensively using various diagnostic systems, such as sampling mass spectrometer, TDLAS systems and fluorescence based systems and *Laser Doppler Velocimetry* (LDV) (see [132]). Experimentally determined quantities have also been found to agree well with simulation data. Among the measured species are acetylene (C_2H_2), methane (CH_4), carbon dioxide (CO_2), carbon monoxide (CO) and water vapor (H_2O), as well as temperature (using radiation corrected thermocouples), providing a broad experimental data base to use for validation.

5.3.1 Experimental Setup

An experimental setup for the validation of SCLAS for in –flame applications needs to allow for flexibility in terms of operating conditions. Instead of operating the burner in different conditions (for most of which no reference measurements are available), it is more useful to translate the burner and measure in different parts of the flame. The setup was therefore split into two parts: WHP burner and SCLAS setup.

Wolfhard Parker burner

The Wolfhard Parker burner provides an atmospheric, laminar, non-premixed methane/air flame, which consists of two flame sheets. This flame is provided by a slotted burner head design. Around a central fuel slot (methane), two air slots are placed. To reduce any end flame effects, nitrogen purge slots are positioned at each end of the flame sheets (see [23]). To stabilize the flame, two wire meshes are placed above the burner head providing surfaces for the flames to attach to. To further stabilize the flame, the complete setup was shielded from air circulations and drafts in the lab. A photographic representation and a CAD rendering of the burner in operation (including the laser beam) are shown in Figure 5.10. The burner itself is mounted on a two-axis translation stage allowing motion along the vertical (z) and lateral (x) axes (see Figure 5.10 for reference).

The burner was operated in accordance with the operating conditions used for obtaining the previously mentioned reference measurements (see [132]). The exit velocity for the fuel (methane) was set to 11 cm/s, while the air slots were set to 22 cm/s, identical to the nitrogen purge slots. The dimensions of the center slot of the burner (fuel slot) are 8 x 41 mm, while the air slots are each 16 x 41 mm. The nitrogen purge slots are 7.5 x 16 mm. Each slot is filled with glass pearls and covered with a mesh (within each slot). The complete assembly is also covered

with an additional single mesh covering all slots simultaneously (see Figure 5.10 and Figure 5.11). These three measures were taken to ensure homogeneous release of the gases from the five slots and therefore provide homogeneous combustion conditions along the y axis.

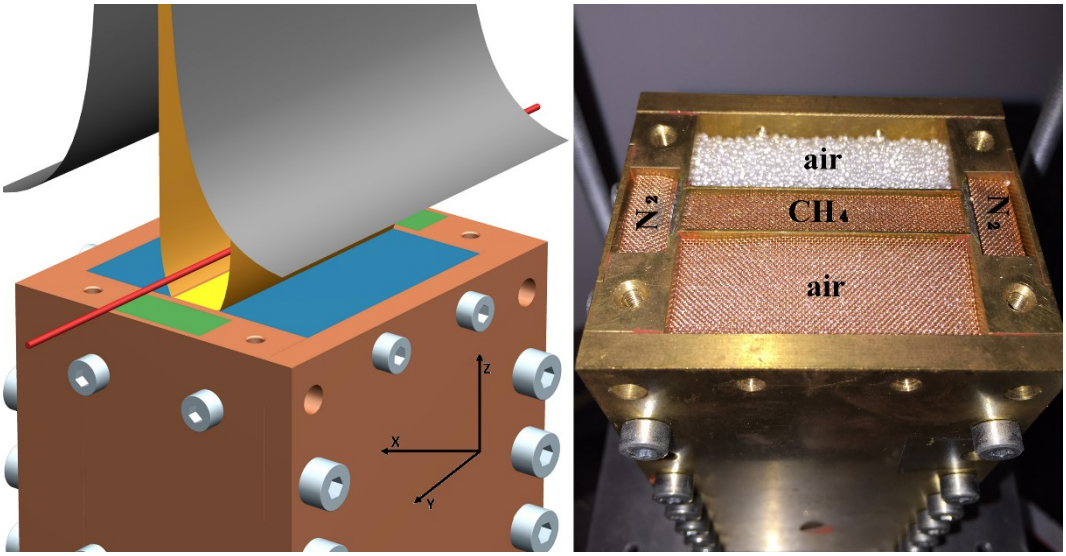

Figure 5.10 CAD rendering and photograph of the WHP burner

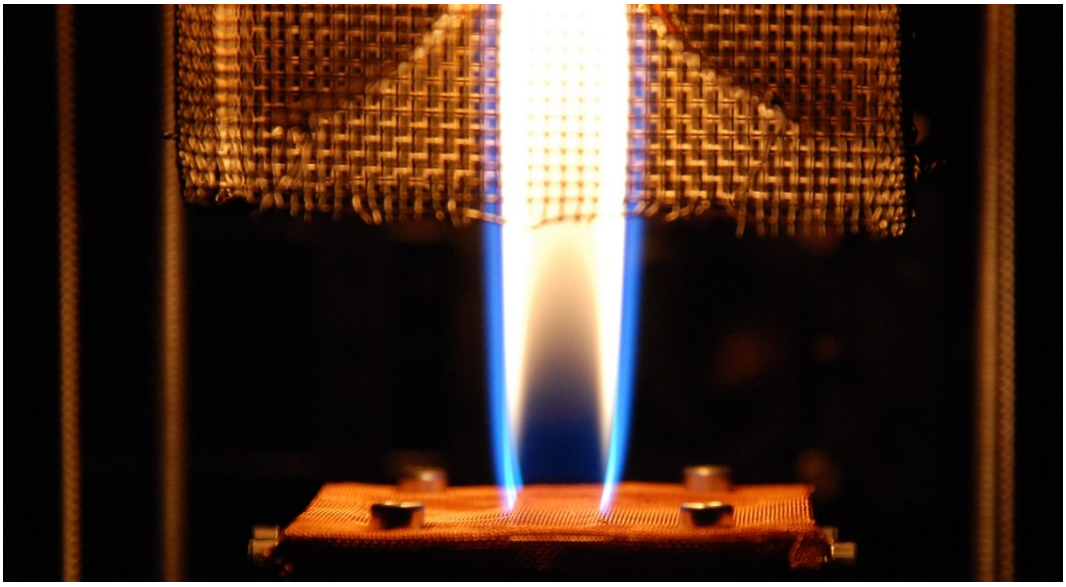

Figure 5.11 Photograph of the two flame sheets formed by central fuel and adjacent air slots (viewed along the y-axis)

SCLAS setup

For the SCLAS measurements a single-pass optical setup was chosen. The beam was collimated to 400 μm waist width and positioned at 7 mm above the burner head. A knife-edge approach was used to align optical setup and the longitudinal axis of the burner (y axis). All SCLAS components as described in Chapter 2.6 were used in this setup. A DCM with a dispersion of – 1500 ps/nm (at 1550 nm) was used in the experiments to achieve an optical resolution

(approx. 0.12 cm^{-1}). The filter (as described in Chapter 2.6) was replaced with a dichroic mirror specifically designed to primarily reflect wavelength from 1520 nm to 1700 nm. Due to the characteristics of dichroic mirrors, the spectral coverage after reflection is broader with a certain amount of intensity outside the specified spectral range. To quantify the spectral content of the beam, measurements with the SCLAS setup and an FTIR (Bruker V80V) were compared. The results of the comparison are shown in Figure 5.12. It is clearly visible that the combination of dichroic mirror and DCM essentially act as a bandpass filter further limiting the transmitted optical range to 1200 nm to 1700 nm, while the dichroic mirror itself also reflected light above 1700 nm, which is due to the dichroic mirror using multi-layer interference for generating the bandpass characteristic The spectral cut-off above 1700 nm is due to the transmission limits of the dispersion-compensating fiber within the DCM.

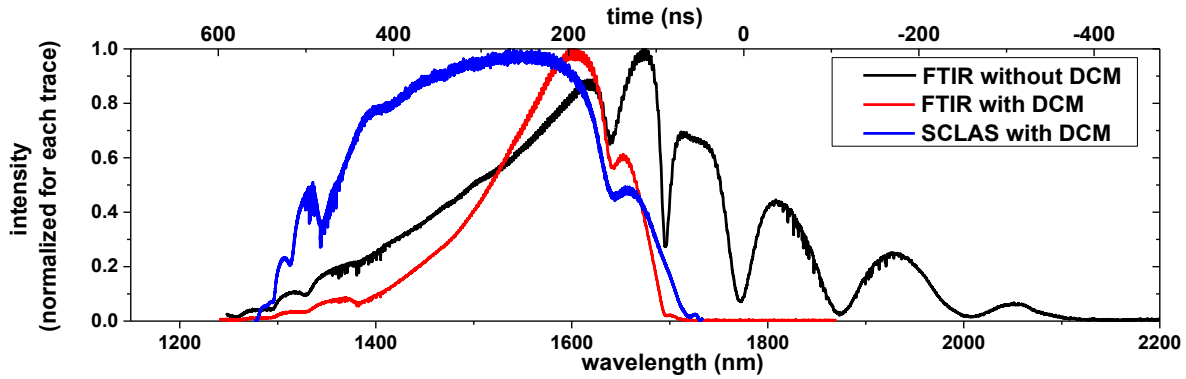

Figure 5.12 Comparison of spectral content at various points along the optical train

The SCL was operated at a repetition rate of 2 MHz (to prevent pulse overlap after dispersion) and 9850 pulses were averaged for a single measurement, resulting in an effective sampling rate for the complete spectrum (spectral coverage: 120 cm^{-1}) of 203 Hz or 24360 cm^{-1}/s.

5.3.2 Evaluation and Results

Before operating the WHP burner with an ignited flame, measurements of so called *cold methane* were recorded to check for inhomogeneity and asymmetrical gas distribution above the slots. Afterwards methane measurements with ignited flame (hot methane) were performed and compared to reference values (see [132]). During both measurements the gas temperature was either measured directly (cold methane) or taken from the reference measurements (hot methane). The evaluation itself focused on the mole fraction of methane. After shortly presenting the results of both measurements, a discussion of the system performance and limitations will follow.

Cold Methane Measurements

When performing measurements in cold methane, in general higher signal to noise levels are expected due to higher absorption strength (see Chapter 2.2 for details). Additionally, mixing

effects have to be taken into consideration when comparing the measured values with the expected results. Since the methane flow from the center slot of the WHP burner is operating at half the speed of the adjacent air and nitrogen slots, this mixing process is aided. Due to this the methane concentration is expected to resemble a peak like shape.

As a representative sample measurement, the measurement at the center line of the fuel slot (x = 0.0 mm) is shown in Figure 5.13. For this measurement, the evaluation process described in Chapter 4 was used without a compensation of the diode ringing. The effects of the diode ringing are visible in the residual around each absorption feature (highest residual in peak center). Based on the peak SNR and the standard deviation of the residual, the mole fraction error is estimated to be approximately 0.6 % (for details on the precision and accuracy see Chapter 4.6). The standard deviation of the measurements was 0.762×10^{-2} when unaffected by absorption features, whereas the overall standard deviation was 2.174×10^{-2}.

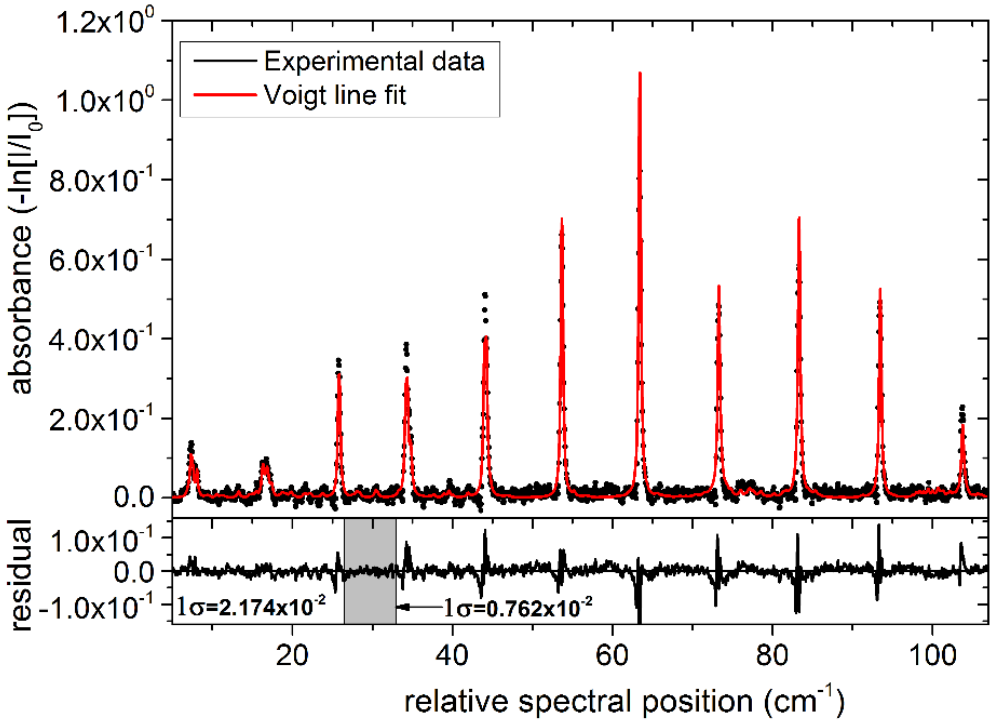

Figure 5.13 Cold methane measurement at 0.0 mm, 1000 mbar, 297 K, SNR 140, CH_4 mole fraction 83.96 %

When combining the measurements from the lateral range of – 6 mm to + 6 mm, the expected peak / bell shaped pattern can be seen (see Figure 5.14). Measurement outside this range were not feasible due to insufficient SNR (the methane mole fraction reached levels well below the detection limit). When comparing the recorded values with a fitted Gaussian peak shape, it appears to be slightly malformed towards a top-hat profile. Since the flow exited the burner head in a top-hat profile, this seems to be last traces of this shape prior to full mixing at a slightly higher level in the z direction.

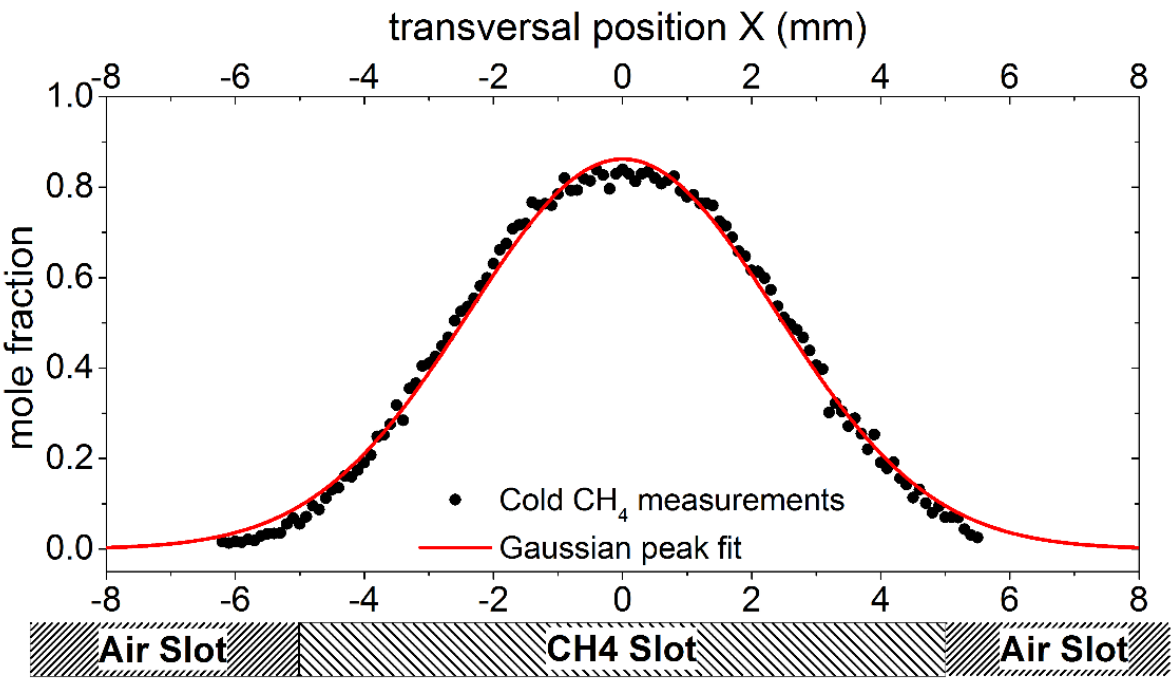

Figure 5.14 Cold methane measurements across transversal axis of WHP burner at 7 mm above the burner head

Hot Methane Measurements

After ignition of the burner, the identical transversal range was covered in the measurements. Giving the reduced absorption strength of the evaluated methane absorption lines, the detection limit is reached earlier and no measurements were possible beyond ± 3 mm. An exemplary measurement of hot methane (x = 0.0 mm) is shown in Figure 5.15. When comparing these measurements with the measurements in Figure 5.13 the recorded absorbance is less than half, which is expected due to the increased temperature and the accompanying reduction in absorption line strength. The aforementioned effects of diode ringing are still visible in the residual, but are reduced in strength since they are related to the level of absorbance. Given a standard deviation of 0.919×10^{-2} (on the same order of magnitude as for cold methane) when unaffected by absorption features, a SNR of 46 is achieved. Given this SNR and standard deviation, the mole fraction error is estimated at ±1.9 %.

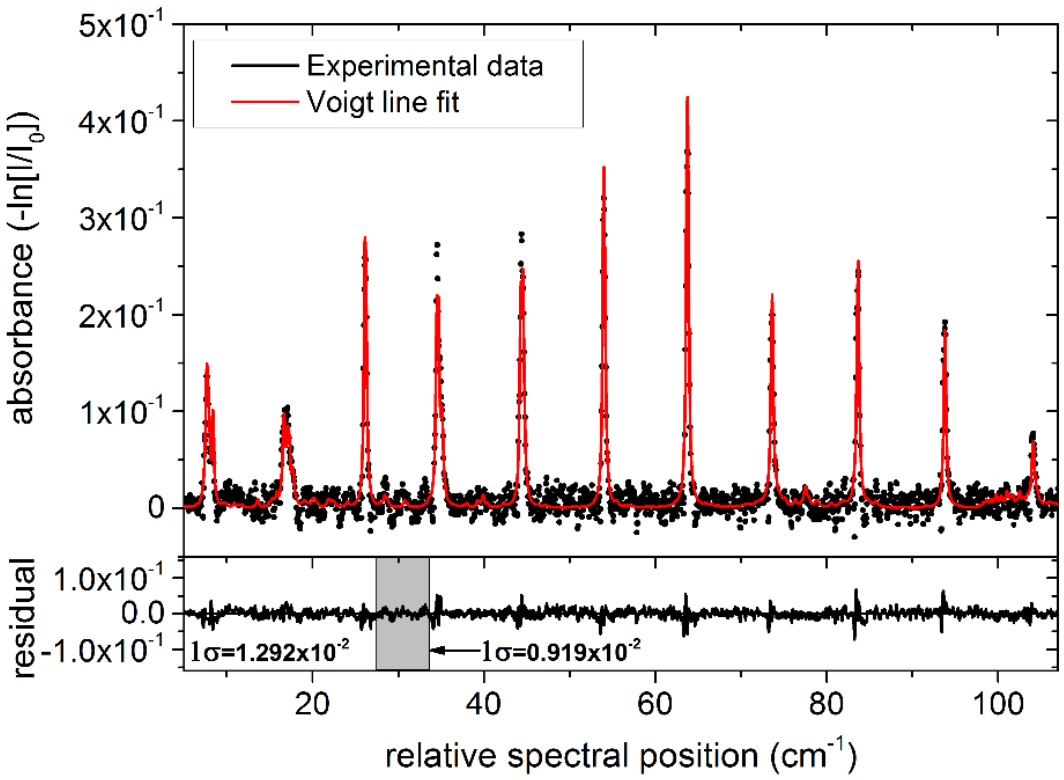

Figure 5.15 Hot methane measurement at 0.0 mm, 1000 mbar, 473 K, SNR 46, CH_4 mole fraction 86.6 %

When comparing the methane SCLAS measurements across multiple positions with the reference values from [132] (shown in Figure 5.16), good agreement is visible. Nevertheless, several deviations and effects can be seen in comparison. First and foremost, it has to be taken into account, that the reference measurements weren't performed across the complete transversal range. Instead measurements were recorded for a single half of the axis and under the assumption of symmetry, the results were mirrored. This is not the case with SCLAS. Therefore SCLAS measurement can show an asymmetry, as opposed to the reference measurements. For easier discussion, a Savitzki-Golay filter (see [134], window of 15 pts and polynomial order of two) is applied to the measurements (as shown in Figure 5.16). The resulting shape can be divided into three sections. In the center section (denoted I), the recorded values coincide very well with the reference measurements and no preference in deviation is visible. Section II shows good agreement on the left-hand side, while there are larger deviations in the right-hand side. On both side, there is a tendency of SCLAS to over-estimate the methane concentration. In section III, this trend is reversed and on both sides SCLAS underestimates the mole fraction for methane. This under-estimation is related to a significantly lower level of SNR in the side lopes of the distribution towards the outer edges. Overall though, the results show that SCLAS can be readily applied in combustion scenarios.

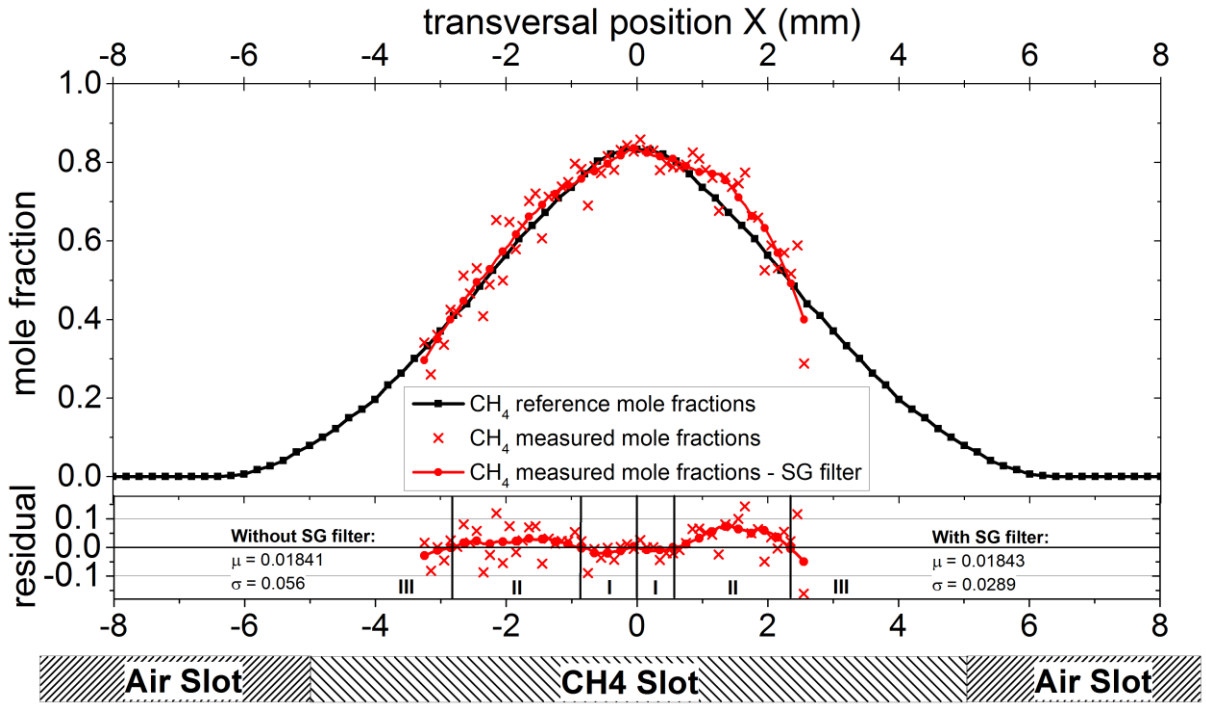

Figure 5.16 Hot methane measurements across transversal axis of WHP burner at 7 mm above the burner head

6 Application of SCLAS in Combustion Diagnostics

After evaluating the performance and uncertainties of SCLAS in the steady-state applications and within a quasi-steady-state laminar burner, this chapter will focus on evaluating SCLAS for transient conditions, which are essentially present in almost all combustion relevant system. Before applying SCLAS to an internal combustion engine (ICE) testbed, it is necessary to apply SCLAS in a system, which offers more control over operating conditions. For this purpose, the aforementioned absorption cell will be extended with a secondary volume to allow for the investigation of mixing and stratification processes within the gas cell (as opposed to homogeneous conditions in Chapter 5). This extension will allow for transients in all fitted parameters simultaneously (temperature, pressure and species concentration). SCLAS will then be applied to an ICE testbed (glass engine) to evaluate its performance in harsh and challenging environments.

6.1 High-Pressure Chamber with Transients

By advancing on the absorption cell used in Chapter 5, it is possible to recreate several phenomena related to combustion, and especially internal combustion engines. These processes include:

- Injection
- Mixing (accompanied by inherent compression)
- Expansion (accompanied by inherent cooling)
- Stratification[1] (accompanied by inhomogeneous conditions)

Given the time-scales of combustion processes, it is necessary to provide sufficient time-resolution. While the setup will not be able to fully recreate the transient conditions in a four-stroke engine, it is sufficient to validate SCLAS in transient conditions (see later on in this chapter for details). To fully utilize the potential of SCLAS, multi-parameter multi-species measurements will be performed. In this case, the concentrations of methane and acetylene (added to the system as a tracer, see following section for details) as well as temperature and pressure for both species will be measured. These experiments were chosen to show that SCLAS is capable of providing multi-parameter multi-species measurements in transient conditions. After previously having validated SCLAS performance in (quasi-) static conditions, the next step is to extend its applicability to transient systems. While creating controlled transient conditions including injection, mixing expansion and stratification in a single setup is difficult, this setup

[1] Stratification in this case does not necessarily refer to the in-cylinder stratification as used in various engine concepts, but rather a more generic stratification, for example within the absorption path.

was chosen accepting the lack of reliable validation data, since it provides a challenge to diagnostic systems that only a multi-parameter multi-species diagnostic system can address. While a different absorption based diagnostic system might measure mole fraction and temperature simultaneously, a separate pressure measurement is required. When investigating this system with SCLAS, no additional sensors are required to reliably determine species concentration, temperature and pressure (based on two different gases). Furthermore, deriving uncertainties for all measured quantities (based on the approach described in Chapter 4.6) allows for an estimation of the confidence of the measured values.

6.1.1 Experimental Setup

As mentioned before, the absorption cell as used in Chapter 5 will be extended by a second gas volume separated by an electronically actuated valve. This valve will allow for timed injection and mixing studies driven by a differential pressure. A similar valve will be added at the exit of the cell as well to allow for rapid release and expansion of the gases. The complete setup is shown schematically in Figure 6.1. See Figure 5.1 for a sectional drawing of the absorption cell showing inlet (right) and outlet (left).

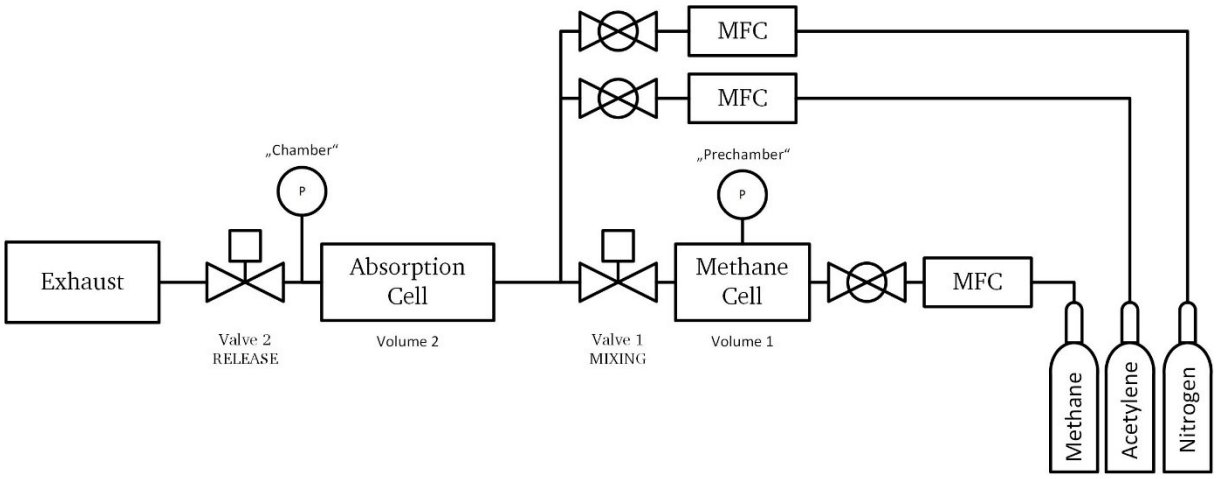

Figure 6.1 System schematic of transient cell including mass-flow controllers and electrically operated valves, as well as pressure sensors to record pressure traces in the chamber and the prechamber.

Furthermore, several *mass flow controllers* (MFCs) in combination with pressure sensors in volumes 1 and 2 will allow for a controlled mixture in both vessels. Given that there mixtures contain methane and acetylene, the mixtures will be generated without oxygen present by using nitrogen as the dilution gas to reduce the risk of combustion. By using narrow stainless-steel tubing (outer diameter: 6 mm, inner diameter: 4 mm) for connections between the volumes and a sequential arrangement of the volumes, stratification effects will take place preventing the gases from reaching homogeneous mixture.

Before detailing the individual steps taking place during a test run, it is necessary to define the relevant system transitions to be investigated with the help of the SCLAS system:

Mixing and Compression

By combining two volumes of different pressures, a mixture of the gases will take place, while one gas will encountered a reduction in pressure (expansion) and the other gases will encounter an increase in pressure (compression). This step is comparable with in-cylinder injections of fuels (neglecting turbulence aiding the mixture formation) and the compression stroke of an ICE in general.

Settling and Homogenization

After the mixing and compression step took place, the inhomogeneous mixture present in the system will slowly homogenize over time. This process is partly influenced by mechanical constraints (narrow tubes, dead volumes and obscured corners and nooks). Given that achieving homogeneous mixture would prevent stratification effects during release and expansion and these effects are intended to be present in the measurements, the time between mixing and release is kept short.

Release and Expansion

Before homogenization of the gases can take place, the gas mixture will be rapidly relaxed by releasing the pressure to the surroundings. Releasing the stratified high-pressure mixture almost instantaneously creates conditions comparable to exhaust valve opening in engine. During the exhaust stroke of a four-stroke engine, gas temperatures within the cylinder can reach temperatures well below ambient conditions due to expansion of the gas mixture. For motored operation of the engine (no combustion, driven by an external electric motor) these temperatures can reach down to 0 °C [25] causing significant condensations in the exhaust tubing. Given the stratification of the gas before release, it is expected to see an increase in concentration for one gas, while the other gas concentration decreases (a detailed description of the expected results will be given later in the chapter). Alongside the concentration changes, a change in temperature for both gases is expected due to the rapid expansion.

Before discussing the obtained measurements, it is helpful to provide a detailed description of the steps throughout an experimental run alongside the expected state of the gases in both volumes. A typical run with this transient-cell will include the following steps:

- Preparation of both volumes with gas mixtures, all valve closed:

  Volume 1: Pure methane (CH_4) at pressures higher than volume 2

  Volume 2: Known mixture of acetylene (C_2H_2) + nitrogen (N_2) (elevated pressure)
- Opening of valve 1, connecting volumes 1 and 2 → **MIXING**
- Concentrations in the volumes can equalize → **SETTLE**

  (only permitted for a short time)
- Opening of valve 2, opening system to surroundings → **RELEASE**

- Closing of valve 2 to keep system separated → **AFTER RELEASE**[1]
  from surroundings after pressure equalization

The SCL was operated at 3.2 MHz and a DCM with a dispersion -1500 ps/nm was used to disperse the pulses in time. The specific instrument function and dispersion function was determined as described in Chapter 2.5 and Chapter 4.4. The pressure sensor in the prechamber is a Keller PAA-33X absolute pressure transducer (0-30 bar) with an uncertainty of ±0.15 bar (0.5 % of full-scale) and an internal sampling rate of 400 Hz. The pressure sensor in the chamber itself is a Keller PAA M5-HB absolute pressure transducer (0-30 bar) with an uncertainty of ±0.15 bar (0.5 % of full-scale) and an internal analog sampling rate of at least 50 kHz (-3dB frequency limit). This difference in internal sampling rates causes the difference in the pressure traces of both sensors.

To resolve the temporal transients, the limited recording time of the oscilloscope is split among four segments within a single experimental run. To ensure proper recording of SCLAS spectra, a trigger system was employed. Based on a master trigger, after an initial delay, four individual trigger signals were sent to the SCLAS system for recording each one segment of data (length: 1.6 ms, consisting of approximately 5200 pulses, equivalent of 7.68 *CAD* for an *ICE* running at 800 RPM). The spacing between segments was dependent on the specific process in question. For MIXING an initial delay of 0.04 *s* was applied, emitting four pulses each spaced 0.0025 *s* (equivalent of 12 *CAD* for an *ICE* running at 800 RPM) apart. The trigger schema for MIXING is shown in Figure 6.2. For this graph, the triggers were recorded parallel to recording of the pressures in the chamber and the prechamber.

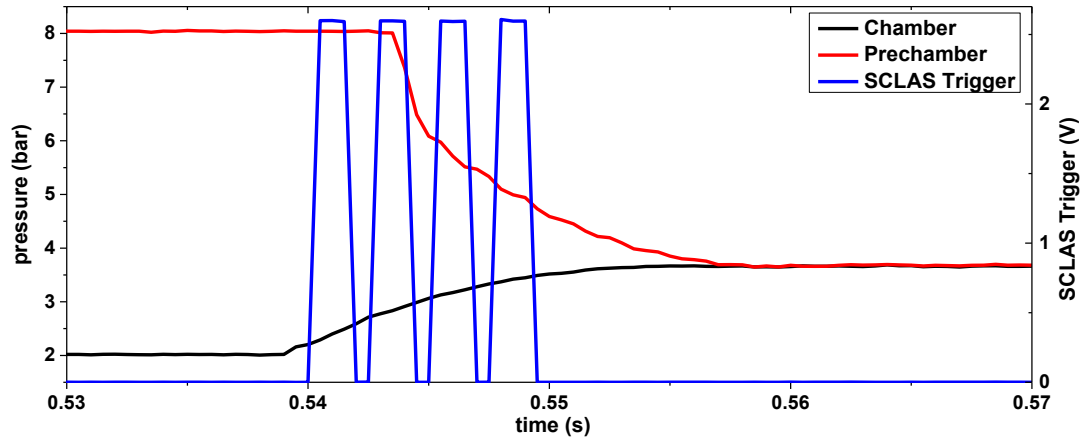

Figure 6.2 Trigger schema for MIXING

For RELEASE an initial delay of 0.03 *s* was applied, emitting four pulses each spaced 0.05 *s* (equivalent of 24 *CAD* for an *ICE* running at 800 RPM) apart. The trigger schema for RELEASE is shown in Figure 6.3. As before, the pressures in the chamber and the prechamber are recorded alongside the trigger pulses.

[1] This step was not performed at all times.

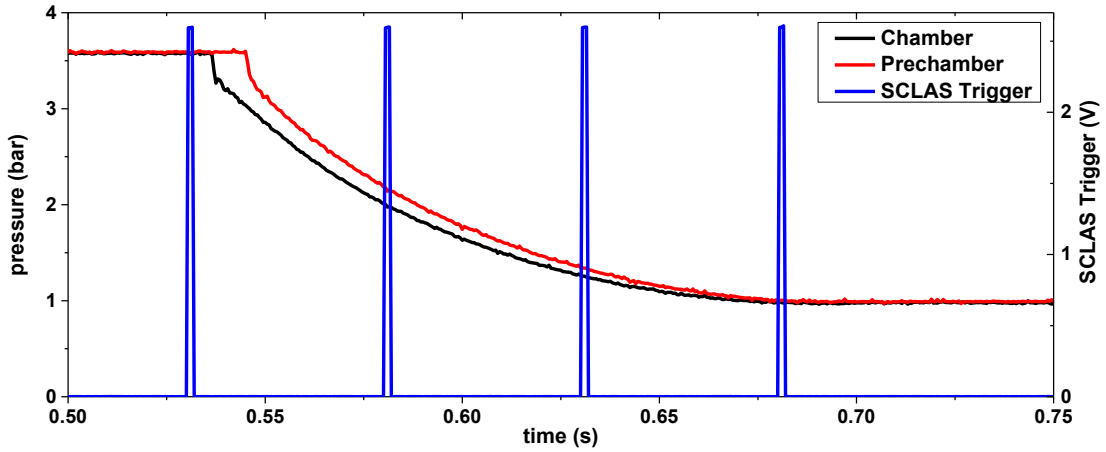

Figure 6.3 Trigger schema for RELEASE

6.1.2 Evaluation and Results

For the processing of the recorded spectra, two separate spectral fits were performed: methane and acetylene. For methane, the spectral range from 5995 cm^{-1} to 6140 cm^{-1} was used and the fitting was only limited in temperature (230 K to 500 K) and pressure (0.1 bar to 20 bar). For acetylene, the spectral range from 6500 cm^{-1} to 6602 cm^{-1} was used and the fitting was only limited in temperature (230 K to 500 K) and pressure (0.1 bar to 20 bar). The species concentration was not limited, except for physicality limits (0 % to 100%). As required, the same instrument function was used for both spectral ranges, while two different dispersion function were derived as outlined in Chapter 2.5. While both spectral range are using the same DCM, each dispersion function is only defined for the spectral fitting range chosen.

Before discussing the obtained results in detail, it is useful to outline several assumptions regarding the expected results:

- While similar pressures are expected for both species during MIXING, SETTLE and RELEASE, the temperature can vary independently for both gases, but this effect is unlikely to occur. This is especially the case, since both gases are compressed to different levels during system preparation. In the case of methane, filling volume 1 to pressures of 8 bar and higher will raise the temperature of the gas.
- Given that the absorption cell is filled with acetylene and nitrogen first, and methane is added later via a narrow tube from one end of the cell (see Figure 5.1), it is expected, that the gases will be stratified along the absorption path.
- During MIXING the added methane will reduce the concentration of acetylene, as well as increase its temperature due to compression which is partly compensated by heat flux to cell itself.
- For methane itself, MIXING is considered a relaxation coinciding with a reduction in temperature.

- During RELEASE, due to the stratification, the acetylene concentration will be reduced, while the methane concentration will increase. Since the outlet valve is placed at the other end of the absorption cell (see Figure 5.1, left side), gases that entered the cell first, will also leave the cell first (assuming no equalization took place). Since methane entered the cell through the inlet after acetylene and nitrogen, it will be the last gas remaining in the cell, effectively increasing the concentration in the cell relative to other gases. The exact mole fraction are not known, since each measurement run is different due to the chaotic nature of the mixing.

Given the limited memory of the oscilloscope, each experimental run will consist of 9 or 10 measurements, depending on whether an AFTER-RELEASE measurement was taken. Among these measurements, the first 5 are part of MIXING (#1 through #4) and SETTLE (#5). The measurement #6 through #9 resemble the RELEASE phase, while an additional measurement #10 represents AFTER-RELEASE.

Experimental Run

The recorded and simulated signals for methane for the measurements #1 through #4 (MIXING) are shown in Figure 6.4. The increase in concentration as well as pressures is clearly visible. The increase in concentration coincides with the area of each absorption line, while the increase in pressure results in a broadening of the absorption lines and therefore a separation of the reference intensity from the recorded signal trace due to overlap between individual absorption lines. The determined parameters for the four measurements of methane and the expected values regarding pressure as well as the SETTLE measurement #5 are given in Table 6.1. The obtained parameters are consistent with the recorded spectra and the expected behavior of the gases and the system overall, but the derived pressures do not agree very well with the separately recorded pressures. This might be caused by insufficient broadening models due to HITRAN relying on broadening by air and not by acetylene or nitrogen. The temperature for measurement #1 is too high, which is caused by the overall very low signal-to-noise ratio of the measurement #1 and should not be considered a reliable value. The following measurements #2 through #4 are consistent with a temperature increase during filling of the pre-chamber and an equalization of the temperatures during SETTLE. Deviations at SETTLE are due to the spectrum not being suited well for temperature measurements at ambient conditions.

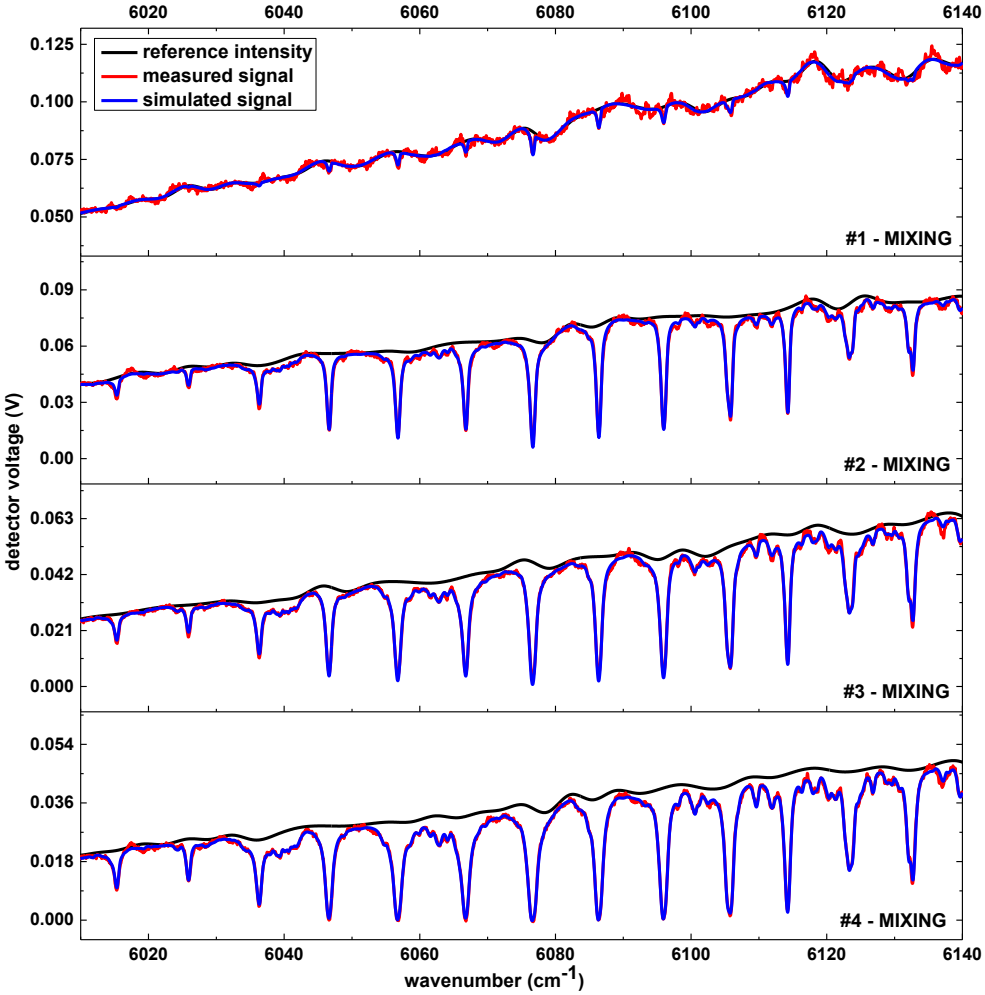

Figure 6.4 Methane spectra for measurements #1 through #4. A significant increase in pressure is visible in the spectra alongside an increase in concentration as is expected for this experiment.

Table 6.1 Parameter sets for measurements #1 through #5 based on methane

Parameter	1	2	3	4	5
Temperature	375 K	342 K	329 K	313 K	304 K
Pressure	3.1840 bar	3.4560 bar	3.7950 bar	3.8711 bar	3.8905 bar
Pressure (reference)	2.366 bar	2.813 bar	3.155 bar	3.421 bar	3.618 bar
Methane concentration	0.8 %	14.9 %	23.9 %	39.45 %	51.24 %

Evaluating the recorded spectra for acetylene yielded the results shown in Table 6.2 for the measurements #1 through #5 (MIXING and SETTLING).

Table 6.2 Parameter sets for measurements #1 through #5 based on acetylene

Parameter	1	2	3	4	5
Temperature	304 K	311 K	320 K	320 K	294 K
Pressure	2.5390 bar	2.8690 bar	3.2425 bar	3.5033 bar	3.6415 bar
Pressure (reference)	2.366 bar	2.813 bar	3.155 bar	3.421 bar	3.618 bar
Acetylene concentration	23.71 %	21.18 %	15.55 %	13.69 %	11.18 %

During the RELEASE phase, a rapid drop in pressure accompanied by a drop in the acetylene concentration and a rise in the methane concentration is expected, as stated previously. The obtained measurements #6 through #9 for methane are shown in Figure 6.5 (spectral absorbance in Figure 6.6), while the obtained parameters are listed in Table 6.3. For acetylene, the recorded measurement and fits are shown in Figure 6.7 (spectral absorbance in Figure 6.8) the derived parameters can be found in Table 6.4.

Table 6.3 Parameter sets for measurements #6 through #9 based on methane

Parameter	6	7	8	9
Temperature	308 K	287 K	282 K	280 K
Pressure	4.0325 bar	2.3506 bar	1.3707 bar	1.0188 bar
Pressure (reference)	3.579 bar	1.995 bar	1.255 bar	0.985 bar
Methane concentration	47.37%	67.00 %	84.05 %	86.33 %

Table 6.4 Parameter sets for measurements #6 through #9 based on acetylene

Parameter	6	7	8	9
Temperature	297 K	278 K	275 K	257 K
Pressure	3.6969 bar	2.4937 bar	1.8175 bar	1.2586 bar
Pressure (reference)	3.579 bar	1.995 bar	1.255 bar	0.985 bar
Acetylene concentration	10.83 %	6.00 %	1.96 %	1.30 %

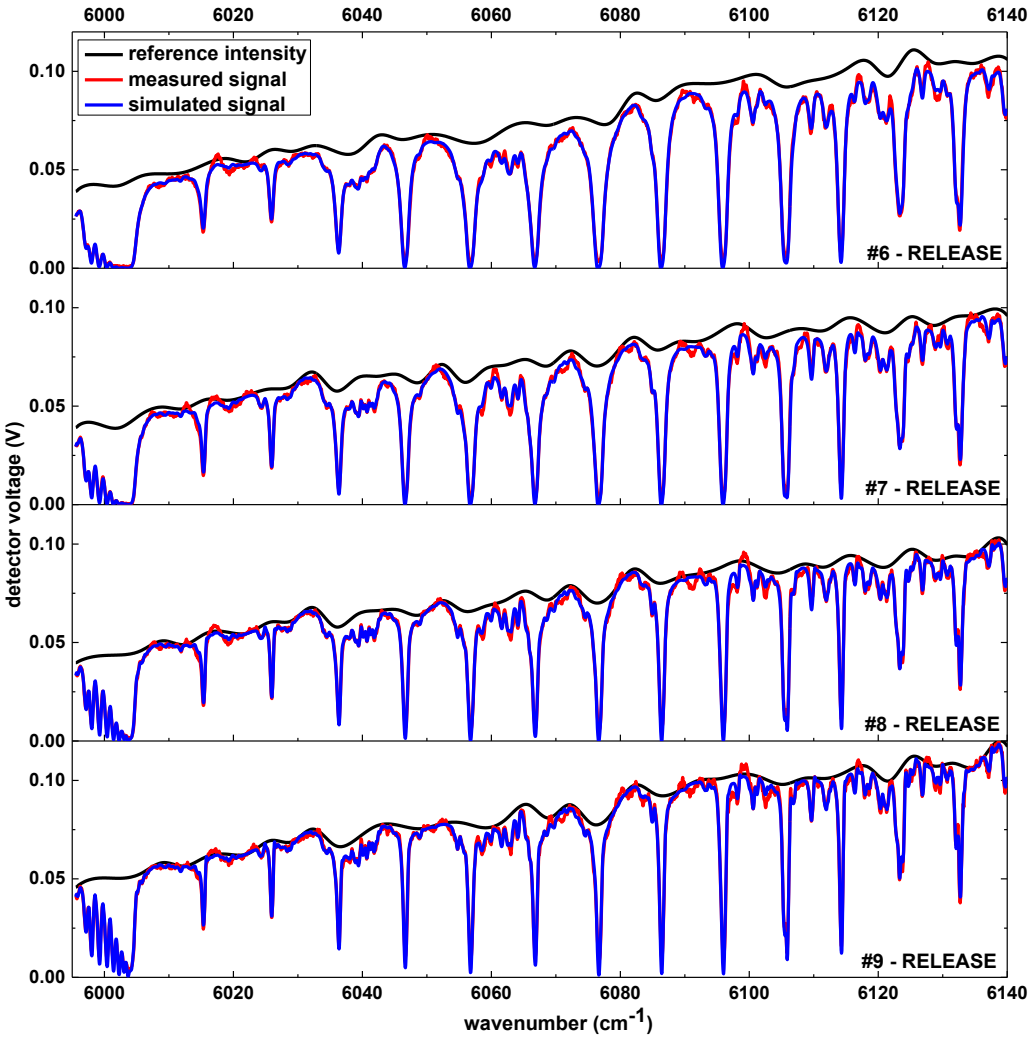

Figure 6.5 Methane spectra for measurements #6 through #9. A drop in pressure is visible by the narrowing of the absorption lines. An increase in concentration is not directly visible.

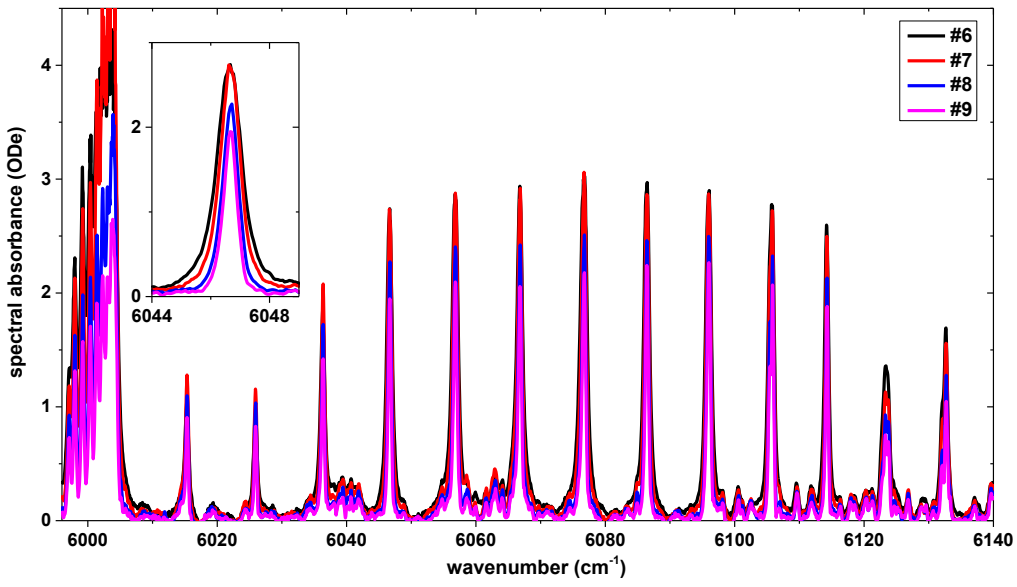

Figure 6.6 Methane spectral absorbance for measurements #6 through #9

From the recorded methane spectra, a reduction in pressure is clearly visible, since for example the fine structure of closely spaced absorption lines around 6000 cm^{-1} becomes visible and all absorption lines experience reduce collisional broadening. In addition, the spectrum does not encounter *lift-off*, which refers to a separation of spectrum and reference intensity over significant spectral ranges. This lift-off is due to overlap of smaller absorption lines at higher pressures. Furthermore, smaller absorption lines become more pronounced (see spectral range around 6040 cm^{-1}). When comparing the recorded spectra of measurements #6 and #9 in the spectral absorbance domain, the line narrowing and reduced *lift-off* due to reduced pressure becomes more visible (see Figure 6.6). Similar effects can be seen in the acetylene spectra as well (see Figure 6.8).

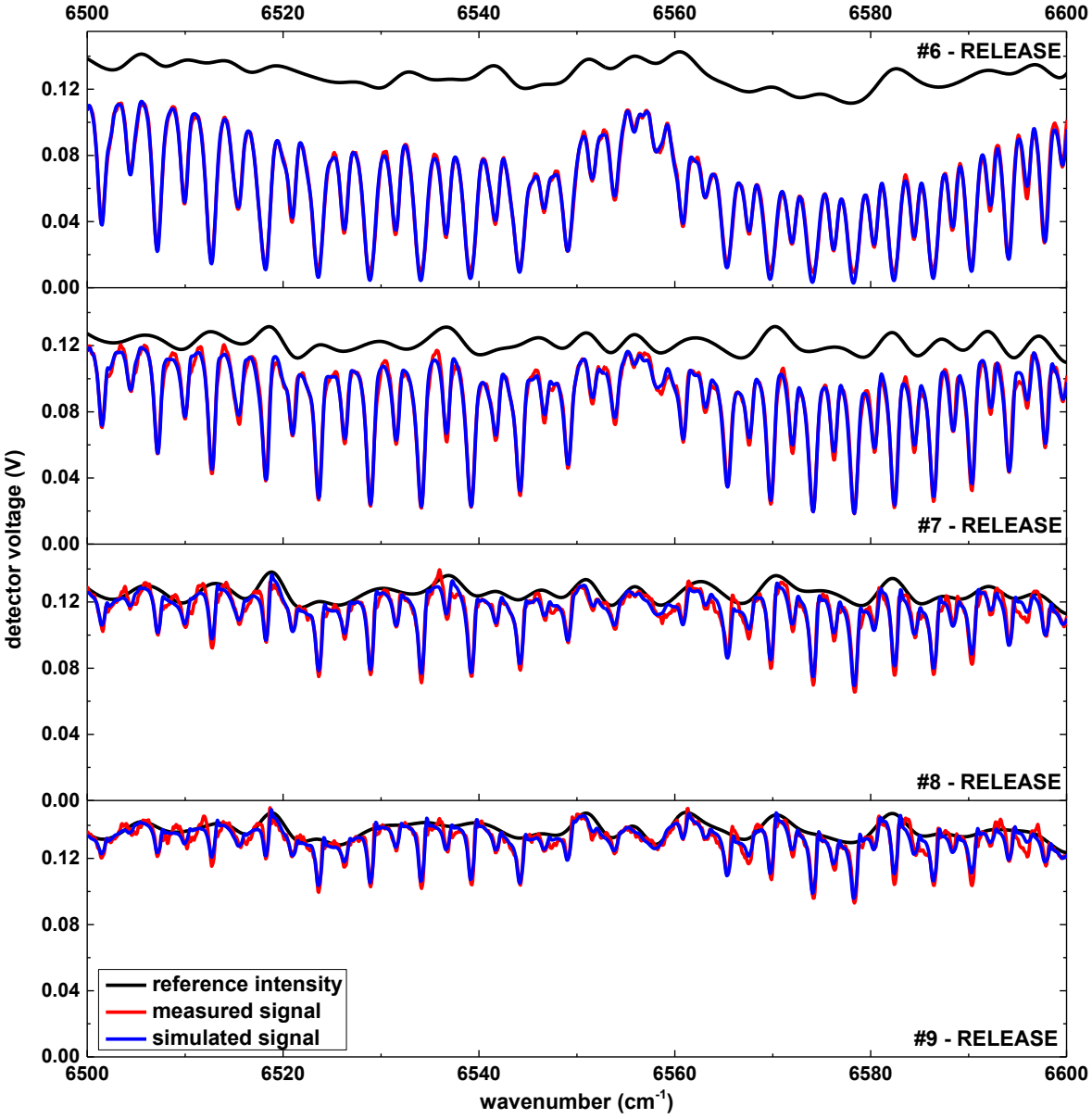

Figure 6.7 Acetylene spectra for measurements #6 through #9. A reduction in concentration can be seen alongside a reduction in pressure.

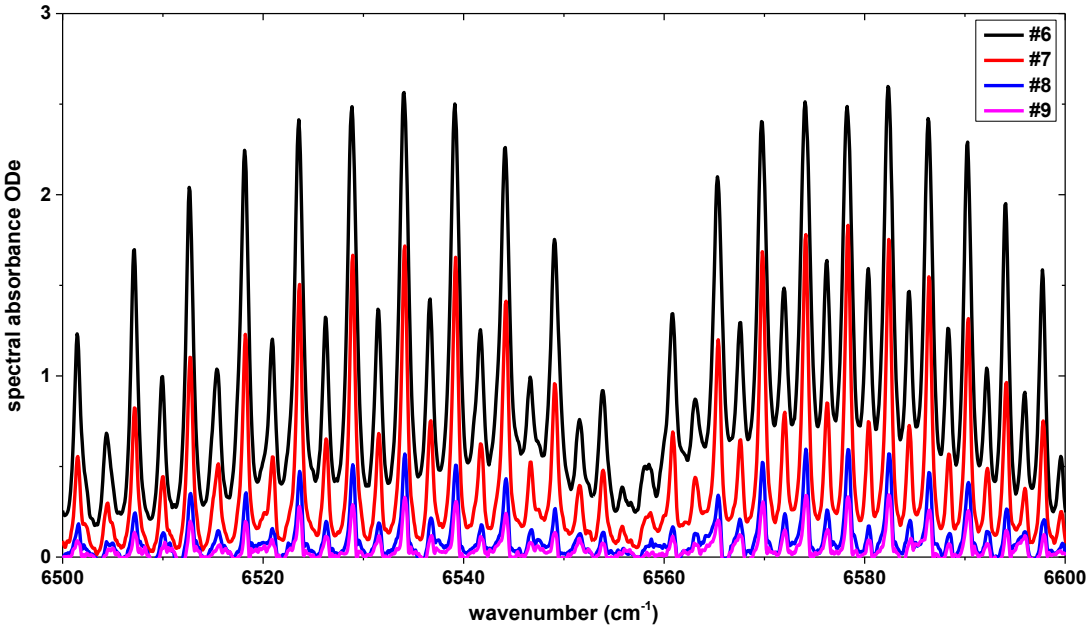

Figure 6.8 Acetylene spectral absorbance for measurements #6 through #9

When considering all measurements together, the assumptions stated at the beginning at this chapter can be considered correct. All derived parameters follow the expected trajectory (see Figure 6.9). Nevertheless, several deviations are visible from the traces. While the concentration values are plausible, but cannot be easily verified with secondary measurements, the pressure traces of acetylene agree well for the MIXING and SETTLE phases. During these phases the pressure based on methane is constantly over-estimated. As stated previously, insufficient modelling of the broadening by an acetylene and nitrogen mixture could cause this. Given that the spectroscopic model is based on HITRAN line data, and therefore its modelling regarding broadening, it is to be expected that the derivation of pressure, which relies highly on the correct modelling of the spectral broadening, is mostly affected by these limitations. Incorporating additional broadening data for all gases in the mixture and advancing the modelling of foreign broadening can improve the quality of pressure measurements with SCLAS. During the RELEASE phase, all traces follow a general downwards trajectory, as expected. While before the methane pressure was over-estimated, in this phase the acetylene pressure is determined incorrectly. The pressure determined on methane, agrees well with the pressure sensor. Given the limited number of measurement points, determining the shape of the parameter changes for example by fitting a function to it, is not viable.

Overall, it can be stated that SCLAS allowed the derivation of all four parameters simultaneously from a single spectral measurement and provided plausible results when compared to reference measurements.

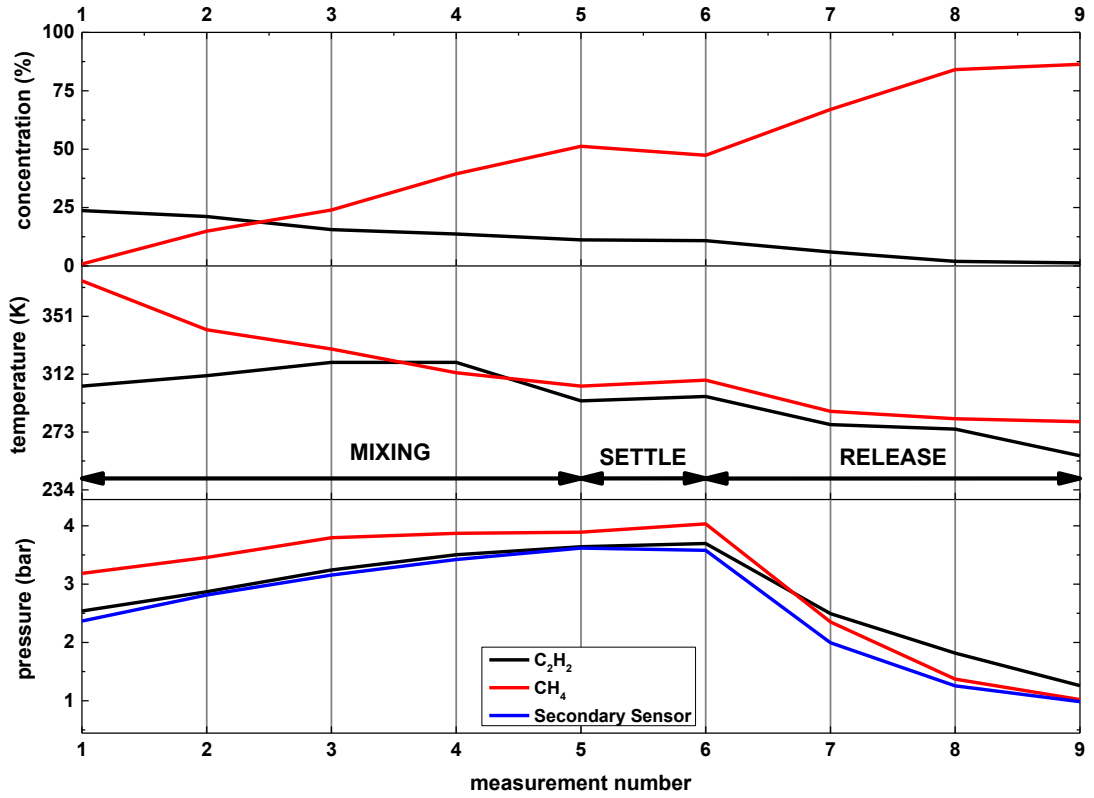

Figure 6.9 Derived parameters for all measurements of an experimental run

6.2 Internal Combustion Engine Measurements using SCLAS

After validating the applicability of SCLAS in transient conditions for combustion research using *Internal Combustion Engine* (ICE) –comparable scenarios, this chapter will cover the application of SCLAS at a glass engine (ICE test bed), pushing the limits of the current state of development of SCLAS for application in harsh environments. In addition, the integration with the engine test bed requires specifically designed hardware due to the all-fiber approach of SCLAS. Within this experiment, the SCLAS is applied to the engine and used to measure the concentration of methane (CH_4) during the compression stroke of the engine (motored operation). Furthermore, a test case with fired engine operation will be discussed as well. Given that SCLAS requires a fiber coupling of the light after transmission, the optical system needs to be more complex to ensure fiber-coupling even under vibrations from the operating engine.

6.2.1 Experimental Setup

The engine test bed for these experiments is shown in Figure 6.10. Since methane will be used for these experiments, manifold injection is used. After injection of the methane in pulsed form, the inlet section of length $15 \cdot D$ ensure proper mixing of fuel and air. The mixture can be verified with a lambda meter in the exhaust side of the system. Due to the trigger and control system of the engine test bed, high speed pressure measurements are available for comparison with the SCLAS results.

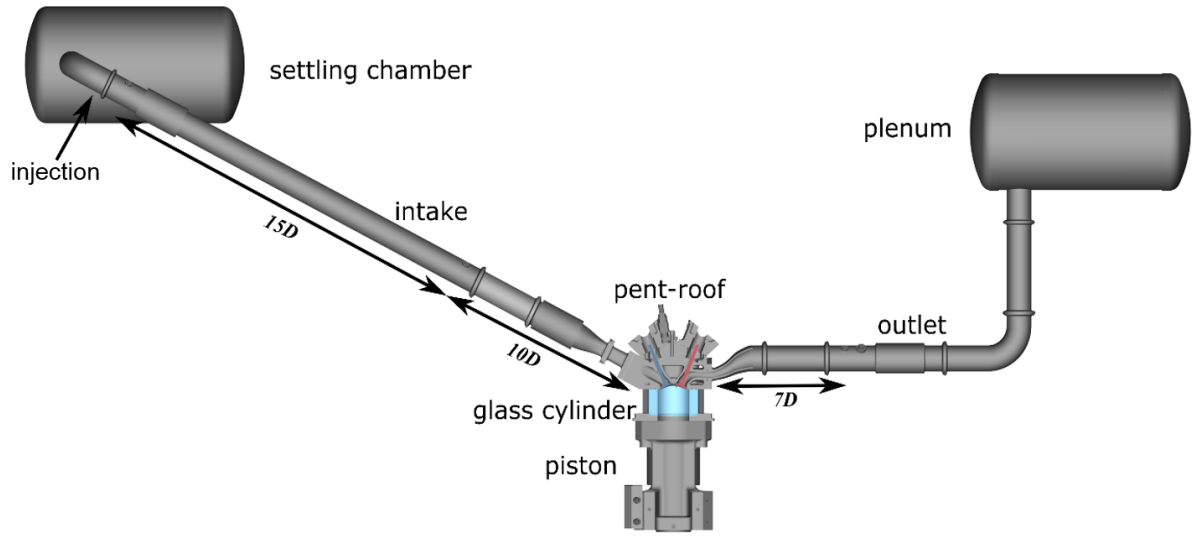

Figure 6.10 Schematic of engine testbed. For this test, the glass cylinder was replaced with a steel cylinder, to which a Sapphire window was fitted.

For these experiments, the glass cylinder wall in the engine test bed has been replaced with a steel version, which provide optical access in form of a single round window using a double-wedged sapphire window (diameter 12 mm, average thickness of 3 mm, sealed up to pressures of 300 bar). On the opposite side of the steel wall liner, a gold mirror is mounted (diameter: ½ inch), which creates a double-pass optical absorption path with a combined length of 0.172 m. After propagating through the absorption volume the light is coupled back into a 50 μm *multi-mode fiber* (MMF) and transmitted to the highspeed photo-diode. By using sufficient length of MMF, proper coupling was ensured to avoid effects on the light. This optical setup is shown in Figure 6.11.

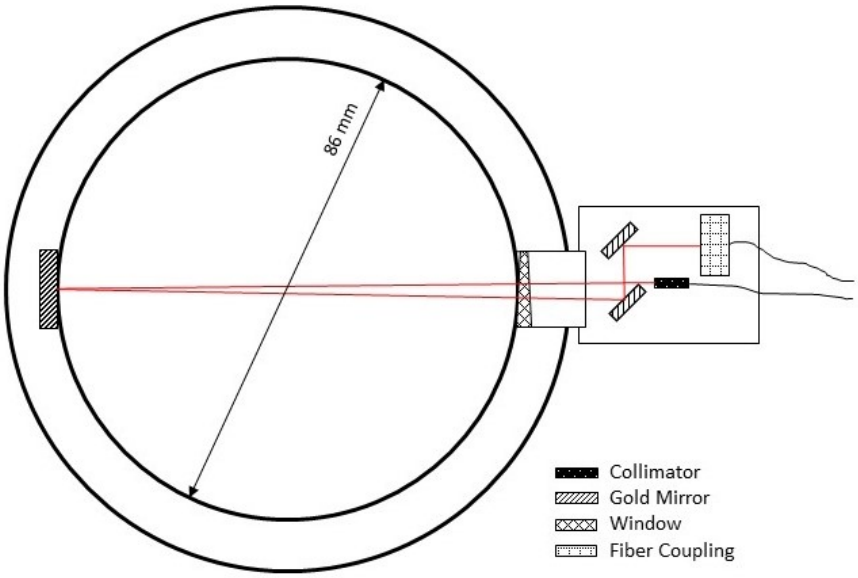

Figure 6.11 Optical access to the single cylinder engine test bed using a Sapphire window, a single-mode collimator to send the light into the volume and a collimator with attached 50 μm multi-mode fiber for collecting the reflected light.

The SCL was operated at 6.6667 MHz (pulse picker ratio 1:12) and a DCM with a dispersion of $-500\ ps/nm$ was used, since the required resolution at pressures of 5 bar and higher is reduced. Compared to the previously reported measurements, the dispersion was reduced to one-third, effectively reducing the optical resolution accordingly to 0.49 cm^{-1}. Due to memory limitations of the oscilloscope, it is not possible to record at multiple times within a single cycle or run. It was therefore necessary to distribute the measurements across multiple runs and record measurements at varying crank angles. Each recording lasted for 2 ms, averaging ~13,300 pulses. The engine was operated at 800 RPM with an inlet pressure of 950 mbar. This resulted in a time resolution of approximately 10 degrees crank angle (9.6 Crank-Angle Degree, CAD) per measurement. In the case of motored operation, a rich air-fuel equivalence ratio of $\lambda = 0.6$ was used to ensure proper signal quality for the SCLAS measurements (correlates with an injection time of 40 ms per cycle). This air-fuel-equivalence ratio correlates with a concentration of 18.96 % of methane. Each engine run contained 200 cycles, while the SCLAS measurements took place in the 150th cycle. Correct triggering was ensured by using the revolution trigger (once per revolution) and 0.2 CAD trigger (every 0.2 CAD) provided by the engine. By combining these two triggers, it is possible to reliably trigger within a specific cycle of the run at a specific crank angle within the revolution.

6.2.2 Evaluation and Results

Given that the engine was operated in motored conditions, it is reasonable to assume constant methane concentration throughout the compression cycle after closing of the intake valve. Furthermore, it is reasonable to assume isentropic compression to derive expected temperature values for different positions in the compression stroke. Using measured in-cylinder gas temperatures (provided by TDLAS measurements) this assumption was found to be valid for the compression stroke [25]. Heat transfer during the compression stroke is mainly limited to wall heat transfer [135] and given the path-averaging nature of SCLAS, spatially limited temperature differences are weighted less on the overall fitted parameters . The temperatures can therefore be calculated from the change in volume using isentropic relationships.

$$T_2 = T_1 \left(\frac{V_1}{V_2}\right)^{\kappa-1} \tag{6.1}$$

where κ refers to the isentropic exponent, V_1 to the in-cylinder volume before compression and V_2 to the in-cylinder volume after compression.

Despite the mixture of methane and air in the cylinder, the isentropic exponent is assumed to be $\kappa = 1.4$. The influence of methane with an isentropic exponent of $\kappa = 1.31$ at ambient temperature can be neglected. Peak temperature for this engine configuration under isentropic compression is approximately 700 K.

For the individual combination of SCL repetition rate and DCM, the system response function and the dispersion function were derived from separate measurements under controlled conditions according to Chapter 4.4. The spectral range from 6050 cm^{-1} to 6150 cm^{-1} was utilized for the determination of methane concentration, pressure and temperature while fitting a spectroscopic model including 715 absorption lines.

An exemplary fit of a recorded signal trace is shown in Figure 6.12, while the results for different crank angles are shown in Table 6.5 in comparison with the recorded pressure measurements and isentropic calculations. Due to the memory limitations only three measurements were performed for motored engine operation at 20 CAD, 15 CAD and 10 CAD before Top-Dead-Center (bTDC, referring to the position of the piston at the end of the compression stroke). The signal quality and fitting algorithm stability allowed for the derivation of all three parameters species concentration, temperature and pressure from the recorded signal traces. These fitted values agree well with the expected results for isentropic compression and the secondary measurements of the engine management system *Indicom*. For temperature, a maximum deviation of 21 K (relative error: 3.3 %) was measured, while for pressure the maximum deviation was 1.152 bar (relative error: 9.8 %). In terms of species concentration, the maximum deviation was 0.89 % (relative error: 4.7 %).

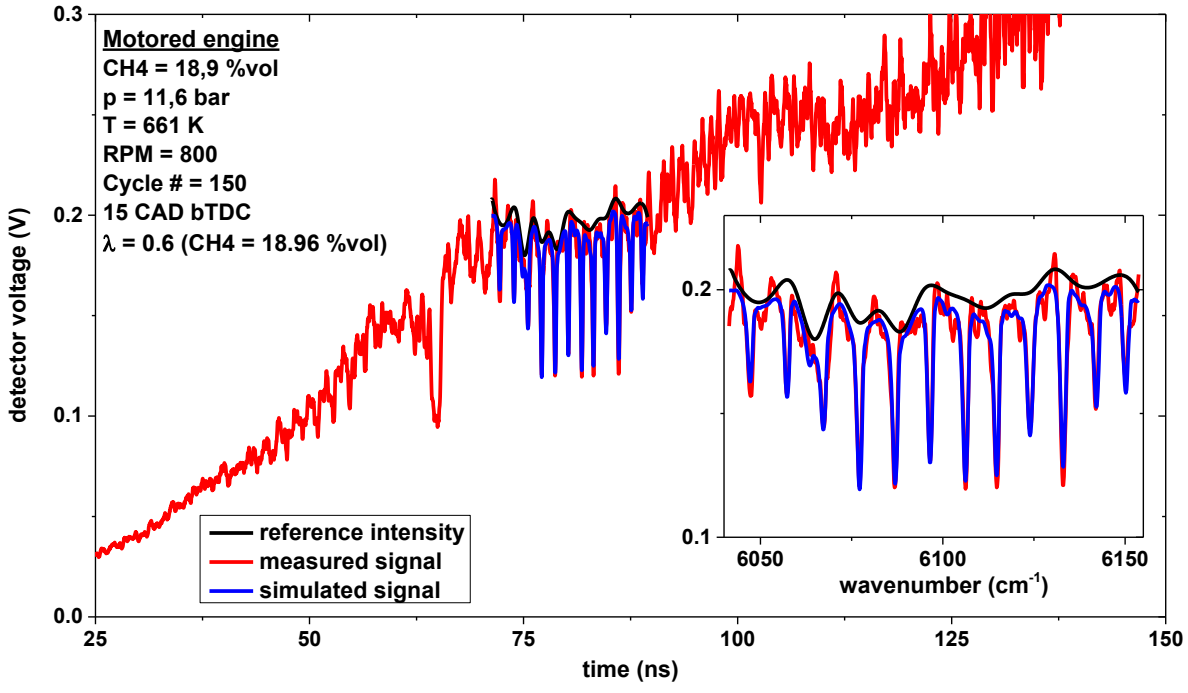

Figure 6.12 Methane measurement in the engine test bed under motored operation with an air-fuel equivalence ratio of 0.6, corresponding with a methane concentration of 18.06 %.

Table 6.5 Results for motored measurements at engine test bed

CAD	Methane Concentration	Pressure SCLAS	Pressure *Indicom*	Temperature SCLAS	Temperature Isentropic
- 20 bTDC	18.07 % (0.89 %)	9.315 bar	9.38 bar (0.065 bar)	608 K	621 K (13 K)
- 15 bTDC	18.90 % (0.06 %)	11.652 bar	10.50 bar (1.152 bar)	661 K	643 K (18 K)
- 10 bTDC	19.57 % (0.61 %)	11.245 bar	11.39 bar (0.145 bar)	680 K	659 K (21 K)

During fired operation, the air-fuel equivalence ratio was increased to $\lambda = 0.8$ to ensure stable combustion throughout each run. Due to poor signal to noise ratio, only temperature and species concentration was derived from the recorded data. The pressure value was obtained from the secondary sensor (*Indicom* system). The measurement at 20 CAD bTDC is shown in Figure 6.13. The derived species concentration agrees well with the expected value of 11.6 % with a deviation of 0.65 % (relative error: 5.6 %), while the temperature is slightly higher compared to the temperatures for isentropic compression. This can be attributed to heated walls caused by previous fired cycles.

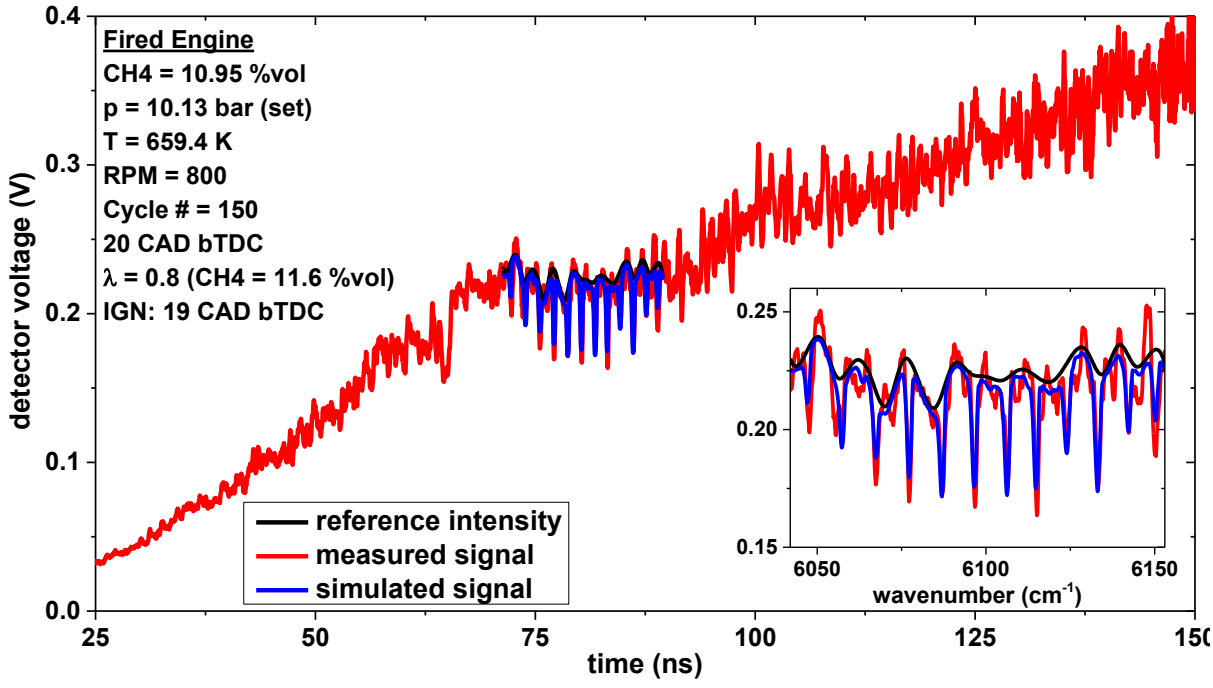

Figure 6.13 Methane measurement in the engine test bed under fired operation with an air-fuel equivalence ratio of 0.8, corresponding with a methane concentration of 11. 6 %.

While the measurements were successful in applying SCLAS to an internal combustion engine, there were several options for improvement. The main limiting factor in this scenario, especially when compared to continuously sampling methods, was the limited memory for spectral recording. With the current configuration, recording phase-averaged data is not possible. Furthermore, the optical setup, though fiber-coupling is required, can be improved to ensure proper fiber-coupling even under harsh conditions, since a free-space operation of the photo diode is unfortunately not possible.

Despite these limitations, the applicability of SCLAS at an ICE is a promising step in extending the applications towards harsher environments. In addition, the increased pressure allowed for an increase in pulse repetition rate and reduction in dispersion while still maintaining sufficient resolution for high pressure measurements.

7 Exploratory Applications and Spectral Modelling Approaches for SCLAS

When a new diagnostic system is validated and applied in several test cases, on the one hand, there are several challenges to be addressed and overcome (see Chapter 4.1). On the other hand, along with these challenges, several new and promising applications of said systems are discovered. These possibilities are worth exploring to further the research options with a new technique as well as provide new options and applications even for other established techniques. Within this chapter one very promising approach with potential for broadband spectra will be further investigated and evaluated regarding its potential, especially in the context of advanced spectral modelling: *Indirect Hard Modelling* (IHM). The necessity to implement advanced spectral modelling tools has already been discussed in general in Chapter 2.3.1. This chapter will therefore focus on details and provide first results of the application to broadband absorption spectra.

When broadband spectra are recorded and need to be evaluated, the available options cover a broad range of approaches to correlate previously known spectra and their corresponding parameters with new measurements. The basic approach of, for example, HITRAN is to implement a spectroscopic model, which relies to a certain degree on assumptions, approximations and physical characteristics (i.e. energy states and transition wavenumbers). The level of assumptions and effects accounted for in the model varies greatly between different models. While HITRAN currently only implements foreign broadening with air at standard conditions (296 K, 1 atm), the model can be extended with additional broadening coefficients if available. There is no need to change the basics of the model (air is in itself only the combination of the foreign broadening effects of nitrogen and oxygen weighted by the composition of air). Such models unfortunately reach limitations, when the investigated molecules become increasingly complex and are hardly usable when liquids are involved. To overcome these issues, several models and approaches for continuous spectra have been discussed previously (see Chapter 2.3). *Indirect Hard Modelling* (IHM, [76, 136–139]) is a promising option. Within this chapter, the basics and details of IHM will be further investigated and initial testing using various test cases will be detailed. Due to the aim and the common field of application of IHM, the first test cases involve spectra of liquids or evaporated complex molecules with overlapping absorption peak structures. Since most of the applications described in this work focus on gas diagnostics, the potential of applying IHM for gas diagnostics will be investigated by means of a theoretical study with methane. The intention behind these trials is not to provide a full assessment of the possible performance enhancements when using advanced spectroscopic models, but to present promising ideas and their potential for further development and adaption to specific use cases in the field of absorption diagnostics and combustion research. Given these initial evaluations, future options and potentials for improvement will be discussed at the end of this chapter.

7.1 Fundamentals of IHM for spectral modelling

The fundamental idea behind Indirect Hard Modelling is the assumption that broadband spectra can be modelled as the sum of distribution functions [136]. This model will then be utilized similarly to other spectral models such as HITRAN (by applying Beer-lambert law, fitting the model to measurements and other additional steps). For the purpose of this work, only the Voigt distribution function will be used for modelling, while IHM is not limited to Voigt functions. Since a Voigt line shape function can be described by four parameters (position, height, Lorentz width, Gauss width, see Chapter 2.2.3 for details) each IHM model comprises of $4 \cdot n$ parameters, where n represents the number of peaks fitted to the spectrum. Since all these parameters are independent of each other, the number of free variables can increase significantly already, when only using a limited number of peaks in the model. Furthermore, by increasing the number of peaks, the complete model usually needs to be refitted to the recorded spectra, since the addition also affects parameters from other peaks. The IHM model therefore requires a trade-off between quality of spectrum reconstruction and complexity in terms of free dimensions. This trade-off can either be set before fitting the model (for example based on previous experience with similar species) or be determined *on-the-fly* during fitting based on the achieved fitting quality.

When deriving an IHM model for a specific spectrum or set of spectra, several approaches can be applied. Most commonly, the residual (difference between recorded spectrum and simulated spectrum) will be used as the indicator if and where an additional peak should be added to the model increasing its complexity [76]. This decision is usually based on a threshold value for the maximum of the residuum. If the threshold is exceed, a new peak will be added at the position of the maximum of the residual. After adding this additional peak to the system, the model will be refitted to the data and the new residual will be used to determine, whether this additional peak improved the resemblance of the spectrum by the model or not. This procedure will be repeated as long as an improvement in the model can be achieved or the remaining difference is exceeding a threshold value. Alternative approaches to this automatic generation include manual designing the IHM model, namely number of peaks and any required fit constraints (for example limitations in wavenumber position). When applying IHM modelling to gas spectra, an additional option for model building involves limiting peaks to known absorption line positions and adding peaks according to the tabulated absorption line strength, effectively creating hybrid models. This approach provides the possibility to actively control the complexity, while also incorporating previous knowledge of the recorded spectra.

After the model has been defined for a set of spectra in terms of number of peaks and limitations in parameters for these peaks, it is necessary to calibrate the model by fitting it to numerous spectra of varying parameters (concentration, temperature, pressure, path length, etc.). When fitting the defined model to recorded or simulated spectra, it is necessary to consider fit limitations to prevent over-fitting. Assuming a model with too high complexity, fitting freely might result in shifting peaks to well outside the relevant spectral range, decreasing their strength to almost zero or fitting peaks to measurement noise. Nevertheless, when limiting the

free fitting range, it is necessary to ensure that this does not prevent the model from being properly calibrated.

Two options are available to store these calibrations (various sets of parameters for all peaks of the model at different conditions) and complete the model building phase:

- Parameter-based *Look-Up Tables* (LUTs) for peak parameters in combination with interpolation
- Model-based storage of peak parameters

In the first case, the established set of peak parameters will simply be stored in a database, being accessible by a set of parameters (usually the parameters that were varied during calibration spectra generation). To give an example, when only the concentration was varied when the calibration spectra were recorded, for each concentration a set of peak parameters for all peaks is stored in the database. When a spectrum for a specific concentration is to be calculated from the model, the appropriate set of parameters is retrieved from the database (given sufficient resolution in the parameter). When required, an interpolation can be applied to create the intermediate spectrum between two stored sets of peak parameters. Similarly, this approach can be extended to spectra with multiple parameters varied during model building by performing linear interpolation between the two closest matching sets of peak parameters. This approach can also simplify IHM model building, since there is no need to identify identical peaks within all spectra used during model building or even have models with identical number of peaks, given that only the sum of the peaks (their envelope) will be used.

In the second case, the changes in the peak parameters, more precisely the changes in the parameters of each peak individually, are modelled by a separate model (*inner model*). These models can be as simple as polynomial functions, but need to provide the required complexity to resemble the behavior of the peak parameters closely. For this approach to work, several assumptions need to be valid. First, and foremost, it must be possible to identify identical peaks in various spectra to track their changes in the peak parameters (see previous section, where this limitation is not necessary). Furthermore, a viable model must exist to represent these changes. On the other hand, having such a model “within the model” allows for seamless calculation of spectra, including combinations never recorded before. In addition, the required storage space is significantly reduced as opposed to storing a large number of peak parameter sets. For the remainder of this work, only the model-based approach using inner models will be used for model calibration.

While the idea behind IHM modelling could be to build peak-based models without knowledge of the inner workings of the absorption spectra, finding a suitable inner model might provide the basis to gain such knowledge. In comparison with HITRAN, it is possible to find something that resembles a “pressure shift” (changes in the parameter proportional to the pressure) in certain parameters, while others do not experience such a behavior. Such knowledge might further improve the models used to represent the peak parameters. Since the intention behind this chapter is to evaluate IHM for broadband spectroscopic utilization, especially for gases, a

purely database-driven approach is not feasible. While it might be an improvement opposed to storing complete spectra in a database, only finding the underlying models for the peak parameters provides the required simplification and improvement of spectra calculation required for an extension of SCLAS and similar techniques to a much broader field of applications.

7.2 IHM Modelling for Absorption Spectra of AdBlue

As an example, the spectra for four different concentrations of AdBlue (DEF) in water (25 %, 50 %, 75 % and 100 %) are shown in Figure 7.1 (with no AdBlue present in the solution, the absorption in this spectral range was zero). The measurements were recorded with a Bruker V80V FTIR spectrometer (DLaTGS detector, Globar MIR light source) and a thickness of the liquid sample of 1 mm (fused silica cuvette). Given the smooth nature of the spectrum a spectral resolution of only 0.24 cm^{-1} was used for the measurement. It is now necessary to recreate the spectrum with an IHM model and then identify underlying regularities within these IHM models that allow for spectrum estimation for various parameter sets. These steps are usually referred to as model determination and model calibration.

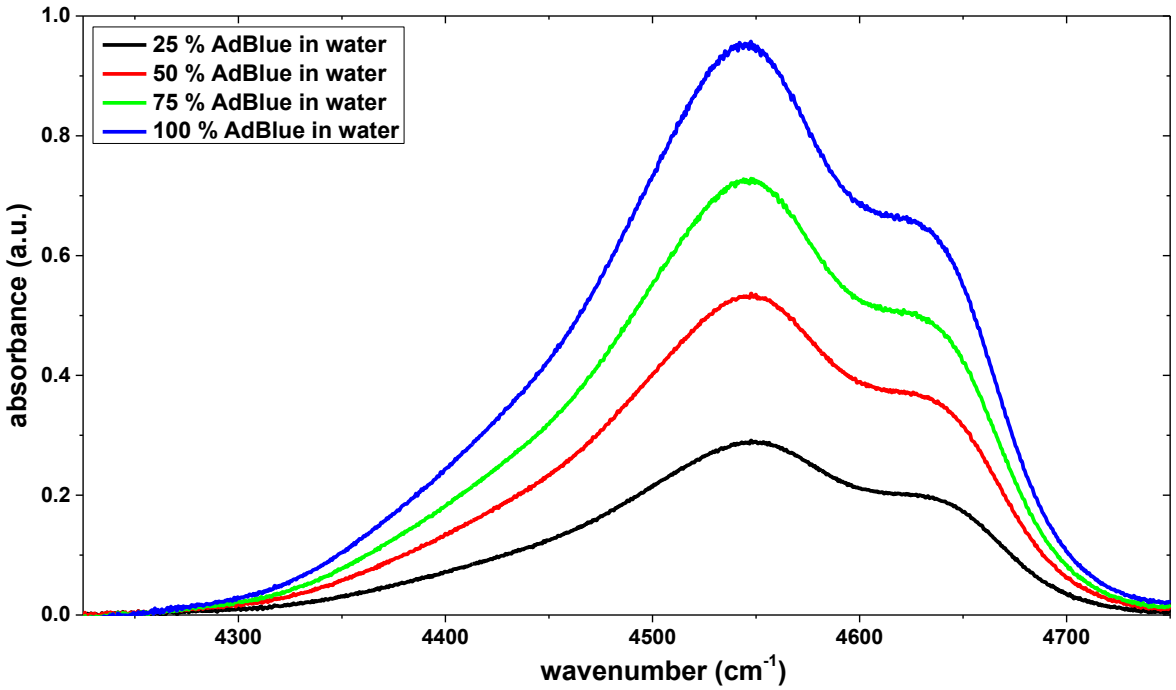

Figure 7.1 Spectra of AdBlue recorded for different concentrations in water (25 %, 50 %, 75 % and 100 % of AdBlue in water)

Utilizing an error-based approached (see [76, 138]), an IHM model can be build semi-automatically given a predetermined number of peaks, the system is supposed to be composed of. Since this number is not previously known, a parameter variation is required to find the optimum number of peaks to represent the spectrum, avoiding over-fitting. An example of such a model derived from the measurement of 100 % AdBlue (no dilution) is shown in

Figure 7.2 with the remaining deviation between model and recorded spectrum plotted as well. For this model three Voigt peak functions were fitted by partially constrained optimization (Levenberg-Marquardt fitting algorithm) only constraining peak parameters to non-negative values. Initial parameters of the peaks were determined according to [76, 138] and were added after each other using the previous model and parameter set as the initial conditions of the model for fitting.

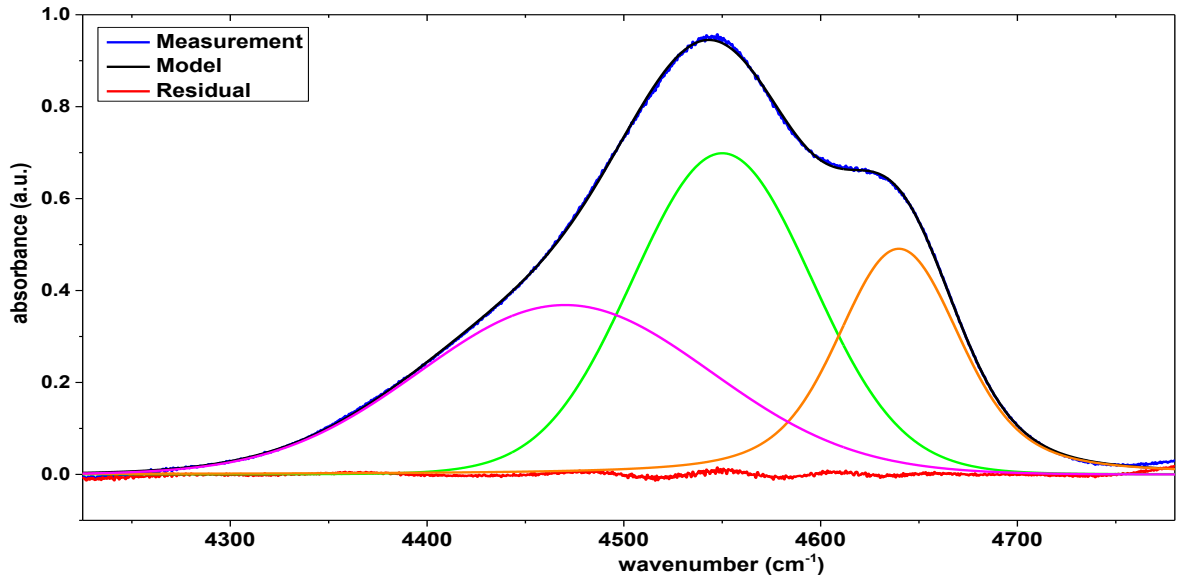

Figure 7.2 Exemplary spectrum of AdBlue (100 %) with an IHM model consisting of three peaks fitted to it; residual after fit is shown in red

In this case, a rather simple model of only three peaks is sufficient to achieve very good agreement between derived model and recorded spectrum (residual at maximum: 0.02067 (~2 % of measurement maximum), at minimum: -0.01373 (~1.5 % of measurement maximum), on average: -1.647×10^{-4} (~0.02 % of measurement maximum)). Given the shape of AdBlue spectra, several effects caused these rather simple models. All spectra are reaching a value of zero at both ends of the spectral range. Additionally, the spectral shape is smooth and no small and narrow peaks are present on the spectrum, despite the spectrum covering over 400 cm^{-1}. As will be discussed later, these are almost ideal conditions for IHM spectroscopic models.

When comparing the fitted IHM model from Figure 7.2 and the shape itself with the shapes of the recorded spectra in Figure 7.1, it appears to be the case that a simple change in amplitude for all peaks could account for the variations in spectrum due to changes in concentration. To evaluate this assumption three-peak models for all four spectra were fitted and are shown overlaid in Figure 7.3. The vertical red lines represent the position of the peak, while the height of this red line is representative of the amplitude of the peak. Representation of the values for both widths of the Voigt peak shape are not present in the figure. It is clearly visible that alongside a prominent change in amplitude, all three peaks also change position with a change

in concentration, although quite subtle. A simple scaling of peaks or various concentrations would therefore be insufficient to resemble the spectra, even with models as simple as three peaks.

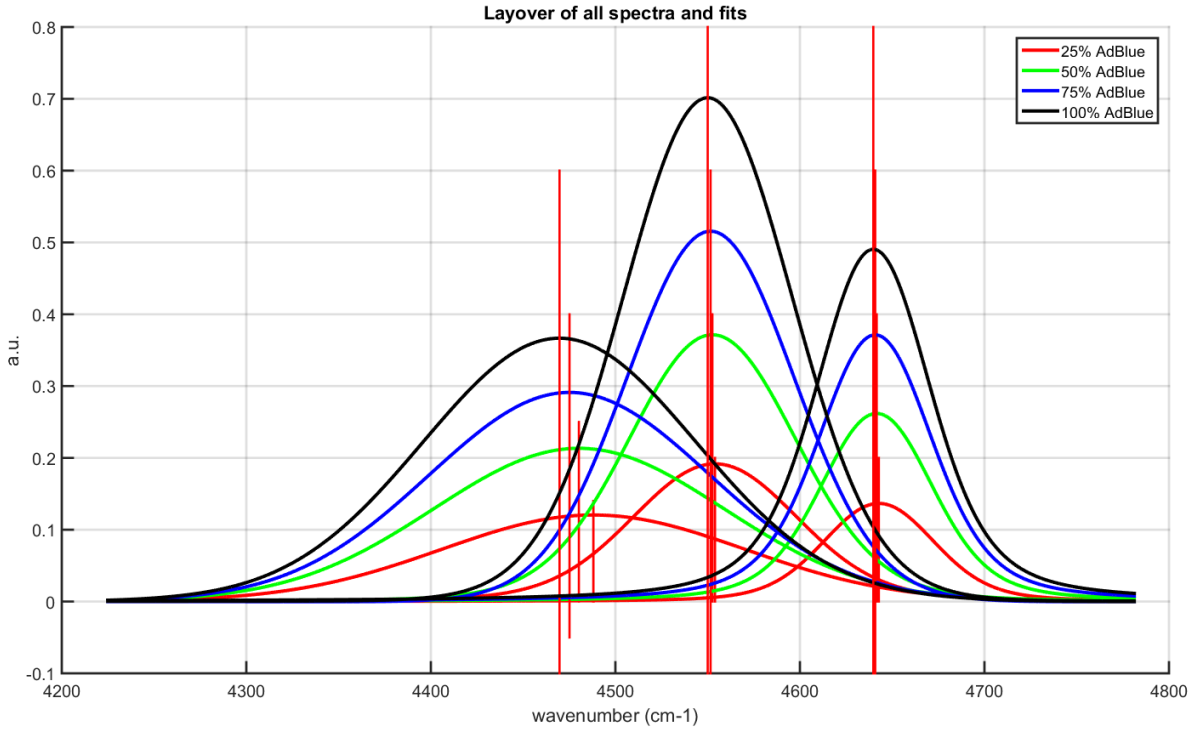

Figure 7.3 Overlay of all derived three-peak models for different AdBlue concentrations

All peaks shift to the lower wavenumbers with an increase in concentration, while the amount of shift varies. The same is true for the amplitude of the individual peaks. All peaks correlate with the increasing concentration, but differ in the strength of this correlation. These observation allow for deriving coarse regularities, that can be further clarified by plotting the changes in the four parameters with respect to the corresponding concentration as the only parameter varied for these measurements. Instead of absolute values, differences to the values for an AdBlue concentration of 100 % are used. These plots are shown in Figure 7.4.

When comparing the shift in position, the previous observation, that the left peak shifts the most, is confirmed, followed by the center peak and the right peak. In terms of amplitude, the center peak encounters the highest changes, followed by the left and right peak. The Lorentz width of the peaks shows a different behavior. The left peak's Lorentz width stays constant, while the Lorentz width decreases with rising concentration of AdBlue for the center peak. Opposite behavior is see for the right peak. With regards to the Gaussian width, the left and right peaks see a decrease in width, while the center peak encounters an increase. While several regularities were identified, there are two irregularities. In the Lorentzian width, the value for a concentration of 75 % seems to divert from the expected behavior. Similarly, a diversion from the expected regularity can be observed for the Gaussian width of the same spectrum. If additional parameters (i.e. temperature) were varied alongside concentration, similar regularities might be derivable from the fitted models. While there is no inherent necessity for

IHM models to show regularities for parameters, it is highly expected that recorded spectra behave according to certain regularities.

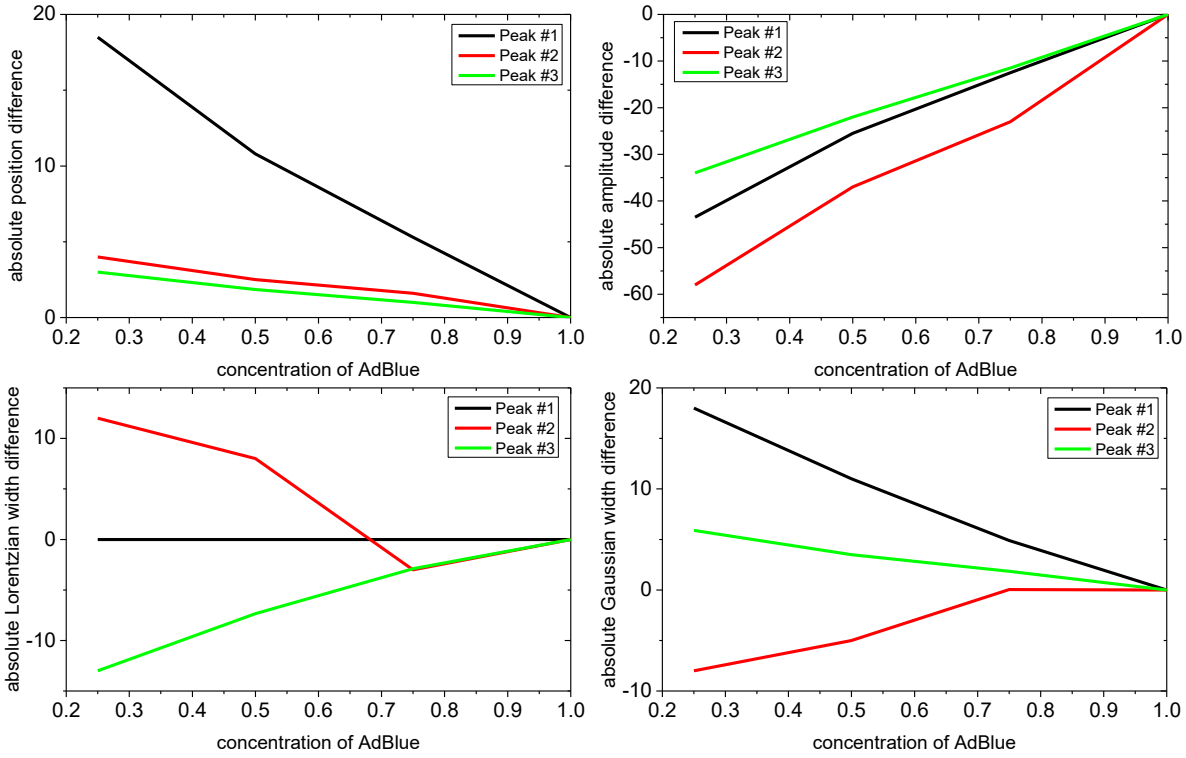

Figure 7.4 Comparison of changes in the four peak parameters with change in concentration (top left: position, top right: amplitude, bottom left: Lorentzian width, bottom right: Gaussian width)

Due to the small number of spectra available for this example, it not possible to derive full regularities according to which the four parameters of each peak change with a change in concentration. For proper determination of the regularities, an extensive dataset is required. One option to obtain such large data sets, as opposed to record spectra for hundreds of parameter combinations, is to rely on other spectral models, which currently represent the state-of-the-art for spectroscopic modelling. In the case of SCLAS (and TDLAS as well) and for gases, this is HITRAN. The benefit of using IHM models for gases with vast line datasets in HITRAN (such as methane) as opposed to line-by-line calculations, is the significant simplification of the model (if processes under investigation permit this simplification).

Given the broad spectral coverage of SCLAS, minor discrepancies between the complex, but computationally expensive HITRAN model (thousands of absorption lines) and a simplified model with between 10 and 20 peak features might be justified given an increase in calculation and processing speed. Furthermore, by deriving an IHM model of the spectrum, it can be investigated if several separate absorption lines can be approximated by a single absorption line (as opposed to having absorption features consisting of multiple and narrowly spaced, but partly very weak absorption lines). These rather weak absorption lines mostly influence the

shape of the outer lobes of a stronger absorption feature, which becomes, especially in high-pressure environments less pronounced due to pressure broadening.

Overall, IHM modelling is a very viable option for modelling AdBlue spectra and spectra of comparable liquids. While the derivation of a conclusive model for the peak parameters was not successful with only four concentrations evaluated, it is valid to assume, that increasing the number of samples will provide the required data for stable model determination and calibration. Furthermore, with only four measurements available, several regularities were already determined, including peak shifting and peak broadening caused by the AdBlue concentration.

7.3 IHM Modelling for Absorption Spectra of Methane

To explore the possibilities of IHM modelling in the context of gas-based combustion diagnostics, the following section will cover the applicability of IHM for gas measurements of methane under various conditions. To simplify the process and achieve comparability with HITRAN-based spectroscopic modelling, spectra simulated using HITRAN were used. Spectra of methane diluted by air in the spectral range from 6030 cm^{-1} to 6120 cm^{-1} were simulated (in the spectral absorbance domain with a Gaussian instrument function of width 0.15 cm^{-1} to resemble the optical resolution of SCLAS) for the following combinations of pressures and mole fraction:

Pressures: 0.5 bar, 1 bar, 3.5 bar, 4.5 bar, … , 13.5 bar, 14.5 bar

Mole fraction: 0.1, 0.2, 0.3, 0.4, 0.5 (10 %, 20 %, … , 50 %)

Temperature variations were omitted for this test to reduce the complexity of the required modelling of the peak parameters (depending on only 2 variables, instead of 3 variables). Given that HITRAN is focused in its application on temperatures relevant for atmospheric research, the error in the spectrum and modelling artifacts increase with temperature. While HITEMP provides line data for certain species at high temperatures, its vast amount of absorption line data provides additional challenges to simulating spectra. Given that the applicability of IHM is under investigation for a gas diagnostics use case, viable conclusion can also be drawn if temperature is omitted from influencing the spectra under investigation. The basic ideas and procedures will nevertheless be applicable in the case of temperature as well.

When evaluating the performance of a methane IHM model for combustion research, several characteristics will be at the focus of the investigation:

- Agreement between the spectra simulated from HITRAN and the IHM-based spectra regarding shape and peak / line parameters
- Internal consistency of the IHM model (model behavior / peak behavior consistent with spectroscopic data regarding line data, pressure shifts and other spectroscopic effects)

- Possibility to model peak parameters with separate models (*inner models*, as described before in Chapter 7.1) as opposed to using *Look-Up Tables*
- Model behavior for high-pressure environments, since most combustion takes place at elevated pressures (for example internal combustion engines)

While the agreement can be easily investigated by determining the residual between both models, the internal consistency of IHM requires a more detailed approach for comparison. Due to the fact, that each peak is modelled as a Voigt line shape profile with four parameters, internal consistency will be judged on the behavior of the individual peak parameters (for example their change with pressure and quantity). This behavior can also be used to investigate the possibilities to model peak parameters by *inner models*. When fitting commonly used functions (i.e. polynomials) to the traces of peak parameter values, the agreement between trace and model can be quantified. Furthermore, the derived *inner models* can be extrapolated to well characterized conditions, for example to the vacuum wavenumber of the transition. These values can than be compared to tabulated values from HITRAN and thereby be used as an indicator for the quality of the *inner models*.

In general, each IHM model (for individual spectra) in this investigation will consist of exactly 10 peaks, freely fitted for each spectrum. For specific cases, this number was increased to 30 peaks to study the influence of the peak number. An example of the comparison between HITRAN-based simulation and IHM model is shown in Figure 7.5 (for a pressure of 14.5 bar and a mole fraction of 10 % methane in air). Due to the limited number of peaks (10 peaks), several deviations between the simulated HITRAN spectrum and the IHM spectrum can be observed. These deviations are mainly limited to parts of the spectrum, which consist mainly of weaker absorption lines. Around 6040 cm^{-1} several weaker absorption lines are located between stronger lines and form a shape that is not modelled by IHM. Instead, the peak towards the lower wavenumbers is shifted and broadened to provide the least square error for this section of the spectrum. Similar effects can be observed around 6062 cm^{-1}, 6100 cm^{-1} and 6110 cm^{-1}, though less pronounced. Neighboring peaks in these case did not shift since the resulting squared error would have been larger overall. This example shows how well an IHM model can agree with the corresponding spectra, but at the same time a fundamental limitation of the approach. Being restricted to specific line shapes and an often fixed and limited number of peaks can lead to insufficient approximating of smaller or more closely spaced peaks. While the chosen line shape is similar to the one used for the HITRAN simulations (Voigt peak), the limitation in the number of peaks is due to the intention of the IHM model. By increasing the number of peaks, the residual could be further decreased. But with increasing number of peaks, the computational cost of calculating spectra would increase as well. The worst-case scenario when compared to HITRAN, would be to fit as many peaks as there are absorption lines in the HITRAN spectrum. On one hand, this would result in identical cost for calculating spectra. On the other hand, this would likely be impossible if those lines were fitted at ambient pressure or higher, given that absorption lines are already broadened significantly at these pressures. HITRAN uses spectra at almost vacuum pressure and theoretical calculations to identify

individual transitions and characterize their behavior, extrapolated from very low pressures to ambient and higher (introducing errors). The effects of such fitting inaccuracies are largely outweighed by the increase in calculation speed and model simplicity (while still providing sufficient spectra).

One option to counter the effects of a limited number of peaks during fitting would be to implement a weighting scheme, which increases the weight of sections of the spectra with higher spectral absorbance while reducing the influence of sections of low spectral absorbance (weaker absorption lines).

The above discussed effects will be significantly more present in the signals, if the pressure is reduced below ambient conditions, since all lines display narrower line shapes and smaller lines, positioned to the side of stronger lines, will influence the peak placement as they start to appear as separate absorption lines. A spectrum at 0.5 bar comparing HITRAN simulation and IHM model is shown in Figure 7.6. A significant narrowing of the peaks is visible alongside a significant increase in deviation. When looking more closely at the peak around 6057 cm^{-1} the described behavior is visible (see inset in Figure 7.6). Due to ta small, but spectrally separated absorption line towards the higher wavenumbers, the peak is shifted in that direction by the fitting algorithm and placed almost between the two lines. While this reduces the overall error sum (as it is the aim of the fitting algorithm), it introduces a large deviation from the simulated spectrum in a spectral section of less importance. The shape of the deviation supports the assumptions of a position-induced error given its highly asymmetrical form (positive residual on one side, a negative residual on the other side of the peak). A peak width-induced error on the other hand would be visible as a symmetrical “W”-like shape.

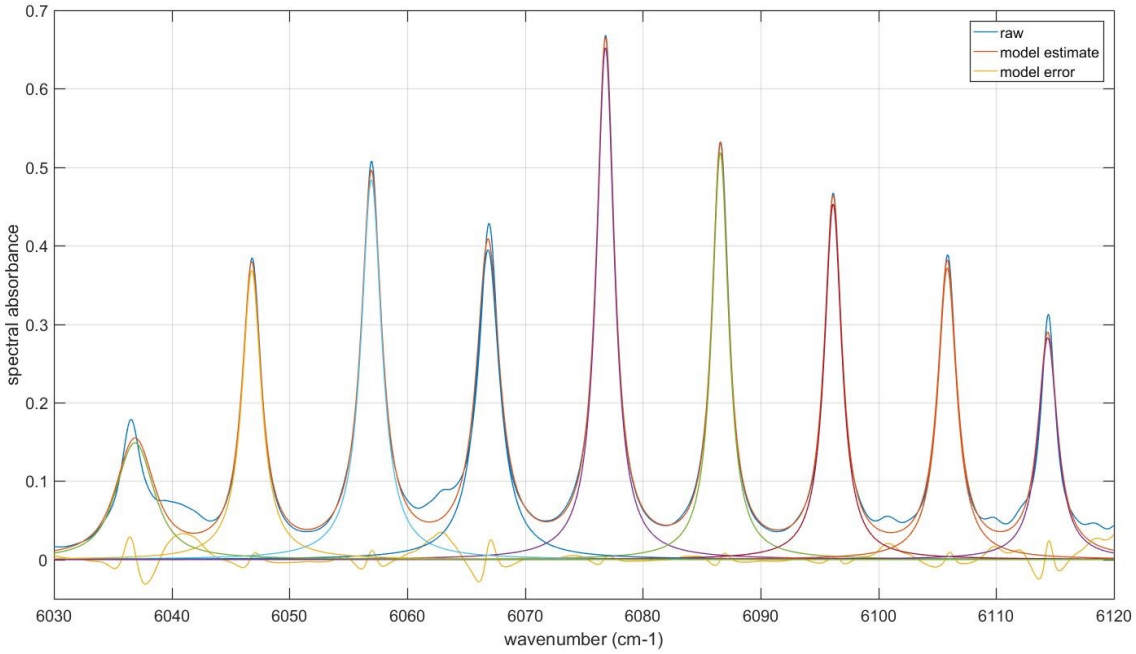

Figure 7.5 Methane IHM modell containing 10 peaks for 14.5 bar, 300 K and 10 % methane (“raw” refers to the HITRAN simulation)

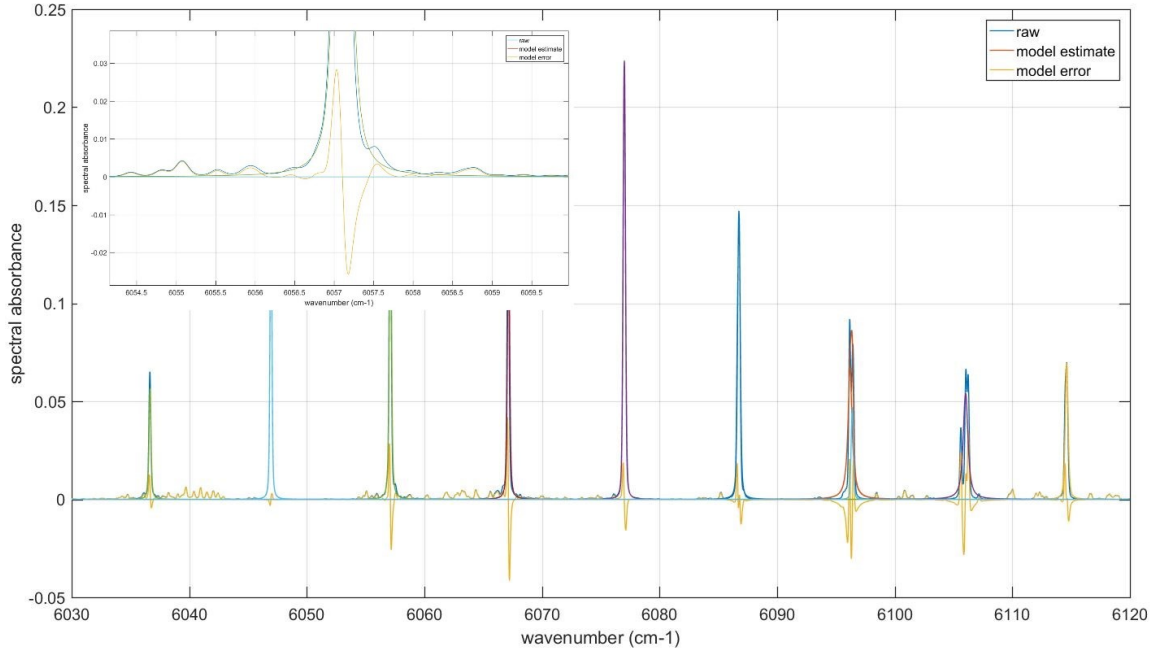

Figure 7.6 Methane IHM modell containing 10 peaks for 0.5 bar, 300 K and 10 % methane ("raw" refers to the HITRAN simulation)

Given the previously described effects, a suitable solution would include increasing the number of peaks per model, since this would allow the optimization algorithm to place individual peaks resembling closely spaced absorption lines. To investigate this option, a simulated spectrum of 10 % methane at a pressure of 7.5 bar was modelled by IHM once with 10 peaks and separately with 30 peaks. The results are shown in the Figure 7.7 and Figure 7.8 with detailed views of a single peak in Figure 7.9.

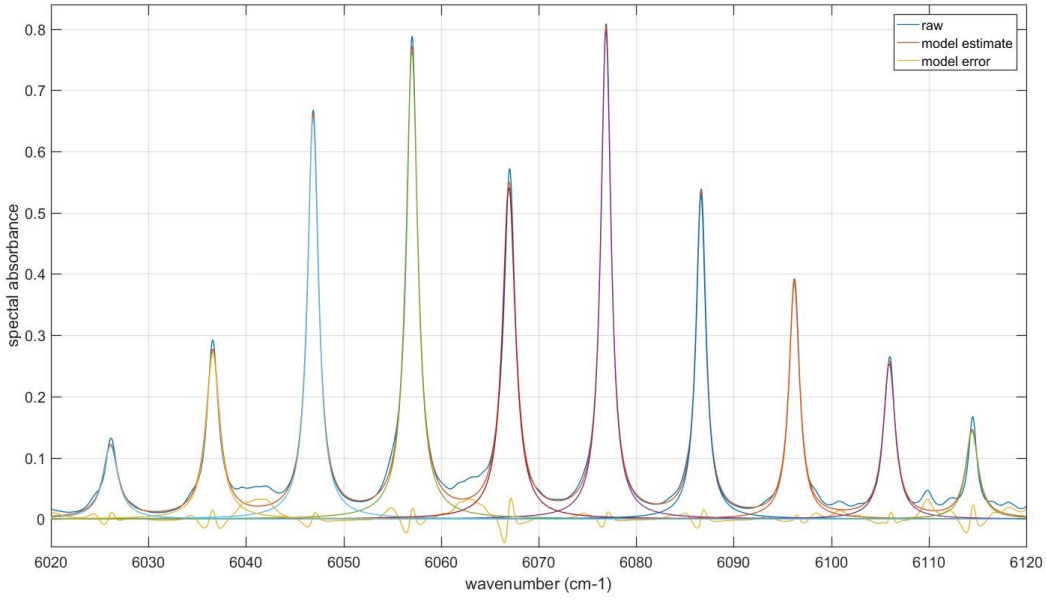

Figure 7.7 Comparison of influence of number of peaks on model approximation quality (10 peaks, 10 % methane, 7.5 bar, 300 K)
("raw" refers to the HITRAN simulation)

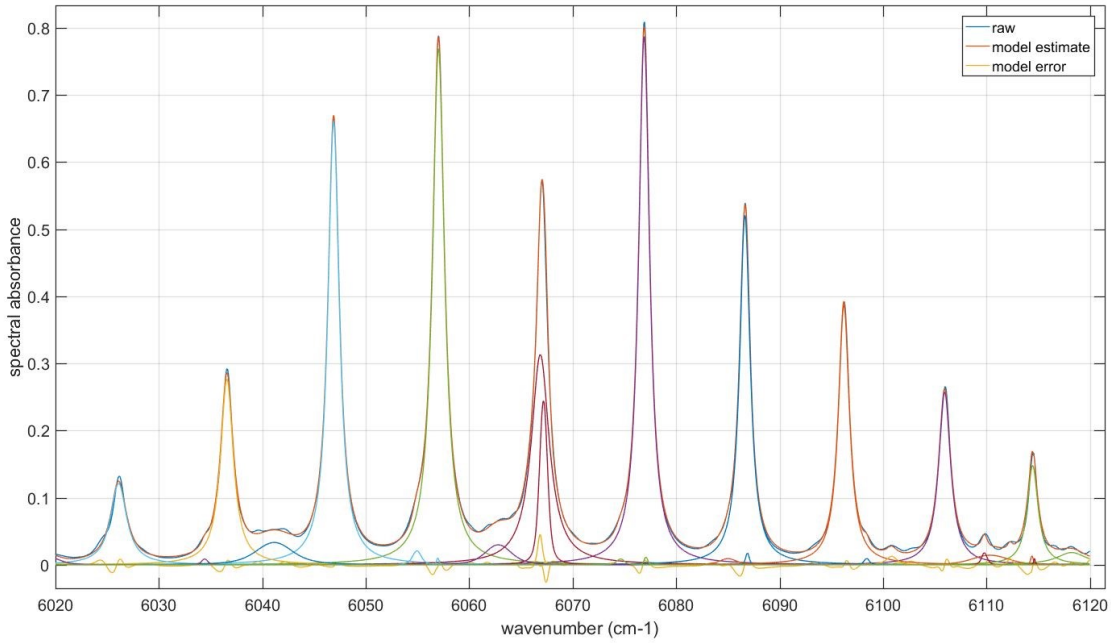

Figure 7.8 Comparison of influence of number of peaks on model approximation quality (30 peaks, 10 % methane, 7.5 bar, 300 K) ("raw" refers to the HITRAN simulation)

The model with 10 peaks is not able to adequately resemble the absorption feature consisting of multiple absorption lines blended together. The model with 30 peaks on the other hand places multiple peaks in close vicinity to better resemble the shape of overlapping of absorption lines. Furthermore, it is able to also recreate weaker absorption lines in-between stronger absorption features. Due to the increase in peak numbers, this model required significantly more time to optimize and requires three times the computation time to calculate the Voigt line shapes for an individual spectrum during fitting to measured data.

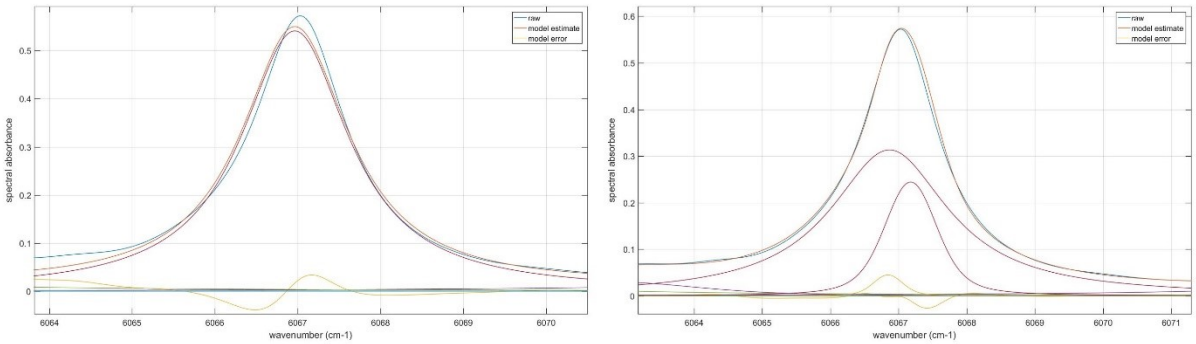

Figure 7.9 Comparison of influence of number of peaks on a single peak (left: 10 peaks in modell, right: 30 peaks in model)

To evaluate the performance of IHM models regarding internal consistency and the possibility to resemble peak parameter behavior by *inner models*, the optimized IHM models with 10 peaks will be utilized. While this does not provide ideal results regarding the residual, it allows for the investigation of the performance of IHM under sub-optimal conditions. For the peaks #3 and #5 (from the left) in Figure 7.5, the changes in the peak parameters with varying pressures

will be discussed first, followed by the changes in parameter values with combined changes in pressure and quantity. Since the applications of IHM are aimed at high-pressure processes, the pressures will range from 3.5 bar to 14.5 bar (since lower pressure show fitting artifacts as described previously). The derived regularities (*inner models*) for the peak parameters will nevertheless be extrapolated to lower pressures and checked for consistency down to vacuum.

The peak positions of peak #3, as plotted in Figure 7.10, show a very good agreement / consistency with an unconstrained 3rd order polynomial (as the *inner model*) fitted to the determined spectral positions. As an indicator for the fit quality, R^2 will be used. When the fitted polynomial is extended towards vacuum, the *vacuum wavenumber* of this peak can be determined. This quantity can be directly compared to HITRAN, since each transition is tracked in HITRAN by its vacuum wavenumber. For a comparison with the IHM peak position, a representative vacuum wavenumber for the various overlapping absorption lines of peak #3 is calculated by a weighted average of all absorption lines in the vicinity of the peak according to their absorption strength. All absorption lines with an absorption strength of $S \geq 1 \cdot 10^{-23}\ cm^{-1}/(molecule \cdot cm^{-2})$ are included in this average. The vacuum wavenumber determined by the IHM model agrees very well with the HITRAN vacuum wavenumber with an absolute deviation of 0.0062 cm^{-1} (relative error: 0.0001 %).

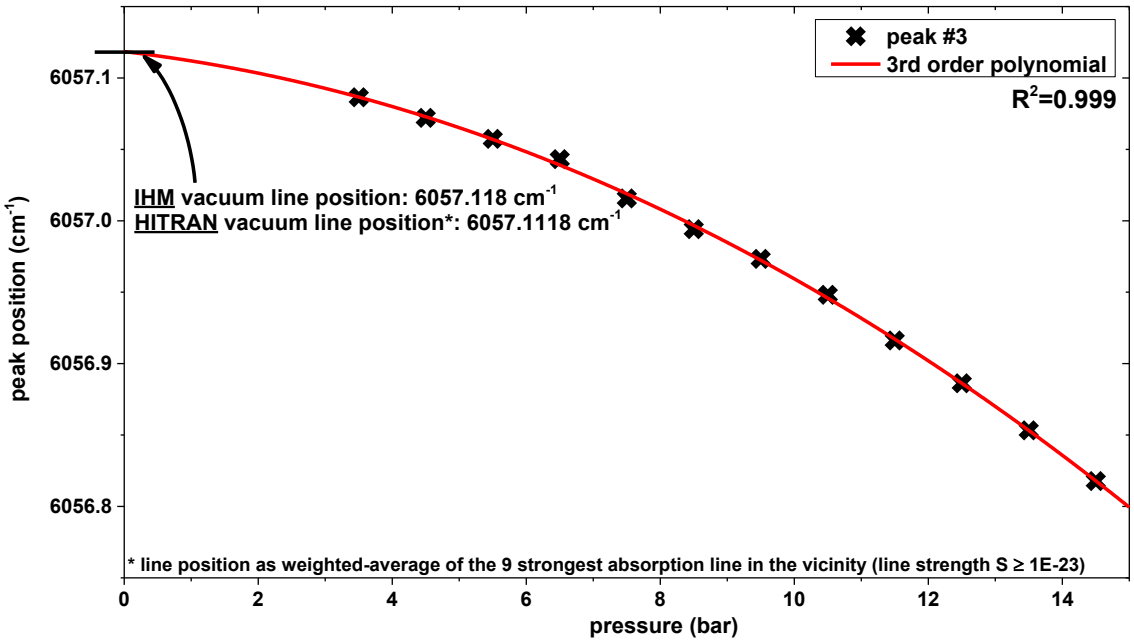

Figure 7.10 Peak positions of peak #3, fitted with unconstrained 3rd order polynomial

When deriving *inner models* for the peak height and Lorentzian peak width (see Figure 7.11), an unconstrained 3rd-order polynomial provided good agreement. The peak height and Lorentzian peak width both show a fitted value of zero for vacuum pressure. The Gaussian peak width was always set to zero by the fitting algorithm during model optimization, which is consistent with the described behavior of absorption lines in Chapter 2.2.

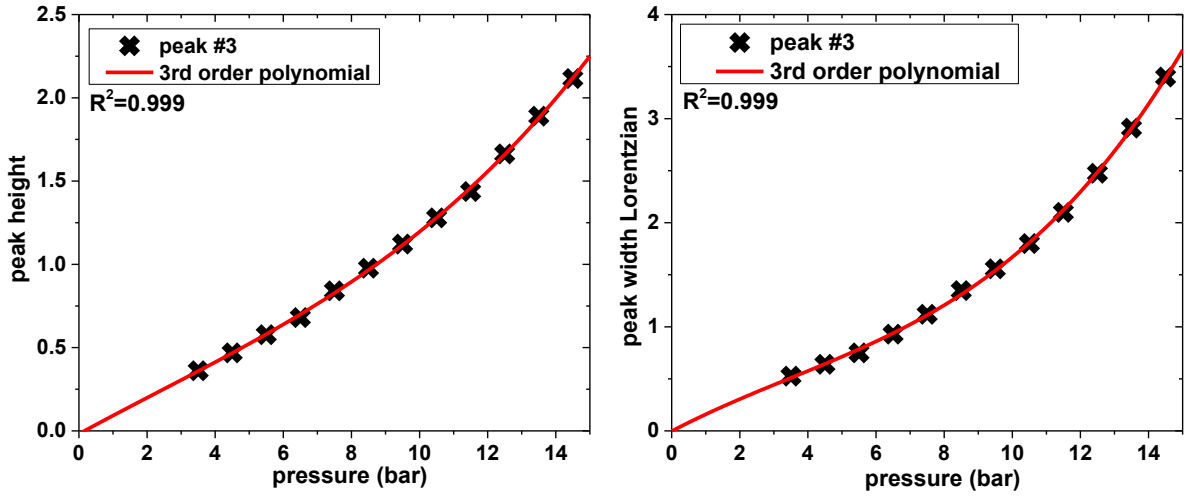

Figure 7.11 Peak height and peak width of peak #3, fitted with unconstrained 3rd order polynomial

The results of the *inner model* of peak #5 are shown in Figure 7.12 and Figure 7.13 accordingly. Differing from the previous modelling using 3rd-order polynomials, in this case a 1st-order polynomial was sufficient to represent the peak height and Lorentzian peak width. The required model for a specific peak and parameter depends on the influence of neighboring absorption features.

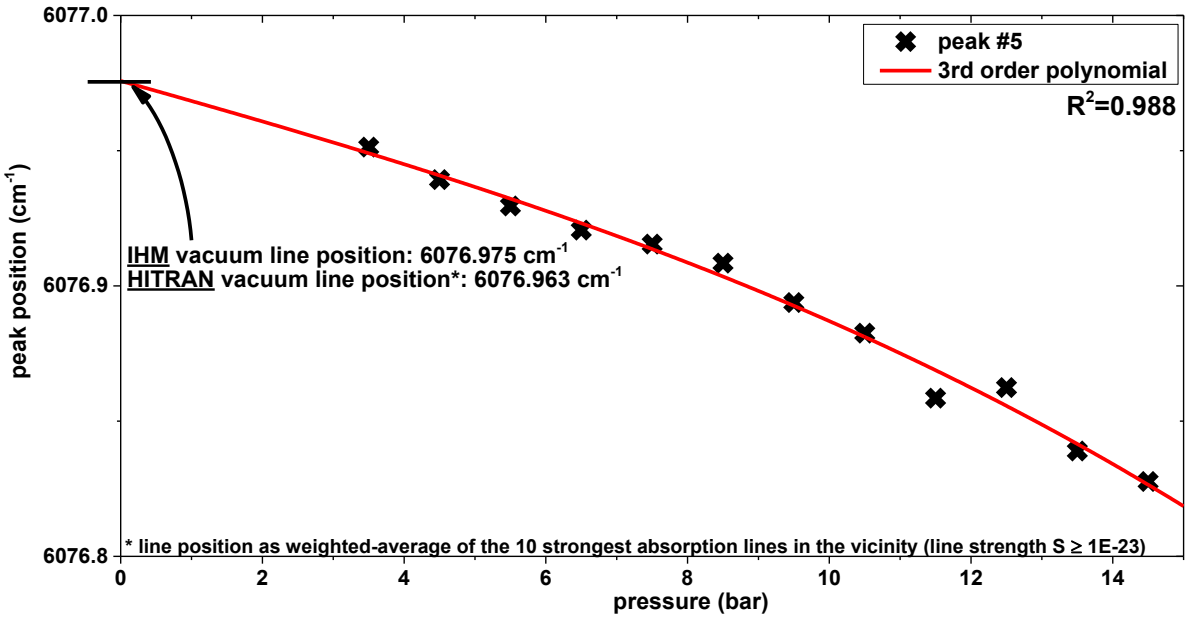

Figure 7.12 Peak positions of peak #5, fitted with unconstrained 3rd order polynomial

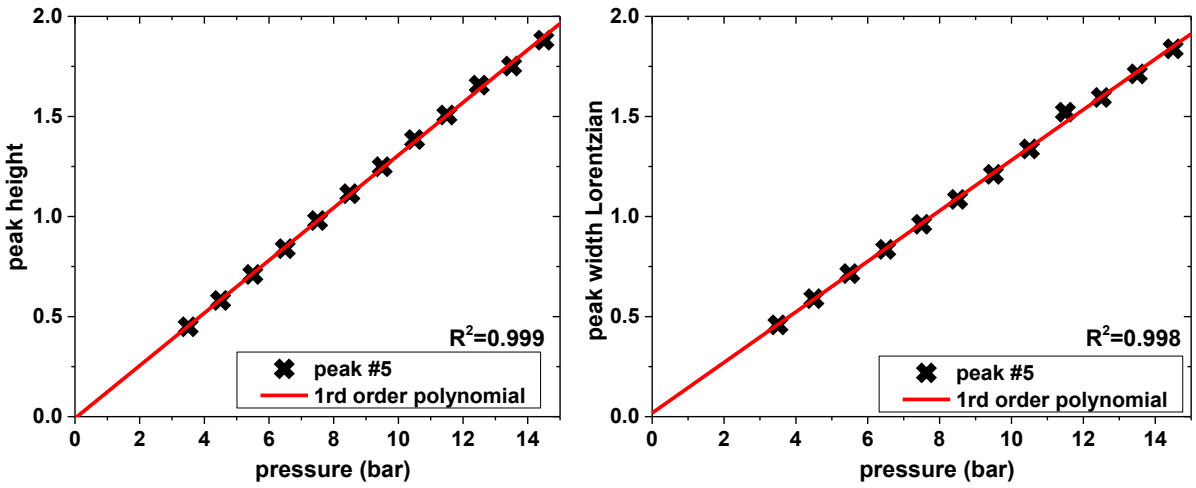

Figure 7.13 Peak positions of peak #5, fitted with unconstrained 1st order polynomial

To investigate internal modelling for combined parameters pressure and quantity, the values for the height of peak #6 is shown in Figure 7.14 depending on pressure and quantity. The resulting continuous and smooth shape can be approximated with a multitude of suitable mathematical function (i.e. combination of polynomials or NURBS, Non-Uniform Rational B-Spline, as used in CAD modelling) to serve as the *inner model* for the peak height.

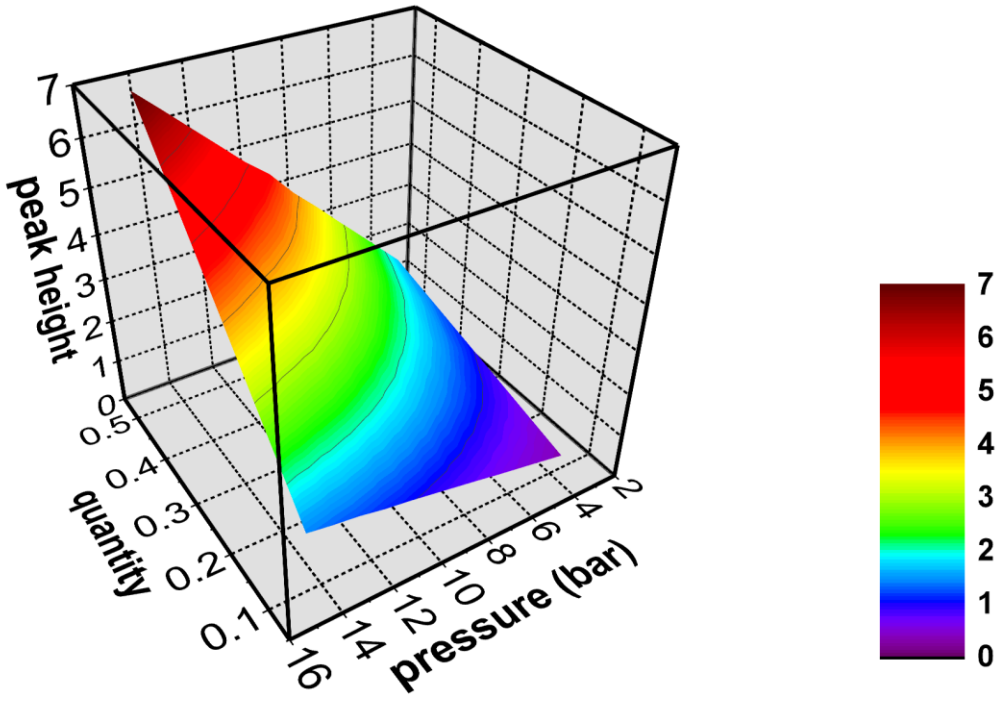

Figure 7.14 Peak height of peak #6 for varying pressure and quantity

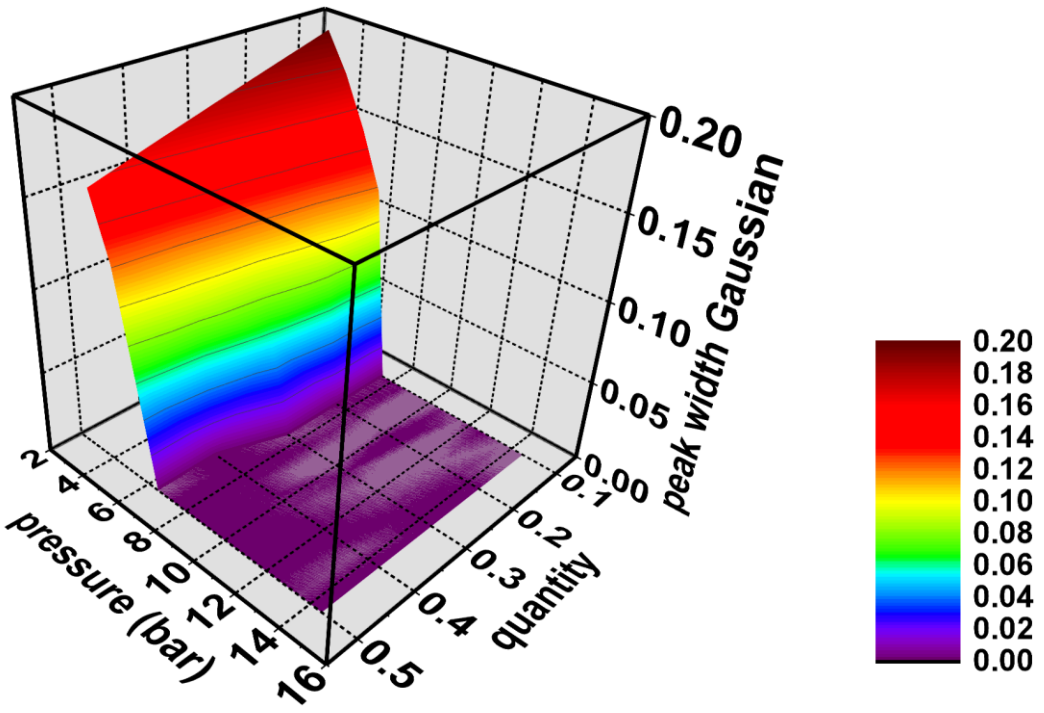

Figure 7.15 Gaussian peak width of peak #6 for varying pressure and quantity

While the Gaussian component of the peak width for peaks #3 and #5 was set to zero by the fitting algorithm, peak #6 behaves differently. As shown in Figure 7.15, with increasing pressure, the Gaussian peak width component is continuously reduced until it reaches zero around 7 bar (for all mole fractions).

Overall, IHM proved to be a valuable tool in terms of advanced spectral modelling. IHM showed its potential to accurately model spectroscopic behavior, especially by identifying the vacuum wavenumbers correctly, while reducing complexity and computational cost significantly. Utilizing IHM in broadband fitting algorithms will be a valuable asset for spectroscopic measurements and applications, as well as research and development in the field of combustion.

8 Summary and Outlook

During recent years, instrumentation and sensors play a more significant role than ever. Due to new trends in industry and society, sensor-enabled systems are present in almost all industrial processes. Alongside this demand for wide-spread sensor systems, the need for highly advanced systems has increased as well. Given stricter emissions regulations and a need for better process control in the chemical industry, in-situ diagnostic systems are essential for the development in future years. Especially optical sensors are commonly needed, since they provide opportunities for interference-free measurements. If such optical systems were able to provide complete multi-scalar data sets, covering species concentrations, pressure and temperature, new insights in to the effects and dependencies within chemical process could be gained.

Supercontinuum Laser Broadband Absorption Spectroscopy (SCLAS) is a unique diagnostic technique based on novel supercontinuum laser light sources (SCLs). Due to the broad spectral coverage and the inherent high temporal resolution of these SCLs, SCLAS is a promising candidate for providing complete sets of process parameters. Due to its all-fiber approach, external disturbances, such as soot and dust, are not interfering with measurements. Furthermore, given its ability to recorded broadband spectra covering hundreds of wavenumbers, SCLAS offers unique diagnostic capabilities for high-pressure environments, where narrowband systems are limited by their spectral coverage due to extensive line broadening. Despite its rather early stage of development, SCLAS can rely on advanced light sources, which are being constantly developed further to improve in performance as well as spectral coverage.

To evaluate the capabilities of SCLAS and its performance, several experiments were performed to characterize the novel light source as one of the key components of a SCLAS system. Given its pulsed behavior, performance indicators regarding stability and repeatability, as well as spectral content and repetition rate needed to be quantified to provide a basis for further development of the diagnostic system. With the knowledge regarding SCLs, challenges for post-processing the recorded data were identified and individually addressed, either by adapting the system to unique situations or by developing a fundamentally different approach to post-processing of broadband spectra. Aside from the extensive spectral coverage, the combination of SCL, specialty fibers for dispersion and the high-speed detection circuitry required the development of system specific instrument functions, which would allow proper spectral simulations. Such spectral simulations are an integral part of data processing in fitting algorithms. Furthermore, in addition to adapting the standard absorption spectroscopic models based on HITRAN to SCLAS, it was necessary to develop alternative models to address both the potential as well as the challenges of SCLAS.

To validate and evaluate the performance of the newly developed system, several experiments were performed including gas absorption cell measurements and in-flame validation measurements using a Wolfhard-Parker laminar burner (WHP). In both cases, good agreement

with secondary sensors could be reached proving the capabilities of SCLAS regarding accuracy and precision. In the case of the WHP burner temperatures ranging from ambient up to 1400 K were measured in combination with methane concentrations from detection limits as low as 2 % to concentrations as high as 85 %. Aside from this experimental validation, several innovations in the algorithms for data post-processing allowed for a theoretical determination of the expected uncertainties from measurements.

To further test SCLAS for combustion research, measurements were performed in transient conditions under variations of pressure, temperature and gas composition, before applying SCLAS to an engine test bed under motored and fired operation. During these tests, SCLAS proved to be a reliable and very capable diagnostic system, specifically for high-pressure environments and multi-species diagnostics. While its all-fiber approach simplified the application at the engine test bed in terms of noise and vibrations as well as isolation from electrical noise, beam steering and fiber-coupling, as required for the high-speed photo detector created new challenges to overcome.

Given its novelty and its challenges, several opportunities were discovered to utilize SCLAS and broadband diagnostic system in a new diagnostic approach. To counter the computational expenses of broadband spectral simulation, alternatives were investigated including Indirect Hard Modelling (IHM). Especially this technique was found to be very promising for applications in broadband systems in general and SCLAS in particular. While the IHM modeling approach relies on so-called gray (-box) models without detailed knowledge of the inner effects of molecules and the resulting spectra, it was proven, that IHM can significantly reduce the required computation for spectral models, while providing similar simulation quality. By comparing the performance of IHM models to HITRAN-based spectral simulations of methane under various conditions, it was shown, that the calculated spectra resemble the HITRAN simulations closely, while only relying on a significantly reduced number of absorption features for modelling. Additionally, it was discovered that an IHM model can be further improved by taking advantage of regularities between the peak parameters of the model (so called *inner models*). Beyond the simplification of spectra calculations and simulations, these advanced IHM models utilizing *inner models* allow for the derivation of spectroscopic models for non-discrete absorption spectra, which are common for liquids and complex gas molecules (such as propane). This was preliminarily tested by applying IHM modelling to AdBlue absorption spectra. In this test case, certain regularities regarding peak positions and peak widths were discovered.

Outlook and Future Work

Aside from further improvements regarding sensitivity and accuracy, the development of SCLAS in the future needs to address three key issues:

- Due to the pumping scheme of the SCL, the emitted pulses vary in spectral content, requiring averaging of recorded pulses. This problem can be addressed from two different angles: Changing the pumping scheme or changing the PCF within the SCL.

- Given the high pulse repetition rates of an SCL, the current data acquisition system cannot provide continuous data acquisition. To fully utilize SCLAS diagnostic system, continuous recording of spectra is beneficial. Options to achieve this include utilization of RF hardware and *on-thy-fly* averaging on *FPGAs* as opposed to averaging after recording.
- Advanced spectral models allow SCLAS to utilize its resources more efficiently. Most molecules with discrete absorption spectra only experience significant broadening at high pressures, while several combustions relevant species do not have discrete spectra under any condition. In both cases, the required optical resolution is reduced, allowing an SCLAS system to be reconfigured with reduced dispersion and increased pulse repetition rate. This will lead to increased time resolution or reduced noise levels. Furthermore, the calculation of spectra will be become computationally easier.
- Extending SCLAS to completely new fields of application by taking advantage of the unique combination of pulsed broadband light source and fiber-based components. Combining SCLAS and interferometric LIDAR (light detection and ranging) with sparse data tomography [9] can create a diagnostic system that is capable of sensing the shape of its surroundings in combination with the distribution of gases around it.
- Extending SCL light sources into the mid-infrared reagion (MIR) [140] can be achieved by using matched PCFs as well as suitable pump lasers. Nevertheless, other components of an all-fiber SCLAS system cannot be easily extended to the MIR. Limitations in the transmission of fibers in combination with insufficient high-speed MIR photo detectors require further development, or even a changed approach altogether to take advantage of the MIR absorption bands.

Aside from the utilization of SCLs in absorption spectroscopy, these sources offers sufficient power and spectral coverage for applications such as Raman spectroscopy or LIF (laser induced fluorescence). When combining SCLAS with emission-based techniques, the added information can provide additional information for the system under investigation. This combination becomes especially promising, if the SCL is used simultaneously for emission-based and absorption-based techniques.

Bibliography

[1] Sullivan M 2017 Sensors for the Internet of Things (IOT): Global Markets *Market Research Reports* https://www.bccresearch.com/market-research/information-technology/sensors-internet-of-things-markets-reports-ift130a.html
[2] Gaurav S G 2017 Fiber Optic Sensors: Global Markets *Market Research Reports* https://www.bccresearch.com/market-research/photonics/fiber-optic-sensors-markets-report-pho010b.html
[3] Dobre M 2017 ATLAS Detector Upgrade Prospects *J. Phys.: Conf. Ser.* **798** 12205
[4] Garrido-Cardenas J, Garcia-Maroto F, Alvarez-Bermejo J and Manzano-Agugliaro F 2017 DNA Sequencing Sensors: An Overview *Sensors* **17** 588
[5] LIGO Scientific Collaboration 2016 Observation of Gravitational Waves from a Binary Black Hole Merger *Phys. Rev. Lett.* **116** 688
[6] National Academy of Engineering NAE GRAND CHALLENGES FOR ENGINEERING http://www.engineeringchallenges.org
[7] Kühnreich B 2016 Absorptionsspektroskopie zur isotopenaufgelösten in situ Bestimmung von Wasserdampf in Eiswolken *Dissertation* Technische Universität Darmstadt, Germany
[8] Buchholz B 2014 Entwicklung, Primärvalidierung und Feldeinsatz neuartiger, kalibrierungsfreier Laser-Hygrometer für Forschungsflugzeuge *Doctoral* Technische Universität Darmstadt, Darmstadt
[9] Stritzke F 2017 Absorptionsspektrometrie zur zeitaufgelösten Untersuchung von Ammoniakverteilungen in Abgas *Dissertation* Technische Universität Darmstadt, Germany
[10] Lewander M, Guan Z G, Persson L, Olsson A and Svanberg S 2008 Food monitoring based on diode laser gas spectroscopy *Appl. Phys. B* **93** 619–25
[11] Lewander M, Lundin P, Svensson T, Svanberg S and Olsson A 2011 Non-intrusive Measurements of Headspace Gas Composition in Liquid Food Packages Made of Translucent Materials *Packag. Technol. Sci.* **24** 271–80
[12] Cocola L, Allermann H, Fedel M, Sønderby S, Tondello G, Bardenstein A and Poletto L 2016 Validation of an in-line non-destructive headspace oxygen sensor *Food Packaging and Shelf Life* **9** 38–44
[13] Cocola L, Fedel M, Poletto L and Tondello G 2015 Laser spectroscopy for totally non-intrusive detection of oxygen in modified atmosphere food packages *Appl. Phys. B* **119** 37–44
[14] Persson L, Andersson M, Cassel-Engquist M, Svanberg K and Svanberg S 2007 Gas monitoring in human sinuses using tunable diode laser spectroscopy *Appl. Phys. B* **12** 54001

[15] Buchholz B, Böse N and Ebert V 2014 Absolute validation of a diode laser hygrometer via intercomparison with the German national primary water vapor standard *Applied Physics B: Lasers and Optics* **116** 1–17

[16] Wadsworth W J, Joly N, Knight J C, Birks T a, Biancalana F and St. Russell P J 2004 Supercontinuum and four-wave mixing with Q-switched pulses in endlessly single-mode photonic crystal fibres *Opt. Express* **12** 299

[17] Orofino T A and Unterleitner F C 1976 Optical fibers for dispersion in the time domain *Applied optics* **15** 1907–9

[18] Moon S and Kim D Y 2006 Ultra-high-speed optical coherence tomography with a stretched pulse supercontinuum source *Opt. Express* **14** 11575

[19] Bondu M, Marques M J, Moselund P M, Lall G, Bradu A and Podoleanu A 2018 Multispectral photoacoustic microscopy and optical coherence tomography using a single supercontinuum source *Photoacoustics* **9** 21–30

[20] Steiner F, Bange S, Vogelsang J and Lupton J M 2015 Spontaneous Fluctuations of Transition Dipole Moment Orientation in OLED Triplet Emitters *J. Phys. Chem. Lett.* **6** 999–1004

[21] Ringsted T, Ramsay J, Jespersen B M, Keiding S R and Engelsen S B 2017 Long wavelength near-infrared transmission spectroscopy of barley seeds using a supercontinuum laser: Prediction of mixed-linkage beta-glucan content *Analytica Chimica Acta* **986** 101–8

[22] Simms J M, An X, Brittelle M S, Ramesh V, Ghandhi J B and Sanders S T 2015 Simultaneous optimization method for absorption spectroscopy postprocessing *Applied optics* **54** 4403–10 (eng)

[23] Wagner S, Fisher B T, Fleming J W and Ebert V 2009 TDLAS-based in situ measurement of absolute acetylene concentrations in laminar 2D diffusion flames *Proceedings of the Combustion Institute* **32** 839–46

[24] Stritzke F, Diemel O and Wagner S 2015 TDLAS-based NH3 mole fraction measurement for exhaust diagnostics during selective catalytic reduction using a fiber-coupled 2.2-μm DFB diode laser *Applied Physics B* **119** 143–52

[25] Bürkle S, Biondo L, Ding C-P, Honza R, Ebert V, Böhm B and Wagner S 2018 In-Cylinder Temperature Measurements in a Motored IC Engine using TDLAS *Flow Turbulence Combust* **101** 139–59

[26] Bürkle S, Dreizler A, Ebert V and Wagner S 2018 Experimental comparison of a 2D laminar diffusion flame under oxy-fuel and air atmosphere *Fuel* **212** 302–8

[27] Ma L, Li X, Sanders S T, Caswell A W, Roy S, Plemmons D H and Gord J R 2013 50-kHz-rate 2D imaging of temperature and H_2O concentration at the exhaust plane of a J85 engine using hyperspectral tomography *Opt. Express* **21** 1152

[28] Goldenstein C S, Spearrin R M, Schultz I A, Jeffries J B and Hanson R K 2014 Wavelength-modulation spectroscopy near 1.4 μm for measurements of H 2 O and temperature in high-pressure and -temperature gases *Measurement Science and Technology* **25** 55101

[29] Rieker G B, Jeffries J B and Hanson R K 2009 Calibration-free wavelength-modulation spectroscopy for measurements of gas temperature and concentration in harsh environments *Applied optics* **48** 5546–60

[30] Rieker GB, Li H, Liu X, Liu JTC, Jeffries JB, Hanson RK, Allen MG, Wehe SD, Mulhall PA, Kindle HS, Kakuho A, Sholes KR, Matsuura T and Takatani S 2007 Rapid measurements of temperature and H2O concentration in IC engines with a spark plug-mounted diode laser sensor *Proceedings of the Combustion Institute* **31** 3041–9

[31] Rieker G B, Li H, Liu X, Jeffries J B, Hanson R K, Allen M G, Wehe S D, Mulhall P a and Kindle H S 2007 A diode laser sensor for rapid, sensitive measurements of gas temperature and water vapour concentration at high temperatures and pressures *Measurement Science and Technology* **18** 1195–204

[32] Li H, Rieker G B, Liu X, Jeffries J B and Hanson R K 2006 Extension of wavelength-modulation spectroscopy to large modulation depth for diode laser absorption measurements in high-pressure gases *Applied optics* **45** 1052

[33] Goldenstein C S, Spearrin RM, Jeffries J B and Hanson R K 2017 Infrared laser-absorption sensing for combustion gases *Progress in Energy and Combustion Science* **60** 132–76

[34] Stein B A, Jayaraman V, Jiang J Y, Cable A and Sanders S T 2012 Doppler-limited H2O and HF absorption spectroscopy by sweeping the 1,321–1,354 nm range at 55 kHz repetition rate using a single-mode MEMS-tunable VCSEL *Appl. Phys. B* **108** 721–5

[35] Rieker G B, Giorgetta F R, Swann W C, Kofler J, Zolot A M, Sinclair L C, Baumann E, Cromer C, Petron G, Sweeney C, Tans P P, Coddington I and Newbury N R 2014 Frequency-comb-based remote sensing of greenhouse gases over kilometer air paths *Optica* **1** 290

[36] Draper A D, Cole R K, Makowiecki A S, Mohr J, Zdanowicz A, Marchese A, Hoghooghi N and Rieker G B 2019 Broadband dual-frequency comb spectroscopy in a rapid compression machine *Optics Express* **27** 10814–25 (eng)

[37] Blume N G, Ebert V, Dreizler A and Wagner S 2016 Broadband fitting approach for the application of supercontinuum broadband laser absorption spectroscopy to combustion environments *Measurement Science and Technology* **27** 15501

[38] Rothman L S, Gordon I E, Babikov Y, Barbe A, Chris Benner D, Bernath P F, Birk M, Bizzocchi L, Boudon V, Brown L R, Campargue A, Chance K, Cohen E A, Coudert L H, Devi V M, Drouin B J, Fayt A, Flaud J-M, Gamache R R, Harrison J J, Hartmann J M, Hill C, Hodges J T, Jacquemart D, Jolly A, Lamouroux J, Le Roy, R. J., Li G, Long D A, Lyulin O M, Mackie C J, Massie S T, Mikhailenko S, Müller, H. S P, Naumenko O V, Nikitin A V, Orphal J, Perevalov V, Perrin A, Polovtseva E R, Richard C, Smith, M. a H, Starikova E, Sung K, Tashkun S, Tennyson J, Toon G C, Tyuterev V G and Wagner G 2013 The HITRAN2012 molecular spectroscopic database *Journal of Quantitative Spectroscopy and Radiative Transfer* **130** 4–50

[39] Cheng T, Zhang L, Xue X, Deng D, Suzuki T and Ohishi Y 2015 Broadband cascaded four-wave mixing and supercontinuum generation in a tellurite microstructured optical fiber pumped at 2 μm *Optics Express* **23** 4125

[40] Kedenburg S, Steinle T, Mörz F, Steinmann A and Giessen H 2015 High-power mid-infrared high repetition-rate supercontinuum source based on a chalcogenide step-index fiber *Opt. Lett.* **40** 2668

[41] Salem R, Jiang Z, Liu D, Pafchek R, Gardner D, Foy P, Saad M, Jenkins D, Cable A and Fendel P 2015 Mid-infrared supercontinuum generation spanning 18 octaves using step-index indium fluoride fiber pumped by a femtosecond fiber laser near 2 μm *Opt. Express* **23** 30592

[42] Dupont S, Qu Z, Kiwanuka S-S, Hooper L E, Knight J C, Keiding S R and Kaminski C F 2014 Ultra-high repetition rate absorption spectroscopy with low noise supercontinuum radiation generated in an all-normal dispersion fibre *Laser Physics Letters* **11** 75601

[43] Blume N G and Wagner S 2015 Novel time-of-flight fiber dispersion measurement technique using supercontinuum light sources and acousto-optical tunable filters *Applied optics* **54** 6406

[44] Emmert J, Blume N G, Dreizler A and Wagner S 2018 Data analysis and uncertainty estimation in supercontinuum laser absorption spectroscopy *Scientific reports* **in review**

[45] Blume N G and Wagner S 2015 Broadband supercontinuum laser absorption spectrometer for multiparameter gas phase combustion diagnostics *Optics letters* **40** 3141

[46] Hanson R K, Spearrin R M and Goldenstein C S 2016 *Spectroscopy and Optical Diagnostics for Gases* (Cham: Springer International Publishing)

[47] Demtröder W 2014 *Laser Spectroscopy 1* (Berlin, Heidelberg: Springer Berlin Heidelberg)

[48] Griffiths P R and Haseth J A de 2007 *Fourier transform infrared spectrometry* 2nd edn (Hoboken, N.J.: Wiley-Interscience; Chichester : John Wiley [distributor])

[49] Meschede D 2015 *Gerthsen Physik* (Berlin, Heidelberg: Springer Berlin Heidelberg)

[50] Rothman L S, Gordon I E, Barber R J, Dothe H, Gamache R R, Goldman A, Perevalov V I, Tashkun S a and Tennyson J 2010 HITEMP, the high-temperature molecular spectroscopic database *Journal of Quantitative Spectroscopy and Radiative Transfer* **111** 2139–50

[51] Jacquinet-Husson N, Crepeau L, Armante R, Boutammine C, Chédin A, Scott N A, Crevoisier C, Capelle V, Boone C, Poulet-Crovisier N, Barbe A, Campargue A, Chris Benner D, Benilan Y, Bézard B, Boudon V, Brown L R, Coudert L H, Coustenis A, Dana V, Devi V M, Fally S, Fayt A, Flaud J-M, Goldman A, Herman M, Harris G J, Jacquemart D, Jolly A, Kleiner I, Kleinböhl A, Kwabia-Tchana F,

Lavrentieva N, Lacome N, Xu L-H, Lyulin O M, Mandin J-Y, Maki A, Mikhailenko S, Miller C E, Mishina T, Moazzen-Ahmadi N, Müller HSP, Nikitin A, Orphal J, Perevalov V, Perrin a, Petkie D T, Predoi-Cross a, Rinsland C P, Remedios J J, Rotger M, Smith MaH, Sung K, Tashkun S, Tennyson J, Toth R A, Vandaele A-C and Vander Auwera J 2011 The 2009 edition of the GEISA spectroscopic database *Journal of Quantitative Spectroscopy and Radiative Transfer* **112** 2395–445

[52] Jacquinet-Husson N, Armante R, Scott N A, Chédin A, Crépeau L, Boutammine C, Bouhdaoui A, Crevoisier C, Capelle V, Boonne C, Poulet-Crovisier N, Barbe A, Chris Benner D, Boudon V, Brown L R, Buldyreva J, Campargue A, Coudert L H, Devi V M, Down M J, Drouin B J, Fayt A, Fittschen C, Flaud J-M, Gamache R R, Harrison J J, Hill C, Hodnebrog Ø, Hu S-M, Jacquemart D, Jolly A, Jiménez E, Lavrentieva N N, Liu A-W, Lodi L, Lyulin O M, Massie S T, Mikhailenko S, Müller HSP, Naumenko O V, Nikitin A, Nielsen C J, Orphal J, Perevalov V I, Perrin a, Polovtseva E, Predoi-Cross a, Rotger M, Ruth A A, Yu S S, Sung K, Tashkun S a, Tennyson J, Tyuterev VG, Vander Auwera J, Voronin B A and Makie A 2016 The 2015 edition of the GEISA spectroscopic database *Journal of Molecular Spectroscopy* **327** 31–72

[53] Pogány A, Klein A and Ebert V 2015 Measurement of water vapor line strengths in the 1.4–2.7 μm range by tunable diode laser absorption spectroscopy *Journal of Quantitative Spectroscopy and Radiative Transfer* **165** 108–22

[54] Goldenstein C S, Jeffries J B and Hanson R K 2013 Diode laser measurements of linestrength and temperature-dependent lineshape parameters of H2O-, CO2-, and N2-perturbed H2O transitions near 2474 and 2482nm *Journal of Quantitative Spectroscopy and Radiative Transfer* **130** 100–11

[55] Arroyo M P, Langlois S and Hanson R K 1994 Diode-laser absorption technique for simultaneous measurements of multiple gasdynamic parameters in high-speed flows containing water vapor *Appl. Opt.* **33** 3296

[56] Humlíček J 1979 An efficient method for evaluation of the complex probability function: The Voigt function and its derivatives *Journal of Quantitative Spectroscopy and Radiative Transfer* **21** 309–13

[57] Humlíček J 1982 Optimized computation of the voigt and complex probability functions *Journal of Quantitative Spectroscopy and Radiative Transfer* **27** 437–44

[58] Schreier F 2011 Optimized implementations of rational approximations for the Voigt and complex error function *Journal of Quantitative Spectroscopy and Radiative Transfer* **112** 1010–25

[59] Liu Y, Lin J, Huang G, Guo Y and Duan C 2001 Simple empirical analytical approximation to the Voigt profile *J. Opt. Soc. Am. B* **18** 666

[60] Letchworth K L and Benner D C 2007 Rapid and accurate calculation of the Voigt function *Journal of Quantitative Spectroscopy and Radiative Transfer* **107** 173–92

[61] Lether F G and Wenston P R 1991 The numerical computation of the Voigt function by a corrected midpoint quadrature rule for $(-\infty,\infty)$ *Journal of Computational and Applied Mathematics* **34** 75–92

[62] McLean A B, Mitchell CEJ and Swanston D M 1994 Implementation of an efficient analytical approximation to the Voigt function for photoemission lineshape analysis *Journal of Electron Spectroscopy and Related Phenomena* **69** 125–32

[63] Dicke R H 1953 The Effect of Collisions upon the Doppler Width of Spectral Lines *Phys. Rev.* **89** 472–3

[64] Galatry L 1961 Simultaneous Effect of Doppler and Foreign Gas Broadening on Spectral Lines *Phys. Rev.* **122** 1218–23

[65] Rautian S G and Sobel'man I I 1967 THE EFFECT OF COLLISIONS ON THE DOPPLER BROADENING OF SPECTRAL LINES *Sov. Phys. Usp.* **9** 701–16

[66] Berman P R 1972 Speed-dependent collisional width and shift parameters in spectral profiles *Journal of Quantitative Spectroscopy and Radiative Transfer* **12** 1331–42

[67] Pickett H M 1980 Effects of velocity averaging on the shapes of absorption lines *The Journal of Chemical Physics* **73** 6090–4

[68] Büning-Pfaue H 2003 Analysis of water in food by near infrared spectroscopy *Food Chemistry* **82** 107–15

[69] Bloomfield M, Andrews D, Loeffen P, Tombling C, York T and Matousek P 2013 Non-invasive identification of incoming raw pharmaceutical materials using Spatially Offset Raman Spectroscopy *Journal of Pharmaceutical and Biomedical Analysis* **76** 65–9

[70] Trygve Helgerud T, Segtnan V H, Wold J P, Ballance S, Knutsen S H, Rukke E O and Afseth N K 2012 Near-infrared Spectroscopy for Rapid Estimation of Dry Matter Content in Whole Unpeeled Potato Tubers *JFR* **1**

[71] Trygg J and Wold S 1998 PLS regression on wavelet compressed NIR spectra *Chemometrics and Intelligent Laboratory Systems* **42** 209–20

[72] Depczynski U, Ketter K, Stockler J, Molt K and Niemoller A 1997 Wavelet Methods in Chemometrics: Quantitative Spectrometric Multicomponent Analysis *15th IMACS World Congress on Scientific Computation, Modelling and Applied Mathematics* **1** 87–92

[73] Balabin R M, Safieva R Z and Lomakina E I 2010 Gasoline classification using near infrared (NIR) spectroscopy data: Comparison of multivariate techniques *Analytica Chimica Acta* **671** 27–35

[74] Adachi D, Katsumoto Y, Sato H and Ozaki Y 2002 Near-Infrared Spectroscopic Study of Interaction between Methyl Group and Water in Water—Methanol Mixtures *Appl Spectrosc* **56** 357–61

[75] Rinnan A, Andersson M, Ridder C and Engelsen S B Recursive weighted PLS (rPLS): an efficient and promising multivariatemethod for spectral variable selection in regression
[76] Alsmeyer F and Marquardt W 2004 Automatic Generation of Peak-Shaped Models *Applied Spectroscopy* **58** 986–94
[77] Emmert J 2016 Weiterentwicklung der Auswerte-Algorithmen für die SCLAS und deren Erprobung mittels Verbrennungsmessdaten *Master* Technische Universität Darmstadt, Darmstadt
[78] Gutés A, Céspedes F, Cartas R, Alegret S, del Valle M, Gutierrez JM and Muñoz R 2006 Multivariate calibration model from overlapping voltammetric signals employing wavelet neural networks *Chemometrics and Intelligent Laboratory Systems* **83** 169–79
[79] Moreno-Barón L, Cartas R, Merkoçi A, Alegret S, del Valle M, Leija L, Hernandez PR and Muñoz R 2006 Application of the wavelet transform coupled with artificial neural networks for quantification purposes in a voltammetric electronic tongue *Sensors and Actuators B: Chemical* **113** 487–99
[80] Pati YC and Krishnaprasad PS 1993 Analysis and synthesis of feedforward neural networks using discrete affine wavelet transformations *IEEE Trans. Neural Netw.* **4** 73–85
[81] Alfano R R 2006 *The Supercontinuum Laser Source - Fundamentals with Updated References* 2nd edn (New York: Springer)
[82] Dudley J M and Coen S 2006 Supercontinuum generation in photonic crystal fiber *Reviews of Modern Physics* **78** 1135–84
[83] Birks T a, Knight J C and Russell P S 1997 Endlessly single-mode photonic crystal fiber *Optics letters* **22** 961–3
[84] Knight J C, Birks T a, St. Russell P J and Atkin D M 1996 All-silica single-mode optical fiber with photonic crystal cladding *Opt. Lett.* **21** 1547
[85] Knight J C, Birks T a, St. Russell P J and Atkin D M 1997 All-silica single-mode optical fiber with photonic crystal cladding: errata *Opt. Lett.* **22** 484
[86] NKT Photonics A/S 2009 Supercontinuum Generation in Photonic Crystal Fibers July
[87] Alfano R R and Shapiro S 1970 Observation of Self-Phase Modulation and Small-Scale Filaments in Crystals and Glasses *Physical Review Letters* **24** 592–4
[88] Alfano R R and Shapiro S 1970 Emission in the Region 4000 to 7000 Å Via Four-Photon Coupling in Glass *Physical Review Letters* **24** 584–7
[89] Baldeck P L, Ho P P and Alfano R R 1987 Effects of self, induced and cross phase modulations on the generation of picosecond and femtosecond white light supercontinua *Revue De łdots* **22** 1677–94
[90] Coen S, Chau a H, Leonhardt R, Harvey J D, Knight J C, Wadsworth W J and Russell P S 2001 White-light supercontinuum generation with 60-ps pump pulses in a photonic crystal fiber *Optics letters* **26** 1356–8

[91] Dudley J M, Provino L, Grossard N, Maillotte H, Windeler R S, Eggleton B J and Coen S 2002 Supercontinuum generation in air–silica microstructured fibers with nanosecond and femtosecond pulse pumping *J. Opt. Soc. Am. B* **19** 765

[92] Aceves A B, Chen R and Chung Y 2009 Analysis of supercontinuum generation under general dispersion characteristics and beyond the slowly varying envelope approximation *arXiv preprint arXiv: łdots* **X**

[93] Choi H-G, Kee C-S, Park H Y and Kim J-E Numerical analysis of supercontinuum generation in highly nonlinear photonic crystal fibers with ultrashort pulses *Journal of Optics A: Pure and Applied Optics* **11** 125101

[94] Coen S, Chau A H L, Leonhardt R, Harvey J D, Knight J C, Wadsworth W J and St. Russell P J 2002 Supercontinuum generation by stimulated Raman scattering and parametric four-wave mixing in photonic crystal fibers *J. Opt. Soc. Am. B* **19** 753

[95] Stolen R H and Ashkin A 1973 Optical Kerr effect in glass waveguide *Appl. Phys. Lett.* **22** 294–6

[96] Heidt A 2011 Novel coherent supercontinuum light sources based on all-normal dispersion fibers *Doctoral* Friedrich-Schiller-Universität Jena, Jena

[97] Moulton P F 1986 Spectroscopic and laser characteristics of Ti:Al_2O_3 *J. Opt. Soc. Am. B* **3** 125

[98] Spence D E, Kean P N and Sibbett W 1991 60-fsec pulse generation from a self-mode-locked Ti:sapphire laser *Opt. Lett.* **16** 42

[99] Aikawa K, Nagasawa Y, Suzuki K, Shimizu S, Suzuki T, Nakayama M, Kaneda K and Himeno K 2002 High-performance Dispersion-slope and Dispersion Compensation Modules *Fujikura Technical Review* **31** 59–64

[100] Zhu Y, Greenberg J A, Husein N A and Gauthier D J 2014 Giant all-optical tunable group velocity dispersion in an optical fiber *Opt. Express* **22** 14382

[101] Durst M E, Kobat D and Xu C 2009 Tunable dispersion compensation by a rotating cylindrical lens *Optics letters* **34** 1195

[102] Brennan J F 2005 Broadband fiber Bragg gratings for dispersion management *Journal of Optical and Fiber Communications Reports* **2** 397–434

[103] Lee G-H, Xiao S and Weiner AM 2006 Optical Dispersion Compensator With 4000-ps/nm Tuning Range Using a Virtually Imaged Phased Array (VIPA) and Spatial Light Modulator (SLM) *IEEE Photonics Technology Letters* **18** 1819–21

[104] Hult J, Watt R S and Kaminski C F 2007 Dispersion Measurement in Optical Fibers Using Supercontinuum Pulses *Journal of Lightwave Technology* **25** 820–4

[105] Sanders ST 2002 Wavelength-agile fiber laser using group-velocity dispersion of pulsed super-continua and application to broadband absorption spectroscopy *Applied Physics B: Lasers and Optics* **75** 799–802

[106] Hult J, Watt R S and Kaminski C F 2007 High bandwidth absorption spectroscopy with a dispersed supercontinuum source *Optics Express* **15** 11385–95

[107] Watt RS, Kaminski C F and Hult J 2007 Generation of supercontinuum radiation in conventional single-mode fibre and its application to broadband absorption spectroscopy *Applied Physics B* **90** 47–53
[108] Watt RS, Kaminski C F and Hult J 2007 High bandwidth H2O absorption spectroscopy in a flame using a dispersed supercontinuum source *Applied Physics B*
[109] Hagen C L and Sanders S 2006 Application of a Novel White Laser Sensor to an HCCI Engine *SAE Technical Paper*
[110] Kranendonk L A, Huber R, Fujimoto J G and Sanders S T 2007 Wavelength-agile H2O absorption spectrometer for thermometry of general combustion gases *Proceedings of the Combustion Institute* **31** 783–90
[111] Walewski JW and Sanders ST 2004 High-resolution wavelength-agile laser source based on pulsed super-continua *Applied Physics B* **79** 415–8
[112] Kaminski C F, Watt RS, Elder AD, Frank JH and Hult J 2008 Supercontinuum radiation for applications in chemical sensing and microscopy *Applied Physics B* **92** 367–78
[113] Kranendonk L A, Caswell A W, Myers A M and Sanders S T 2003 Wavelength-Agile Laser Sensors for Measuring Gas Properties in Engines *SAE Technical Paper*
[114] Watt R S, Laurila T, Kaminski C F and Hult J 2009 Cavity enhanced spectroscopy of high-temperature H(2)o in the near-infrared using a supercontinuum light source *Applied Spectroscopy* **63** 1389–95
[115] Werblinski T, Engel S R, Engelbrecht R and Will S 2013 Temperature and multi-species measurements by supercontinuum absorption spectroscopy for IC engine applications *Optics Express* **21** 3291–8
[116] Werblinski T, Mittmann F, Altenhoff M, Seeger T, Zigan L and Will S 2014 Temperature and water mole fraction measurements by time-domain-based supercontinuum absorption spectroscopy in a flame *Applied Physics B* **118** 153–8
[117] Werblinski T, Mittmann F, Zigan L and Will S 2014 Temperature measurements in gas flows at elevated pressures using supercontinuum absorption spectroscopy *ltces.dem.ist.utl.pt* 7–10
[118] Cooley J W and Tukey J W 1965 An Algorithm for the Machine Calculation of Complex Fourier Series *Mathematics of Computation* **19** 297
[119] Michelson A A 1891 XXVIII. Visibility of interference-fringes in the focus of a telescope *The London, Edinburgh, and Dublin Philosophical Magazine and Journal of Science* **31** 256–9
[120] Nielsen F D and Blume N G Discussion with Frederik D. Nielsen, Ph.D, NKT Photonics A/S
[121] Werle P, Mcke R and Slemr F 1993 The limits of signal averaging in atmospheric trace-gas monitoring by tunable diode-laser absorption spectroscopy (TDLAS) *Appl. Phys. B* **57** 131–9
[122] Levenberg K 1944 A method for the solution of certain non-linear problems in least squares *Quart. Appl. Math.* **2** 164–8

[123] Sorensen D C 1982 Newton's Method with a Model Trust Region Modification *SIAM J. Numer. Anal.* **19** 409–26
[124] Goldenstein C S and Hanson R K 2015 Diode-laser measurements of linestrength and temperature-dependent lineshape parameters for H2O transitions near 1.4μm using Voigt, Rautian, Galatry, and speed-dependent Voigt profiles *Journal of Quantitative Spectroscopy and Radiative Transfer* **152** 127–39
[125] Wagner G, Birk M, Gamache R R and Hartmann J-M 2005 Collisional parameters of lines: Effect of temperature *Journal of Quantitative Spectroscopy and Radiative Transfer* **92** 211–30
[126] Gamache R R and Hartmann J-M 2004 Collisional parameters of H2O lines: Effects of vibration *Journal of Quantitative Spectroscopy and Radiative Transfer* **83** 119–47
[127] Bürkle S, Walter N and Wagner S 2018 Laser-based measurements of pressure broadening and pressure shift coefficients of combustion-relevant absorption lines in the near-infrared region *Appl. Phys. B* **124** 121
[128] Nassar R and Bernath P 2003 Hot methane spectra for astrophysical applications *Journal of Quantitative Spectroscopy and Radiative Transfer* **82** 279–92
[129] Rey M, Nikitin A V and Tyuterev V G 2014 THEORETICAL HOT METHANE LINE LISTS UP TO T = 2000 K FOR ASTROPHYSICAL APPLICATIONS *ApJ* **789** 2
[130] Burrell K H 1990 Error analysis for parameters determined in nonlinear least-squares fits *American Journal of Physics* **58** 160–4
[131] Kent J H, Jander H and Wagner H G 1981 Soot formation in a laminar diffusion flame *Symposium (International) on Combustion* **18** 1117–26
[132] Norton T S, Smyth K C, Miller J H and Smooke M D 1993 Comparison of Experimental and Computed Species Concentration and Temperature Profiles in Laminar, Two-Dimensional Methane/Air Diffusion Flames *Combustion Science and Technology* **90** 1–34
[133] Houston Miller J, Elreedy S, Ahvazi B, Woldu F and Hassanzadeh P 1993 Tunable diode-laser measurement of carbon monoxide concentration and temperature in a laminar methane–air diffusion flame *Applied optics* **32** 6082
[134] Savitzky A and Golay M J E 1964 Smoothing and Differentiation of Data by Simplified Least Squares Procedures *Anal. Chem.* **36** 1627–39
[135] Peterson B, Baum E, Böhm B, Sick V and Dreizler A 2014 Evaluation of toluene LIF thermometry detection strategies applied in an internal combustion engine *Appl. Phys. B* **117** 151–75
[136] Alsmeyer F, Koß H-J and Marquardt W 2004 Indirect Spectral Hard Modeling for the Analysis of Reactive and Interacting Mixtures *Applied Spectroscopy* **58**
[137] Kriesten E, Mayer D, Alsmeyer F, Minnich CB, Greiner L and Marquardt W 2008 Identification of unknown pure component spectra by indirect hard modeling *Chemometrics and Intelligent Laboratory Systems* **93** 108–19

[138] Kriesten E, Alsmeyer F, Bardow A and Marquardt W 2008 Fully automated indirect hard modeling of mixture spectra *Chemometrics and Intelligent Laboratory Systems* **91** 181–93

[139] Beumers P, Engel D, Brands T, Koß H-J and Bardow A 2018 Robust analysis of spectra with strong background signals by First-Derivative Indirect Hard Modeling (FD-IHM) *Chemometrics and Intelligent Laboratory Systems* **172** 1–9

[140] Petersen C R, Møller U, Kubat I, Zhou B, Dupont S, Ramsay J, Benson T, Sujecki S, Abdel-Moneim N, Tang Z, Furniss D, Seddon A and Bang O 2014 Mid-infrared supercontinuum covering the 1.4–13.3 μm molecular fingerprint region using ultra-high NA chalcogenide step-index fibre *Nature Photon* **8** 830–4